Correlative light and electron microscopy to study ciliogenesis

DISSERTATION ZUR ERLANGUNG DES DOKTORGRADES DER NATURWISSENSCHAFTEN (DR. RER. NAT.) DER FAKULTÄT FÜR BIOLOGIE UND VORKLINISCHE MEDIZIN DER UNIVERSITÄT REGENSBURG

vorgelegt von

Korbinian Bürger

aus

Freyung

im Jahr

2021

Das Promotionsgesuch wurde eingereicht am:

Die Arbeit wurde angeleitet von:

Prof. Dr. Ralph Witzgall

Unterschrift:

_____

Korbinian Bürger

The following two manuscripts were published in context with the present thesis:

Buerger, K., Schmidt, K.N., Fokkema, J., Gerritsen, H.C., Maier, O. & Vries, U. de *et al.* (2021). **On-section correlative light and electron microscopy of large cellular volumes using STEM tomography**. *Methods in Cell Biology*, 162: 171–203.

Contribution: The author of the present thesis performed molecular cloning, cell culture, fluorescence microscopy and overlay generation. He further contributed to sample preparation for electron microscopy. He wrote the first version of the manuscript and was involved in proofreading and subsequent corrections.

Asam, C., **Buerger, K.**, Felthaus, O., Brébant, V., Rachel, R. & Prantl, L. et al. (2019). **Subcellular localization of the chemotherapeutic agent doxorubicin in renal epithelial cells and in tumor cells using correlative light and electron microscopy**. *Clinical Hemorheology and Microcirculation*, 73: 157–167.

Contribution: The author of the present thesis provided hints for sample preparation for correlative light and electron microscopy and for fluorescence microscopy, instructed and assisted in overlay generation and was involved in proofreading and optimizing the manuscript.

Table of Contents

1 Introduction

1.1 Function of primary cilia and ciliopathies

"The Cilium: Cellular Antenna and Central Processing Unit" (Malicki & Johnson 2017): titles similar to this one of a recent review impressively demonstrate how much the awareness of the importance of cilia is present nowadays (Satir *et al.* 2010; Witzgall 2018b). Similar to an antenna (Ishikawa & Marshall 2011) this organelle emanates with its membrane-surrounded microtubule core from the apical plasma membrane of a cell (Mukhopadhyay *et al.* 2017; Pedersen *et al.* 2012; Satir *et al.* 2010) and is anchored via the basal body (Breslow & Holland 2019). The basal body develops from the mother centriole which is part of the centrosome along with the younger daughter centriole and the pericentriolar material (Anderson *et al.* 2008; Breslow & Holland 2019; Kobayashi & Dynlacht 2011).

Cilia can be discriminated in motile or immotile so-called primary cilia (Sorokin 1968) and therefore have different functions; reviewed in (Reiter & Leroux 2017; Satir *et al.* 2010). Whereas motile cilia predominantly are important for a variety of movement sequences in the whole body (including embryonic development) (Reiter & Leroux 2017), primary cilia are indispensable for mechanosensation, chemosensation and cellular signaling pathways (Anderson *et al.* 2008; Witzgall 2018a). The complexity of the formation and structure of cilia as well as the importance of their function is apparently considering the large number of diseases – so-called ciliopathies – resulting from ciliary dysfunction (Gerdes *et al.* 2009; Reiter & Leroux 2017). Some ciliopathies are even lethal (Reiter & Leroux 2017). Reiter & Leroux 2017 classified ciliopathies depending on whether the disease is caused by proteins which are part of the cilium or basal body (first-order ciliopathies) or by proteins that are not located within the "ciliary compartment" (Hu & Nelson 2011) but are indispensable for its functionality (second-order ciliopathies) (Reiter & Leroux 2017). As an impaired function of some ciliary proteins can also cause diseases with "phenotypes that are unrelated to ciliary function" (Reiter & Leroux 2017) it is obvious that the cilium is in close interaction with the rest of the cell body (Reiter & Leroux 2017).

In contrast to the long-standing assumption that primary cilia represent only rudiments (Satir *et al.* 2010; Witzgall 2018a), their importance is now undisputed (Breslow & Holland 2019; Davenport & Yoder 2005; Ishikawa & Marshall 2011), as it is known that an impaired function of these immotile cilia affects a large variety of organs such as the brain, heart, liver, kidney but also the

skeleton, the olfaction, taste and hearing (Davenport & Yoder 2005; Reiter & Leroux 2017). For example, patients with polycystic kidney disease (PKD) suffer i.a. from cyst formation within their kidneys resulting in renal failure (Harris & Torres 2009). The reason of these diseases are mutations in genes, in case of the autosomal dominant disorders of the two genes PKD1 and PKD2 encoding for the membrane proteins Polycystin-1 and Polycystin-2 which are important for the function of primary cilia (Harris & Torres 2009; Mukhopadhyay *et al.* 2017). In addition, primary cilia are important for signal transduction pathways (Gerdes *et al.* 2009; Kobayashi & Dynlacht 2011; Reiter & Leroux 2017; Witzgall 2018a) with Wnt signaling and Hedgehog signaling being the most prominent ones (Gerdes *et al.* 2009). While in canonical Wnt signaling extracellular stimuli specifically can activate transcription of some genes, the noncanonical pathway counteracts this activation (Benzing *et al.* 2007; Gerdes *et al.* 2009). Primary cilia play an essential role in maintaining this balance (Gerdes *et al.* 2009). As already pointed out by Reiter & Leroux 2017 the contribution of primary cilia to Hedgehog signaling is even more apparent (Reiter & Leroux 2017). The Hedgehog pathway is initialized by binding of ligands to the receptor Patched which is located within the ciliary membrane, a membrane compartment which encloses the axoneme (Gigante & Caspary 2020; Pedersen *et al.* 2016; Reiter & Leroux 2017). Upon Hedgehog ligand binding Patched is no longer detected at the cilium but the transmembrane protein Smoothened (Corbit *et al.* 2005) is enriched (Gigante & Caspary 2020; Reiter & Leroux 2017) and Patched loses its inhibitory effect on Smoothened (Gerdes *et al.* 2009; Gigante & Caspary 2020). These processes result in an altered processing of glioma proteins whereby the repressing effect of these transcription factors is converted into an activating one (Gerdes *et al.* 2009; Gigante & Caspary 2020; Reiter & Leroux 2017). Furthermore, there are "Smoothened-independent […] non-canoncial" (Pietrobono *et al.* 2019) Hedgehog pathways leading to glioma protein activation (Pietrobono *et al.* 2019). Due to their involvement in Hedgehog signaling pathological cilia formation and disassembly even contribute to carcinogenesis and affect treatment (Breslow & Holland 2019; Wang & Dynlacht 2018).

As the formation of primary cilia – ciliogenesis – is a "multistep process" (Pitaval *et al.* 2017) which requires the function of a variety of proteins (Sánchez & Dynlacht 2016) it is frequently linked to ciliopathies (Reiter & Leroux 2017). Despite intensive research in the last years (Sánchez & Dynlacht 2016) ciliogenesis remains "poorly understood" (Bershteyn *et al.* 2010) so far. The generation of more detailed knowledge about the events taking place during ciliogenesis thus will

result in better understanding of related diseases (Breslow & Holland 2019; Reiter & Leroux 2017). The following chapters provide an overview of the structure of primary cilia as well as the processes that contribute to their formation. Various sources have been used to structure the first main section of the present work (Gürster 2013; Schmidt 2013; Witzgall 2018b).

1.2 The primary cilium and its components

The primary cilium is a complex organelle with a variety of ultrastructural details (Fig. 1) (Gerdes *et al.* 2009). An overview of the main components of primary cilia is given in the following and some information about their respective functions is listed as well.

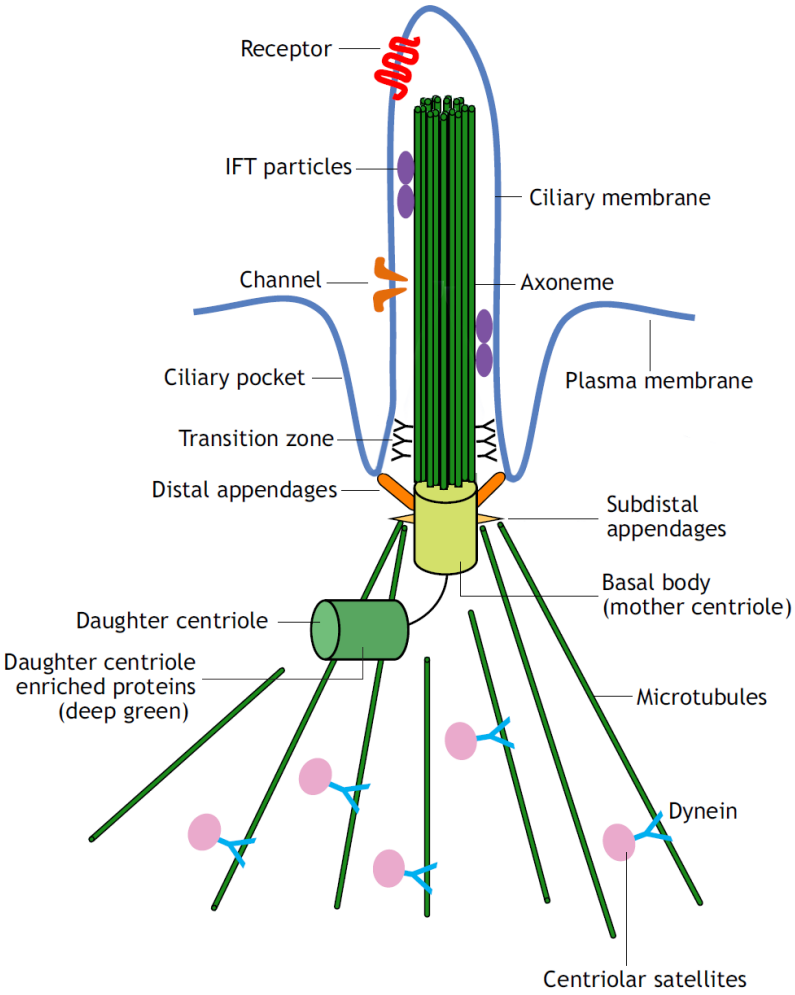

Figure 1: Schematic drawing of the primary cilium. The core of the primary cilium is a "microtubule-based axoneme" (Conkar & Firat-Karalar 2020) (dark green) which is enclosed by "a specialized extension of the cell membrane" (Wood & Rosenbaum 2015) (blue). Several receptors (red) and channels (orange) important for the function of primary cilia are located within the ciliary membrane (Wang & Dynlacht 2018). The axoneme "extends from a basal body" (Satir *et al.* 2010) (light green), a differentiated version of the mother centriole. The basal body is

docked to the cell membrane via its distal appendages (orange) (Schmidt *et al.* 2012). The subdistal appendages (yellow) of the basal body are associated with microtubules (dark green) (Mogensen *et al.* 2000). Within the transition zone champagne glass-shaped structures (black) link the axoneme with the ciliary membrane (Gilula & Satir 1972). Intraflagellar transport (IFT) particles (purple) mediate "the transport of cargo along the ciliary axoneme" (Malicki 2012). The ciliary pocket – "an invagination of the plasma membrane" (Molla-Herman *et al.* 2010) – is formed during the formation of primary cilia in some cell types. "Nonmembranous, electron-dense particles" (Kobayashi *et al.* 2014) – the satellites (Bernhard & Harven 1960) – are removed from the pericentriolar region. Further details regarding the structural components of the primary cilium shown in this figure are explained in detail in chapter 1.2. Image was adapted from Wang & Dynlacht 2018 with permission of Development, The Company of Biologists (https://dev.biologists.org/content/145/18/dev151407).

1.2.1 The basal body and microtubule core

During ciliogenesis the older of the two centrioles of the centrosome which is called mother centriole differentiates into the basal body (Anderson *et al.* 2008; Breslow & Holland 2019; Kobayashi & Dynlacht 2011). Both centrioles/basal bodies and the ciliary axoneme are formed by microtubules. The structural unit of microtubules are heterodimers consisting of the two proteins α- and β-tubulin. These tubulin dimers polymerize linearly to form a protofilament; reviewed in (Pedersen *et al.* 2012). A microtubule in turn consists of 13 linear protofilaments which laterally interact with each other to form a circular structure with a central hole (Tilney *et al.* 1973); reviewed in (Pedersen *et al.* 2012). Since microtubules are formed by heterodimers, they have a polarity, i.e. a fast polymerizing plus and a slower polymerizing minus end (Allen & Borisy 1974); reviewed in (Pedersen *et al.* 2012). While the minus end is stabilized by a ring-shaped complex of γ-tubulin (Zheng *et al.* 1995) periods of growth and microtubule depolymerization alternate at the plus end; reviewed in (Pedersen *et al.* 2012). Post-translational modifications of tubulins such as acetylation (L'Hernault & Rosenbaum 1983) are found on stabilized microtubules; reviewed in (Pedersen *et al.* 2012).

Each centriole or basal body consists of nine circular arranged triplet microtubules (A, B and C tubule) with the plus end of the microtubules at the centriole's distal end. The C tubule of the triplet terminates proximal to the A and B tubule which further polymerize to form the axoneme of the cilium thus consisting of nine doublet microtubules. Whereas the A tubule is formed by 13 protofilaments, the B tubule is incomplete (only 11 protofilaments); reviewed in (Anderson *et al.* 2008; Breslow & Holland 2019; Nachury *et al.* 2010; Pedersen *et al.* 2012; Prevo *et al.* 2017; Welsch *et al.* 2014). The doublet microtubules within the axoneme are connected with each other

via nexin (Stephens 1970); reviewed in (Pedersen *et al.* 2012). In contrast to most motile cilia, primary cilia have neither a central pair of microtubules (9+0) ("central filaments are absent" (Porter 1957); reviewed in (Barnes 1961)) nor dynein arms or radial spokes; reviewed in (Anderson *et al.* 2008; Pedersen *et al.* 2012; Satir *et al.* 2010; Satir 2017). However, in performing cryo-electron tomography a recent study revealed evidence that the axoneme of mammalian primary cilia consists not of a microtuble doublet arrangement but rather of an "unstructured bundle […] of microtubules" (Kiesel *et al.* 2020). At the proximal end of the basal body the filamentous striated rootlets penetrate into the cell interior (Tachi *et al.* 1974); reviewed in (Pedersen *et al.* 2012; Seeley & Nachury 2010). The function of these structures particularly consisting of the protein rootletin (Yang *et al.* 2002) is obscure besides the fact that they seem to be dispensable for ciliogenesis; reviewed in (Seeley & Nachury 2010).

At the distal end of the mother centriole (but not of the daughter centriole) there are the nine subdistal and distal appendages (Paintrand *et al.* 1992); reviewed in (Pedersen *et al.* 2012; Rohatgi & Snell 2010; Yang *et al.* 2018). The distal appendages consist of "pinwheel-like" (Yang *et al.* 2018) alar sheets (Anderson 1972; Anderson & Brenner 1971) and the intervening distal appendage matrix (Yang *et al.* 2018). Whereas "CEP83 is located at the root of the" (Lo *et al.* 2019) blades, CEP164 is the outermost protein within the blades (Yang *et al.* 2018). The proteins of the blades are essential for docking of membranes to the mother centriole (Schmidt *et al.* 2012; Yang *et al.* 2018). According to Viol *et al.* 2020 there are two different groups of distal appendage proteins: whereas proteins of the first group are permanently associated with the mother centriole, proteins of the second group are removed via kinases such as NEK2 before the cell enters mitosis (Viol *et al.* 2020). Proximal to the distal appendages the subdistal appendages are located at the mother centriole (Paintrand *et al.* 1992); reviewed in (Pedersen *et al.* 2012). These structures, also called basal feet (Gibbons 1961) at ciliated basal bodies, have contact to the minus end of microtubules and thus contribute to anchoring the cilium to the microtubule cytoskeleton (Mogensen *et al.* 2000); reviewed in (Pedersen *et al.* 2012; Seeley & Nachury 2010).

In the pericentrosomal region there are cytoplasmic granules – the satellites (Bernhard & Harven 1960) – which contribute to vesicular trafficking to the centrosome and also have an impact on ciliogenesis (see section 1.3.1); reviewed in (Pedersen *et al.* 2012; Wang & Dynlacht 2018). For example proteins required for cilia formation such as CEP290 (Kim *et al.* 2008) i.a. "localize to centriolar satellites" (Reiter & Leroux 2017).

1.2.2 The intraciliary transport mechanism

Proteins important for ciliogenesis and the function of cilia "are transported along axonemal microtubules" (Satir *et al.* 2010) via intraflagellar transport (IFT) (Kozminski *et al.* 1993; Pazour *et al.* 2002a); reviewed in (Pedersen *et al.* 2008). Pleas note that much of the current knowledge described in this chapter is based on studies from motile cilia (Pedersen *et al.* 2008; Prevo *et al.* 2017). Although IFT trains were detected in primary cilia of mammalian cells as well, it still has to be elucidated to which extent structure and function of IFT in motile cilia is comparable to IFT in primary cilia (Kiesel *et al.* 2020).

Intraflagellar transport takes place "between the outer doublet microtubules and the" (Rosenbaum & Witman 2002) ciliary membrane and is bidirectional, i.e. from cilia base to tip (anterograde) as well as from cilia tip to base (retrograde) (Kozminski *et al.* 1993); reviewed in (Pedersen *et al.* 2008). The heart of the "IFT machinery" (Prevo *et al.* 2017) are motor proteins, which perform mechanical work, i.e. movement, upon ATP hydrolysis; reviewed in (Prevo *et al.* 2017). The anterograde transport is directed towards the microtubule plus end (Kozminski *et al.* 1995) along the B tubule of the doublet microtubules (Stepanek & Pigino 2016) and "is mediated by the heterotrimeric kinesin" (Gerdes *et al.* 2009)-II complex (Walther *et al.* 1994); reviewed in (Pedersen *et al.* 2008; Prevo *et al.* 2017; Rosenbaum & Witman 2002). Cytoplasmic dynein-2 complex (Gibbons & Rowe 1965) contributes to retrograde movement along the A tubule of the doublet microtubules (Stepanek & Pigino 2016) which is directed towards their minus ends (Pazour *et al.* 1999); reviewed in (Pedersen *et al.* 2008; Prevo *et al.* 2017; Rosenbaum & Witman 2002). In addition to the motor complexes, the "IFT machinery" (Prevo *et al.* 2017) also contains so-called IFT particle polypeptides (Piperno & Mead 1997); reviewed in (Pedersen *et al.* 2008; Rosenbaum & Witman 2002). These polypeptides are organized in the two complexes (Cole *et al.* 1998); reviewed in (Pedersen *et al.* 2008; Rosenbaum & Witman 2002; Taschner *et al.* 2012). Complex A (IFT-A) is involved in retrograde transport and consists of six polypeptides, complex B (IFT-B) of a "salt-stable core complex" (Taschner *et al.* 2012) (ten polypeptides) and of a peripheral complex (six polypeptides) and contributes to anterograde transport; reviewed in (Hao & Scholey 2009; Prevo *et al.* 2017; Taschner *et al.* 2012). The proteins of both IFT complexes can interact with each other as well as bind to the motor complexes and other cargo proteins; reviewed in (Pedersen *et al.* 2008; Prevo *et al.* 2017; Taschner *et al.* 2012).

The mechanism of canonical IFT is often described using a six-phase model (Hao & Scholey 2009; Ishikawa & Marshall 2017; Pedersen *et al.* 2008). First the "anterograde IFT machinery" (Pedersen *et al.* 2008) is assembled at the base of the forming cilium, whereby cargo proteins are bound (Hao & Scholey 2009; Ishikawa & Marshall 2011, 2017; Pedersen *et al.* 2008; Prevo *et al.* 2017). Next the "anterograde IFT machinery" (Pedersen *et al.* 2008) is moving along the outer doublet microtubules towards the tip of the cilium (Hao & Scholey 2009; Ishikawa & Marshall 2011, 2017; Pedersen *et al.* 2008; Prevo *et al.* 2017). Once the ciliary tip has been reached, the components of IFT machinery dissociate (Pedersen *et al.* 2008). The "retrograde IFT machinery" (Prevo *et al.* 2017) is formed at the tip of the cilium and dynein-2 mediates the transport back to the ciliary base where the machinery disassembles. (Hao & Scholey 2009; Ishikawa & Marshall 2011, 2017; Pedersen *et al.* 2008; Prevo *et al.* 2017). Please note that IFT mediates not only cargo transport in mature cilia but also during cilia formation and thus is important for establishing primary cilia (Moyer *et al.* 1994); reviewed in (Pedersen *et al.* 2008; Rosenbaum & Witman 2002).

1.2.3 The ciliary membrane

The axoneme of primary cilia is enclosed by a "highly specialized" (Rohatgi & Snell 2010) lipid bilayer, which is called the ciliary membrane and "is continuous with the [cell's] plasma membrane" (Porter 1957); reviewed in (Pedersen *et al.* 2012; Rohatgi & Snell 2010; Satir 2017). On the one hand, "the composition of the lipids of […] [the ciliary membrane] is markedly different from that of" (Smith *et al.* 1970) the plasma membrane (Smith *et al.* 1970; Tyler *et al.* 2009); reviewed in (Garcia *et al.* 2018; Gürster 2013; Kaneshiro 1990; Nachury *et al.* 2010). So-called lipid rafts, membrane regions rich in sterols and sphingolipids, are frequent components of e.g. the flagellar membrane (Tyler *et al.* 2009). Due to their higher order, lipid rafts have a lower fluidity than the surrounding membrane (Tyler *et al.* 2009). On the other hand, the specialized lipid composition results in a different protein composition as well (Garcia *et al.* 2018; Tyler *et al.* 2009). Ciliary membrane proteins are ion channels or special mechanosensory transmembrane proteins such as the polycystic kidney disease proteins Polycystin-1 (Yoder *et al.* 2002) and Polycystin-2 (Pazour *et al.* 2002b; Yoder *et al.* 2002) contributing to the function of primary cilia; reviewed in (Garcia *et al.* 2018; Nachury *et al.* 2010; Pedersen *et al.* 2012; Rohatgi & Snell 2010; Witzgall 2018a). In addition, there are also receptors such as Patched1 (Rohatgi *et al.* 2007) or Smoothened (Corbit *et al.* 2005) which are components of ciliary signal transduction cascades; reviewed in (Garcia *et al.* 2018; Gigante & Caspary 2020; Pedersen *et al.* 2012; Rohatgi & Snell 2010).

1.2.4 The ciliary pocket

The membrane surrounding the ciliary membrane at the base of primary cilia is called periciliary membrane (Garcia *et al.* 2018; Garcia-Gonzalo & Reiter 2012; Long & Huang 2019; Pedersen *et al.* 2016). Due to the intracellular pathway of ciliogenesis of some cell types (see section 1.3.1) a part of the cilium (Molla-Herman *et al.* 2010; Sorokin 1962) or even the entire cilium (Mazo *et al.* 2016) is embedded within the cell body and the periciliary membrane shows an invagination, which is called the ciliary pocket (Molla-Herman *et al.* 2010); reviewed in (Garcia-Gonzalo & Reiter 2012; Ghossoub *et al.* 2011; Long & Huang 2019). Ghossoub *et al.* 2011 defined the area as a ciliary pocket, which spans from the docking site of the basal body "to the region where the […] [cilium] emerges in the extracellular milieu" (Ghossoub *et al.* 2011). The proximal part of this pocket near the envelope often appears widened, while the distal part is only a narrow space (Benmerah 2013). The ciliary pocket membrane interacts with actin filaments (Molla-Herman *et al.* 2010); reviewed in (Ghossoub *et al.* 2011). This actin network is important for maintaining the pocket's morphology (García-Salcedo *et al.* 2004); reviewed in (Ghossoub *et al.* 2011).

Endocytic events as clathrin-coated pits can be detected frequently at the ciliary pocket membrane (Molla-Herman *et al.* 2010); reviewed in (Ghossoub *et al.* 2011). Clathrin-mediated endocytosis has no impact on the formation of primary cilia (Molla-Herman *et al.* 2010) but substantially contributes to the ciliary function (Clement *et al.* 2013); reviewed in (Pedersen *et al.* 2016). For example, transforming growth factor β signaling at the cilium of human foreskin fibroblasts is reduced after inhibition of clathrin-mediated endocytosis using the drug Dynasore (Clement *et al.* 2013).

1.2.5 The transition zone and diffusion barrier

The transition zone is located at the region housing the transition of the distal end of the basal body to the axoneme; reviewed in (Garcia-Gonzalo & Reiter 2012; Pedersen *et al.* 2012). There are two structural components in this region: the transition fibers, also called alar sheets (Anderson 1972; Anderson & Brenner 1971) and the Y-shaped connectors/links (synonymous with the term champagne-glass structure) (Gilula & Satir 1972); reviewed in (Garcia-Gonzalo & Reiter 2012; Hu & Nelson 2011; Pedersen *et al.* 2012) (see Fig. 1).

The nine transition fibers are counterclockwise faced trapezoidal sheet-like structures (Anderson 1972; Anderson & Brenner 1971); reviewed in (Nachury *et al.* 2010; Seeley & Nachury 2010).

They represent distal appendages of the basal body that connect the distal region of the triplet microtubules of the basal body with the membrane at the proximal end of the ciliary shaft (Anderson 1972); reviewed in (Garcia-Gonzalo & Reiter 2012; Nachury *et al.* 2010; Pedersen *et al.* 2012; Rohatgi & Snell 2010). Nachury *et al.* 2010 postulated based on electron micrographs of Anderson 1972 that only particles with a diameter up to 60 nm can pass "the space between two" (Nachury *et al.* 2010) adjacent alar sheets. Components of the "intraflagellar transport machinery" (Prevo *et al.* 2017) can dock to transition fibers (Deane *et al.* 2001) making them indispensable for ciliary cargo transport; reviewed in (Pedersen *et al.* 2012; Rosenbaum & Witman 2002).

Y-shaped connectors/links are located distal to the transition fibers and connect doublet microtubules with the ciliary membrane (Gilula & Satir 1972); reviewed in (Garcia-Gonzalo & Reiter 2012; Pedersen *et al.* 2012). As the ciliary membrane contains particle strings at this region, this region is often referred to as the ciliary necklace (Gilula & Satir 1972); reviewed in (Pedersen *et al.* 2012; Satir *et al.* 2010). A large number of proteins is involved in the formation of these "champagne glass-shaped structures" (Garcia-Gonzalo & Reiter 2012) which are in contact with transmembrane proteins of the ciliary membrane; reviewed in (Garcia-Gonzalo & Reiter 2012) (Fig. 2). For example the protein CEP290 is present at the central part of the Y-shaped connectors (Craige *et al.* 2010; reviewed in Garcia-Gonzalo & Reiter 2012) and loss of CEP290 in *Chlamydomonas reinhardtii* results in disruption of the ultrastructure of Y-shaped connectors and impaired "microtubule-membrane connections" (Craige *et al.* 2010).

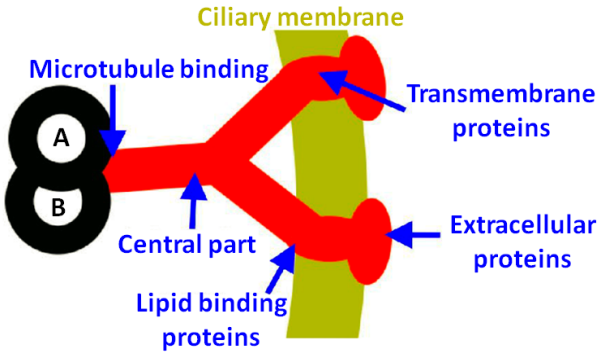

Figure 2: Schematic drawing of a cross-section of a Y-link. The Y-link (red) consists of proteins anchoring it to the doublet microtubules (black), proteins as CEP290 form its central part (Craige *et al.* 2010), proteins with lipid-binding domains and transmembrane proteins gain a contact with the ciliary membrane (ocher colored). Additional, proteins interact with the transmembrane proteins at the extracellular side of the ciliary membrane; reviewed in (Garcia-Gonzalo & Reiter 2012). Image was taken from Garcia-Gonzalo & Reiter 2012, labeling was modified. Permission was kindly granted by The Journal of Cell Biology, The Rockefeller University Press.

Since the cilium has a "composition […] distinct from that of the surrounding cytosol and plasma membrane" (Garcia-Gonzalo & Reiter 2012), there must be a barrier regulating molecule exchange according to several authors (Garcia-Gonzalo & Reiter 2012; Nachury *et al.* 2010; Pedersen *et al.* 2012; Rohatgi & Snell 2010). However, different theories exist regarding the ultrastructural localization of this barrier. (Nachury *et al.* 2010). Nachury *et al.* 2010 discuss two possibilities: the barrier could be located at the base of the ciliary shaft "at the docking site of [the] transition fibers" (Benmerah 2013) to the membrane (Ghossoub *et al.* 2011; Nachury *et al.* 2010). In contrast, the barrier could be "positioned at least 0.5 μm away from the base of the ciliary shaft" (Nachury *et al.* 2010) towards the surrounding plasma membrane (Nachury *et al.* 2010).

Furthermore, there is no detailed knowledge regarding the composition of the barrier and various components are discussed in reviews (Hu & Nelson 2011; Nachury *et al.* 2010; Rosenbaum & Witman 2002). For example, loss of the transition zone protein CEP290 results in "abnormal protein composition" (Craige *et al.* 2010) of flagella (i.e. motile cilia) of *Chlamydomonas reinhardtii* (Craige *et al.* 2010); reviewed in (Garcia-Gonzalo & Reiter 2012). Based on their findings Craige *et al.* 2010 hypothesized that components of the transition zone such as Y-shaped connectors are involved in barrier formation at the base of flagella/cilia. In addition to the Y-links (Hu & Nelson 2011) the transition fibers (Rosenbaum & Witman 2002) are thought to limit the access to the cilium due to their distance from each other, are considered to be part of the barrier (Anderson 1972; Nachury *et al.* 2010). Although the two membranes are continuous with each other (Porter 1957; reviewed in Pedersen *et al.* 2012; Rohatgi & Snell 2010; Satir 2017), the ciliary membrane has a different composition than the plasma membrane (Smith *et al.* 1970; Tyler *et al.* 2009; reviewed in Garcia *et al.* 2018; Nachury *et al.* 2010) further indicating the existence of a barrier (Rohatgi & Snell 2010). The strong membrane curvature at the ciliary base and its interaction with the transition fibers are discussed to form a barrier (Rohatgi & Snell 2010). According to Nachury *et al.* 2010 the compartmentalization of the cell membrane (Fujiwara *et al.* 2002) could also contribute to barrier formation (Nachury *et al.* 2010): in close vicinity to "the cytoplasmic side of the plasma membrane" (Nachury *et al.* 2010) there is an actin network (Morone *et al.* 2006) to which transmembrane proteins are anchored and thus immobilized; reviewed in (Nachury *et al.* 2010). The compartmentalization of the membrane caused by the immobilization drastically slows down the diffusion of the molecules within the membrane resulting in a kind of barrier function; reviewed in (Nachury *et al.* 2010). Several more candidates are enumerated to be

part of the barrier (Hu & Nelson 2011). In addition to CEP290 (Craige *et al.* 2010; reviewed in Ishikawa & Marshall 2011), septin GTPases (Hu *et al.* 2010), which can "form ring-like structures" (Hu & Nelson 2011; Pedersen *et al.* 2012) are located at the transition zone of primary cilia and contribute to the barrier function as well; reviewed in (Hu & Nelson 2011; Pedersen *et al.* 2012).

Since there are data (Dishinger *et al.* 2010; Kee *et al.* 2012) indicating that the ciliary barrier is organized similarly to the nuclear pore, the term "pore complex" (Rosenbaum & Witman 2002) is also used in this context; reviewed in (Nachury *et al.* 2010; Pedersen *et al.* 2012; Rosenbaum & Witman 2002). Proteins transported to the cilium – such as the kinesin-II motor protein KIF17 – have a ciliary localization sequence similar to the nuclear localization signal (Dishinger *et al.* 2010); reviewed in (Pedersen *et al.* 2012). Furthermore, components that are indispensable for the functionality of the nuclear pore complex, such as RAN-GTP or Importin β2, were detected at the cilium as well (Dishinger *et al.* 2010); reviewed in (Pedersen *et al.* 2012).

Due to the lack of knowledge, there are also various theories how proteins can pass the barrier (Nachury *et al.* 2010). Cytoplasmic proteins are believed to diffuse to the base of the cilium (Garcia-Gonzalo & Reiter 2012) or are transported along microtubules as e.g. demonstrated for the protein GLI2 (Kim *et al.* 2009); reviewed in (Garcia-Gonzalo & Reiter 2012). Small molecules can pass the barrier freely (Kee *et al.* 2012); reviewed in (Garcia *et al.* 2018; Garcia-Gonzalo & Reiter 2012; Nachury *et al.* 2010; Pedersen *et al.* 2012). In contrast, transmembrane proteins are transported via vesicles to the ciliary base targeted by their ciliary localization sequence (Geng *et al.* 2006; Tam *et al.* 2000) and finally are exocytosed; reviewed in (Nachury *et al.* 2010; Pedersen *et al.* 2008; Rosenbaum & Witman 2002). IFT particles such as IFT20 (Follit *et al.* 2006) contribute to this "delivery of [...] membrane proteins [...] to the cilium" (Follit *et al.* 2006); reviewed in (Garcia-Gonzalo & Reiter 2012; Nachury *et al.* 2010). Furthermore, there are data indicating that the BBSome – a complex of eight proteins (Loktev *et al.* 2008; Nachury *et al.* 2007); reviewed in (Garcia *et al.* 2018; Prevo *et al.* 2017) – is involved in targeting membrane proteins as e.g. Somatostatin receptor 3 to cilia (Jin *et al.* 2010); reviewed in (Nachury *et al.* 2010). However, some transmembrane proteins such as Smoothened (Milenkovic *et al.* 2009; Monis *et al.* 2017) are not initially transported to the ciliary base but to the plasma membrane and then taken up into the ciliary membrane via a lateral transport; reviewed in (Long & Huang 2019; Nachury *et al.* 2010). IFT could mediate the transport of this transmembrane proteins through the ciliary barrier (Nachury *et al.* 2010).

1.3 Ciliogenesis

The biogenesis of primary cilia, also called ciliogenesis, takes place during the G_1/G_0 phase of the cell cycle (Archer & Wheatley 1971); reviewed in (Pedersen *et al.* 2012; Plotnikova *et al.* 2009). As already reviewed several times, ciliogenesis of primary cilia was first described by Sergei Sorokin (Sorokin 1962) and was divided in ultrastructural distinct stadia; reviewed in (Ghossoub *et al.* 2011; Pedersen *et al.* 2012). There are two different cell type-dependent ways how primary cilia can form (Molla-Herman *et al.* 2010; Sorokin 1968); reviewed in (Ghossoub *et al.* 2011; Pedersen *et al.* 2012). The extracellular pathway is characteristic for polarized epithelial cells and ciliogenesis occurs in vicinity to the apical plasma membrane (Molla-Herman *et al.* 2010; Sorokin 1968); reviewed in (Benmerah 2013; Ghossoub *et al.* 2011; Pedersen *et al.* 2012; Walia *et al.* 2019). Furthermore, at an early developmental stadium a contact between the mother centriole and the plasma membrane is established (Molla-Herman *et al.* 2010; Sorokin 1968); reviewed in (Ghossoub *et al.* 2011; Pedersen *et al.* 2012). In contrast, the intracellular pathway of e.g. fibroblasts comprises an almost complete cilium maturation inside the cell body before it is linked to the plasma membrane (Molla-Herman *et al.* 2010; Sorokin 1962); reviewed in (Ghossoub *et al.* 2011; Pedersen *et al.* 2012).

1.3.1 Intracellular pathway

As summarized by Ghossoub *et al.* 2011, retinal pigment epithelial 1 (RPE1) cells are a common model to investigate the intracellular pathway (Ghossoub *et al.* 2011) because serum starvation/withdrawal effectively stimulates ciliogenesis within these cells (Ganga *et al.* 2021; Ghossoub *et al.* 2011; Katoh *et al.* 2017; Pitaval *et al.* 2010; Saito *et al.* 2018; Walia *et al.* 2019; Wu *et al.* 2018). Please note, however, with polarized epithelial cells typically following the extracellular pathway of ciliogenesis (Molla-Herman *et al.* 2010; Sorokin 1968; reviewed in Benmerah 2013; Ghossoub *et al.* 2011; Pedersen *et al.* 2012; Walia *et al.* 2019), the RPE1 cell line is an exception; reviewed in (Breslow & Holland 2019). The detailed molecular mechanisms promoting ciliogenesis after serum starvation in RPE1 cells are currently subject of research (Walia *et al.* 2019). Removal of "protein-based growth factors" (Walia *et al.* 2019) present in fetal bovine serum (Zheng *et al.* 2006) has probably no effect on ciliogenesis (Walia *et al.* 2019). Walia *et al.* 2019 demonstrated that the presence of another serum component, the lipid mitogen lysophosphatidic acid, impairs the so-called "Rab11-Rabin8-Rab8 signaling cascade" (Wu *et al.*

2018) which promotes ciliogenesis (Westlake *et al.* 2011) (see chapter 1.3.1.3). This regulation of ciliogenesis via lysophosphatidic acid is "independent of cell cycle alterations" (Walia *et al.* 2019).

The intracellular pathway has been divided into four ultrastructural distinct developmental stadia: the docking "of small distal appendage vesicles" (Yee & Reiter 2015) to the mother centriole, their subsequent fusion into a single large ciliary vesicle, the coordinated outgrowth of this vesicle and the ciliary axoneme, and in the last step the fusion of the ciliary membrane with the plasma membrane (Lu *et al.* 2015; Sorokin 1962); partially reviewed in (Pedersen *et al.* 2012) (Fig. 3).

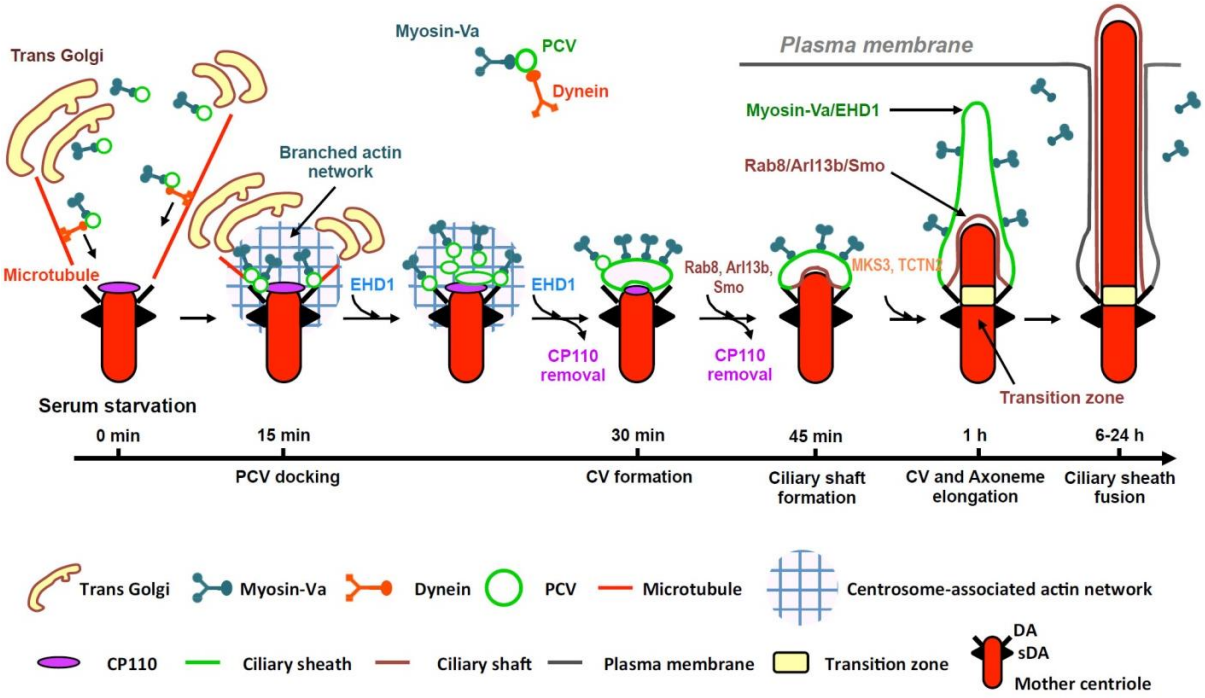

Figure 3: Overview of the major steps of the intracellular pathway of ciliogenesis according to Wu *et al.* 2018. In a first step, small vesicles (preciliary vesicle, PCV, green) dock to distal appendages (DA) of the mother centriole and subsequently fuse to one ciliary vesicle (CV, green). Next, the ciliary vesicle and the axoneme (light red) grow out simultaneously. In the last step the ciliary sheath (green) "fuses with the plasma membrane" (Ghossoub *et al.* 2011) (gray) (Anderson *et al.* 2008; Wu *et al.* 2018). sDA: subdistal appendages. See text for details regarding the role of the molecular players. Image taken from Wu *et al.* 2018. Permission was kindly granted by Springer Nature.

1.3.1.1 Distal appendage vesicle docking

As already mentioned, the intracellular pathway of ciliogenesis starts with the docking of distal appendage vesicles (DAVs) to the distal appendages of the mother centriole (Lu *et al.* 2015). This step also marks the beginning of "the conversion of the mother centriole into the basal body" (Schmidt *et al.* 2012) (Kobayashi & Dynlacht 2011; Lu *et al.* 2015; Sánchez & Dynlacht 2016).

Although the Golgi apparatus is debated (Sorokin 1962) the origin of the vesicles remains largely unknown so far (Witzgall 2018b). Recent, yet unpublished data indicate that endocytosed membrane material contributes to ciliogenesis (Witzgall 2018b). However, the mechanism responsible for their "transportation to the mother centriole" (Wu *et al.* 2018) was elucidated: these vesicles are associated with the actin motor protein Myosin-Va and are transported via microtubules in a dynein-dependent manner (Wu *et al.* 2018). Once the Myosin-Va-associated vesicles have reached the pericentrosomal region Myosin-Va uses the "Arp2/3-mediated centrosomal branched actin" (Wu *et al.* 2018) network to transport the "vesicles to the distal appendages of the mother centriole" (Wu *et al.* 2018). For example, it was visualized by electron microscopy that within a Myosin-Va knockout RPE1 cell line ciliogenesis is inhibited as the cells did not enter the distal appendage vesicle stadium after serum starvation (Wu *et al.* 2018). Furthermore, even the accumulation of vesicles in vicinity to the distal end of the mother centriole was impeded (Wu *et al.* 2018).

In addition to Myosin-Va-mediated vesicle transport, centriolar satellites – "nonmembranous, electron-dense particles surrounding centrosomes" (Kobayashi *et al.* 2014) – must be removed from the pericentriolar region prior to vesicle accumulation at and/or docking to the distal end of the mother centriole (Kobayashi *et al.* 2014). The proteins TALPID3 and the centrosomal protein CEP290 contribute to this centriolar satellite removal (Kobayashi *et al.* 2014).

For vesicle docking to the distal appendages of the mother centriole a centrosomal protein with a molecular mass of 164 kDa (CEP164) (Graser *et al.* 2007) is indispensable (Schmidt *et al.* 2012). "The localization pattern of" (Viol *et al.* 2020) CEP164 at the mother centriole throughout the cell cycle is dependent on mitotic kinases such as NEK2 which is important for CEP164 removal from the mother centriole before mitosis (Viol *et al.* 2020). During the interphase of the cell cycle, however, CEP164 is enriched at the distal appendages of the mother centriole (Schmidt *et al.* 2012). As CEP164 is the outermost of the proteins forming the backbone of the distal appendages (Yang *et al.* 2018) it is considered to be "an acceptor molecule" for vesicular docking (Schmidt *et al.* 2012). In addition to CEP164, coiled-coil domain containing 41 (CCDC41) – also called CEP83 (Adamiok-Ostrowska & Piekiełko-Witkowska 2020; Kurtulmus *et al.* 2018) – is another protein contributing to the docking of vesicles (Joo *et al.* 2013). Similar to CEP164, CCDC41 is a component of the distal appendages of the mother centriole (Joo *et al.* 2013). Furthermore, depletion of either CCDC41 or IFT20 in RPE1 cells impaired the docking of vesicles to the mother

centriole (Joo *et al.* 2013). Based on their findings, Joo *et al.* 2013 suggested that an interaction between IFT20 and CCDC41 is another mechanism contributing to the docking of vesicles (Joo *et al.* 2013). IFT20 in turn was shown to be involved "in the delivery of ciliary membrane proteins from the Golgi complex to the cilium" (Follit *et al.* 2006) (Monis *et al.* 2017); reviewed in (Garcia-Gonzalo & Reiter 2012; Nachury *et al.* 2010).

1.3.1.2 Ciliary vesicle formation

The next major step during the intracellular pathway of ciliogenesis is the "fusion of the distal appendage vesicles to" (Witzgall 2018a) form one large so-called ciliary vesicle (CV) at the distal end of the basal body (Lu *et al.* 2015); reviewed in (Sánchez & Dynlacht 2016; Witzgall 2018a). While more and more vesicles gradually accumulate in the pericentrosomal region (Lu *et al.* 2015; Sánchez & Dynlacht 2016; Wu *et al.* 2018), the membrane-associated proteins EHD (Eps15 homology domain) 1 and 3 are transported probably via vesicles from the endosome recycling compartment to the mother centriole (Lu *et al.* 2015). An siRNA-mediated knockdown of EHD1 in RPE1 cells suppressed the fusion of Myosin-Va-associated distal appendage vesicles (Lu *et al.* 2015; Wu *et al.* 2018) and Lu *et al.* 2015 hypothesize that EHD1 and EHD3 contribute to the mutual approximation of these vesicles (Lu *et al.* 2015). Downstream of EHD1, the SNARE protein and EHD1/3 interaction partner SNAP29 localizes to the distal appendages, probably recruited by EHD1 itself (Lu *et al.* 2015). Since SNAP29 is a "membrane fusion regulator", Lu *et al.* 2015 hypothesize that ciliary vesicle formation is brought to an end by "SNAP29-dependent fusion" after their mutual approximation (Lu *et al.* 2015).

The small GTPase RAB34 also contributes to ciliogenesis (Ganga *et al.* 2021; Oguchi *et al.* 2020; Xu *et al.* 2018). Electron micrographs of ultrathin sections of neuroepithelial cells from Rab34 mutant mice show that the formation of the ciliary vesicle stadium is impaired during ciliogenesis (Xu *et al.* 2018). High-resolution volumetric analysis in RAB34 knockout RPE1 cells using focused ion beam scanning electron microscopy further demonstrate that ciliogenesis was arrested at the distal appendage vesicle stadium within these cells (Ganga *et al.* 2021). Therefore RAB34 is required for the fusion of the distal appendage vesicles to form a ciliary vesicle (Ganga *et al.* 2021). Underlying molecular mechanisms have only been partially elucidated so far: on the one hand, RAB34 is involved in EHD1 recruitment to the mother centriole (Ganga *et al.* 2021). On the other hand, there are hints that RAB34 has the ability to "directly shape[…] the [distal appendage vesicle]

[…] membranes" (Ganga *et al.* 2021). This influence of RAB34 on ciliogenesis, however, seems to be restricted to cell lines following the intracellular pathway of ciliogenesis (Ganga *et al.* 2021).

1.3.1.3 RAB8 recruitment

The third stadium of the intracellular pathway includes the coordinate extension of both, ciliary membrane and axoneme; reviewed in (Blacque *et al.* 2018; Garcia-Gonzalo & Reiter 2012; Sánchez & Dynlacht 2016). The RAB8 protein plays a key role in membrane expansion (Nachury *et al.* 2007); reviewed in (Blacque *et al.* 2018; Witzgall 2018b). As the function of RAB8 during ciliogenesis was reviewed by Blacque *et al.* 2018 and Witzgall 2018b the following chapter of the present work is based on these publications. RAB8 exists in two isoforms RAB8A and RAB8B which are identical in their amino acid sequence to 82% (Sato *et al.* 2014; Westlake *et al.* 2011; Witzgall 2018b); the protein has been extensively studied over the past few years; reviewed in (Blacque *et al.* 2018). This protein belongs to the subfamily of RAS-like GTPases, i.e. proteins with intrinsic GTPase activity; reviewed in (Blacque *et al.* 2018; Witzgall 2018b). The activation or inactivation of RAB proteins is achieved by exchanging of GDP by GTP or of GTP by GDP respectively; reviewed in (Blacque *et al.* 2018; Witzgall 2018b). This "GDP to GTP exchange" (Blacque *et al.* 2018) to activate RABs is regulated by so-called GTP exchange factors (GEFs) or suppressed by guanine nucleotide dissociation inhibitors (GDIs); reviewed in (Blacque *et al.* 2018; Witzgall 2018b). Furthermore, "GTPase activating proteins (GAPs) [...] stimulate GTP hydrolysis" (Cherfils & Zeghouf 2013); reviewed in (Blacque *et al.* 2018; Witzgall 2018b). GTP-bound RAB protein are able to activate effector proteins by their binding; reviewed in (Blacque *et al.* 2018).

Although there are some data, the exact function of RAB8 during ciliogenesis was not fully elucidated so far (Blacque *et al.* 2018). RAB8 interacts with several proteins (e.g. CEP164) (Schmidt *et al.* 2012) contributing to ciliogenesis; reviewed in (Blacque *et al.* 2018) and transient overexpression of the GDP-locked, dominant-negative version of RAB8A leads to a significant reduction of the percentage of ciliated RPE1 cells (Nachury *et al.* 2007; Yoshimura *et al.* 2007); reviewed in (Blacque *et al.* 2018; Witzgall 2018b). Regarding the impact of RAB8B on ciliogenesis, however, contradictory data exist in the literature: Westlake *et al.* 2011 report on both, the localization of EGFP-tagged RAB8B at the primary cilium after transient overexpression in RPE1 cells and a reduced percentage of ciliated RPE1 cells after siRNA treatment against RAB8B (Westlake *et al.* 2011). Yoshimura *et al.* 2007, however, did not detect any ciliary localization of

EGFP-tagged RAB8B after transient overexpression in RPE1 cells and overexpression of the GDP-locked, dominant-negative version of RAB8B did not impair ciliogenesis (Yoshimura *et al.* 2007).

To visualize the centrosomal RAB8A recruitment during ciliogenesis, Westlake *et al.* 2011 performed live-cell imaging of RPE1 cells expressing both, EGFP-tagged RAB8A and "Centrin2 tagged with the" (Westlake *et al.* 2011) Tag-red fluorescent protein as centriolar marker. After serum starvation a punctiform EGFP-RAB8A signal reminiscent of "a single vesicular structure" (Westlake *et al.* 2011) localizes to the basal body (Westlake *et al.* 2011). Later on Lu *et al.* 2015 demonstrated by performing live-cell imaging of RPE1 cells as well, that RAB8A is recruited to the basal body downstream of EHD1. The intensity of the EGFP-RAB8A signal at the distal end of the basal body increases and the punctiform signal progressively elongates indicating that EGFP-RAB8A localizes to the outgrowing cilium as well (Westlake *et al.* 2011). Nachury *et al.* 2007 also expressed EGFP-RAB8A in RPE1 cells and showed that it localizes to primary cilia before tubulin acetylation takes place. Finally, after long periods of time of serum starvation (>24 h) EGFP-RAB8A is displaced from mature cilia (Westlake *et al.* 2011).

Electron micrographs demonstrate that cilium formation of RPE1 cells arrests at the ciliary vesicle stadium upon siRNA-mediated knockdown of RAB8A+8B (Lu *et al.* 2015). Transient overexpression of GTP-locked RAB8Q67L leads to an elongation of the ciliary membrane and the axoneme in RPE1 cells comparable to wild-type RAB8 expression (Nachury *et al.* 2007). Even overexpression of wild-type RAB8 has a rescue effect on cilia formation (Schmidt *et al.* 2012) after depletion of "ciliogenic proteins" (Blacque *et al.* 2018). Taken these findings together, RAB8-associated vesicles may localize to the ciliary vesicle and "promote the docking and fusion of exocytic vesicles" (Nachury *et al.* 2007) which results in "ciliary vesicle extension" (Maharjan *et al.* 2020) in cell culture (Lu *et al.* 2015; Nachury *et al.* 2007; Westlake *et al.* 2011).

However, contradicting data: for example, RAB8A+B double knockout and RAB8A+B+RAB10 triple knockout RPE1 cell lines show only a slight but not statistically significant reduction of the percentage of ciliated cells compared to parental RPE1 cells (Oguchi *et al.* 2020). As summarized by Witzgall 2018b the impact of RAB8 on ciliogenesis in the mouse model is even more complex than *in vitro*: Rab8a+b double knockout mice show abnormalities of the small intestine but form normal cilia (Sato *et al.* 2014); reviewed in (Witzgall 2018b). Only the additional knockdown of Rab10 in Rab8a+b double knockout mouse embryonic fibroblasts impaired ciliogenesis (Sato et

al. 2014); reviewed in (Witzgall 2018b). Witzgall 2018b provided one possible explanation for these data showing no impaired ciliogenesis after RAB8A+B double knockout: knockout of (RAB) proteins could give cells enough time to develop compensatory mechanisms (Witzgall 2018b).

Much more, however, is known about the activation of RAB8 (Fig. 4). The so-called "Rab11-Rabin8-Rab8 signaling cascade" (Wu *et al.* 2018) seems to be an important mechanism (Westlake *et al.* 2011); reviewed in (Blacque *et al.* 2018; Witzgall 2018b). The focus of this cascade is on RABIN8, the GTP exchange factor (GEF) for RAB8 (Hattula *et al.* 2002); reviewed in (Blacque *et al.* 2018; Nachury *et al.* 2007; Witzgall 2018b). Only the activated GTP-bound RAB8 is able to localize to the developing cilium and promotes membrane extension of the ciliary vesicle (Lu *et al.* 2015; Nachury *et al.* 2007). At the beginning of the "Rab11-Rabin8-Rab8 signaling cascade" (Wu *et al.* 2018) is the GTPase RAB11 which is characteristic for the recycling endosome (Ullrich *et al.* 1996); reviewed in (Blacque *et al.* 2018; Klumperman & Raposo 2014). Geranylgeranylation of RAB11 (Joberty *et al.* 1993) is responsible for its anchoring to lipid membranes; reviewed in (Chiba *et al.* 2013). These vesicles are not only associated with RAB11 but also with phosphatidylserine (Chiba *et al.* 2013). The combined binding of RABIN8 to activated/GTP-bound RAB11 (Knödler *et al.* 2010) and phosphatidylserine (Chiba *et al.* 2013) anchors RABIN8 to these vesicles (Chiba *et al.* 2013); reviewed in (Blacque *et al.* 2018). Recent studies have shown that the "Rab11 family-interacting protein 3 (FIP3)" (Vetter *et al.* 2015a) also contributes to the formation of a stable RAB11- RABIN8 complex (Vetter *et al.* 2015a; Walia *et al.* 2019): RABIN8 and FIP3 can both bind RAB11 (on different binding sites) and RABIN8 is stably incorporated in the "Rab11-FIP3-Rabin8 complex" (Vetter *et al.* 2015a) via a "direct interaction between RABIN8 and FIP3" (Vetter *et al.* 2015a) (Walia *et al.* 2019). The formation of the RAB11- RABIN8 complex, however, is precisely regulated (Walia *et al.* 2019): the lysophosphatidic acid present in fetal bovine serum of cell culture media activates the PI3K/AKT pathway via the lysophosphatidic acid receptor 1 (Walia *et al.* 2019). The serine/threonine kinase AKT phosphorylates the RAB11 effector RAB11-binding protein (RAB11BP) (Zeng *et al.* 1999), also called WDR44 (Vetter *et al.* 2015b) (Walia *et al.* 2019). AKT mediated phosphorylation of WDR44 increases WDR44 binding affinity to RAB11 resulting in RAB11-RABIN8 complex destabilization due to competitive displacement of FIP3 from the complex (Walia *et al.* 2019). After the formation of the RAB11-RABIN8 complex, RAB11 finally mediates the transport of RAB11/RABIN8-associated vesicles

to the centrosome probably along microtubules (Westlake *et al.* 2011); reviewed in (Blacque *et al.* 2018; Witzgall 2018b).

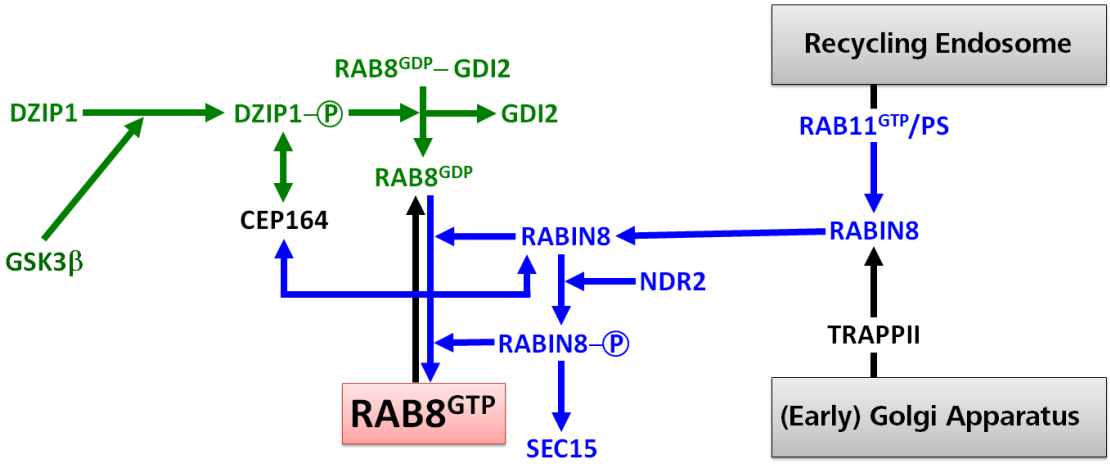

Figure 4: Summarized overview of RAB8 recruitment to the basal body and subsequent activation. The "Rab11-Rabin8-Rab8 signaling cascade" (Wu *et al.* 2018) is drawn in blue, the "GSK3β-DZIP1-Rab8 cascade" (Zhang *et al.* 2015) in green. Further molecular mechanisms in involved in centrosomal RAB8 recruitment as well as RAB8 activity regulation during ciliogenesis are drawn in black. See text for details, PS: phosphatidylserine. Scheme adapted from Ralph Witzgall (Witzgall 2018b).

In addition to RAB11, some components of the transport protein particle II (TRAPPII) complex also are involved in RABIN8 recruitment (Westlake *et al.* 2011); reviewed in (Witzgall 2018b). TRAPPC14 (alternative names: C7orf43 or microtubule associated protein 11), a recently identified component of the TRAPPII complex acts as a linker between RABIN8 and TRAPPII complex core proteins (Cuenca *et al.* 2019). TRAPPC14 is important for the transport of RABIN8-associated vesicles to the centrosome and keeps these vesicles in close proximity to the distal appendages of the mother centriole/basal body via its interaction with CEP83 (Cuenca *et al.* 2019).

Having reached the mother centriole/basal body, RABIN8 activates RAB8 as described above (Hattula *et al.* 2002); reviewed in (Blacque *et al.* 2018; Chiba *et al.* 2013; Nachury *et al.* 2007; Witzgall 2018b). One effector protein of RAB8 is SEC15 (Wu *et al.* 2005), a component of the octameric protein complex exocyst; reviewed in (Blacque *et al.* 2018; Chiba *et al.* 2013; Feng *et al.* 2012; Witzgall 2018b). RAB11+RABIN8-associated vesicles are linked to the mother centriole/basal body via an interaction of RABIN8 with SEC15 (Feng *et al.* 2012) as the exocyst is anchored to the mother centriole (Hehnly *et al.* 2012); reviewed in (Blacque *et al.* 2018; Chiba *et al.* 2013; Witzgall 2018b). According to Chiba *et al.* 2013 this anchoring of RABIN8 is further

improved due to a direct interaction of RABIN8 with the distal appendage protein CEP164 (Schmidt *et al.* 2012) and NDR2 (serine/threonine kinase) mediated phosphorylation of RABIN8 (Chiba *et al.* 2013); reviewed in (Blacque *et al.* 2018; Witzgall 2018b). This phosphorylation may result in a conformational change of the RABIN8 protein which reduces the affinity (Chiba *et al.* 2013) of RABIN8 to bind RAB11 (Knödler *et al.* 2010) and phosphatidylserine (Chiba *et al.* 2013) but increases its affinity to bind SEC15 (Chiba *et al.* 2013; Feng *et al.* 2012); reviewed in (Blacque *et al.* 2018). Consequently, RABIN8 dissociates from RAB11-associated vesicles and is anchored to the mother centriole/basal body via the interaction with SEC15 (Chiba *et al.* 2013). In contrast, the serine/threonine kinase AKT, has an inhibitory effect on ciliogenesis as AKT mediated phosphorylation of RABIN8 impairs its ability to activate RAB8 (Walia *et al.* 2019).

As reviewed by Blacque *et al.* 2018 and Witzgall 2018b not only GTP exchange factors (GEFs) but also guanine nucleotide dissociation inhibitors (GDIs) contribute to the regulation of the activity of RAB proteins (e.g. RAB8). GDI2, a "member[…] of the mammalian GDI protein class" (Shisheva *et al.* 1999) interacts with various RAB proteins including RAB8 (Shisheva *et al.* 1999); reviewed in (Blacque *et al.* 2018; Zhang *et al.* 2015). The inhibitory effect of GDI2 on RAB8 activity during ciliogenesis is regulated by the so-called "GSK3β-DZIP1-Rab8a cascade" (Zhang *et al.* 2015); reviewed in (Blacque *et al.* 2018; Witzgall 2018b) (Fig. 4). DZIP1 a ~110 kDa protein with a zinc finger domain (Zhang *et al.* 2015) localizes i.a. to the mother centriole (Zhang *et al.* 2015), interacts with CEP164 (Wang *et al.* 2013) and binds to the $RAB8^{GDP}$-GDI2 complex (Zhang *et al.* 2015). During G_0-phase a phosphorylation of DZIP1 via the serine/threonine glycogen synthase kinase 3β (GSK3β) takes place (Zhang *et al.* 2015); reviewed in (Witzgall 2018b). DZIP1 phosphorylation results in a binding affinity increase of DZIP1 to GDI2 with a simultaneous decrease of its binding affinity to $RAB8^{GDP}$-GDI2 ending with "the dissociation of […] [$RAB8^{GDP}$] from GDI2" (Zhang *et al.* 2015); reviewed in (Blacque *et al.* 2018; Witzgall 2018b). Consequently $RAB8^{GDP}$ is accessible for the "GDP to GTP exchange" (Blacque *et al.* 2018), which is promoted by the RAB11- RABIN8 cascade (see above); reviewed in (Blacque *et al.* 2018; Witzgall 2018b).

1.3.1.4 CP110 removal

In addition to RAB8, CP110 – a centrosomal protein with a molecular mass of 110 kDa – is another key regulator during ciliogenesis (Kobayashi *et al.* 2011; Spektor *et al.* 2007; Walentek *et al.* 2016); reviewed in (Blacque *et al.* 2018; Kobayashi & Dynlacht 2011) (Fig. 5). CP110 has an inhibitory effect and therefore must specifically be removed from the distal end of the basal body prior to axoneme growth (Spektor *et al.* 2007). Please note, in addition to vesicle docking to the mother

centriole (Kobayashi & Dynlacht 2011; Lu *et al.* 2015; Sánchez & Dynlacht 2016), CP110 removal is a further step which converts the mother centriole into the basal body according to the definition of some authors (Kobayashi & Dynlacht 2011; Spektor *et al.* 2007; Wu *et al.* 2018). The exact point in time at which CP110 is removed from the basal body during ciliogenesis has not unambiguously been identified so far. On the one hand, there are data demonstrating that CP110 is removed after docking the distal appendage vesicles to the mother centriole but before the ciliary vesicle formation is completed (Insinna *et al.* 2019; Lu *et al.* 2015; Wu *et al.* 2018). On the other hand, data from Kuhns *et al.* 2013 indicate in an indirect manner that CP110 is only removed from the basal body after the ciliary vesicle is completely formed. Furthermore, there is no detailed knowledge regarding the molecular "mechanism through which CP110" (Yadav *et al.* 2016) inhibits ciliogenesis; reviewed in (Yadav *et al.* 2016). However, several pathways are discussed (Spektor *et al.* 2007; Tsang *et al.* 2008); reviewed in (Yadav *et al.* 2016).

First, it is known that CP110 forms a kind of "cap" (Kobayashi *et al.* 2011) at the distal end of the mother and daughter centriole (Kobayashi *et al.* 2011; Tsang *et al.* 2008) and functions as "an inhibitory barrier" (Spektor *et al.* 2007); reviewed in (Yadav *et al.* 2016). Another way how CP110 affects ciliogenesis is "through its interaction with" (Tsang *et al.* 2008) CEP290; reviewed in (Gerdes *et al.* 2009; Yadav *et al.* 2016). CEP290 which is localized at the distal end of centrioles (Tsang *et al.* 2008) can bind to both CP110 and RAB8A (Tsang *et al.* 2008), is indispensable for RAB8A recruitment to the centrosome (Tsang *et al.* 2008) and contributes to the fusion of distal appendage vesicles via an unknown mechanism (Kobayashi *et al.* 2014). The "CEP290-CP110 interaction" (Tsang *et al.* 2008) could keep CEP290 in its inactive state which results in suppression of ciliogenesis (Tsang *et al.* 2008). Furthermore, CP110 can bind to TALPID3 which is located at the distal ends of mother and daughter centrioles and promotes ciliogenesis by "recruiting RAB8A to the centrosome" (Tsang *et al.* 2008) probably via its ability to remove centriolar satellites (see above) (Kobayashi *et al.* 2014). However, the role of CP110 during ciliogenesis is much more complex *in vivo* as CP110 knockout mice suffered manifold impairments of ciliogenesis which led to animal death "within a few hours of birth" (Yadav *et al.* 2016); reviewed in (Huang *et al.* 2018).

For better understanding the CP110 displacement, the NEK2-KIF24-MPP9-CEP97-CP110 pathway (Huang *et al.* 2018; Kim *et al.* 2015; Kobayashi *et al.* 2011; Spektor *et al.* 2007) – a mechanism which is responsible for the recruitment of CP110 to the mother centriole – will be explained first (Fig. 5). The first protein involved in this pathway is the serine/threonine kinase

NEK2 (Kim *et al.* 2015). Additional to its localization at the proximal end of mother and daughter centriole during the G_1 phase of the cell cycle, NEK2 co-localizes with CEP164 at the distal end of the mother centriole during S/G_2 phase as well (Kim *et al.* 2015; Viol *et al.* 2020). Upon co-localization NEK2 promotes the removal of some components of the distal appendages such as CEP164 before mitosis via an unknow mechanism (Viol *et al.* 2020). Furthermore, NEK2 can bind to and phosphorylate the M-kinesin protein KIF24 which is also located at the distal end of the mother centriole or basal body (Kim *et al.* 2015; Kobayashi *et al.* 2011). A phosphorylation-induced conformational change of KIF24 stimulates its microtubule-depolymerizing activity (Kim *et al.* 2015). Another function of KIF24 is its interaction with and recruitment of the ciliogenesis suppressor M-Phase Phosphoprotein 9 (MPP9) (Huang *et al.* 2018). MPP9 in turn is able to recruit the centrosomal protein CEP97 which finally recruits and interacts with CP110 (Huang *et al.* 2018; Spektor *et al.* 2007). KIF24 can also interact directly with CEP97 and with CP110 and thus "stabilize and/or recruit CP110" (Kobayashi *et al.* 2011) at the distal end of the mother centriole (Kobayashi *et al.* 2011).

There are several cellular mechanisms that can intervene with the NEK2-KIF24-MPP9-CEP97-CP110 pathway and partially interrupt it so that CP110 is no longer stabilized and/or recruited at the distal end of the basal body (Fig. 5).

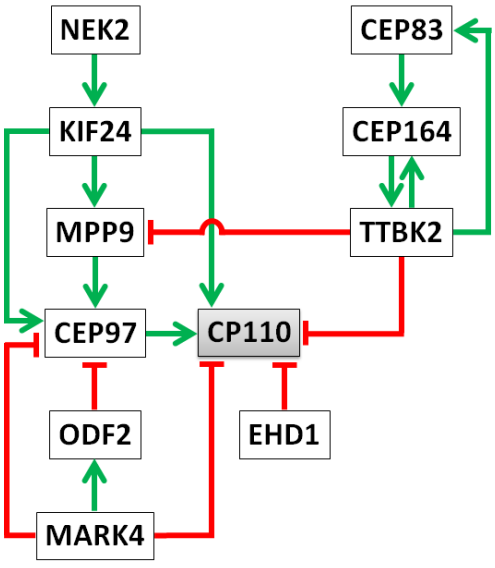

Figure 5: Regulation of CP110 level at the basal body during ciliogenesis. Green arrows represent recruitment of the respective protein to the mother centriole/basal body and/or its activation, red bars represent removal from the mother centriole/basal body. See text for details. Scheme based on an unpublished design by Ralph Witzgall, Institute for Molecular and Cellular Anatomy, University of Regensburg, Regensburg.

One way to promote ciliogenesis is CP110 removal via the serine/threonine kinase Tau Tubulin Kinase 2 (TTBK2) (Čajánek & Nigg 2014; Goetz *et al.* 2012; Huang *et al.* 2018). TTBK2 is recruited to the mother centriole in a CEP164-dependent manner as CEP164 can bind TTBK2 and generate a stable "TTBK2-Cep164 complex" (Čajánek & Nigg 2014). Subsequent TTBK2-mediated CEP164 phosphorylation likely contributes to CEP164 stabilization at the mother centriole (Čajánek & Nigg 2014). There are hints that Centrin2, a protein which "is concentrated within the distal lumen of centrioles" (Paoletti *et al.* 1996; reviewed in Kobayashi & Dynlacht 2011; Tsang *et al.* 2008), is required for the formation of an intact and functional "TTBK2-Cep164 complex" (Čajánek & Nigg 2014) (Prosser & Morrison 2015). TTBK2 is no longer preferentially recruited to the mother centriole in Centrin2-deficient RPE1 cells (Prosser & Morrison 2015) and CEP164 localizes to both mother and daughter centriole "with a marked dispersion of the Cep164 [...] away from [its] [...] normal localization at the distal end of the centrioles" (Prosser & Morrison 2015). A recent study showed that after its centrosomal recruitment TTBK2 is shifted from the periphery towards the roots of the distal appendages in close proximity to CEP83 (Lo *et al.* 2019). In a next step "CEP83 is phosphorylated by TTBK2" (Lo *et al.* 2019). Ciliogenesis is finally promoted by TTBK2 in two ways: on the one hand the "TTBK2-Cep164 complex" (Čajánek & Nigg 2014) recruits components of the intraflagellar transport (IFT) machinery, which is responsible for the outgrowth of the axoneme (Čajánek & Nigg 2014; Goetz *et al.* 2012). On the other hand TTBK2 promotes the removal of CP110 from the basal body (Čajánek & Nigg 2014) via "TTBK2-mediated phosphorylation of MPP9" (Huang *et al.* 2018) which is known to recruit CP110-CEP97 to the mother centriole (Huang *et al.* 2018). This phosphorylation of MPP9 leads to its ubiquitination and proteasomal degradation which in turn results in "removal of the CEP97-CP110 complex from" (Huang *et al.* 2018) the distal end of the basal body (Huang *et al.* 2018).

Various other pathways contribute to CP110 removal. For example, if the serine/threonine kinase MARK4 (microtubule affinity regulating kinase 4) is depleted in RPE1 cells CP110 persists at the basal body after serum starvation and ciliary axoneme formation is blocked (Kuhns *et al.* 2013). Using electron microscopy it was elucidated that ciliogenesis of MARK4-depleted RPE1 cells arrests at the ciliary vesicle stadium (Kuhns *et al.* 2013). Same results were found after siRNA-mediated knockdown of outer dense fiber 2 protein (ODF2) (Kuhns *et al.* 2013). ODF2 is a part of the subdistal appendages (Nakagawa *et al.* 2001; Singla *et al.* 2010; Yang *et al.* 2018) and thus is required for their formation (Ishikawa *et al.* 2005); reviewed in (Kuhns *et al.* 2013). Furthermore,

ODF2 is probably accumulated at centrioles in a MARK4-dependent manner as siRNA-mediated knockdown of MARK4 impairs ODF2 association with centrioles (Kuhns *et al.* 2013). Finally, EHD1 and PACSIN proteins also remove CP110 via unknown mechanisms as EHD1 (Lu *et al.* 2015) or PACSIN depletion (Insinna *et al.* 2019) in RPE1 cells impairs CP110 removal after serum starvation.

As already summarized and discussed by Huang *et al.* 2018, degradation of CP110 during G_0 phase of the cell cycle is also a complex and so far poorly understood process as diverging data exist. On the one hand there are studies indicating the CP110 ubiquitination and subsequent proteasomal degradation in which the ubiquitin ligase cofactor Neuralized homologue 4 (NEURL4) is involved (Li *et al.* 2012; Loukil *et al.* 2017); reviewed in (Huang *et al.* 2018). On the other hand Kasahara *et al.* 2014 could not confirm that the "protein level [of CP110] was […] regulated by proteasomal degradation after serum starvation" (Kasahara *et al.* 2014) in RPE1 cells; reviewed in (Huang *et al.* 2018).

1.3.1.5 Intraflagellar transport during ciliogenesis

After RAB8 recruitment and CP110 removal, all prerequisites for the outgrowth of the ciliary shaft are given. Ciliary precursors such as ciliary membrane proteins (Follit *et al.* 2006) or tubulins (Hao *et al.* 2011) are transported along the forming axoneme via intraflagellar transport (IFT); reviewed in (Ishikawa & Marshall 2011; Nachury *et al.* 2010; Pedersen *et al.* 2008; Prevo *et al.* 2017; Rosenbaum & Witman 2002). As the functional principle as well as the composition of the "IFT machinery" (Prevo *et al.* 2017) was already described in chapter 1.2.2, this section will focus on the recruitment of some IFT components during ciliogenesis.

For example, the "TTBK2-Cep164 complex" (Čajánek & Nigg 2014) recruits IFT81 to the mother centriole (Čajánek & Nigg 2014). TTBK2 plays an additional role in "the recruitment or retention" (Goetz *et al.* 2012) of further IFT proteins such as IFT140 (IFT-A complex component) or IFT88 (IFT-B complex component) during ciliogenesis (Goetz *et al.* 2012). Knockdown experiments in RPE1 cells using siRNA against EHD1 demonstrated that EHD1 is needed for centrosomal IFT20 localization (Lu *et al.* 2015) which in turn is involved in vesicle transport of ciliary membrane proteins (e.g. Polycystin-2) "from the Golgi apparatus to the cilium" (Monis *et al.* 2017) of mammalian cells (Follit *et al.* 2006); reviewed in (Pedersen *et al.* 2008). The Orofaciodigital Syndrome 1 (OFD1) protein which is located at the distal end of the "microtubule barrel" (Singla

et al. 2010) of centrioles co-localizes with IFT88 in ciliated and unciliated mammalian cells and is indispensable for its recruitment (Singla *et al.* 2010); reviewed in (Pedersen *et al.* 2012).

It has to be pointed out that the function of IFT during ciliogenesis is not limited to manage axoneme growth. For example, there are hints that the IFT-B core complex component IFT88 (reviewed in Taschner *et al.* 2012) contributes to the stabilization of docked vesicles at the distal appendages of the basal body (Joo *et al.* 2013). This hypothesis is based on the finding that the percentage of RPE1 cells having "a basal body associated with a" (Spektor *et al.* 2007) ciliary vesicle did not increase although the percentage of ciliated RPE1 cells was reduced after an siRNA-mediated knockdown of IFT88 in RPE1 (Joo *et al.* 2013).

Elucidating the functional variety of IFT121/WDR35, a component of the IFT-A complex, impressively demonstrates the manifold contribution of IFT in regulating ciliogenesis (Fu *et al.* 2016). WDR35 not only can bind cargo proteins via its WD40 domains but also indirectly via interaction with other IFT-A subunits (Fu *et al.* 2016). In addition to its contribution to retrograde IFT, RAB8 cooperation is another important function of WDR35 (Fu *et al.* 2016). After a WDR35-independent initial docking of RAB8-associated vesicles to the basal body, WDR35 is indispensable for the further fusion/growth of these vesicles (Fu *et al.* 2016). Fu *et al.* 2016 further showed that WDR35 can interact with several components of the IFT-A complex as well as with ciliary membrane proteins like ARL13B "a member of the [...] ADP ribosylation factor [...] related [...] subfamily" (Caspary *et al.* 2007) or somatostatin receptor 3 (SSTR3) (Händel *et al.* 1999) which both contribute to the ciliary function; reviewed in (Gerdes *et al.* 2009; Pedersen *et al.* 2012). The formation of ARL13B- or SSTR3-positive cilia is almost completely prevented in WDR35 knockout RPE1 cells (Fu *et al.* 2016). Therefore this network of interactions is needed for entry of "ciliary membrane cargoes" (Fu *et al.* 2016) into the forming cilium (Fu *et al.* 2016).

1.3.1.6 Externalization of the forming cilium

The last, so far poorly understood step of ciliogenesis exposes the forming cilium on the cell surface so that it reaches the extracellular milieu to fulfill its functions (Sorokin 1962); reviewed in (Ghossoub *et al.* 2011; Pedersen *et al.* 2012). During IFT-mediated ciliary growth, the axoneme invaginates the ciliary vesicle which results in the formation of a double membrane consisting of an inner ciliary shaft and an outer ciliary sheath membrane (Sorokin 1962); reviewed in (Pedersen *et al.* 2012; Rohatgi & Snell 2010). Already at this stadium of ciliogenesis a membrane

compartmentalization is present, as the proteins Myosin-Va and EHD1 are exclusively located at the ciliary sheath membrane and ARL13B, Smoothened and RAB8A at the ciliary shaft membrane (Wu *et al.* 2018). However, it is unknown at which stadium of ciliogenesis this compartmentalization takes place and where the barrier between both membrane compartments is located exactly.

Processes taking place during ciliogenesis initiate a shift of "the centrosome towards the apical" (Wang & Dynlacht 2018) plasma membrane (Pitaval *et al.* 2017); reviewed in (Wang & Dynlacht 2018). "Microtubule nucleation and stabilization" (Pitaval *et al.* 2017) result in a bundle of microtubules at the basal side of the centrosome in RPE1 cells (Pitaval *et al.* 2017); reviewed in (Wang & Dynlacht 2018). Together with an asymmetrical actin network contraction, pushing forces are exerted that move the nucleus out of the cell center and the centrosome apically (Pitaval *et al.* 2017); reviewed in (Wang & Dynlacht 2018).

Next, the ciliary "sheath [membrane] fuses with the plasma membrane" (Sorokin 1962) and the ciliary pocket is formed (Molla-Herman *et al.* 2010; Sorokin 1962); reviewed in (Apodaca 2018; Garcia-Gonzalo & Reiter 2012; Ghossoub *et al.* 2011; Witzgall 2018a; Wu *et al.* 2018). Exocytotic processes are discussed in literature as one possible mechanism contributing to this fusion event, however molecular players are entirely unknown (Garcia-Gonzalo & Reiter 2012). Another mechanism has been discovered recently using three-dimensional focused ion beam-scanning electron microscopy in combination with correlative light and electron microscopy (Insinna *et al.* 2019): tubule-like structures originating from the membranes docked to the basal body start to form towards the cell surface during ciliogenesis (Insinna *et al.* 2019). EHD1 and PACSIN proteins are essential for this process (Insinna *et al.* 2019). A fusion of these tubules with the plasma membrane links the cilium to the extracellular space (Insinna *et al.* 2019). Please note that cilia of cells following the intracellular pathway of ciliogenesis usually "are submerged in a deep membrane invagination […] surrounded by cytoplasm" (Mazo *et al.* 2016). Therefore membrane tubules can be several micrometers in length (Insinna *et al.* 2019).

1.3.2 Extracellular pathway

As summarized in a recent review of Breslow & Holland 2019, the extracellular pathway of ciliogenesis is only known rudimentary so far (Breslow & Holland 2019; Ghossoub *et al.* 2011). This extracellular pathway is a characteristic of polarized epithelial cells (Molla-Herman *et al.*

2010; Sorokin 1968) and inner medullar collecting duct (IMCD) cells are a common model for studying this mechanism; reviewed in (Benmerah 2013; Breslow & Holland 2019; Ghossoub *et al.* 2011; Molla-Herman *et al.* 2010; Pedersen *et al.* 2012). Since its initial description by Sergei Sorokin three ultrastructural distinct developmental stadia are reported for the extracellular pathway of ciliogenesis (Sorokin 1968); reviewed in (Breslow & Holland 2019; Ghossoub *et al.* 2011; Pedersen *et al.* 2012; Witzgall 2018b): in the first step, the centrosome moves towards the apical cell pole, then the mother centriole docks to the apical plasma membrane and, finally, the cilium grows out; reviewed in (Breslow & Holland 2019; Ghossoub *et al.* 2011; Pedersen *et al.* 2012). Whereas the last step, i.e. the outgrowth of the cilium, seems to be comparable to the intracellular pathway, including RAB8 recruitment, CP110 removal and IFT-mediated outgrowth of the axoneme, the first two steps differ; reviewed in (Breslow & Holland 2019). Recent studies demonstrated that a strict categorization of ciliogenesis into intracellular vs extracellular pathway cannot be sustained, at least not in the manner of the definition described above (Lu *et al.* 2015; Molla-Herman *et al.* 2010; Wu *et al.* 2018); reviewed in (Ghossoub *et al.* 2011). At the beginning of ciliogenesis in IMCD cells, Myosin-Va-associated distal appendages vesicles and a ciliary vesicle are formed (Wu *et al.* 2018). The actin motor protein Myosin-Va contributes to vesicle transport to the mother centriole (Wu *et al.* 2018) which is considered to be one of the first steps of the intracellular pathway of ciliogenesis (Lu *et al.* 2015). However, using three-dimensional structured illumination microscopy Wu *et al.* 2018 visualized that after 15 min of serum starvation ~30% of IMCD cells showed Myosin-Va-associated vesicles surrounding one centriole and after 30 min of serum starvation almost ~50% of IMCD cells showed a large Myosin-Va-associated vesicle in contact with one centriole. The authors further verified their results using electron microscopy analysis of ultrathin sections: ~83% of IMCD cells had distal appendage vesicles at 15 min after beginning of serum starvation and 76% a ciliary vesicle 30 min after the start of serum starvation (Wu *et al.* 2018). Furthermore, the two proteins EHD1 and EHD3, which contribute to the formation of the ciliary vesicle "and localize to the ciliary pocket membrane" (Lu *et al.* 2015) in RPE1 cells, are important for ciliogenesis in IMCD cells as well (Lu *et al.* 2015). There is a reduction in the percentage of ciliated IMCD cells after siRNA treatment against EHD1, EHD3 or EHD1+3 and EGFP-tagged EHD1 or EHD3 can be "detected in the proximal ciliary region in 8% [on average]" (Lu *et al.* 2015) in IMCD cells (Lu *et al.* 2015). Finally, the ciliary pocket, a characteristic of the intracellular pathway, could also be detected within a small portion of IMCD cells (Molla-Herman *et al.* 2010); reviewed in (Ghossoub *et al.* 2011). Therefore Molla-Herman *et*

al. 2010 hypothesize that at least a portion of polarized epithelial cells can be able to follow the intracellular pathway whereupon the intracellular developmental stadia of cilia probably show "faster kinetics than in non-polarised cells" (Molla-Herman *et al.* 2010) resulting in a fusion with the plasma membrane at early stadia of ciliogenesis (Molla-Herman *et al.* 2010); reviewed in (Breslow & Holland 2019; Ghossoub *et al.* 2011).

Taking recent findings into account, Wu *et al.* 2018 reconstructed the following procedure for the extracellular pathway (Fig. 6): comparable to the intracellular pathway, distal appendage vesicles first appear and then fuse to form a ciliary vesicle (Lu *et al.* 2015; Wu *et al.* 2018). The proteins Myosin-Va and EHD1/EHD3 contribute to this step in IMCD cells (Lu *et al.* 2015; Wu *et al.* 2018). The docking of membrane structures is distal appendage-dependent: for example, the CEP83 protein which is a component of the backbone of distal appendages (Yang *et al.* 2018) is indispensable for docking (Tanos *et al.* 2013); reviewed in (Breslow & Holland 2019). This was shown using electron micrographs which reveal that after CEP83-depletion mother centrioles of IMCD cells were unable to interact with membranes (Tanos *et al.* 2013). After the centrosome moved towards the apical cell pole a fusion with/docking to the plasma membrane occurs; reviewed in (Breslow & Holland 2019; Ghossoub *et al.* 2011; Pedersen *et al.* 2012). For "polarized renal epithelial cells" (Bernabé-Rubio *et al.* 2016) it was shown that the "actin network beneath the apical plasma membrane" (Francis *et al.* 2011) is disassembled before a connection between mother centriole and plasma membrane is established (Francis *et al.* 2011); reviewed in (Breslow & Holland 2019).

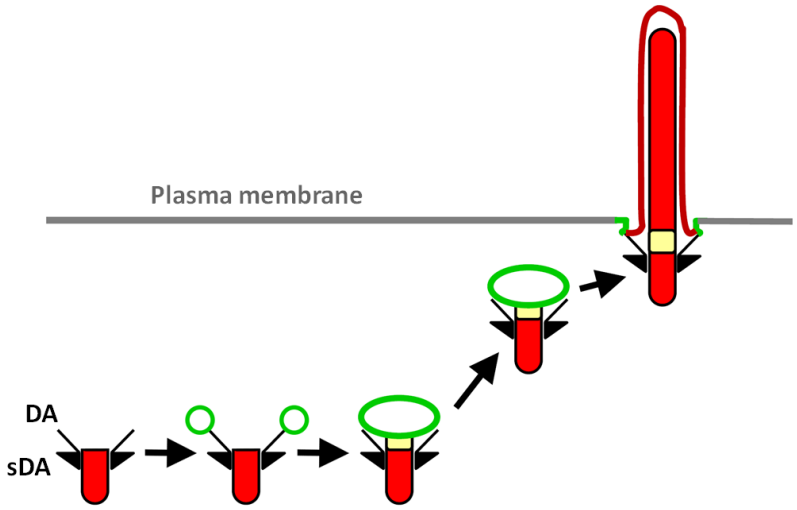

Figure 6: Overview of the extracellular pathway of ciliogenesis according to Wu *et al.* 2018. Shown is the mother centriole/basal body (light red) with its distal (DA) and subdistal (sDA) appendages. The transition zone is marked in

yellow. In a first step, vesicles (green) dock to the distal appendages and form a ciliary vesicle (green) (Wu *et al.* 2018). No intracellular elongation of the ciliary vesicle occurs (Wu *et al.* 2018) but "the [basal body] […] migrates to the" (Blacque *et al.* 2018) apical plasma membrane (gray) and docks (Breslow & Holland 2019; Pedersen *et al.* 2012). In a last step, the axoneme (light red) and the ciliary membrane (dark red) grow out (Breslow & Holland 2019; Pedersen *et al.* 2012). Image adapted from Wu *et al.* 2018. Permission was kindly granted by Springer Nature.

To sum it up, according to current knowledge and the definition of Wu *et al.* 2018, the characteristics of the extracellular pathway are the lack of intracellular extension of the ciliary vesicle as well as the lack of intracellular axoneme outgrowth but a fusion of the ciliary vesicle with the plasma membrane during early ciliogenesis (Molla-Herman *et al.* 2010; Wu *et al.* 2018).

1.4 Aim of the study

Primary cilia are singular organelles “of most mammalian cell types” (Satir *et al.* 2010) and fulfill a plurality of sensory functions so that they are often called the “cell’s antenna” (Ishikawa & Marshall 2011; Singla & Reiter 2006). As defects of primary cilia can lead to severe diseases, they have become an object of intensive research during the last two decades (Harris & Torres 2009; Satir *et al.* 2010). Much knowledge was gained regarding the molecular mechanisms contributing to their formation, a process called ciliogenesis. In cell culture the small GTPase RAB8 seems to be one of the key proteins contributing to ciliogenesis (Nachury *et al.* 2007; Westlake *et al.* 2011); reviewed in (Sato *et al.* 2014). Knockdown experiments in retinal pigment epithelial (RPE1) cells elucidated that RAB8 “functions in [ciliary vesicle] […] extension” (Lu *et al.* 2015) a “prerequisite for axoneme elongation” (Seeley & Nachury 2010) (Lu *et al.* 2015; Nachury *et al.* 2007). However, studies investigating the localization of RAB8 as well as the ciliary ultrastructure prior to axoneme outgrowth on a three-dimensional level are rare to date. To identify and visualize large cellular structures in three dimensions with up to several hundred nanometers in diameter and length such as forming primary cilia, it was the aim to establishe a correlative light and electron microscopy (CLEM) technique which combines fluorescence microscopy with bright-field scanning transmission electron microscopy (STEM) tomography operating with “an electron beam with small semi-convergence angle [(1-2 mrad)]” (Rachel *et al.* 2020) . Using this CLEM-STEM approach RPE1 cells showing ciliogenetic stadia with an mCherry-tagged version of RAB8A having just been recruited to the centrosome will be selected in the current study and the ultrastructure of forming cilia will be visualized in three dimensions by subsequent STEM tomography. Such a systematic investigation will provide detailed insights into membrane remodeling processes during ciliogenesis at the point in time of RAB8A recruitment. Since it is known that the “endosomal system” (Klumperman & Raposo 2014) is involved in both ciliogenesis in general and RAB8A recruitment to the centrosome in particular (Knödler *et al.* 2010; Westlake *et al.* 2011), the endocytic compartment(s) contributing to these processes can be identified as well.

At the ciliary base there is a diffusion barrier which regulates the exchange of molecules between the “ciliary compartment” (Hu & Nelson 2011) and the cytosol (Benmerah 2013; Nachury *et al.* 2010). However, it has neither been proven so far whether it is rather a structural barrier or a functional one or a combination of both, nor where this barrier is exactly located (Nachury *et al.* 2010). Since the constitutively active M2 (Incardona *et al.* 2002; Xie *et al.* 1998) mutant of murine

Smoothened (SmoM2) is permanently located at the ciliary membrane (Corbit *et al.* 2005; reviewed in Hoffmeister *et al.* 2011; Lu *et al.* 2015; Yee & Reiter 2015), it will be used as marker protein during the current work. Applying a histochemical reaction (Connolly *et al.* 1994; Graham & Karnovsky 1966; reviewed in Witzgall 2018b) the distribution of the SmoM2 protein and thus the ciliary membrane will be visualized by electron microscopy on an ultrastructural level. This will also allow to locate the transition of the ciliary membrane to the plasma membrane "with a resolution in the nanometer range" (Buerger *et al.* 2021). In summary, the second part of the present study should contribute to a better understanding of the dimension of the "ciliary compartment" (Hu & Nelson 2011).

2 Materials and Methods

Some of the methods have already been described, for this reason several sources (Asam *et al.* 2019; Baumgarten 2015; Buerger *et al.* 2021; Gürster 2013; Hoffmeister 2008; Setzer 2018) were used for writing this chapter in addition to the sources given at the indicated places.

Please note, materials and methods for on-section CLEM experiments are already listed in Buerger *et al.* 2021 and therefore not mentioned once again in the following chapter.

2.1 Materials

2.1.1 Chemicals

- Acetic acid, puriss. p.a., ≥99.8%, cat. no. 33209-2.5L-M, Sigma-Aldrich/Merck, Darmstadt, Germany
- Acetone, puriss. p.a. ≥99.5%, cat. no. 32201-2.5L-M, Sigma-Aldrich/Merck, Darmstadt, Germany
- Agarose NEEO ultra-quality, cat. no. 2267.4, Carl Roth, Karlsruhe, Germany
- Albumin Fraction V, ≥98%, from bovine plasma, cat. no. 8076.3, Carl Roth, Karlsruhe, Germany
- Ammonium chloride, cat. no. 101145.1000, Merck, Darmstadt, Germany
- Ammonium peroxodisulfate, purum p.a., ≥98.0%, cat. no. 09920, Sigma-Aldrich/Merck, Darmstadt, Germany
- Ampicillin sodium salt, cat. no. K029.2, Carl Roth, Karlsruhe, Germany
- Amplex UltraRed reagent, cat. no. A36006, Thermo Fisher Scientific, Waltham, USA
- Bacto Agar, cat. no. 214010, Becton Dickinson, Heidelberg, Germany
- Bacto Tryptone, cat. no. 211705, Becton Dickinson, Heidelberg, Germany
- Bacto Yeast Extract, cat. no. 212750, Becton Dickinson, Heidelberg, Germany
- bisBenzimide H 33258, cat no. B2883-100MG, Sigma-Aldrich/Merck, Darmstadt, Germany
- bisBenzimide H 33342 trihydrochloride, cat no. 14533-100MG, Sigma-Aldrich/Merck, Darmstadt, Germany
- Cacodylic acid sodium salt trihydrate, cat. no. 5169.2, Carl Roth, Karlsruhe, Germany
- Calcium chloride, cat. no. A119.1, Carl Roth, Karlsruhe, Germany

- Carbon dioxide, Linde Gases Division, Pullach, Germany
- Chloroform, p.a., cat. no. 383770025, Acros Organics, New Jersey, USA
- 3,3´-Diaminobenzidine tetrahydrochloride hydrate, cat. no. D-5637, Sigma-Aldrich/ Merck, Darmstadt, Germany
- Dimethyl sulfoxide, ≥99.5%, cat. no. D5879-500ML, Sigma-Aldrich/Merck, Darmstadt, Germany
- 1,4-Dithiothreit (DTT), ≥99 %, p.a., cat. no. 6908.3, Carl Roth, Karlsruhe, Germany
- Dodecylsulfat-Na-salt in pellets, cat. no. 20765.03, SERVA Electrophoresis, Heidelberg, Germany
- Ethanol, absolute, ≥99.8%, cat. no. 32205-2.5L-M, Sigma-Aldrich/Merck, Darmstadt, Germany
- Ethidium bromide, cat. no. E8751, Sigma-Aldrich/Merck, Darmstadt, Germany
- Ethylendiamine tetraacetic acid disodium salt dihydrate, cat. no. 8043.2, Carl Roth, Karlsruhe, Germany
- Epoxy embedding medium, cat. no. 45345, Sigma-Aldrich/Merck, Darmstadt, Germany
- Epoxy embedding medium, hardener DDSA, cat. no. 45346, Sigma-Aldrich/Merck, Darmstadt, Germany
- Epoxy embedding medium, hardener MNA, cat no. 45347, Sigma-Aldrich/Merck, Darmstadt, Germany
- Glycerin, ≥99.5%, cat. no. 3783.2, Carl Roth, Karlsruhe, Germany
- Glycidether accelerator DMP-30, cat. no. 8621.1, Carl Roth, Karlsruhe, Germany
- Glycine, puriss. p.a., cat. no. 33226-1KG, Sigma-Aldrich/Merck, Darmstadt, Germany
- Guanidine hydrochloride, cat. no. 6069.1, Carl Roth, Karlsruhe, Germany
- G418 disulfate salt, cat. no. A1720-5G, Sigma-Aldrich/Merck, Darmstadt, Germany
- Kanamycin sulphate, ≥750 IU/mg, art. No. T832.2, Carl Roth, Karlsruhe, Germany
- Manganese chloride tetrahydrate, cat. no. M-3634, Sigma-Aldrich/Merck, Darmstadt, Germany
- Magnesium chloride hexahydrate, cat. no. M2670-100G, Sigma-Aldrich/Merck, Darmstadt, Germany
- Magnesium sulfate heptahydrate, cat. no. 00991, Ferak Laborat, Berlin, Germany
- 2-Mercaptoethanol, cat. no. 8.05740.0250, Merck, Darmstadt, Germany

- Methanol, ≥99.9%, cat. no. M/4000/17, Fisher Scientific, Schwerte, Germany
- MOPS, ≥99%, cat. no. 6979.2, Carl Roth, Karlsruhe, Germany
- Mowiol 4-88, cat. no. 0713.2, Carl Roth, Karlsruhe, Germany
- Nitrogen, liquid, Linde Gases Division, Pullach, Germany
- N,N,N′,N′-Tetramethylethylenediamine (TEMED), cat. no. T9281-50ML, Sigma-Aldrich/Merck, Darmstadt, Germany
- Nonidet P 40, cat. no. 74385, Fluka BioChemika/Merck, Darmstadt, Germany
- Paraformaldehyde, cat. no. 1.04005.1000, Merck, Darmstadt, Germany
- Phenylmethylsulfonylfluorid, cat no. 32395.02, SERVA Electrophoresis, Heidelberg, Germany
- Pioloform cat. no. R1275, Plano, Wetzlar, Germany
- PIPES, ≥99%, cat. no. 9156.2, Carl Roth, Karlsruhe, Germany
- PlusOne Bromophenol Blue, cat. no. 17-1329-01, Pharmacia Biotech/Cytiva Europe, Freiburg, Germany
- Polyethylene glycol, cat. no. P-3640, Sigma-Aldrich/Merck, Darmstadt, Germany
- Potassium acetate, cat. no. 1.04820.1000, Merck, Darmstadt, Germany
- Potassium chloride, cat no. LC-5916.1, neoFroxx, Einhausen, Germany
- Potassium dihydrogen phosphate, cat. no. 104873.1000, Merck, Darmstadt, Germany
- Potassium hydroxide, pellets for analysis, cat. no. 1.05033.100, Merck, Darmstadt, Germany
- 2-Propanol ≥99.7%, cat. no. 20842.330, VWR International, Darmstadt, Germany
- Protease Inhibitor Cocktail Tablets, cOmplete Tablets EDTA-free, *EASYpack*, cat. no. 04693132001, Roche/ Merck, Darmstadt, Germany
- Puromycin dihydrochloride, cat. no. P8833-100MG, Sigma-Aldrich/Merck, Darmstadt, Germany
- Rubidium chloride, cat. no. R-2252, Sigma-Aldrich/Merck, Darmstadt, Germany
- Sodium chloride, cat. no. 3957.2, Carl Roth, Karlsruhe, Germany
- Sodium deoxycholate ≥97% (titration), cat. no. D6750-25G, Sigma-Aldrich/Merck, Darmstadt, Germany
- Sodium dihydrogen phosphate dihydrate, cat. no. T879.1, Carl Roth, Karlsruhe, Germany
- Sodium hydroxide pellets for analysis, cat. no. 1064981000, Merck, Darmstadt, Germany

- Sodium orthovandate BioChemica, cat. no. A2196,0005, AppliChem, Darmstadt, Germany
- Sucofin Skimmed Milk Powder, TSI, Zeven, Germany
- TRIS, cat. no. AE15.2, Carl Roth, Karlsruhe, Germany
- Tris-hydrochloride, cat. no. 9090.1, Carl Roth, Karlsruhe, Germany
- Triton X 100, cat. no. 3051.2, Carl Roth, Karlsruhe, Germany
- Tween 20, cat. no. 9127.2, Carl Roth, Karlsruhe, Germany
- Uranyl acetate dihydrate, cat. no. 1.08473, Merck, Darmstadt, Germany
- Xylene cyanol FF, cat. no. 38505, SERVA Electrophoresis, Heidelberg, Germany

2.1.2 Equipment

- Agarose gel electrophoresis chamber
    - HORIZON 58, Gibco BRL Horizontal Gel Electrophoresis Apparatus, Life Technologies/Thermo Fisher Scientific Waltham, USA
    - Owl EasyCast B2 Mini Gel Electrophoresis System, Thermo Fisher Scientific, Waltham, USA
- Autoclave
    - Tuttnauer 2540ML, Biomedis, Gießen, Germany
    - Tuttnauer 5050 ELV, Biomedis, Gießen, Germany
- Bunsen burner
    - GASI, schuett-biotec, Göttingen, Germany
    - Type 1230/1, Carl Friedrich Usbeck, Radevormwald, Germany
- Carbon coater 208carbon, high vacuum, Cressington Scientific Instruments, Watford, UK
- Cell sorting system BD FACSAria IIu, Becton Dickinson, Heidelberg, Germany, with
    - 488 nm laser
    - filter set: 530/30 filter (for EGFP) and a 610/20 filter (for mCherry)
- Centrifuge
    - Heraeus Multifuge 3 L-R with rotor 75006445, Kendro Laboratory Products, Langenselbold, Germany
    - Heraeus Pico 17 with 24 x 1.5/2.0 ml rotor (cat. no. 75003424), Thermo Fisher Scientific, Waltham, USA

    - himac CT15RE with rotor T15A61-5006 (both by Hitachi Koki), VWR International, Darmstadt, Germany
    - Micro Star 12 with rotor GRF-m2.0-12-b, VWR International, Darmstadt, Germany
- Chemiluminescence system FUSION FX7 with software Fusion (version 15.18), Vilber Lourmat, Eberhardzell, Germany
- Counting chamber Neubauer (depth 0.100 mm), Paul Marienfeld, Lauda-Königshofen, Germany
- CO_2 incubator CB 210, Binder, Tuttlingen, Germany
- Diamond knife histo 45°, cat. no. DH4560, Diatome, Nidau, Switzerland
- Electron microscope
    - Field emission electron microscope JEM-2100F, 200 kV, JEOL, Freising, Germany with
        - Camera TemCam F416 for TEM mode, TVIPS, Gauting, Germany
        - Software EM-MENU 5 (version 5.0.17) for TEM mode, TVIPS, Gauting, Germany
        - Software EM-TOOLS (version 1.9.5/2.0.0) for STEM mode, TVIPS, Gauting, Germany
        - STEM bright-field detector EM-24541SIOD, JEOL, Freising, Germany
        - Universal scan generator for STEM mode, TVIPS, Gauting, Germany
    - Transmission electron microscope EM 902, 80 kV, Carl Zeiss, Oberkochen, Germany with
        - Slow-scan CCD-Camera for TEM, 2K-Wide-angle, type 7899 inside, TRÖNDLE Restlichtverstärkersysteme, Moorenweis, Germany
        - Software ImageSP (version 1.2.10.20) by SYSPROG & TRS, TRÖNDLE Restlichtverstärkersysteme, Moorenweis, Germany
- Electrophoresis Power Supply EV261, Consort, Turnhout, Belgium
- Forceps (Various types, including reverse forceps), Plano, Wetzlar, Germany
- Freezer
    - Freezers -20°C, various types, Privileg/Bauknecht Hausgeräte, Stuttgart, Germany and Liebherr-International Deutschland, Biberach an der Riß, Germany

    - HERAfreeze HFU T Series -86°C Upright Ultra-Low Temperature Freezer, Thermo Fisher Scientific, Waltham, USA
- Freezing container Corning CoolCell FTS30, Merck, Darmstadt, Germany
- Fume hood (type TA 1800 x 900-900) with electrical module (type KLV 3), Laborsystem mc6, WALDNER Laboreinrichtungen, Wangen, Germany
- Gel documentation system
    - UV-SYSTEME, INTAS Science Imaging Instruments, Göttingen, Germany
    - Video Copy Processor P93E, Mitsubishi Electric Europe, Ratingen, Germany
- Glassware (various products), Schott, Mainz, Germany and VWR International, Darmstadt, Germany
- Heating and drying table, MEDAX, Neumünster, Germany
- Heating block LS 1, VLM, Bielefeld, Germany
- Heating plate with magnetic stirrer MR 3001, Heidolph Instruments, Schwabach, Germany
- Ice machine, Ziegra, Isernhagen, Germany
- Incubator shaker Unitron, type AJ 260, Infors, Bottmingen, Switzerland
- Laboratory pH meter CG 842, Schott, Mainz, Germany with pH electrode SenTix60, WTW/Xylem Analytics Germany, Weilheim, Germany
- Laminar flow bench
    - LaminAir HA 2448 GS, Heraeus Instruments, Hanau, Germany
    - HERAsafe, Heraeus Instruments, Hanau, Germany
- Light microscope
    - Inverted microscope Axiovert 200M, Carl Zeiss, Oberkochen, Germany with
        - Filter set: D 350/50 excitation, ET 460/50 emission filter (for Alexa350 and bisBenzimide H), ET 470/40 excitation, ET 525/50 emission filter (for EGFP) and ET 560/40 excitation, ET 630/75 emission filter (for mCherry)
        - HXP 120 V Compact Light Source, Leistungselektronik JENA, Jena, Germany
        - Objective Fluar 40x/1.30 oil immersion, Zeiss, Oberkochen, Germany
        - Objective Plan-NEOFLUAR 16x/0.50 oil immersion, Zeiss, Oberkochen, Germany
        - sCMOS camera pco.edge 4.2, PCO, Kelheim, Germany

        - Software VisiView (version 4.1.0.4), Visitron Systems, Puchheim, Germany
    - Inverted microscope ECLIPSE TS100, Nikon Instruments Europe, Amsterdam, The Netherlands with
        - Objective Plan Fluor 4x/0.13, PhL DL, Nikon Instruments Europe, Amsterdam, The Netherlands
        - Objective 10x/0.25, Ph1 ADL, Nikon Instruments Europe, Amsterdam, The Netherlands
- Microwave 8016 G, Privileg/Bauknecht Hausgeräte, Stuttgart, Germany
- Oven
    - Type Tv26u, Memmert, Schwabach, Germany
    - Type T 6200, Heraeus Instruments, Hanau, Germany
- PIPETBOY acu and PIPETBOY acu 2, INTEGRA Biosciences, Biebertal, Deutschland
- Pipettes (PIPETMAN Classic P2, P20, P200, P1000), Gilson Germany/Austria, Limburg-Offheim, Germany
- Plasma cleaner PDC-3XG, Harrick Plasma, Ithaca, USA
- Precision balances:
    - Science Education, VWR International, Darmstadt, Germany
    - KERN 770, KERN & Sohn, Balingen-Frommern, Germany
- Pressure regulator K 98, Kayser, Koblenz, Germany
- Refrigerators, 4°C, various types, Privileg/Bauknecht Hausgeräte, Stuttgart, Germany and Philipp Kirsch, Willstätt-Sand, Germany
- Rotation mixer, Elektronik Werkstatt, University of Regensburg, Regesnburg, Germany
- Shaker/Mixer, Heidolph Instruments, Schwabach, Germany
    - Duomax 1030
    - Unimax 2010
- Semi-dry transfer cell Trans-Blot SD Cell, Bio-Rad Laboratories, Feldkirchen, Germany
- Slide Duplicating With Cover Slip Mold, cat. no. E70172, Science Services, München, Germany
- Spectrophotometer

    - EVOLUTION 201 with software Thermo INSIGHT (version 1.4.45), Thermo Fisher Scientific, Waltham, USA
    - Hitachi U-2000, Scientific Instruments, Schwäbisch Gmünd, Germany
    - NanoDrop 2000 with software NanoDrop 2000/2000c (version 1.6.198), Thermo Fisher Scientific, Waltham, USA
- Standard Flat Embedding Mold, cat. no. E70901, Science Services, München, Germany
- Standard Power Pack P25, Biometra, Göttingen, Germany
- Stereomicroscope M5, Wild Heerbrugg, Heerbrugg, Switzerland with light source LED control unit, Photonic Optische Geräte, Vienna, Austria
- Thermal cycler
    - Mastercycler gradient, Eppendorf, Hamburg, Germany
    - MyCycler, Bio-Rad Laboratories, Feldkirchen, Germany
    - T100, Bio-Rad Laboratories, Feldkirchen, Germany
- Thermomixer 5436, Eppendorf, Hamburg, Germany
- Ultramicrotome EM UC6, Leica Microsystems, Wetzlar, Germany
- Ultrapure water unit Seralpur PRO 90 CN, SERAL Erich Alhäuser, Ransbach-Baumbach, Germany with filter Supor DCF (Electronics Grade, 0.2µm), Pall Corporation, Dreieich, Germany
- Vacuum pump
    - Mini diaphragm vacuum pump VP 86, VWR International, Darmstadt, Germany
    - Mini diaphragm vacuum pump LABOPORT, KNF (supplier), VWR International, Darmstadt, Germany
- Vertical gel electrophoresis cell Mini-PROTEAN Tetra Cell, Bio-Rad Laboratories, Feldkirchen, Germany
- Vessel ARPEGE 170, long term storage of cryo-vials, AIR LIQUIDE Medical, Düsseldorf, Germany
- Vortexer
    - VF2 Janke & Kunkel/IKA-Werke, Staufen, Germany
    - Reax I, Heidolph Instruments, Schwabach, Germany

2.1.3 Consumables

- Aluminum foil, cat. no. 0954.1, Carl Roth, Karlsruhe, Germany
- Biosphere Filter Tips, Sarstedt, Nümbrecht, Germany
    - 0.5-20 µl: cat. no. 70.1116.210
    - 2-20 µl: cat. no. 70.760.213
    - 2-200 µl: cat. no. 70.760.211
    - 100-1000 µl: cat. no. 70.762.211
- Carbon Rods, cat. no. P/N 85103, Cressington Scientific Instruments, Watford, UK
- Cover Glass, thickness no. 1, cat. no. 631-0146, VWR International, Darmstadt, Germany
- CryoPure Tubes 1.8 ml, cat. no. 72.379.006, Sarstedt, Nümbrecht, Germany
- Cuvettes, Polysterene, cat. no. 67.742, Sarstedt, Nümbrecht, Germany
- Disposable Cell Scraper, cat. no. 83.1831, Sarstedt, Nümbrecht, Germany
- Disposable Glass Pasteur Pipettes 150 mm, cat. no. 612-1701, VWR International, Darmstadt, Germany
- Disposable Gloves Nitrile, rotiprotect-NITRIL, cat. no. AYA8.1, Carl Roth, Karlsruhe, Germany
- Disposable hydremic needle, B. Braun Melsungen, Melsungen, Germany
    - 20 Gauge: cat. no. 4657519
    - 21 Gauge: 4657527
- Disposable scalpels, cat. no. 146210, Mergo, Wesel, Germany
- Double Edged Razor Blades, cat. no. 72000, Science Services, München, Germany
- Eppendorf Tubes 5.0 ml, cat. no. 0030119401, Eppendorf, Hamburg, Germany
- Filter Discs, diameter 110 mm, cat. no. FT-3-303-110, Sartorius, Göttingen, Germany
- Filtropur S, Sarstedt, Nümbrecht, Germany
    - 0.2 µm: cat. no. 83.1826.001
    - 0.45 µm: cat. no. 83.1826
- Glass Bottom Culture Dishes, 35 mm Glass Bottom, P35G-1.5-14-CGRID, MatTek Corporation, Ashland, USA
- Household towels Wischfix, Fripa, Miltenberg, Germany

- Immersion oil, Immersol 518 F, refractive index: 1.518, cat. no. 444962-0000-000, Carl Zeiss Microscopy, Jena, Germany
- Indicator tape (for steam sterilization), Mercateo Deutschland, München, Germany
- KIMTECH Science, Delicate Task Wipes-White, Kimberly-Clark Professional, Koblenz/ Rheinhafen, Germany
- Microscope Cover Glasses, 10 mm diameter, thickness no. 1, cat. no. 631-1576, VWR International, Darmstadt, Germany*
- Microscope Cover Slips, 22 mm diameter, cat. no. P235.1, Carl Roth, Karlsruhe, Germany*
- Microscope Slides, cat. no. 03-0004, R. Langenbrinck, Emmendingen, Germany
- Microscope Slides, SuperFrost, cat. no. 2119, Carl Roth, Karlsruhe, Germany
- Micro tube 1.5 ml, cat. no. 72.690.001, Sarstedt, Nümbrecht, Germany
- Multiply-Pro cup 0.2 ml PP, cat. no. 72.737.002, Sarstedt, Nümbrecht, Germany
- Parafilm M PM-996, Bemis Company, Oshkosh, USA
- Pasteur pipettes, long form 230 mm, art. no. M4230NO2505P4, Kimble Chase Life Science and Research Products, Meiningen, Germany
- Petri dish 92 x 16mm with cams (for agar plates), cat. no. 82.1473, Sarstedt, Nümbrecht, Germany
- Plastic cylinder, cat. no. cat. no. 10580, Plano, Wetzlar, Germany
- Pipette tips, Sarstedt, Nümbrecht, Germany
    - 10 µl: cat. no. 70.1130
    - 200 µl: 70.760.002
    - 1000 µl: 70.762
- Polystyrene sticks (for diamond knife cleaning), Diatome, Nidau, Switzerland
- Pre-Separation Filters 30 µm, cat. no. 130-041-407, Miltenyi Biotec, Bergisch Gladbach, Germany
- PVDF blotting membrane Amersham Hybond P 0.45 PVDF, 0.45 µm, supplier GE Healthcare, cat. no. 10600023, VWR International, Darmstadt, Germany
- SafeSeal micro tube 2ml, cat. no. 72.695.500, Sarstedt, Nümbrecht, Germany
- Serological Pipettes, Sarstedt, Nümbrecht, Germany
    - 5 ml: cat. no. 86.1253.001
    - 10 ml: cat. no. 86.1254.001

    - 25 ml: cat. no. 86.1685.001
- Single-use fine dosage syringes Injekt-F, 1 ml, cat. no. 9166017V, B. Braun Melsungen, Melsungen, Germany
- Single-use syringes NORM-JECT, Henke-Sass, Wolf, Tuttlingen, Germany
    - 10 ml (12 ml): cat. no. 4100-000V0
    - 20 ml (24 ml): cat. no. 4200-000V0
- Sterile indicator strip Comply, hot air sterilisation, cat. no. H590.1, Carl Roth, Karlsruhe, Germany
- Stirrup-shaped blades Type 210, cat. no. CK07.1, Carl Roth, Karlsruhe, Germany
- Superglue, liquid, UHU, Bühl, Germany
- TC Dishes, Standard, Sarstedt, Nümbrecht, Germany
    - 35: cat no. 83.3900
    - 60: cat. no. 83.3901
    - 100: 83.3902
- TC Plate, Standard.F, Sarstedt, Nümbrecht, Germany
    - 6 Well: 83.3920.005
    - 12 Well: cat. no. 83.3921
    - 24 Well: cat. no. 83.3922.005
    - 96 Well: cat. no. 83.3924
- Tissue Culture dishes 35 x 10 mm, cat. no. 83.1800, Sarstedt, Nümbrecht, Germany
- Transfer pipettes, Sarstedt, Nümbrecht, Germany
    - 1 ml: cat. no. 86.1180
    - 3.5 ml: cat. no. 86.1171 and 86.1172
- Tubes, Sarstedt, Nümbrecht, Germany
    - 15 ml: cat. no. 62.554.502
    - 50 ml: 62.547.254
- Whatman paper, 3 MM CHR, cat. no. 3030-917, GE Healthcare, Solingen, Germany
- Whatman paper, lens cleaning tissue, cat. no. 2105-841, GE Healthcare, Solingen, Germany
- 1.5 ml SC Micro Tube PCR-PT, cat. no. 72.703.406, Sarstedt, Nümbrecht, Germany
- 2 mm x 1 mm slot copper grids, cat. no. G2500C, Plano, Wetzlar, Germany

- 5 ml Polystyrene Round-Bottom Tubes with Cell-Strainer Cap, cat. no. 352235, Corning, Wiesbaden, Germany
- 200 mesh thin bar copper grids 3.05 mm, cat. no. G2002, Plano, Wetzlar, Germany

* 10 mm cover glasses and 22 mm cover slips were incubated in acetone for at least 2-3 h, dried using KIMTECH task wipes and sterilized at 180°C for at least 6 h prior to use for cell culture.

2.1.4 Buffers and solutions

This chapter is structured in analogy to the methods section 2.2. Buffers and solutions are listed in the same order as they are mentioned within the text. Each buffer/solution is listed only once. If a buffer/solution was already mentioned in a section, it is not listed again in other chapters even though it was used. All manufacturer supplied buffers/solutions are listed at the end of the chapter.

2.1.4.1 Molecular cloning

Polymerase chain reaction

Buffer/Solution	Components
2 mM dNTP stock solution (stored at -20°C)	– 2 mM dATP (from 100 mM dATP) – 2 mM dCTP (from 100 mM dCTP) – 2 mM dGTP (from 100 mM dGTP) – 2 mM dTTP (from 100 mM dTTP) – sterile filtered dH_2O

Gel electrophoresis

Buffer/Solution	Components
10 M NaOH	– 10 M NaOH (from pellets, MW: 40 g/mol) – dH_2O
0.5 M Na_2EDTA x 2 H_2O, pH 8.0, autoclaved	– 0.5 M Na_2EDTA x 2 H_2O – NaOH pellets to dissolve Na_2EDTA x 2 H_2O – dH_2O – Hydrochloric acid 37% to adjust pH

50x TAE buffer, autoclaved	– 2 M Tris – 50 mM Na_2EDTA x 2 H_2O (from 0.5 M Na_2EDTA x 2 H_2O, pH 8.0) – 5.71% (v/v) Acetic acid – dH_2O
1x TAE buffer (from 50x TAE buffer)	– 40 mM Tris – 1 mM Na_2EDTA x 2 H_2O – 0.11% (v/v) Acetic acid
1 mg/ml Ethidium bromide stock	– 1 g/l Ethidium bromide (MW: 394.31 g/mol) – dH_2O
10x DNA loading buffer (stored at 4°C)	– 0.25% (w/v) Bromophenol blue (MW: 669.99 g/mol) – 0.25% (w/v) Xylene cyanol (MW: 538.6 g/mol) – 50% (v/v) Glycerin – dH_2O
0.1 mg/ml 1 kb Plus DNA Ladder (stored at 4°C)	– 0.1 mg/ml 1 kb Plus DNA Ladder (from 1mg/ml stock) – 1x Gel Loading Dye, Purple, no SDS (from 6x stock) – dH_2O

Chemically competent bacteria and transformation

Buffer/Solution	Components
Transformation and storage solution, sterile filtered (stored at 4°C)	– 10% (w/v) Polyethylene glycol (av. MW: 3350 g/mol) – 5% (v/v) Dimethyl sulfoxide – 25 mM $MgSO_4$ x 7 H_2O – LB medium
1 M KOH	– 1 M KOH (pellets) – dH_2O
1 M $MgCl_2$ stock solution, sterile filtered	– 1 M $MgCl_2$ x 6 H_2O – dH_2O
1 M $MgSO_4$ stock solution, sterile filtered	– 1 M $MgSO_4$ x 7 H_2O – dH_2O

500 mM PIPES stock solution, pH 6.7	– 500 mM PIPES – dH_2O – 1 M KOH or 1 M HCl to adjust pH
100 mM MOPS stock solution, pH 7.0	– 100 mM MOPS – dH_2O – 1 M Sodium hydroxide solution to adjust pH
FTB buffer, sterile filtered (stored at 4°C)	– 10 mM PIPES (from 500 mM PIPES stock solution) – 55 mM $MnCl_2$ – 15 mM $MgCl_2$ – 250 mM KCl
FTP buffer, sterile filtered (stored at 4°C)	– 10 mM MOPS (from 100 mM MOPS stock solution) – 75 mM CaCl2 – 10 mM RbCl – 12% (w/v) Glycerin
100 mg/ml Ampicillin stock solution, sterile filtered (stored at -20°C)	– 100 mg/ml Ampicillin sodium salt (MW: 371.39 g/mol) – dH_2O
50 mg/ml Kanamycin stock solution, sterile filtered (stored at -20°C)	– 50 mg/ml Kanamycin sulphate (≥750 UI/ml, MW: 582.58 g/mol) – dH_2O

DNA purification: Miniprep

Buffer/Solution	Components
1 M Tris, pH 8.0	– 1 M Tris – dH_2O – Hydrochloric acid 37% to adjust pH
20% SDS solution	– 20% (w/v) Dodecylsulfat-Na-salt in pellets (MW: 288.38 g/mol) – dH_2O

10 mg/ml RNase stock (store at -20°C)	– 10 mg/ml RNase (85.5 U/mg) – dH_2O
Buffer P1 (stored at 4°C)	– 20 mM Tris, pH 8.0 (from 1 M Tris) – 10 mM Na_2EDTA x 2 H_2O (from 0.5 M Na_2EDTA x 2 H_2O, pH 8.0) – 100 µg/ml RNase (from 10 mg/ml RNase stock) – dH_2O
Buffer P2 (stored at 4°C)	– 0.2 M NaOH (from 10 M NaOH) – 1% (w/v) SDS (from 20% SDS stock solution) – dH_2O
Buffer P3, pH 5.5 (stored at 4°C)	– 3 M Potassium acetate – dH_2O – Acetic acid to adjust pH
70% Ethanol	– 70% (v/v) Ethanol – dH_2O

DNA purification: Midiprep

Buffer/Solution	Components
40% Glycerin in 1x PBS, autoclaved/sterile filtered	– 40% (v/v) Glycerin – 1x PBS, pH 7.4

2.1.4.2 Cell culture

Freezing and thawing of cells

Buffer/Solution	Components
10x PBS, autoclaved	– 1.37 M NaCl – 27 mM KCl – 17.6 mM KH_2PO_4 – 100 mM Na_2HPO_4 x 2 H_2O – dH_2O

1x PBS, pH 7.4, autoclaved (from 10x PBS buffer)	– 137 mM NaCl – 2.7 mM KCl – 1.76 mM KH_2PO_4 – 10 mM Na_2HPO_4 x 2 H_2O – dH_2O
1 mg/ml Puromycin stock solution, sterile filtered (stored at -20°C)	– 1 mg/ml Puromycin dihydrochloride (MW: 544.43 g/mol) – 1x PBS, pH 7.4, autoclaved

80 mg/ml G418 stock solution, sterile filtered (stored at -20°C)	– 80 mg/ml G418 disulfate salt (MW: 692.7 g/mol) – 1x PBS, pH 7.4, autoclaved

FACS analysis and subcloning of cell lines

Buffer/Solution	Components
FACS buffer	– 2 mM Na_2EDTA x 2 H_2O (from 0.5 M Na_2EDTA x 2 H_2O, pH 8.0) – 0.2 % (v/v) FCS – 1x PBS (pH 7.4), autoclaved

2.1.4.3 Immunofluorescence

Buffer/Solution	Components
4% Formaldehyde in 1x PBS, pH 7.4, sterile filtered (stored at -20°C)	– 4% (w/v) Paraformaldehyde – dH_2O and drops of 1 M NaOH for solving – 1x PBS (from 10x PBS)
4% Formaldehyde in 1x PBS, pH >10, sterile filtered (stored at -20°C)	– 4% (w/v) Paraformaldehyde – 20 mM NaOH (from 1 M NaOH) – 1x PBS (pH 7.4)
50 mM NH_4Cl in 1x PBS, pH 7.4	– 50 mM NH_4Cl – 1x PBS, pH 7.4

1% Triton X-100 in 1x PBS	– 1% (v/v) Triton X-100 – 1x PBS, pH 7.4
0.1% Triton X-100 in 1x PBS	– 0.1% (v/v) Triton X-100 (from 1% Triton X-100 in 1x PBS) – 1x PBS, pH 7.4
Blocking solution, sterile filtered (stored at -20°C)	– 0.5% (w/v) bovine Albumin Fraction V (MW: ~ 66´000 g/mol) – 0.1% (v/v) Triton X-100 (from 1% Triton X-100 in 1x PBS) – 1x PBS, pH 7.4
5mg/ml bisBenzimide H 33258 stock solution	– 5 mg/ml bisBenzimide H 33258 (MW: 533.88 g/mol) – dH_2O
5mg/ml bisBenzimide H 33342 stock solution	– 5 mg/ml bisBenzimide H 33342 (MW: 561.93 g/mol) – dH_2O
Mowiol (store at -20°C)	– 10 g Mowiol 4-88 – 40 ml 1x PBS, pH 7.4 Stirring at room temperature for 24 h – 20 ml Glycerin Stirring at room temperature for 24 h Centrifugation at 4´000 g for 15 min at room temperature → use supernatant

2.1.4.4 Western blot analysis

Cell lysis preparation

Buffer/Solution	Components
100 mM PMSF stock solution (store at -20°C)	– 100 mM Phenylmethylsulfonylfluorid – Dimethyl sulfoxide
1 M DTT stock solution (store at -20°C)	– 1 M 1,4-Dithiothreit – dH_2O

100 mM Na_3VO_4 stock solution (store at -20°C)	– 1.84 g sodium orthovandate BioChemica – 60 ml dH_2O – Boiling and cooling on ice until solution turns yellow – Hydrochloric acid 37% to adjust pH to 10 – Boiling and cooling on ice until solution turns clear – dH_2O to a total volume of 100 ml – 5 M NaOH to adjust pH to 10
25x cOmplete EDTA-free protease inhibitor stock solution (store at -20°C)	– One cOmplete tablet of EDTA-free protease inhibitor – 2 ml RIPA buffer (before addition of PMSF, DTT, Na_3VO_4 and EDTA-free protease inhibitor)
Lysis buffer (= RIPA buffer) (RIPA buffer before addition of PMSF, DTT, Na_3VO_4 and EDTA-free protease inhibitor is stored at 4°C)	– 50 mM Tris, pH 8.0 (from 1 M Tris, pH 8.0) – 150 mM NaCl – 1% (v/v) Nonidet P 40* – 1% (w/v) sodium deoxycholate (MW 414.55 g/mol) – 1 mM Na_2EDTA x 2 H_2O (from 0.5 M Na_2EDTA x 2 H_2O, pH 8.0) Add right before use: – 1 mM PMSF (from 100 mM PMSF stock solution) – 1 mM DTT (from 1 M DTT stock solution) – 2 mM Na_3VO_4 (from 100 mM Na_3VO_4 stock solution) – 1x cOmplete EDTA-free protease inhibitor (from 25x cOmplete EDTA-free protease inhibitor stock solution)
3x SDS sample buffer (buffer before addition of 200 mM DTT is stored at 4°C)	– 188 mM Tris, pH 6.8 – 30% (v/v) Glycerin – 6% (v/v) SDS (from 20% SDS stock solution) – 0.04% (w/v) Bromophenol blue (MW: 669.99 g/mol) Add right before use: – 200 mM DTT (from 1 M DTT stock solution)

*According to Merck Customer Support Nonidet P 40 and IGEPAL CA-630 can be used equivalently.

Bradford protein assay

Buffer/Solution	Components
Bradford reagent, light-protected	– 1x ROTI-Quant (from ROTI-Quant, 5x conc.) – dH_2O
50 mg/ml BSA stock solution (stored at -20°C)	– 50 mg/ml bovine Albumin Fraction V (MW: ~ 66´000 g/mol) – dH_2O

BSA concentration series	– 0.1, 0.25, 0.5, 1.5, 2.5, and 5 mg/ml 50 mg/ml bovine Albumin Fraction V (from 50 mg/ml BSA stock solution) – dH_2O

SDS polyacrylamide gel electrophoresis

Buffer/Solution	Components
10% SDS solution	– 10% (w/v) SDS (from 20% SDS solution) – dH_2O
1.5 M Tris, pH 8.8	– 1.5 M Tris – dH_2O
0.5 M Tris, pH 6.8	– 0.5 M Tris – dH_2O
10% APS stock solution	– 10% (w/v) Ammonium peroxodisulfate (MW: 228.20 g/mol) – dH_2O
10x SDS running gel buffer	– 0.25 M Tris – 1.9 M Glycine – 10 g/l SDS (MW: 288.38 g/mol) – dH_2O

1x SDS running gel buffer (from 10x Running gel buffer)	– 25 mM Tris – 0.19 M Glycine – 1 g/l SDS (MW: 288.38 g/mol) – dH_2O

Semi-dry blot

Buffer/Solution	Components
Transfer buffer	– 25 mM Tris – 192 mM Glycine – 20% (v/v) Methanol – 0.025% (w/v) SDS (from 20% SDS solution) – dH_2O
1x PBS-T, pH 7.4	– 1x PBS, pH 7.4 – 0.1% (v/v) Tween 20
Blocking solution (5% skimmed milk powder in 1x PBS-T)	– 5% (w/v) skimmed milk powder – 0.1% (v/v) Tween 20 – 1x PBS, pH 7.4
Stripping buffer, pH 7.5	– 6 M Guanidine hydrochloride – 0.2% (v/v) Triton X-100 – 20 mM Tris – 0.1 M 2-Mercaptoethanol
140 mM NaCl in 10 mM Tris, pH 7.2	– 140 mM NaCl – 10 mM Tris

2.1.4.5 Correlative light and electron microscopy

Fluorescence microscopy

Buffer/Solution	Components
0.1 M Sodium cacodylate buffer, pH 7.4, sterile filtered	– 0.1 M Cacodylic acid sodium salt trihydrate – dH_2O

4% Formaldehyde in 0.1 M sodium cacodylate buffer, pH 7.4, sterile filtered (stored at -20°C)	– 4% (w/v) Paraformaldehyde – drops of 1 M NaOH for solving – 0.1 M sodium cacodylate buffer, pH 7.4

Preparation for electron microscopy

Buffer/Solution	Components
2% Glutardialdehyde in 0.1 M sodium cacodylate buffer sterile filtered	– 2% (v/v) Glutardialdehyde (from Glutaraldehyde 25% solution in water) – 0.1 M Sodium cacodylate buffer, pH 7.4
1% OsO_4 in 0.1 M sodium cacodylate buffer	– 1% (v/v) OsO_4 (from Osmium tetroxide 4% aqueous solution) – 0.1 M Sodium cacodylate buffer, pH 7.4
4% Uranyl acetate stock solution	– 4% (w/v) Uranyl acetate dihydrate (MW: 424.15 g/mol) – dH_2O 37-40°C tempered and if necessary ultrasonic bath to dissolve
1% Uranyl acetate solution sterile filtered	– 1% (w/v) Uranyl acetate dihydrate (from 4% Uranyl acetate stock solution) – dH_2O
Ethanol series	– 20%, 30%, 50%, 60%, 70%, 80%, 90%, 95% and 96% (v/v each) Ethanol – dH_2O
Epon embedding resin (stored at -20°C)	– 46.00 g Epoxy embedding medium – 28.50 g Hardener DDSA – 25.10 g Hardener MNA Stirring for 30 min – 1.50 g Glycidether accelerator DMP-30 Stirring for 30 min
Acetone-Epon mix	– 50% (v/v) Epon – 50% (v/v) Acetone

Ultramicrotomy

Buffer/Solution	Components
1.5% Pioloform in chloroform (stored at 4°C, light-protected)	– 1.5% (w/v) Pioloform – Chloroform

Electron microscopy

Buffer/Solution	Components
Protein A conjugated gold particle solution (1:40 dilution)	– 2.5% (v/v) Fiducial Gold 15 nm (optical density of the protein A bound gold: 9.55 for batch J1708) – dH_2O

2.1.4.6 Histochemistry for electron microscopy

Amplex UltraRed labelling

Buffer/Solution	Components
10 mM Amplex UltraRed stock solution (stored at -20°C, light-protected)	– 1 mg (= one vial, supplied by manufacturer) Amplex UltraRed reagent (MW: ~300 g/mol) – add 340 µl Dimethyl sulfoxide
50 µM Amplex UltraRed and 6.7 mM H_2O_2 in 1x PBS	– 50 µM Amplex UltraRed (from 10 mM Amplex UltraRed solution – 6.7 mM H_2O_2 (from Hydrogen peroxide 30%) – 1x PBS, pH 7.4

Histochemistry for electron microscopy

Buffer/Solution	Components
2% Glutardialdehyde and 2 mM $CaCl_2$ in 0.1 M sodium cacodylate buffer sterile filtered	– 2% (v/v) Glutardialdehyde (from Glutaraldehyde 25% solution in water) – 2 mM $CaCl_2$ – 0.1 M Sodium cacodylate buffer, pH 7.4
Blocking solution sterile filtered	– 20 mM Glycine – 0.1 M Sodium cacodylate buffer, pH 7.4

50 mM Tris-HCl, pH 7.6 sterile filtered	– 20 mM Tris-hydrochloride – dH_2O
10 mg/ml 3,3´-Diaminobenzidine stock solution sterile filtered, stored at -20°C	– 10 mg/ml 3,3´-Diaminobenzidine (MW: 360.11 g/mol) – dH_2O
0.5 mg/ml 3,3´-Diaminobenzidine and 6.7 mM H_2O_2 in 50 mM Tris-HCl, pH 7.6, sterile filtered	– 0.5 mg/ml 3,3´-Diaminobenzidine (from 10 mg/ml 3,3´-Diaminobenzidine stock solution) – 6.7 mM H_2O_2 (from Hydrogen peroxide 30%) – 50 mM Tris-HCl, pH 7.6

2.1.4.7 Manufacturer supplied buffers/solutions

- Acrylamide/Bis Solution, 37.5:1, 30% (w/v), cat. no. 10688.01, SERVA Electrophoresis, Heidelberg, Germany
- CutSmart Buffer, 10x, cat. no. B7204S, New England Biolabs, Frankfurt am Main, Germany
- dNTP set, 100 mM each, cat. no. R0181, Thermo Fisher Scientific, Waltham, USA
- Fetal Bovine Serum, sterile filtered, cat. no. P30-3306, lot. no. P150508, PAN-Biotech, Aidenbach, Germany
- Fiducial Gold 15 nm, 400 µl, cat. no. FG 15 nm, batch J1708, University Medical Center Utrecht, Utrecht, The Netherlands
- Glutaraldehyde 25% solution in water, cat. no. 23114.02, SERVA Electrophoresis, Heidelberg, Germany
- Hydrochloric acid, 1 M, cat. no. 30024.290, VWR International, Darmstadt, Germany
- Hydrochloric acid 37%, cat. no. 20252.420, VWR International, Darmstadt, Germany
- Hydrogen peroxide 30%, cat. no. 1.07209.1000, Merck, Darmstadt, Germany
- L-Glutamine solution, 200 mM, cat. no. G7513-100ML, Sigma-Aldrich/Merck, Darmstadt, Germany
- Osmium tetroxide 4% aqueous solution, cat. no. 19150, Electron Microscopy Sciences, Hatfield, USA
- Penicillin- Streptomycin solution, 10´000 U/ml penicillin and 10 mg/ml streptomycin, steril filtered, cat. no. P4333-100ML, Sigma-Aldrich/Merck, Darmstadt, Germany

- *Pfu* 10X Reaction Buffer (with 20 mM MgSO4), cat. no. M776A, Promega, Walldorf, Germany
- ROTI-Quant, 5x conc., cat. no. K015.1, Carl Roth, Karlsruhe, Germany
- RT-PCR Grade Water, cat. no. AM9935, Invitrogen/Thermo Fisher Scientific, Waltham, USA
- Sodium bicarbonate solution, 7.5%, cat. no. S8761-100ML, Sigma-Aldrich/Merck, Darmstadt, Germany
- Sodium hydroxide solution, 1 M, cat. no. 35256-1L, Sigma-Aldrich/Merck, Darmstadt, Germany
- ThermoPol Reaction Buffer (includes $MgSO_4$), 10x, cat. no. B9004S, New England Biolabs, Frankfurt am Main, Germany
- Trypsin-EDTA Solution, 0.25%, sterile filtered, cat. no. T4049-100ML, Sigma-Aldrich/Merck, Darmstadt, Germany
- T4 DNA Ligase Reaction Buffer (10X), cat. no. B0202A, New England Biolabs, Frankfurt am Main, Germany
- WesternBright Chemilumineszenz Substrat Sirius, cat. no. 541020, Biozym Scientific, Hessisch Oldendorf, Germany
- 5X Phusion HF Reaction Buffer, cat. no. B0518S, New England Biolabs, Frankfurt am Main, Germany

2.1.5 Markers

- 1 kb Plus DNA Ladder, 1mg/ml, cat. no. N3200S, New England Biolabs, Frankfurt am Main, Germany
- Gel Loading Dye, Purple (6X), no SDS, cat no. B7025S, New England Biolabs, Frankfurt am Main, Germany
- PageRuler Prestained Protein Ladder, cat. no. 26616, Thermo Fisher Scientific, Waltham, USA

2.1.6 Kits and transfection reagents

- E.Z.N.A. Gel Extraction Kit, cat. no. D2500-01, Omega Bio-tek, Norcross, USA
- FuGENE 6 Transfection Reagent, cat. no. E2691, Promega, Walldorf, Germany

- Lipofectamine 3000 Transfection Kit, cat. no. L3000-008, Invitrogen/Thermo Fisher Scientific, Waltham, USA
- Plasmid Plus Midi Kit, cat. no. 12945, QIAGEN, Hilden, Germany

2.1.7 Enzymes

- AgeI-HF restriction enzyme, 20´000 U/ml, cat. no. R3552L, New England Biolabs, Frankfurt am Main, Germany
- HindIII-HF restriction enzyme, 20´000 U/ml, cat. no. R3104S, New England Biolabs, Frankfurt am Main, Germany
- NheI-HF restriction enzyme, 20´000 U/ml, cat. no. R3131S, New England Biolabs, Frankfurt am Main, Germany
- Penicillin-Streptomycin solution, 10´000 U/ml penicillin and 10 mg/ml streptomycin, sterile filtered, cat. no. P4333-100ML, Sigma-Aldrich/Merck, Darmstadt, Germany
- Phusion High-Fidelity DNA Polymerase, 2´000 U/ml, cat. no. M0530S, New England Biolabs, Frankfurt am Main, Germany
- *Pfu* DNA Polymerase, 3 U/µl, cat. no. M774B, Promega, Walldorf, Germany
- RNase A, 85.5 U/mg, cat. no. A3832,0250, AppliChem, Darmstadt, Germany
- RNase A, part of Plasmid Plus Midi Kit, cat. no. 12945, QIAGEN, Hilden, Germany
- *Taq* DNA Polymerase, 5´000 U/ml, cat. no. M0267L, New England Biolabs, Frankfurt am Main, Germany
- Trypsin-EDTA Solution, 0.25%, sterile filtered, cat. no. T4049-100ML, Sigma-Aldrich/Merck, Darmstadt, Germany
- T4 DNA Ligase, 400´000 U/ml, cat. no. M0202S, New England Biolabs, Frankfurt am Main, Germany
- XhoI, restriction enzyme, 20´000 U/ml, cat. no. R0146S, New England Biolabs, Frankfurt am Main, Germany

2.1.8 Plasmids and primers

Plasmids:

Name, Number*	Information	Source
pCAG/HRP-TM, OP #1078	mammalian expression vector, contains i.a. cDNA of HRP, ampicillin resistance gene	Addgene plasmid #44441**
pCAG/HRP-TM_02, OC #1532	mammalian expression vector, contains i.a. cDNA of HRP, cDNA of HRP with silent point mutation to remove internal *XhoI* site, ampicillin resistance gene	
pEGFP-C1, OP #163	mammalian expression vector, kanamycin and neomycin resistance genes	Clontech Laboratories/Takara Bio USA, Madison, USA
pEGFPN1/ARL3B	pEGFP-N1 vector backbone, contains cDNA of human wild-type ARL13B, transcript variant 1, NM_182896.3	Construct was generated by Kerstin N. Schmidt (unpublished)
pEGFPC1/RAB5A(S34N)	pEGFP-C1 vector backbone, contains cDNA of RAB5A(S34N) (GDP-locked mutant of human wild-type RAB5A, transcript variant 1, NM_004162.5)	RAB5(S34N) was published in Stenmark *et al.* 1994, construct was generated by Kerstin N. Schmidt (unpublished)
pEGFPC1/RAB7A(T22N)	pEGFP-C1 vector backbone, contains cDNA of RAB7A(T22N) (GDP-locked mutant of human wild-type RAB7A, NM_004637.6)	RAB7(T22N) was published in Feng *et al.* 1995, construct was generated by Kerstin N. Schmidt (unpublished)
pEGFPC1/RAB8A, OC #1389	pEGFP-C1 vector backbone, contains cDNA of human wild-type RAB8A (NM_005370.5)	Construct was generated by Kerstin N. Schmidt (Schmidt *et al.* 2012)
pEGFPC1/RAB8A(T22N), OC #1406	pEGFP-C1 vector backbone, contains cDNA of RAB8A(T22N) (GDP-locked mutant of human wild-type RAB8A, NM_005370.5)	Construct was generated by Kerstin N. Schmidt (Schmidt *et al.* 2012)
pEGFPC1/RAB11A(S25N)	pEGFP-C1 vector backbone, contains cDNA of RAB11A(S25N) (GDP-locked mutant of human wild-type RAB11A, transcript variant 1, NM_004663.5)	RAB11(S25N) was published in Ullrich *et al.* 1996, construct was generated by Kerstin N. Schmidt (unpublished)
pEGFP-N1, OP #493	mammalian expression vector, kanamycin and neomycin resistance genes, with multiple cloning site and EGFP gene	Clontech Laboratories/Takara Bio USA, Madison, USA

pEGFPN1/mSmoM2-APEX2_02, OC #1323	pEGFP-C1 vector backbone (*NheI*/*SalI* sites were used for cloning to remove *XhoI* site of backbone), contains cDNA of M2 (Xie *et al.* 1998) mutant (W539L) of murine wild-type Smoothened (NM_176996.4) and the cDNA*** of APEX2 (Lam *et al.* 2015) with 5' and 3' flanking flexible linker sequences cloned into mSmoM2 cDNA using its internal *XhoI* site	murine SmoM2 cDNA was a gift from Rajat Rohatgi (Sandford University, USA), murine SmoM2 mutant was already published in Incardona *et al.* 2002
pEGFPN1/HRP-mSmoM2, OC #1362	pEGFP-C1 vector backbone (*NheI*/*SalI* sites were used for cloning to remove *XhoI* site of backbone), contains cDNA of M2 (Xie *et al.* 1998) mutant (W539L) of murine wild-type Smoothened (NM_176996.4) and the cDNA of HRP (with silent point mutation to remove internal *XhoI* site) with 5' and 3' flanking flexible linker sequences cloned into mSmoM2 cDNA using its internal *XhoI* site	murine SmoM2 cDNA was a gift from Rajat Rohatgi (Sandford University, USA), murine SmoM2 mutant was already published in Incardona *et al.* 2002
pJET/Myko, OP #986	PCR product (for nested PCR see section 2.2.2.8) of a *Mycoplasma* contaminated sample was cloned into the pJET plasmid	Construct was generated by Andreas Winterpacht, Universitätsklinikum Erlangen, Erlangen, Germany
pmCherry-C1	mammalian expression vector, kanamycin and neomycin resistance genes, with multiple cloning site and mCherry gene	Clontech Laboratories/Takara Bio USA, Madison, USA
pmCherryC1/RAB5A(S34N)	pmCherry-C1 vector backbone, contains cDNA of RAB5A(S34N) (GDP-locked mutant of human wild-type RAB5A, transcript variant 1, NM_004162.5)	Construct was generated by Kerstin N. Schmidt (unpublished)
pmCherryC1/RAB7A(T22N)	pmCherry-C1 vector backbone, contains cDNA of RAB7A(T22N) (GDP-locked mutant of human wild-type RAB7A, NM_004637.6)	Construct was generated by Kerstin N. Schmidt (unpublished)
pmCherryC1/RAB8A	pmCherry-C1 vector backbone, contains cDNA of human wild-type RAB8A (NM_005370.5)	Construct was generated by Kerstin N. Schmidt (Schmidt *et al.* 2012)

pmCherryC1/RAB11A(S25N)	pmCherry-C1 vector backbone, contains cDNA of RAB11A(S25N) (GDP-locked mutant of human wild-type RAB11A, transcript variant 1, NM_004663.5)	Construct was generated by Kerstin N. Schmidt (unpublished)
pUC18, OP #52	DNA plasmid used for testing transformation efficiency of generated *DH5α* chemically competent *E. coli* cells, ampicillin resistance gene	Boehringer Mannheim, Mannheim, Germany
pWE3, OP #328	mammalian expression vector, puromycin resistance gene	American Type Culture Collection (Cockett *et al.* 1997)

* Number from the data base of the Institute for Molecular and Cellular Anatomy, University of Regensburg, Regensburg, Germany.

** pCAG-HRP-TM was a gift from Alice Ting (Addgene plasmid # 44441; http://n2t.net/addgene:44441; RRID:Addgene_44441) (Rhee *et al.* 2013).

*** APEX2-OMM was a gift from Alice Ting (Addgene plasmid # 79056; http://n2t.net/addgene:79056 ; RRID:Addgene_79056) (Lam *et al.* 2015).

Primer:

Name/Number*	5'-3' Sequence	Information/Source
CMV-for	CGCAAATGGGCGGTAGGCGTG	forward primer for sequencing of pEGFP-N plasmids (Clontech), Standard Primer List, Microsynth Seqlab
EGFP-N-rev	GCTTGCCGTAGGTGGCATC	reverse primer for sequencing of pEGFP-N plasmids (Clontech), Standard Primer List, Microsynth Seqlab
HRP-for2, #4087	TTTCTCGAGGGGGCGCGCCAAGGGCTCGGGCTCGACCTCGGGCTCGGGCATGCAGTT	forward primer with flexible linker sequence for cloning of HRP cDNA in *XhoI* site of mSmoM2 cDNA, HRP cDNA, flanking *XhoI* site
HRP-mut-for3-1, #4075	AAAACCGGTCGCCACCATGGA	forward primer for 5' insert fragment for overlap extension polymerase chain reaction to remove internal *XhoI* site of HRP cDNA, flanking *AgeI* site
HRP-mut-for3-2, #4077	GTCTGAATCGTTCGAGTGACC	forward primer for 3' insert fragment for overlap extension polymerase chain reaction to remove internal *XhoI* site of HRP cDNA

HRP-mut-rev3-1, #4076	GGTCACTCGAACGATTCAGAC	reverse primer for 5' insert fragment for overlap extension polymerase chain reaction to remove internal *XhoI* site of HRP cDNA
HRP-mut-rev3-2, #4078	AAAAAGCTTCTAACGTGGCTTCTT	reverse primer for 3' insert fragment for overlap extension polymerase chain reaction to remove internal *XhoI* site of HRP cDNA, flanking *HindIII* site
HRP-rev1, #4053	TTTCTCGAGCTTCCGCGGGCTCCACCCCCTCCACTACCTCCTCCTCCTGAAGAGTTGC	reverse primer with flexible linker sequence for cloning of HRP cDNA in *XhoI* site of mSmoM2 cDNA, HRP cDNA without stop codon, flanking *XhoI* site
MCGpF1, #3253	ACACCATGGGAGCTGGTAAT	forward primer for first polymerase chain reaction for evaluation of *Mycoplasma* contamination (see chapter 2.2.2.8), primer design by TaKaRa Bio (TaKaRa Bio)
MCGpF2, #3255	GTTCTTTGAAAACTGAAT	forward primer for second polymerase chain reaction for evaluation of *Mycoplasma* contamination (see chapter 2.2.2.8), primer design by TaKaRa Bio (TaKaRa Bio)
MCGpR1, #3254	CTTCWTCGACTTYCAGACCCAAGGCAT	reverse primer for first polymerase chain reaction for evaluation of *Mycoplasma* contamination (see chapter 2.2.2.8), primer design by TaKaRa Bio (TaKaRa Bio)
MCGpR2, #3256	GCATCCACCAWAWACTCT	reverse primer for second polymerase chain reaction for evaluation of *Mycoplasma* contamination (see chapter 2.2.2.8), primer design by TaKaRa Bio (TaKaRa Bio)
mSmoM2-sequrev1, #4026	ACACGTTGTAGCGCAAAGG	reverse primer for sequencing of mSmoM2 cDNA, binds at bp 226-244
M13-pUC-rev, #4051	AGCGGATAACAATTTCACACAGG	reverse primer for sequencing of pCAG plasmids, binds at lacZ gene (design by Sequencing Primer List, Addgene)
pCAG-F, #4050	GCAACGTGCTGGTTATTGTG	forward primer for sequencing of pCAG plasmids, binds at rabbit beta-globin intron (design by Sequencing Primer List, Addgene)

* Number from the data base of the Institute for Molecular and Cellular Anatomy, University of Regensburg, Regensburg, Germany.

2.1.9 Antibodies

Primary antibodies:

- Anti-acetylated tubulin monoclonal antibody, produced in mouse, protein concentration by Biuret 32.6 mg/ml, cat. no. T6793, batch no. 102M4800, Sigma-Aldrich/Merck, Darmstadt, Germany → working dilution for immunofluorescence: 1:1´000
- Anti-actin polyclonal antibody, produced in rabbit, protein concentration 0.4-0.8 mg/ml, cat. no. A2066-2ML, LOT: 106M4770V, Sigma-Aldrich/Merck, Darmstadt, Germany → diluted 1:1 with glycerin and stored at -20°C, working dilution for Western blot analysis: 1:2´500 (from glycerin dilution)
- Anti-ARL13B polyclonal antibody, produced in rabbit, 41 µg/150 µl, cat. no. 17711-1-AP, LOT: 00049885, Proteintech Group, Rosemont, USA → working dilution for immuno-fluorescence: 1:2´000
- Anti-green fluorescent protein (GFP) polyclonal antibody, produced in rabbit, cat. no. A6455, LOT: 1571723, Sigma-Aldrich/Merck, Darmstadt, Germany → working dilution for Western blot analysis: 1:1´000
- Anti-red fluorescent protein (RFP) monoclonal antibody, produced in mouse, cat. no. 6g6, LOT: 51020014B, ChromoTek, Planegg-Martinsried, Germany → working dilution for Western blot analysis: 1:2´000
- Anti-γ-tubulin monoclonal antibody, produced in mouse, LOT: 088M4786V, cat. no. T6557-2ML, Sigma-Aldrich/Merck, Darmstadt, Germany → working dilution for immunofluorescence: 1:2´000
- Anti-γ-tubulin polyclonal antibody, produced in rabbit, cat. no. T3559-2ML, LOT: 087M4788V, Sigma-Aldrich/Merck, Darmstadt, Germany → working dilution for immunofluorescence: 1:1´000

Secondary antibodies:

- Alexa Fluor 350, goat anti-mouse IgG, polyclonal antibody, 2 mg/ml, cat. no. A11045, LOT: 1458644, Invitrogen/Thermo Fisher Scientific, Waltham, USA → working dilution for immunofluorescence: 1:100
- Alexa Fluor 350, goat anti-rabbit IgG, polyclonal antibody, 2 mg/ml, cat. no. A11046, LOT: 1556077, Invitrogen/Thermo Fisher Scientific, Waltham, USA → working dilution for immunofluorescence: 1:100

- Alexa Fluor 568, donkey anti-mouse IgG, polyclonal antibody, 2 mg/ml, cat. no. A10037, LOT: 1827879, Invitrogen/Thermo Fisher Scientific, Waltham, USA → working dilution for immunofluorescence: 1:500
- Alexa Fluor 568, donkey anti-rabbit IgG, polyclonal antibody, 2 mg/ml, cat. no. A10042, LOT: 2136776, Invitrogen/Thermo Fisher Scientific, Waltham, USA → working dilution for immunofluorescence: 1:500
- Peroxidase conjugate, goat anti-mouse IgG, polyclonal antibody, protein by UV absorbance 8.3 mg/ml, cat. no. A3682-1ML, LOT: 074K4766, Sigma-Aldrich/Merck, Darmstadt, Germany → working dilution for Western blot analysis: 1:10´000
- Peroxidase conjugate, goat anti-rabbit IgG, polyclonal antibody, concentration 6.6 mg/ml, cat. no. A0545, LOT: 034K4836, Sigma-Aldrich/Merck, Darmstadt, Germany → working dilution for Western blot analysis: 1:15´000

2.1.10 Media

Media for bacteria

Medium	Components
LB medium, autoclaved	– 10 g Bacto Tryptone – 5 g Bacto Yeast Extract – 10 g NaCl – dH_2O to 1 l
TY medium, autoclaved	– 10 g Bacto Tryptone – 5 g Bacto Yeast Extract – 5 g NaCl – dH_2O to 1 l
SOB medium, autoclaved	– 20 g Bacto Tryptone – 5 g Bacto Yeast Extract – 0.5844 g (= 10 mM) NaCl – 0.19 g (= 2.5 mM) KCl – dH_2O to 980 ml, autoclaving – 10 ml (= 10 mM final) of 1 M $MgCl_2$ stock solution – 10 ml (= 10 mM final) of 1 M $MgSO_4$ stock solution

LB agar plates, autoclaved (stored at 4°C)	– 15 g Bacto Agar – LB medium to 1 l
TY agar plates, autoclaved (stored at 4°C)	– 20 g Bacto Agar – TY medium to 1 l

If necessary, antibiotic was added: 50 µg/ml kanamycin or 100 µg/ml ampicillin was added to TY medium, 25 µg/ml kanamycin or 100 µg/ml ampicillin was added to TY agar plates using 100 mg/ml ampicillin stock solution or 50 mg/ml kanamycin stock solution (see section 2.1.4.1)

Media for eukaryotic cell lines

Medium	Components
RPE1 cell culture medium	– 500 ml DMEM/Ham's F12 medium – Addition of 10% (v/v) FCS (centrifuged at 4´000 g for 7 min) – Addition of 2 mM L-glutamine – Addition of 0.26% sodium bicarbonate
Cell culture medium for serum starvation of RPE1 cells	– 500 ml DMEM/Ham's F12 medium – Addition of 2 mM L-glutamine – Addition of 0.26% sodium bicarbonate
RPE1 conditioned medium	RPE1 cell culture medium of wild-type RPE1 cells at a confluence of ~90% → Centrifugation at 4´000g for 7 min → Supernatant filtered (pore size 0.45 µm) – 50% (v/v) filtered supernatant (see above) – 50% (v/v) fresh RPE1 cell culture medium
LLC-PK_1 cell culture medium	– DMEM high glucose medium – Addition of 10% (v/v) FCS

Manufacturer supplied media

- Dulbecco's Modified Eagle's Medium/Nutrient Mixture F-12 Ham, cat. no. D6421-500ML, Sigma-Aldrich/Merck, Darmstadt, Germany
- Dulbecco's Modified Eagle's Medium - high glucose, cat. no. D6429-500ML, Sigma-Aldrich/Merck, Darmstadt, Germany

2.1.11 Bacteria

DH5α Escherichia coli cells, New England Biolabs, Frankfurt am Main, Germany

2.1.12 Eukaryotic cell lines

- hTERT-RPE1 (Clontech): human retinal pigment epithelial cells (Katoh *et al.* 2017); telomerase-immortalized (CLONTECH Laboratories, Inc. 1999); has hygromycin resistance as it was used by the manufacturer for stable selection (CLONTECH Laboratories, Inc. 1999) but also puromycin resistance (plasmid used for stable selection by the manufacturer has also a puromycin-resistance gene) (Katoh *et al.* 2017). The cell line was a kind gift of Gislene Pereira (Center for Organismal Studies, University of Heidelberg, Germany). This cell line was cultured without any antibiotic addition to the cell culture medium during the current work.
- RPE1/Centrin1-EGFP (Uetake *et al.* 2007): hTERT-RPE1 cell line constitutively producing a fusion protein of human Centrin1 with EGFP (COOH-terminus of Centrin1 fused with EGFP); has hygromycin resistance as it was used by the manufacturer for stable selection (CLONTECH Laboratories, Inc. 1999) and puromycin resistance (plasmid used for stable selection by the manufacturer has also a puromycin-resistance gene) (Katoh *et al.* 2017). Please note, the cell line does not show G418 resistance although it was used for stable selection (Uetake *et al.* 2007). The cell line was a kind gift of Gislene Pereira (Center for Organismal Studies, University of Heidelberg, Germany). This cell line was cultured without any antibiotic addition to the cell culture medium during the current work.
- RPE1/Centrin1-EGFP, EGFP-ARL3B: hTERT-RPE1 cell line constitutively producing a fusion protein of human Centrin1 with EGFP (COOH-terminus of Centrin1 fused with EGFP) and of human ARL13B with EGFP (COOH-terminus of ARL13B fused with EGFP); has hygromycin resistance as it was used by the manufacturer for stable selection (CLONTECH Laboratories, Inc. 1999), puromycin resistance (plasmid used for stable selection by the manufacturer has also a puromycin-resistance gene) (Katoh *et al.* 2017) and G418 resistance. This cell line was cultured with an addition of 800 µg/ml of G418 to the cell culture medium during the current work.
- RPE1/Centrin1-EGFP, ARL13B-EGFP, mCherry-RAB8A: hTERT-RPE1 cell line constitutively producing a fusion protein of human Centrin1 with EGFP (COOH-terminus of Centrin1 fused with EGFP), of human ARL13B with EGFP (COOH-terminus of

ARL13B fused with EGFP) and of human RAB8A with mCherry (NH_2-terminus of RAB8A fused with mCherry); has hygromycin resistance as it was used by the manufacturer for stable selection (CLONTECH Laboratories, Inc. 1999), puromycin resistance (plasmid used for stable selection by the manufacturer has also a puromycin-resistance gene) (Katoh *et al.* 2017) and G418 resistance. This cell line was cultured with an addition of 800 µg/ml of G418 as well as 2 µg/ml puromycin to the cell culture medium during the current work.

- LLC-PK_1 (Hull *et al.* 1976): Lilly Laboratories cell porcine kidney 1 (LLC-PK_1) cell line is a porcine kidney epithelial cell line (Miyamoto *et al.* 2019). The cell line is from the European Collection of Authenticated Cell Cultures, Public Health England and was bought (cat. no. 86121112) via Sigma-Aldrich/Merck, Darmstadt, Germany.
- LLC-PK_1/HRP-SmoM2-EGFP: LLC-PK_1 cell line constitutively producing a fusion protein of the M2 (Incardona *et al.* 2002; Xie *et al.* 1998) mutant (W539L) of murine Smoothened with *horseradish peroxidase* (HRP, inserted into SmoM2) and with EGFP (COOH-terminus of SmoM2 fused with EGFP) ; has puromycin resistance. This cell line was cultured with an addition of 1 µg/ml puromycin to the cell culture medium during the current work.

2.1.13 Programs

- Adobe Illustrator CS5, version 15.0.0, Adobe, San José, USA
- Adobe Photoshop CS5, Adobe, San José, USA
- Amira, version 5.6.0 and 2020.2, FEI/ Thermo Fisher Scientific, Waltham, USA
- Citavi, version 6.4.0.35, Swiss Academic Software GmbH, Wädenswil, Switzerland
- Coot, version 0.9, University of York, York, UK (Emsley & Cowtan 2004)
- eC-CLEM, version 1.0.1.5, University of Nantes, Nantes, France (Paul-Gilloteaux *et al.* 2017)
- EM-MENU 5, version 5.0.17, TVIPS, Gauting, Germany
- EM-TOOLS, version 1.9.5/2.0.0, TVIPS, Gauting, Germany
- FileMakrer Pro, version 6.0Dv4, FileMaker, Santa Clara, USA
- Fusion, version 15.18, Vilber Lourmat, Eberhardzell, Germany
- GENtle, version 1.9.4, Magnus Manske, University of Cologne, Cologne, Germany

- Icy, version 2.0.0.0, Institute Pasteur, Paris, France (Chaumont *et al.* 2012)
- ImageJ, National Institutes of Health, Bethesda, USA (Rueden *et al.* 2017; Schindelin *et al.* 2012)
- ImageSP, version 1.2.10.20, by SYSPROG & TRS, TRÖNDLE Restlichtverstärkersysteme, Moorenweis, Germany
- IMOD, version 4.10.23 or later, University of Colorado, Boulder; USA (Kremer *et al.* 1996)
- Microsoft Office Professional Plus 2019 (including Excel, Word and PowerPoint), Redmond, USA
- MODELLER, version 9v22, Ben Webb, University of California San Francisco, San Francisco, USA
- NanoDrop 2000/2000c, version 1.6.198, Thermo Fisher Scientific, Waltham, USA
- TvipsCLEM, version 1.0.0.1, TVIPS, Gauting, Germany
- Thermo INSIGHT, version 1.4.45, Thermo Fisher Scientific, Waltham, USA
- Origin, version 2020 SR1, OriginLab Corporation, Northampton, USA
- SnapGene Viewer, version 5.0.6, GSL Biotech, San Diego, Germany
- UCSF Chimera, University of California, San Francisco, USA (Pettersen *et al.* 2004)
- VisiView, version 4.1.0.4, Visitron Systems, Puchheim, Germany

2.1.14 Internet databases and tools

- BLAST, https://blast.ncbi.nlm.nih.gov/Blast.cgi, National Center for Biotechnology Information, Bethesda, USA
- Gene, https://www.ncbi.nlm.nih.gov/gene, National Center for Biotechnology Information, Bethesda, USA
- Human Protein Reference Database, https://www.hprd.org (Keshava Prasad *et al.* 2009; Peri *et al.* 2003)
- JPred 4, http://www.compbio.dundee.ac.uk/jpred4/index.html, University of Dundee, Dundee, UK (Drozdetskiy *et al.* 2015)
- LIGation.CALCulator, IN.SILICO, Ulrich Krauss, Heinrich Heine University Düsseldorf (Heinrich-Heine-Universität Düsseldorf)
- Protein, https://www.ncbi.nlm.nih.gov/protein, National Center for Biotechnology Information, Bethesda, USA

- PubMed, https://pubmed.ncbi.nlm.nih.gov, National Center for Biotechnology Information, Bethesda, USA
- Research Collaboratory for Structural Bioinformatics Protein Data Bank (RCSB PDB), https://www.rcsb.org/, Rutgers University, New Brunswick, USA; University of California San Diego, La Jolla, USA; University of California, San Francisco, USA (Berman *et al.* 2000)
- Reverse Complement, https://www.bioinformatics.org/sms/rev_comp.html, The Sequence Manipulation Suite, Paul Stothard, University of Alberta, Edmonton, Canada (Stothard 2000)
- *Saccharomyces* Genome Database, https://www.yeastgenome.org, Stanford University, Stanford, USA (Cherry *et al.* 2012)
- SNP, https://www.ncbi.nlm.nih.gov/snp, National Center for Biotechnology Information, Bethesda, USA
- Translate, https://web.expasy.org/translate/, ExPASy, SIB Swiss Institute of Bioinformatics, Lausanne, Switzerland

2.2 Methods

2.2.1 Molecular cloning

2.2.1.1 Mutagenesis polymerase chain reaction

For inserting specific point mutations (e.g. a silent mutation into the cDNA of the protein *horseradish peroxidase* (HRP) to remove the internal *XhoI* restriction enzyme site) an overlap extension polymerase chain reaction was used. In a first step two overlapping insert fragments were amplified via two separate polymerase chain reactions (Fig. 7). The reverse primer of the 5' insert fragment contained the point mutation and was complementary to the cDNA sequence of the forward primer of the 3' insert fragment. The design of the forward primer of the 5' insert fragment and reverse primer of the 3' fragment flanked the template cDNA (e.g. HRP) with restriction recognition sites at their ends respectively.

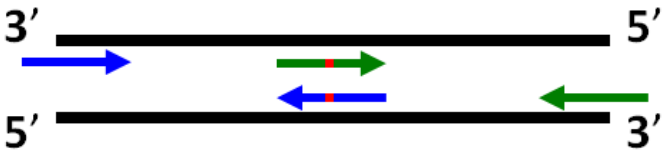

Figure 7: Schematic overview of primer design for overlap extension polymerase chain reaction. Strands of the template cDNA are shown in black. Primer pair for amplification of 5' insert fragment are shown in blue and of 3' insert fragment in green. The sequence of reverse primer of 5' insert fragment and of the forward primer of the 3' fragment show the specific point mutation (red).

Polymerase chain reaction mix for amplification of either the 3' or 5' insert fragment:

- 50 ng cDNA template
- 0.2 mM dNTPs
- 1 µM forward primer for 3' insert fragment or 5' insert fragment
- 1 µM reverse primer for 3' insert fragment or 5' insert fragment
- 1x Reaction Buffer (with $MgSO_4$)
- 1.25 U *Pfu* DNA Polymerase
- dH_2O to a total volume of 50 µl

The polymerase chain reaction program for amplification (Table 1) was the same for both insert fragments and was performed according to the manufacturer's instruction (Promega Corporation 2013).

Initial denaturation: 95°C for 2 min	
Denaturation at 95°C for 30 s Annealing* at 58°C for 45 s Extension** at 72°C for 80 s	34 cycles
Final extension at 72°C for 10 min	
Final holding step at 12°C	

Table 1: Polymerase chain reaction program for amplification of insert fragments. Table design based on *Pfu* DNA Polymerase Protocol Usage Information form Promega Corporation 2013.

*The annealing temperature for primer pairs HRP-mut-for3-1/-rev3-1 as well as for HRP-mut-for3-2/-rev3-2 was 2°C below the calculated melting temperature.

** Extension time for amplification of insert fragments of the cDNA of (HRP) was chosen according to the extension rate (0.5 kb/min) of *Pfu* DNA Polymerase and giving the polymerase an additional period of time of about 30% of the calculated extension time.

Amplified insert fragments were loaded on an agarose gel (2% (w/v) for insert fragments of HRP). After separation in the electric field, bands of insert fragments were cut out and gel extraction was carried out according to the manufacturer's instructions using E.Z.N.A. Gel Extraction Kit (Omega Bio-tek). DNA concentrations were measured using a NanoDrop spectrophotometer. See section 2.2.1.4 and 2.2.1.5 for detailed information regarding agarose gel electrophoresis and gel extraction.

In a next step, annealing of both insert fragments was performed. One hundred ng of the 5' insert fragment were used, 3' insert fragment was added with a molar ratio of 1:1 and dH_2O was added to a total volume of 21.58 µl. The program for annealing of insert fragments was as follows:

- 98°C for 10 min
- Gradient with -1°C/min from 98°C to 25°C
- Final holding step at 4°C

Next, the annealed insert fragments were extended for 15 min at 72°C using a polymerase chain reaction cycler. To achieve this, following components were added to the annealing mix to achieve a total volume of 30 µl:

- 3 µl 10x Reaction Buffer (with $MgSO_4$) → final concentration: 1x

- 5 µl of a 2 mM dNTP stock solution → final concentration: ~0.3 mM
- 1.25 U *Pfu* DNA Polymerase

In a last step the extended insert fragments were amplified. Therefore following components were added again to the mix:

- 2 µl 10x Reaction Buffer (with $MgSO_4$) → final concentration: 1x
- 1 µM forward primer of 3' insert fragment
- 1 µM reverse primer of 5' insert fragment
- dH_2O to a total volume of 50 µl

The polymerase chain reaction program for amplification (Table 2) was performed according to the manufacturer's instruction (Promega Corporation 2013).

Initial denaturation: 95°C for 2 min	
Denaturation at 95°C for 30 s Annealing* at 58°C for 45 s Extension** at 72°C for 140 s	34 cycles
Final extension at 72°C for 10 min	
Final holding step at 12°C	

Table 2: Polymerase chain reaction program for amplification of insert fragments. Table design based on *Pfu* DNA Polymerase Protocol Usage Information form Promega Corporation 2013.

*The annealing temperature for primer pairs HRP-mut-for3-1 and HRP-mut-rev3-2 was 2°C below the calculated melting temperature.

** Extension time for amplification of the cDNA of *horseradish peroxidase* (HRP) was chosen according to the extension rate (0.5 kb/min) of *Pfu* DNA Polymerase and giving the polymerase an additional period of time of about 25% of the calculated extension time.

Polymerase chain reaction product formation was verified using agarose gel electrophoresis (see section 2.2.1.4 for details). The mutated cDNA of the HRP protein, was purified after polymerase chain reaction using E.Z.N.A. Gel Extraction Kit (Omega Bio-tek). The following paragraph is a slightly modified, brief summary of the protocol of the manufacturer's product manual (Omega Bio-tek 2019). A volume of Binding Buffer (XP2) was added to the mix after polymerase chain reaction in a 1:1 ratio, vortexed, centrifuged for few seconds and transferred to a HiBind DNA Mini Column. Samples were centrifuged at 10´000 g for 1 min, filtrates were discarded, 700 µl

SPW Wash Buffer were added per sample and centrifuged at 17´000 g for 1 min. Filtrates were discarded and the washing step with SPW Wash Buffer was repeated for a second time. The HiBind DNA Mini Column (with bound cDNA) was centrifuged at 17´000 g for 2 min. HiBind DNA Mini Column were transferred to an empty 1.5 ml microcentrifuge tube, 15 µl Elution Buffer or autoclaved dH_2O were added per column, let sit at 37°C for 2 min and centrifuged at 17´000 g for 1 min. The elution step was repeated for a second time with another 15 µl of Elution Buffer or dH_2O. DNA concentrations were measured using a NanoDrop spectrophotometer and the samples were stored at -20°C for further treatment.

2.2.1.2 Polymerase chain reaction for cloning

A hot start polymerase chain reaction was performed for the amplification of the cDNA of proteins. For subsequent cloning, primer pairs were designed flanking the 5' and 3' end of the protein's cDNA and having restriction recognition sites at their 5' or 3' end respectively. As a temperature gradient was applied for annealing, several identical polymerase chain reaction mixtures were prepared for the amplification of the cDNA of one protein. For hot start polymerase chain reaction each of these mixtures consisted of the following components:

Mix A:	Mix B:
250 ng DNA template	0.2 mM dNTPs
1x Phusion HF Reaction Buffer	1x Phusion HF Reaction Buffer
1 µM forward primer	1 U Phusion HF Polymerase
1 µM reverse primer	dH_2O to a total volume of 12.5 µl
dH_2O to a total volume of 37.5 µl	

The polymerase chain reaction program was started using Mixtures A only. After an initial denaturation at 99°C for 5 min, the temperature was held at 99°C and Mixtures B were added respectively. The further program was as follows:

- Denaturation at 95°C for 30 s
- Annealing at 50.0-65.5°C for 45 s
- Extension at 72°C for 4 min

Thirty-four cycles were performed, followed by a final extension step at 72°C for 10 min and a holding step at 12°C at the end. For the annealing a gradient with different temperatures was used. A 4 min extension time for amplification of the mutated HRP cDNA (930 bp) was chosen to give the Phusion HF Polymerase more time than calculated according to the extension rate (1.5 kb/min).

Polymerase chain reaction product formation was verified using agarose gel electrophoresis (see section 2.2.1.4 for details). Reaction mixtures showing a specific cDNA amplification of the protein of interest after polymerase chain reaction were pooled and purified using E.Z.N.A. Gel Extraction Kit (Omega Bio-tek) as described in section 2.2.1.5 and stored at -20°C until further treatment.

2.2.1.3 Restriction enzyme digestion

To generate sticky ends, purified polymerase chain reaction amplification products as well as cDNA of proteins and DNA plasmids were digested using restriction enzymes according to the following mixture:

- 30 µl of a purified polymerase chain reaction product or 5 µg of a DNA plasmid
- 1x CutSmart Buffer
- 10 U of each restriction enzyme*
- dH_2O to a total volume of 50 µl

Polymerase chain reaction products were digested at 37°C overnight, cDNA of proteins and DNA plasmids at 37°C for 5 h.

* If the restriction enzyme for the 5’ end was the same as for the 3’ end, 20 U were used.

Analytical restriction enzyme digestion was performed to verify that the DNA of the protein of interest was successfully ligated with the plasmid. Therefore an aliquot of 1 µl or 3 µl of the DNA solution was used after DNA isolation

Mix for analytical digestion:

- 1 or 3 µl of isolated DNA plasmid
- 1x CutSmart Buffer
- 10 U of each restriction enzyme*
- dH_2O to a total volume of 10 µl

* If the restriction enzyme for the 5’ end was the same as for the 3’ end, 20 U were used.

DNA plasmids were digested at 37°C for 90 min.

2.2.1.4 Gel electrophoresis

The digested cDNA of all proteins of interest as well as the linearized DNA plasmids were loaded on agarose gels to separate DNA molecules in the electric field. If the DNA molecule of interest was smaller than 1 kb, a 1.5% (w/v) agarose gel was used, if the molecule was larger than 1 kb a

1% (w/v) agarose gel was used. A 2% (w/v) gel (see section 2.1.1.4) was used only for separation of insert fragments after overlap extension polymerase chain reaction and for the nested polymerase chain reaction to check for *Mycoplasma* contamination. Agarose was mixed with 1x TAE buffer in respective ratio, heated up to boiling and with constant stirring, ethidium bromide was added to a final concentration of 0.5 µg/ml. A total volume of 130 ml was used for gel extraction and 30 ml for analytical gels. Liquid gel was poured into the molds of the gel chamber and allowed to polymerize by cooling. The gel was covered with 1x TAE buffer and DNA samples were loaded. Prior to loading DNA solutions were mixed with 10x loading buffer to a final concentration of 1x. "1 kb Plus DNA Ladder" was used as molecular mass standard. DNA molecules were separated according to their molecular mass in an electrical field (for 130 ml gels 150 V were used and for 30 ml gels 110 V were used). For visualization of DNA molecules after gel electrophoresis fluorescent ethidium bromide which intercalates with nucleic acids (Reinhardt & Krugh 1978) was used in combination with UV light (excitation ~312 nm) of a gel documentation system.

2.2.1.5 Gel extraction

After gel electrophoresis for gel extraction, bands of interest were cut out with a scalpel and gel extraction was performed using E.Z.N.A. Gel Extraction Kit (Omega Bio-tek). The following paragraph is a slightly modified, brief summary of the protocol of the manufacturer's product manual (Omega Bio-tek 2019). Cut out agarose gel slices containing DNA molecules of interest were weighed to determine their approximate volume. A volume of Binding Buffer (XP2) was added to the gel slice in a 1:1 ratio, and incubated at 60°C for 7 min with continuous shaking. Vortexing was performed in between every 2 min. The solution was transferred to a HiBind DNA Mini Column and centrifuged at 10´000 g for 1 min. Filtrates were discarded, 300 µl Binding Buffer (XP2) were added per column and centrifuged at 17´000 g for 1 min. Filtrates were discarded, 700 µl SPW Wash Buffer were added per sample and centrifuged at 17´000 g for 1 min. The HiBind DNA Mini Column (with bound DNA) was centrifuged at 17´000 g for 2 min. HiBind DNA Mini Column were transferred to an empty 1.5 ml microcentrifuge tube, 15 µl Elution Buffer or autoclaved dH_2O were added per column, let sit at 37°C for 2 min and centrifuged at 17´000 g for 1 min. The elution step was repeated for a second time with another 15 µl of Elution Buffer or dH_2O. DNA concentrations were measured using a NanoDrop spectrophotometer and the samples were stored at -20°C for further treatment.

2.2.1.6 Ligation

To generate constructs, the cDNA of the protein of interest and the respective DNA plasmid were ligated using sticky ends after restriction enzyme digestion. The mix for ligation was as follows:

- 20 ng of digested DNA plasmid/vector
- cDNA of protein of interest (insert) in different molar ratios*
- 1x T4 DNA Ligase Buffer (containing 1 mM ATP)
- 400 U T4 DNA Ligase
- Elution buffer (E.Z.N.A. Gel Extraction Kit) to a total volume of 10 µl

* Commonly used vector/insert molar ratios were 1:4 and 1:8. For cloning of the cDNA of mutated HRP into the cDNA of the M2 mutant of the Smoothened protein vector/insert molar ratios of 1:30 and 1:45 had to be used to increase efficiency of undirected cloning. For calculating vector/insert molar ratios the online tool LIGation.CALCulator from IN.SILICO was used (Heinrich-Heine-Universität Düsseldorf).

Ligation mixtures were either incubated at room temperature for 5 h or in an 18°C tempered water bath in a closed Styrofoam box, which was put in a 4°C environment overnight. Transformation into bacterial cells (see section 2.2.1.7) was carried out immediately after the incubation period.

2.2.1.7 Chemically competent bacteria and transformation

Generation of chemically competent bacteria

DH5α chemically competent *Escherichia coli* (*E. coli*) cells were generated according to two different procedures.

Procedure 1 (this procedure was carried out by Larissa Osten, Institute for Molecular and Cellular Anatomy, University of Regensburg): *DH5α E. coli* cells were stored at -80°C in a 33% glycerin stock solution. A small amount of bacteria cells was removed from the frozen glycerin stock by scraping with a pipette tip, cells were streaked on LB agar plates (no antibiotic addition) and incubated at 37°C overnight. The next day one clone was picked, transferred into a 15 ml centrifuge tube with 5 ml LB medium and incubated overnight at 37°C and 250 rpm. At the next morning the bacterial suspension was diluted in a 1:100 ratio and a portion of the dilution was incubated in a shake flask at 37°C and 250 rpm until the OD_{600} reached a value of ~0.4-0.5. Thirty ml of the bacterial suspension were transferred into a 50 ml centrifuge tube each and centrifuged at 4°C and ~1´350 g for 10 min. The supernatant was discarded, the cell pellet (from 30 ml suspension) was

resuspended in 3 ml transformation and storage solution, 100 µl aliquots were prepared in 1.5 ml microcentrifuge tubes and stored at -80°C.

Procedure 2 (this procedure was carried out by Kerstin N. Schmidt, Institute for Molecular and Cellular Anatomy, University of Regensburg): *DH5α E. coli* cells were stored at -80°C in a 33% glycerin stock solution. A small amount of bacteria cells was removed from the frozen glycerin stock by scraping with a pipette tip, cells were streaked on TY agar plates (no antibiotic addition) and incubated at 37°C overnight. The next day 10-20 clones were picked, all transferred into a 5 ml centrifuge tube with 3 ml SOB medium and incubated for ~6 h at 37°C and 250 rpm. One ml of the bacterial suspension was transferred into 250 ml fresh SOB medium and incubated at 18°C and 250 rpm until the OD_{600} reached a value of ~0.6. Next, the bacterial suspension was centrifuged at 4°C and 2´000 g for 10 min. The supernatant was discarded, the cell pellet was resuspended in ~83 ml chilled FTB buffer and incubated on ice for 10 min. Next, the suspension was centrifuged at 4°C and 2´000 g for 10 min, the supernatant was discarded, the cell pellet was resuspended in ~20.8 ml chilled FTP buffer. Dimethyl sulfoxide was added to a final concentration of 7% (v/v) and the suspension was incubated on ice for 10 min. One hundred µl aliquots of the bacterial suspension were prepared in 1.5 ml microcentrifuge, quick-frozen in liquid nitrogen and stored at -80°C.

To check transformation efficiency, 95 µl each of the generated *DH5α* chemically competent *E. coli* cells were thawed and 1 pg or 10 pg or 0.1 ng or 1 ng of the DNA plasmid pUC18 (with an ampicillin resistance gene) were added. The subsequent procedure was identical to the next paragraph (see Transformation using *DH5α* chemically competent *E. coli* cells). One day after plating, grown clones per agar plate were counted and plotted against the amount of pUC18 used for each transformation. Transformation efficiency was considered to be sufficient if at least ~10^9 clones had grown after transformation with 1 ng pUC18.

Transformation using *DH5α* chemically competent *E. coli* cells

For transformation of ligated constructs and for amplification of DNA plasmids, chemically competent cells were used. 95 µl bacteria suspension were added to the ligation mix or to 20 ng DNA plasmid in a 1.5 ml microcentrifuge tube, mixed and incubated for 30 min on ice. Next, the microcentrifuge tubes were transferred into a 42°C water bath and incubated for 90 s followed by a 2 min incubation period on ice. Seven hundred µl TY medium were added to the suspension and

the tubes were incubated at 37°C and 250 rpm for 60 min. Bacteria suspensions were centrifuged at 2´200 g for 2 min. After centrifugation, a large portion of the supernatant was discarded, the bacteria were resuspended in the residual medium and plated on TY agar plates (containing the respective antibiotic). Plated bacteria were incubated at 37°C overnight.
The next day, grown clones were picked with a pipette tip and overnight cultures were prepared for DNA purification. For this purpose, the pipette tip bearing the clone, was placed in a glass tube with 3 ml TY medium (containing the respective antibiotic), the tube was covered with a cap and incubated overnight at 37°C and 250 rpm.

2.2.1.8 DNA purification: Miniprep

In order to check the nucleic acid sequence of a cloned construct, 2 ml overnight cultures were used to perform Minipreps. 2 ml of the overnight culture were transferred into a 2 ml microcentrifuge tube. The remaining volume of the overnight culture was stored at 4°C. Tubes were centrifuged at 17´000 g for 2 min, the supernatant was discarded, 250 µl buffer P1 were added and the samples were vortexed until the bacterial pellet was fully dissolved. Two hundred and fifty µl buffer P2 were added per tube and the samples were inverted. Three hundred and fifty µl buffer P3 were added per tube and the samples were again inverted. Tubes were centrifuged at 17´000 g for 10 min, the supernatant was transferred into a 1.5 ml microcentrifuge tube with 500 µl isopropanol and inverted. Centrifugation at 17´000 g was performed for 10 min, the supernatant was discarded, and 70% ethanol was added to the pellet. Samples were centrifuged at 17´000 g for 5 min, the supernatant was discarded and pellets were dried at 37°C for at least 30 min with the lid of the microcentrifuge tube open in order to let the ethanol evaporate completely. In a last step, 50 µl of dH_2O were added per microcentrifuge tube to the pellet to dissolve the DNA and tubes were incubated at 37°C for at least 30 min under continuous shaking. After DNA isolation (analytical) restriction enzyme digestion and gel electrophoresis were performed as described in section 2.2.1.3 and 2.2.1.4 to verify that the DNA of the protein of interest was successfully ligated with the plasmid.

For cloning of the cDNA of mutated HRP into the cDNA of the M2 mutant of Smoothened, the same restriction enzyme was used for both, the 5’ and 3’ end of the mutated HRP insert. In order to verify the 5’-3’ orientation of the mutated HRP insert after cloning, an additional analytical digestion was carried out, which cuts asymmetrically in the cDNA of the mutated HRP.

One construct showing a specific insert band after gel electrophoresis was sent to Microsynth Seqlab for Sanger sequencing. If a standard primer from Microsynth Seqlab was used, 9 µl dH_2O were added to 3 µl DNA solution. If individually designed sequencing primers were required, 2 µM of a sequencing primer was used together with 3 µl DNA solution in a total volume of 15 µl. Sequencing results were checked using the programs GENtle and SnapGene Viewer.

2.2.1.9 DNA purification: Midiprep

After ensuring by Sanger sequencing that cDNA of the proteins of interest were correct, overnight cultures were inoculated for Midiprep: 500 µl of the bacterial suspension of the overnight culture for Miniprep (section 2.2.1.8) were added to 100 ml TY medium (containing the respective antibiotic) in a shake flask and incubated at 37°C and 250 rpm overnight. The overnight culture was transferred into 50 ml centrifuge tubes. Prior to plasmid DNA isolation a bacterial glycerin stock was prepared by mixing 280 µl of a 40% glycerin stock solution with 470 µl of bacterial suspension from overnight culture. All 15% glycerin bacterial stocks were stored at -80°C. Midiprep was performed as described by the manufacturer which is why the following paragraph is closely geared to the manufacturer´s protocol (QIAGEN 2012): the overnight culture was centrifuged at 4´000 g at 4°C for 10 min. The supernatant was discarded, 4 ml Buffer P1 were added to the pellet of one overnight culture and the pellet was resuspended by pipetting. Four ml Buffer P2 were added, the sample was mixed manually and incubated for 3 min at room temperature. Four ml Buffer S3 were added, the sample was mixed by manual shaking, the sample was transferred into QIAfilter Cartrige and incubated for 10 min at room temperature. Thereafter, the lysate was transferred into a 50 ml centrifuge tube with 2 ml Buffer BB using the plunger-filter system of the QIAfilter Cartrige. The sample was mixed manually, transferred into the QIAGEN Plasmid Plus spin column which was mounted on the QIAvac 24 Plus together with a Tube Extender and vacuum was added “until the liquid has been drawn through [...] [the] column[...]” (QIAGEN 2012). The QIAGEN Plasmid Plus spin column was transferred into a collecting vessel provided by the manufacturer, 700 µl Buffer ETR were added and centrifuged at 10´000 g for 1 min. The filtrate was discarded and 700 µl Buffer PE were added and centrifugation was performed at 10´000 g for 1 min. Again, the filtrate was discarded and the column was centrifuged for further 2 min. The QIAGEN Plasmid Plus spin column was transferred into a sterile 1.5 ml microcentrifuge tube, 250 µl autoclaved dH_2O were added and the set-up was incubated at room temperature for 2 min prior to centrifugation at 10´000 g for 1 min. The DNA concentrations were measured using a

NanoDrop spectrophotometer. Care was taken that the measured ratio of the absorbance at 260 nm to 280 nm (indicates i.a. protein contamination) was approximately 1.8 and that the measured ratio of the absorbance at 260 nm to 230 nm (indicates i.a. contamination of DNA plasmids with residual reagents of DNA isolation kits) was approximately in the range of 2.0-2.2 (Matlock 2015). Analytical restriction enzyme digestion followed by gel electrophoresis was performed as described in sections 2.2.1.3 and 2.2.1.4 using 1 µg DNA plasmid. In some cases 12 µl of the DNA plasmid with a concentration of 100 ng/µl were prepared for sequencing (see section 2.2.1.8). All samples were stored at -20°C.

2.2.2 Cell culture

All human telomerase reverse transcriptase (hTERT) immortalized retinal pigment epithelium 1 (RPE1) cell lines were cultured in DMEM/Ham's F12 medium with an addition of 10% fetal calf serum (FCS), 2 mM L-glutamine and 0.26% sodium bicarbonate (= "RPE1 cell culture medium") in a humid environment at 37°C under 5% CO_2. All Lilly Laboratories cell porcine kidney 1 (LLC-PK_1) cell lines – porcine kidney epithelial cells (Miyamoto *et al.* 2019) – were cultured in DMEM high glucose medium with an addition of 10% FCS (= "LLC-PK_1 cell culture medium") in a humid environment at 37°C under 5% CO_2.

2.2.2.1 Freezing and thawing of cell lines

Freezing of cells

For freezing, all cell lines were cultured in petri dishes with a growth area of 58 cm^2 (TC Dish 100, Standard). In the case of LLC-PK_1 cell lines, cells were trypsinized (see below) and split in a 1:2 ratio one day prior to freezing to facilitate the trypsinization of this strongly adhering cell lines imminently before freezing. Prior to freezing, it was verified by light microscopy that all cell lines were free of bacterial and fungal contamination and an approximate confluence of 80-90% was reached. The following steps were the same for all cell lines. The respective cell culture medium was removed using a vacuum pump, cells were washed briefly with 10 ml 1x PBS per petri dish 2 ml Trypsin-EDTA solution were added per petri dish, removed immediately afterwards and incubated for 5 min at 37°C and 5% CO_2. After verifying by light microscopy that all cells had detached from the petri dish, cells were resuspended in 5 ml respective culture medium per petri dish, all cells of one cell line were pooled and transferred into one 50 ml centrifuge tube. The tubes were centrifuged at 300 g for 5 min at room temperature to pellet cells and the supernatant was

removed using a vacuum pump. Pellets of LLC-PK_1 cell lines were resuspended in a mix consisting of 90% FCS and 10% dimethyl sulfoxide. Pellets of RPE1 cell lines were resuspended in a mix consisting of 70% FCS, 20% "RPE1 cell culture medium" and 10% dimethyl sulfoxide. Aliquots (1.8 ml) of the cell suspension were transferred into one CryoPure Tube. At the end, cells from one 58 cm^2 petri dish were divided into two CryoPure Tubes. The tubes were either kept on ice for 30 min before storing them at -80°C or transferred into a CoolCell FTS30 freezing container, and were immediately stored at -80°C so that cells were cooled at -1°C/minute. CryoPure Tubes containing frozen cells were transferred from the -80°C freezer into a liquid nitrogen dewar after ensuring via a polymerase chain reaction (see section 2.2.2.8.) that cells were free of *Mycoplasma* contamination and only *Mycoplasma*-free cells were used for experiments during this work.

Thawing of cells

A frozen cell suspension in one CryoPure Tubes was thawed in portions by pipetting room tempered cell culture medium into the CryoPure Tube. Once an aliquot of the cell suspension was thawed it was transferred into 50 ml centrifuge tube containing 20 ml of cell culture medium. The tube was centrifuged at 300 g for 5 min at room temperature to pellet cells and the supernatant was removed using a vacuum pump. Cells were resuspended in 10 ml cell culture medium and plated in a petri dish with a growth area of 58 cm^2 (TC Dish 100, Standard). The dish was swung in a cross shape to distribute the cells homogeneously within the petri dish. Cells were cultured at 37°C under 5% CO_2 for approximately 6-8 hours until they had adhered to the bottom of the dish. After verifying by light microscopy that the cells had settled down, the cell culture medium was exchanged to remove the last residues of dimethyl sulfoxide. If an antibiotic was needed for culturing a cell line, it was also added at this point in time.

2.2.2.2 Passaging cells

Since exclusively immortalized cell lines were used in the present work, cells had to be passaged as soon as they reached a confluence of approximately 80-90%. All cell lines were cultured in 10 ml growth medium and petri dishes with a growth area of 58 cm^2 (TC Dish 100, Standard). The respective cell culture medium was removed using a vacuum pump, cells were washed briefly with 10 ml 1x PBS per petri dish, 2 ml Trypsin-EDTA solution were added per petri dish and removed immediately afterwards. Cells were kept in a humid environment at 37°C and under 5% CO_2 for 5 min and next it was checked by light microscopy whether all cells had detached from the bottom

of the culture dish. Cells of one petri dish were resuspended in 10 ml cell culture medium, split in various ratios (typically between 1:5 and 1:15) and plated again in a petri dish with a growth area of 58 cm^2 (TC Dish 100, Standard). If an antibiotic was needed for culturing a cell line, it was also added. The dish was swung in a cross shape to distribute the cells homogeneously within the petri dish.

If possible, care was taken not to use cells with passage numbers higher than 30 for wild-type cell lines and 40 for stably expressing cell lines. However, this was not possible with some stably expressing cell lines generated during this work.

2.2.2.3 Plating cells at defined density

Defined cell densities were required for most of the experiments. After trypsinization (see section 2.2.2.2) the concentration of the cells per ml medium was determined using a *Neubauer* counting chamber and the cell suspension was diluted to the desired concentration. Finally, a defined number of cells within a defined volume of cell culture medium was plated in a well of a cell culture plate or a petri dish. Various types of culture plates and petri dishes were used during this work.

2.2.2.4 Transfection

Transient transfection of RPE1 cell lines

Transfection of all RPE1 cell lines was performed using the transfection reagent FuGENE6. For this purpose, cells were seeded (see section 2.2.2.3) either on coverslips in wells (with a growth area of ~8.9 cm^2) of a 6-well cell culture plate or in gridded glass bottom dishes (with a growth area of ~9.6 cm^2) with 3 ml cell suspension per well/dish. Cells were transfected ~19-24 h after plating. Depending on the experiment, different ratios of cell number to FuGENE6 volume to the mass of DNA plasmids were used.

- Overexpression of dominant-negative RAB8A: 1.8 x 10^5 wild-type RPE1 cells were plated per well of a 6-well cell culture plate. Transfection was performed using a mix consisting of 100 µl DMEM/Ham's F12 medium (no additions), 6.7 µl FuGENE6 and 2.1 µg pEGFPC1 or pEGFPC1/RAB8A(T22N).
- Overexpression of dominant-negative RAB5A or RAB7A or RAB11A: 2.0 x 10^5 wild-type RPE1 cells were plated per well of a 6-well cell culture plate. Transfection was performed using a mix consisting of 100 µl DMEM/Ham's F12 medium (no additions), 6.55 µl

FuGENE6 and 2.05 µg pEGFPC1 or pEGFPC1/RAB5A(S34N) or pEGFPC1/RAB7A(T22N) or pEGFPC1/ RAB11A(S25N).

- Overexpression of dominant-negative RAB5A or RAB7A or RAB11A together with wild-type RAB8A each: 2 x 10^5 wild-type RPE1 cells were plated per well of a 6-well cell culture plate. Transfection was performed using a mix consisting of 100 µl DMEM/Ham's F12 medium (no additions), 8 µl FuGENE6, 1.25 µg pEGFPC1/RAB8A and 1.25 µg pmCherryC1 or pmCherryC1/RAB5A(S34N) or pmCherryC1/RAB7A(T22N) or pmCherryC1/RAB11A(S25N).
- Overexpression of mCherry for CLEM experiments: 5 or 6 x 10^4 RPE1 cells producing the proteins Centrin1-EGFP and ARL13B-EGFP were plated per gridded glass bottom dish. Transfection was performed using a mix consisting of 50 or 30 µl DMEM/Ham's F12 medium (no additions), 1.8 or 1.5 µl FuGENE6, 0.75 or 0.625 µg pmCherryC1.

The procedure was identical for all experiments: DMEM/Ham's F12 medium and FuGENE6 were warmed to room temperature and FuGENE6 was vortexed for a few seconds right before use. FuGENE6 was pipetted into a sterile 1.5 ml microcentrifuge tube with DMEM/Ham's F12 medium without touching the tube in the indicated amounts and the tube was briefly vortexed prior to incubating the mix for 5 min at room temperature. In parallel, solutions containing the respective DNA plasmid were centrifuged at 12´300 g for 2 min. After the 5 min incubation period, DNA plasmids were added to the respective 1.5 ml microcentrifuge tube as well, the solutions were mixed manually and incubated for 20 min at room temperature. Medium was not exchanged prior to transfection and the transfection reagent mix was added drop by drop to the well/petri dish with growing cells in 3 ml "RPE1 cell culture medium". Cell culture plates and gridded glass bottom dishes were swung in a cross shape to mix the transfection reagent homogeneously with the "RPE1 cell culture medium".

Stable transfection of RPE1 cell lines

Stable transfection of RPE1 cell lines was carried out analogously to the transient transfection (see above) with the exception that different ratios of cell number, FuGENE6 volume and mass of DNA plasmids were used.

- Generation of a RPE1 cell line producing the fusion proteins Centrin1-EGFP and ARL13B-EGFP: 2 x 10^5 RPE1 cells producing Centrin1-EGFP (Uetake *et al.* 2007) were plated per well of a 6-well cell culture plate. Transfection was performed using a mix consisting of

100 µl DMEM/Ham's F12 medium (no additions), 6 µl FuGENE6, 2.5 µg pEGFPN1/ARL13B. The neomycin resistance gene of the pEGFPN1/ARL13B was used for subsequent selection (see section 2.2.2.5).

- Generation of a RPE1 cell line producing the fusion proteins Centrin1-EGFP, ARL13B-EGFP and mCherry-RAB8A: 2 x 10^5 RPE1 cells producing Centrin1-EGFP and ARL13B-EGFP were plated per well of a 6-well cell culture plate. Transfection was performed using a mix consisting of 100 µl DMEM/Ham's F12 medium (no additions), 6 µl FuGENE6, 0.25 µg pWE3 and 2.25 µg pmCherryC1/RAB8A. The puromycin resistance plasmid pWE3 (Cockett *et al.* 1997) was used for subsequent selection (see section 2.2.2.6) and the mass of pWE3 used for stable transfection was 10% of the total mass of plasmid DNA.

In order to check transfection efficiency of the cells in wells of 6-well cell culture plates prior to antibiotic selection, cell suspensions of 8 x 10^4 cells in 1.2 ml "RPE1 cell culture medium" were plated on coverslips (10 mm diameter) in wells of 12-well cell culture plates in parallel to the cells of the 6-well cell culture plates. One day after plating, transfection was performed together with the cells seeded in 6-well cell culture plates (see above). One collective mix was prepared for a well of the 6-well cell culture plate and a well of the 12-well cell culture plate and then divided for respective wells. For transfection of cells in a 12-well cell culture plate, 40 µl DMEM/Ham's F12 medium (no additions), 2.4 µl FuGENE6 and 1 µg DNA plasmid were used. If pWE3 plasmid was required, the mass of pWE3 was 10% of the total mass (1 µg) of DNA plasmids. One day after transfection, coverslips were either fixed with formaldehyde and mounted between glass slides and cover glasses as described in section 2.2.3. To get an impression of the transfection efficiency to decide further procedure (see section 2.2.2.5 or section 2.2.2.6) cells were imaged by fluorescence microscopy.

Stable transfection of LLC-PK_1 cells

For stable transfection of wild-type LLC-PK_1 cells, 1.676 x 10^6 cells in 6.7 ml "LLC-PK_1 cell culture medium" were plated per petri dish with a growth area of 21 cm² (TC Dish 60, Standard). Twenty-four h after plating, transfection of LLC-PK_1 cells was performed using the transfection reagent Lipofectamine according to the manufacturer's instruction. "LLC-PK_1 cell culture medium" was replaced by ~4.5 ml new "LLC-PK_1 cell culture medium" per petri dish right before transfection. Mix A was prepared in a sterile 1.5 ml microcentrifuge tube: 278.8 µl DMEM high glucose medium (without FCS addition) and 5.98 µl Lipofectamine were pipetted into the tube and

vortexed for 2-3 s. Next, Mix B was prepared in a sterile 1.5 ml microcentrifuge tube as well: 278.8 µl DMEM high glucose medium (without FCS addition), 0.29 µg pWE3, 2.51 µg pEGFPN1/HRP-mSmoM2 and 5.58 µl P3000 were pipetted into the tube. The puromycin resistance plasmid pWE3 (Cockett *et al.* 1997) was used for subsequent selection (see section 2.2.2.5). The mass of pWE3 used for stable transfection was 10% of the total mass of plasmid DNA. Finally, Mix A was added to Mix B, and the transfection solution was incubated for 15 min at room temperature prior to pipetting it drop by drop into a petri dish with growing LLC-PK_1 cells. Petri dishes were swung in a cross shape to mix the transfection reagent homogenously with the "LLC-PK_1 cell culture medium". Further steps for generating stably expressing cell lines are described in section 2.2.2.5.

2.2.2.5 Generation of stably expressing cell lines

As the RPE1 cell line producing the fusion proteins Centrin1-EGFP, ARL13B-EGFP and mCherry-RAB8A was established using fluorescence-activated cell sorting (FACS) analysis all steps are described in section 2.2.2.6.

RPE1 cells stably expressing the fusion proteins Centrin1-EGFP and ARL13B-EGFP

Twenty-four h after stable transfection (see section 2.2.2.4), RPE1/Centrin1-EGFP cells of 6-well cell culture plates were washed with 1x PBS, trypsinized using 500 µl Trypsin-EDTA per well at 37°C for 5 min, resuspended in 6 ml "RPE1 cell culture medium" and centrifuged at 300 g for 5 min. The supernatant was removed, the cells were resuspended in "RPE1 cell culture medium", distributed equally over eight petri dishes each with a growth area of 58 cm^2 (TC Dish 100, Standard) and "RPE1 cell culture medium" was added to a total volume of 10 ml per petri dish. After culturing the cells for ~6-8 h in a humid environment at 37°C under 5% CO_2, G418 was added to a final concentration of 800 µg/ml. Although the RPE1/Centrin1-EGFP cell line was generated using G418 (Uetake *et al.* 2007) cells showed no G418 resistance in our hands which enabled the use of G418 for selection in the present work. "RPE1 cell culture medium" with 800 µg/ml G418 was replaced twice a week.

After approximately 10 days, selection medium was replaced and grown clones were marked at the outside of the bottom of the petri dishes with a permanent marker under a light microscope. Clones were picked at sterile conditions by scraping a clone off the bottom of the petri dish with a pipette and simultaneously taking cells up into the pipette. Clones were transferred into wells each with 1 ml selection medium of 24-well cell culture plates. One clone was placed per well. If cell clones in

the 24-well cell culture plates had reached a confluence of ~80%, they were trypsinized using 100 µl Trypsin-EDTA per well at 37°C for 5 min, resuspended with 900 µl selection medium per well and each clone was distributed equally into one well of a 6-well cell culture plate with 2 ml selection medium and one well of a 24-well plate with a coverslip and 1 ml selection medium.

If the clones in the 24-well cell culture plates had reached a confluence of at least ~50%, serum starvation was performed (see section 2.2.2.7) for three days to induce ciliogenesis, cells were fixed using formaldehyde and coverslips were mounted between glass slides and cover glasses as described in section 2.2.3. Clones with cells showing EGFP-positive primary cilia were selected by fluorescence microscopy. Out of 132 imaged clones (please note that not all picked clones were imaged), four were selected and all others were discarded. Subsequently, cells of selected clones were cultured in several petri dishes with a growth area of 58 cm^2 (TC Dish 100, Standard) for freezing as described in section 2.2.2.1. Clone #53 was used for all further experiments as cells of this clone showed bright EGFP-positive centrosomes, bright EGFP-positive primary cilia and a high percentage of ciliated cells (positive for EGFP and anti-acetylated tubulin staining).

LLC-PK_1 cells stably expressing the fusion protein HRP-SmoM2-EGFP

Twenty-four h after stable transfection (see section 2.2.2.4), transfected LLC-PK_1 cells of each petri dish with a growth area of 21 cm^2 (TC Dish 60, Standard) were trypsinized as described in section 2.2.2.2 and resuspended in 14 ml "LLC-PK_1 cell culture medium". Next, 10 ml, 3 ml and 1 ml of the cell suspension were plated in one petri dish with a growth area of 58 cm^2 (TC Dish 100, Standard) respectively and "LLC-PK_1 cell culture medium" was added to a total volume of 10 ml each. Petri dishes were swung in a cross shape to distribute cells homogeneously.

At the next day, the selection antibiotic puromycin was added to a final concentration of 1 µg/ml. "LLC-PK_1 cell culture medium" with 1 µg/ml puromycin was replaced twice a week. After approximately two weeks, selection medium was replaced and afterwards grown cell clones were picked under a light microscope by scraping a clone off the bottom of the petri dish with a pipette and simultaneously taking it up into the pipette. Clones were transferred into wells each with 1 ml selection medium of 24-well cell culture plates. One clone was placed per well. To ensure homogenous growth of clones, the clones were trypsinized after six to eight days using 100 µl Trypsin-EDTA per well, cells were separated by pipetting up and down and plated again into the wells. If cell clones in the 24-well cell culture plates had reached a confluence of ~80%, they were

trypsinized using again 100 µl Trypsin-EDTA and transferred to wells of a 6-well cell culture plate, with one coverslip (10 mm diameter) and 3 ml selection medium per well.

If the clones in the 6-well cell culture plates had reached a confluence of at least ~50%, the coverslips were fixed, nuclei were stained and coverslips were mounted between a glass slide and a cover glass as described in section 2.2.3. Using fluorescence microscopy (see section 2.2.5.2) 101 clones were imaged (please note that not all picked clones were imaged) and only clones with cells showing an enhanced green fluorescent protein (EGFP) signal were selected. All other clones were discarded. Clones with cells showing an EGFP signal were cultured in several petri dishes with a growth area of 58 cm^2 (TC Dish 100, Standard) for freezing as described in section 2.2.2.1.

In parallel to freezing, it was checked whether cells of selected clones did not only show EGFP signals within their cytoplasm but also within their primary cilia. To do so, 3 x 10^5 cells per clone were plated in a well of a 12-well cell culture plate on two coverslips (10 mm in diameter). The medium was removed three days after plating, coverslips were fixed and immunolabeling of centrosomes (anti-γ-tubulin) and cilia (anti-ARL13B) was performed as described in section 2.2.3. Coverslips were mounted between a glass slide and a cover glass with 40% glycerin in 1x PBS. Clone #101 was used for all further experiments as cells of this clone showed bright EGFP-positive primary cilia and a high percentage of ciliated cells by fluorescence microscopy.

2.2.2.6 FACS Analysis and subcloning of cell lines

Twenty-four h after stable transfection of RPE1 cells producing Centrin1-EGFP and ARL13B-EGFP with pmCherryC1/RAB8A and pWE3 and after checking transfection efficiency by fluorescence microscopy as described in section 2.2.2.5, cells of each 6-well cell culture plate were distributed equally over three petri dishes each with a growth area of 58 cm^2 (TC Dish 100, Standard). After culturing the cells for ~6-8 h in a humid environment at 37°C under 5% CO_2, antibiotics were added with a final concentration of 800 µg/ml G418 and 2 µg/ml puromycin. As RPE1 cells already show puromycin resistance (Katoh *et al.* 2017), a high puromycin concentration was used for selection as discussed by Katoh *et al.* 2017. "RPE1 cell culture medium" with 800 µg/ml G418 and 2 µg/ ml puromycin was replaced twice a week. After approximately two weeks, grown clones were trypsinized as described in section 2.2.2.2, cells were separated by pipetting up and down – i.e. individual clones were mixed with each other – and cells were plated in half the amount of petri dishes (growth area of 58 cm^2, each with one 10 mm diameter coverslip) than prior.

Once the cells had a confluence of almost 100%, coverslips were removed from petri dishes, fixed and mounted between glass slides and cover glasses as described in section 2.2.3. Once having verified by fluorescence microscopy that at least some cells grown on coverslips showed mCherry signals, the cells of the petri dishes were prepared for the FACS analysis. After trypsinization as described in section 2.2.2.2, cells of all petri dishes were pooled by resuspending them in FACS buffer (2 mM EDTA and 0.2% FCS in 1x PBS) and centrifuged at 300 g for 5 min. The supernatant was removed, all cells were resuspended in 0.5 ml FACS buffer and filtered into a 5 ml Polystyrene Round-Bottom Tube with Cell-Strainer Cap. Tubes were kept on ice until FACS analysis. Cells were filtered once again using 30 µm Pre-Separation Filters and right afterwards, FACS analysis was carried out by Rüdiger Eder and Irina Fink (Regensburg Center for Interventional Immunology, University Hospital Regensburg) and performed as described in Buerger *et al.* 2021: a "BD FACSAria™ IIu cell sorting system […] operating with a 488nm laser together with a 530/30 filter for EGFP and a 610/20 filter for mCherry" (Buerger *et al.* 2021) was used. Cells showing both, EGFP and mCherry signals were sorted into a 5 ml Polystyrene Round-Bottom Tube with 1 ml ice chilled FACS buffer. After sorting, 5 ml Polystyrene Round-Bottom Tubes were centrifuged at 300 g for 5 min, the supernatant was carefully removed using a pipette and cells were resuspended in 3 ml "RPE1 cell culture medium" and plated in a well of a 6-well cell culture plate. Approximately 4-5 h after plating penicillin-streptomycin was added to a final concentration of 100 U/ml penicillin and 100 µg/ml streptomycin for approximately 10 days. One day after plating, medium was replaced by "RPE1 cell conditioned medium" (see section 2.1.10), penicillin-streptomycin was added as described above together with selection antibiotics to a final concentration of 800 µg/ml G418 and 2 µg/ml puromycin.

After reaching a confluence of ~90%, cells were trypsinized using 500 µl Trypsin-EDTA per well at 37°C for 5 min, resuspended in 10 ml "RPE1 cell culture medium" with 800 µg/ml G418 and 2 µg/ml puromycin and plated in a petri dish with a growth area of 58 cm^2 (TC Dish 100, Standard) with coverslips (10 mm diameter). Once the cells showed a confluence of at least ~50-60%, coverslips were removed from petri dishes, transferred into wells of a 24-well cell culture plate and serum starved for 24 h or 48 h or 72 h (see section 2.2.2.7). After serum starvation, cells were fixed, nuclei were stained and coverslips were mounted between glass slides and cover glasses as described in section 2.2.3. It was verified by fluorescence microscopy that cells show mCherry-positive cilia.

In parallel, cells were seeded on petri dishes with a growth area of 58 cm^2 (TC Dish 100, Standard) for freezing (see section 2.2.2.1) as well as in 96-well cell culture plates for subcloning to get a homogenous population of cells showing mCherry-positive cilia. "To generate a monoclonal cell line after FACS sorting, limiting dilution was performed by seeding cells at a concentration of 0.5 cells/well in 96-well plates" (Buerger *et al.* 2021). Grown subclones were washed with 1x PBS, trypsinized using 50 µl Trypsin-EDTA per well and resuspended with 150 µl "RPE1 cell culture medium" with selection antibiotics. Eighty µl of the cell suspension of each subclone were plated in a well of a 24-well cell culture plate with a coverslip and 1 ml "RPE1 cell culture medium" with selection antibiotics, 120 µl in a well of a 6-well cell culture plate with 3 ml "RPE1 cell culture medium" with selection antibiotics. After reaching a confluence of ~50-80% subclones in 24-well cell culture plates were serum starved (see section 2.2.2.7) for 24 h, fixed and coverslips were mounted between glass slides and cover glasses (see section 2.2.3). Sixty-six subclones were imaged by fluorescence microscopy, 4 subclones were selected with subclone #63 having been used for all further experiments as cells of this clone showed bright mCherry-positive primary cilia and a high percentage of ciliated cells (positive for mCherry and anti-acetylated tubulin staining). Only selected subclones were frozen (see section 2.2.2.1), all other subclones were discarded.

2.2.2.7 Serum starvation

Serum starvation was performed either one day after plating or one day after transfection of RPE1 cells to induce ciliogenesis (Katoh *et al.* 2017; Saito *et al.* 2018). For this purpose, serum-containing "RPE1 cell culture medium" was removed with a pump and the cells were washed twice with 3 ml DMEM/Ham's F12 medium with an addition of 2 mM L-glutamine and 0.26% sodium bicarbonate but without FCS per well/petri dish. Finally, 3 ml DMEM/Ham's F12 medium with an addition of 2 mM L-glutamine and 0.26% sodium bicarbonate but without FCS were added per well/petri dish.

2.2.2.8 Evaluation of Mycoplasma contamination

It was verified via a nested polymerase chain reaction that all cell lines used in the current study were free of *Mycoplasma* contamination. This test was typically carried out on a semiannual basis by technical staff (Larissa Osten, Institute for Molecular and Cellular Anatomy, University of Regensburg).

Cell lines were cultured in respective cell culture medium (no antibiotics added) in a humid environment at 37°C and under 5% CO_2 for ~3-4 days until they reached a confluency of at least ~80-90%. The cell culture medium was not replaced during this period of time and at the end an aliquot of the cell culture medium was transferred into a sterile1.5 ml microcentrifuge tube under sterile conditions and stored at -20°C for subsequent polymerase chain reaction. Prior to polymerase chain reaction, the cell culture medium aliquot was thawed, centrifuged at 17´000 g at room temperature for 3 min and 5 µl of the supernatant were used. All mixtures were prepared on ice under sterile conditions as follows:

- 5 µl cell culture medium supernatant (see above) or 5 µl RT-PCR Grade Water (negative control) or 50 ng of pJET/Myko (positive control)
- 0.2 mM dNTPs
- 1x ThermoPol Reaction Buffer
- 0.2 µM primer MCGpF1
- 0.2 µM primer MCGpR1
- 1.25 U *Taq* DNA Polymerase
- RT-PCR Grade Water to a total volume of 50 µl

Program for the first polymerase chain reaction (Table 3):

Initial denaturation: 94°C for 3 min	
Denaturation at 94°C for 30 s Annealing at 55°C for 2 min Extension at 68°C for 1 min	35 cycles
Final extension at 68°C for 5 min	
Final holding step at 10°C	

Table 3: Program for first polymerase chain reaction. Table design based on *Pfu* DNA Polymerase Protocol Usage Information form Promega Corporation 2013.

Next the mix for the second polymerase chain reaction was prepared on ice under sterile conditions as follows:

- 0.5 µl of the 50 µl mix after the first polymerase chain reaction
- 0.2 mM dNTPs

- 1x ThermoPol Reaction Buffer
- 0.2 µM primer MCGpF2
- 0.2 µM primer MCGpR2
- 1.25 U *Taq* DNA Polymerase
- RT-PCR Grade Water to a total volume of 50 µl

The program for the second polymerase chain reaction was identical to the program of the first reaction (see Table 3). Product formation after both polymerase chain reactions was verified by loading 5 µl polymerase chain reaction product each onto a 2% agarose gel and gel electrophoresis was performed (see section 2.2.1.4 for details). Product formation at a size of ~145-240 bp after the second polymerase chain reaction indicated *Mycoplasma* contamination.

2.2.3 Immunofluorescence

For immunofluorescence staining, cells were grown on coverslips with a diameter of 10 mm. Staining was either performed 24 h after transfection or after serum starvation for various periods of time. Each coverslip was transferred into a well of a 24-well cell culture plate, washed with 1x PBS and fixed with 4% formaldehyde in 1x PBS for 20 min at room temperature in a light-protected environment to minimize potential photobleaching. Usually, a formaldehyde solution with pH 7.4 was used. Only if subsequent staining with the rabbit or murine anti-γ-tubulin antibody was performed a solution with pH >10 was used. After fixation, coverslips were washed again with 1x PBS and incubated in 50 mM NH_4Cl in 1x PBS for 10 min. Coverslips were washed with 1x PBS and were either stored in 1x PBS at 4°C in a light-protected environment for a maximum of three days or permeabilization was performed right after washing with 0.1 % Triton X-100 in 1x PBS for 5 min. Coverslips were incubated in 200 µl of 0.5% (w/v) bovine Albumin Fraction V and 0.1% Triton X-100 in PBS (blocking solution) for 30 min at room temperature. Meanwhile, primary antibody solution was prepared, by diluting the antibodies with blocking solution to the respective final concentration as listed in section 2.1.9. The microcentrifuge tube with the antibody dilution was centrifuged at 17´000 g for 2 min at room temperature and subsequently kept on ice. After incubation in blocking solution, Parafilm was put onto the bottom of a plastic box and coverslips were placed upside down on a 30 µl drop of primary antibody dilution pipetted onto the Parafilm. Coverslips were incubated for 1 h at 37°C in a moist chamber. Afterwards, coverslips were put back into the wells of the 24-well plate, three rinses with 1x PBS each with 10 min incubation time

were performed. In parallel, the secondary antibody solution was prepared in analogy to the primary antibody solution. Coverslips were placed upside down on a 30 µl drop of secondary antibody dilution and incubated for 30 min at room temperature in a humid and light-protected environment. Coverslips were put back into the wells of the 24-well plate again and three rinses using 1x PBS each 10 min incubation time were performed. If staining of nuclei was needed, coverslips were only washed two times with 1x PBS for 10 min before incubating them in 0.5 µg/ml bisBenzimide H 33342 or 33258 in 1x PBS for 1 min and washing them afterwards once with 1x PBS for 10 min. At the end, coverslips were mounted between glass slides and cover glasses using either 40% glycerin in 1x PBS or Mowiol. Coverslips mounted with 40% glycerin in 1x PBS were imaged right afterwards and were subsequently stored at 4°C, coverslips mounted with Mowiol were imaged at least one day afterwards and were stored at -20°C.

In some cases, nuclear staining without immunofluorescence was needed. For this purpose, coverslips were fixed with formaldehyde as described above and washed with 1x PBS. Permeabilization was performed with 0.1 % Triton X-100 in 1x PBS for 5 min and coverslips were incubated in 0.5 µg/ml bisBenzimide H 33342 or 33258 in 1x PBS for 1 min. However, during some experiments permeabilization was omitted and coverslips were incubated in 0.5 µg/ml bisBenzimide H 33342 in 1x PBS for 10 min after fixation as it was shown that bisBenzimide H 33342 is able to penetrate cells without additional permeabilization (Buerger *et al.* 2021). Coverslips were washed with 1x PBS and mounted between glass slides and cover glasses using either Mowiol or 40% glycerin in 1x PBS as described above.

Image acquisition and data analysis

Fluorescence microscopy after immunofluorescence and/or bisBenzimide H staining was performed in similar way as described in section 2.2.5.2. Typically, *z* stacks with 11-21 focus steps with 0.4 µm each were recorded and additionally to the filters described in section 2.2.5.2, a D 350/50 excitation, ET 460/50 emission filter was used for Alexa350 and bisBenzimide H.

Fluorescence microscopic images were analyzed using the software ImageJ (Rueden *et al.* 2017; Schindelin *et al.* 2012). Centrosomes and cilia of images acquired after immunofluorescence staining were counted using the ImageJ plugin “Cell Counter” of Kurt De Vos (University of Sheffield, Sheffield, UK). Statistics was performed as described in section 2.2.7.

2.2.4 Western blot analysis

For Western blot analysis, two petri dishes with a growth area of 58 cm^2 (TC Dish 100, Standard) per cell line and condition were used. In the case of RPE1 cell lines 1 x 10^6 cells were plated per petri dish in 10 ml "RPE1 cell culture medium", in the case of LLC-PK_1 cell lines ~4.64 x 10^6 cells were plated per petri dish in 10 ml "LLC-PK_1 cell culture medium". For comparison of cycling and non-cycling RPE1 cells, serum starvation (see section 2.2.2.7) was performed two days after plating in some petri dishes.

2.2.4.1 Cell lysate preparation

Cell lysates were prepared three days after plating of cells. Cells were kept on ice through the whole procedure. Cells were washed with ice-chilled 1x PBS, 1 ml ice-chilled 1x PBS was added per petri dish, cells were scraped off the bottom of the petri dishes using a cell scraper and transferred into 15 ml centrifuge tubes. Six ml 1x PBS were added per dish to collect residual cells as well. Cells of one condition were pooled from the two petri dishes. Centrifugation was performed at 1´000 g for 5 min at 4°C, the supernatant was removed using a pump and cells within the 15 ml centrifuge tubes were immediately frozen in liquid nitrogen. Two hundred µl freshly prepared lysis buffer (see section 2.1.4.4) were added per centrifuge tube, the cell pellet was dissolved by pipetting up and down and the suspension was transferred into a 1.5 ml microcentrifuge tube. Cells were incubated under continuous rotation at 4°C for 20 min and the suspension was mixed by pipetting up and down until the solution appeared clear. Tubes were centrifugated at 15´000 g for 15 min at 4°C. The supernatant was transferred into a new 1.5 ml microcentrifuge tube, the pellet was discarded and 20 µl of the supernatant were immediately stored at -80°C for subsequent Bradford protein assay. In parallel, 3x SDS sample buffer was prepared as described in section 2.1.4.4 and was added to the residual 180 µl of the supernatant to a final concentration of 1x. RPE1 cell lines were heated at 100°C for 5 min, LLC-PK_1 cell lines were incubated at 37°C for 15 min to detect transmembrane proteins later on and all tubes were stored at -80°C for further treatment.

2.2.4.2 Bradford protein assay

To prepare the Bradford reagent, 5x ROTI-Quant was diluted 1:5 with dH_2O and stored at room temperature. Bradford reagent was placed in cuvettes with 1000 µl reagent per cuvette. A bovine serum albumin (BSA) concentration series (0.1, 0.25, 0.5, 1.5, 2.5, and 5 mg/ml bovine Albumin Fraction V in dH_2O) was prepared and 10 µl of each BSA concentration or 10 µl of each cell lysate (see section 2.2.4.1) or 10 µl lysis buffer were added per cuvette already containing the Bradford

reagent. In addition, a cuvette with 1000 µl dH_2O (without Bradford reagent) and 1000 µl Bradford reagent (without further additions) were prepared. Solutions were mixed by covering the cuvettes with Parafilm and inverting them. Subsequently, solutions were incubated for ~5 min. The protein concentration of the lysates was determined by measuring absorbance at 590 nm and 450 nm using spectrophotometry. First, the cuvette containing dH_2O only was measured followed by the cuvette containing Bradford reagent (without further additions). Then the standard curve was recorded using the BSA concentration series. Next, cuvettes with cell lysates and the cuvette with lysis buffer only were measured. The protein concentration in µg/µl of the cell lysates was determined using the standard curve and was subsequently corrected by the concentration of the lysis buffer.

2.2.4.3 Sodium dodecyl sulfate polyacrylamide gel electrophoresis

Proteins were separated according to their molecular mass using discontinuous sodium dodecyl sulfate (SDS) polyacrylamide gel electrophoresis. Depending on the molecular mass of the protein of interest, a 4% stacking gel and a 10% separation gel were used for cell lysates of RPE1 cell lines, a 4% stacking gel and 8% separation gel for lysates of LLC-PK_1 cell lines.

The gel chamber was assembled and the separation gel was prepared in a first step by mixing 3.3 ml of a 30% (w/v) acrylamide/bis solution for a 10% or 2.7 ml for an 8% separation gel; 2.5 ml of 1.5 M Tris (pH 8.8), 100 µl of a 10% SDS solution, 10 µl TEMED, 32 µl of a 10% APS solution and dH_2O were added to a total volume of 10 ml. The mix was inverted, ~7 ml of the mix was poured into the chamber, covered with 1-2 ml isopropanol and allowed to polymerize for ~40 min. After polymerization of the separation gel, isopropanol was removed and the 4% stacking gel solution was prepared by mixing 1.3 ml of a 30% (w/v) acrylamide/bis solution; 2.5 ml of 0.5 M Tris (pH 6.8), 100 µl of a 10% SDS solution, 10 µl TEMED, 100 µl of a 10% APS solution and dH_2O were added to a total volume of 10 ml. The mix was inverted, ~2.5 ml of the mix was poured into the chamber, combs were inserted into the chamber and allowed to polymerize for ~30 min.

"Gels were mounted into separation chambers and filled with 1x [SDS] running gel buffer" (Setzer 2018). Right before the lysates, stored at -80°C (see section 2.2.4.1), were loaded onto the gel, Cell lysates were heated once again as described in section 2.2.4.1. PageRuler Prestained Protein Ladder was used as molecular mass standard with 3 µl per gel, 60 µg protein of each cell lysate with the SDS sample buffered were loaded onto gels and remaining pockets of a gel were filled with a

mixture of SDS sample buffer and dH_2O. Proteins were separated in the electric field first for ~10 min at 80 V and subsequently at 150 V.

2.2.4.4 Semi-dry blot

Blotting of proteins onto PVDF membrane

After gel electrophoresis, the chamber was disassembled and the stacking gel was removed and discarded. A polyvinylidene fluoride (PVDF) membrane and sheets of Whatman paper were cut to the size of the separation gel. The PVDF membrane was incubated for 1 min in pure methanol for activation. For equilibration the PVDF membrane, sheets of Whatman paper and the separation gel were stored in transfer buffer for 10 min. In a next step, the Semi-dry blot system was assembled: three sheets of Whatman paper were put onto the anode plate of a blotting chamber followed by the PVDF membrane, the separation gel and another three sheets of Whatman paper. "Air bubbles were removed" (Setzer 2018), the lid (cathode) of the chamber was mounted and blotting was performed at 22 V for 75 min.

Antibody staining

After blotting of proteins onto the PVDF membrane, the chamber was disassembled, the membrane was removed, briefly washed two times in 1x PBS-T and incubated with continuous shaking in a blocking solution consisting of 5% skimmed milk powder in 1x PBS-T at room temperature for 30 min or at 4°C overnight. Primary antibodies diluted in blocking solution to their respective final concentration (see section 2.1.9) were added and incubated with continuous shaking either at room temperature for 3 h or at 4°C overnight. After the incubation period, the membrane was briefly washed twice with 1x PBS-T, followed by additional rinses with 1x PBS-T, two for 5 min each and two for 10 min each. Secondary antibodies conjugated with peroxidase were also diluted using the blocking solution (see section 2.1.4.4) and incubated with continuous shaking at room temperature for 1 h. The membrane was washed twice briefly with 1x PBS-T, followed by additional rinses, four with 1x PBS-T for 5 min each and one with 1x PBS (without Tween 20) for 5 min.

Chemiluminescence reaction

For detection of proteins via an HRP-mediated chemiluminescence reaction the substrate "WesternBright Chemilumineszenz Substrat Sirius" was used. WesternBright Peroxide and

WesternBright Sirius were mixed in a 1:1 ratio, the membrane was removed from 1x PBS buffer, WesternBright mix was added onto it and the membrane was put into a transparency film. Protein bands were documented using the FUSION FX7 system. Various exposure times were used and acquired images were stored.

Antibody stripping

In order to detect different proteins transferred onto one PVDF membrane with different antibodies, previously used antibodies were stripped off from the membrane after each chemiluminescence reaction. For this purpose, the membrane was washed twice with stripping buffer (see section 2.1.4.4) at room temperature for 5 min, followed by additional rinses, four with 140 mM NaCl in 10 mM Tris buffer (pH 7.2) for 3 min each and two with 1x PBS-T for 5 min each. Chemiluminescence reaction was performed as described above to verify sufficient stripping of antibodies. The membrane was washed twice with 1x PBS-T for 5 min each and twice with blocking solution for 15 min each and incubated in blocking solution at 4°C until further treatment.

2.2.5 Correlative light and electron microscopy

Correlative light and electron microscopy (CLEM) is the combined imaging of one sample by both, light and electron microscopy (Bykov *et al.* 2016). During so-called pre-embedding techniques the samples/cells are imaged by light and in particular fluorescence microscopy prior to sample preparation for electron microscopy (Bykov *et al.* 2016). Please note, sample preparation for on-section CLEM-STEM was already described in Buerger *et al.* 2021 and is therefore not repeated in this chapter.

2.2.5.1 Cell culture

For investigating the localization of RAB8A during ciliogenesis, a RPE1 cell line stably expressing the proteins Centrin1-EGFP, ARL13B-EGFP and mCherry-RAB8A was used. Cells were plated with various densities (6, 7, 8, 8.5 or 9 x 10^5 cells per dish) in gridded glass bottom dishes (growth area of ~9.6 cm^2). Cells were cultured without antibiotic addition. As a control RPE1 cells stably expressing the proteins Centrin1-EGFP and ARL13B-EGFP were plated and transiently transfected with an mCherry expression plasmid as described in section 2.2.2.4. Approximately one day after plating, serum starvation (see section 2.2.2.7) was performed for ~3 h, ~3.5 h or ~10 h to induce ciliogenesis.

2.2.5.2 Fixation and fluorescence microscopy

After serum starvation, cells were fixed using 4% formaldehyde in 0.1 M sodium cacodylate buffer (pH 7.4) at room temperature for 30 min in light-protective environment, washed twice with 0.1 M sodium cacodylate buffer (pH 7.4) without formaldehyde addition for 2 min each and incubated in 0.1 M sodium cacodylate buffer (pH 7.4) during fluorescence microscopy. Fluorescence microscopy of cells within gridded glass bottom dishes was performed similar to Buerger *et al.* 2021: cells showing an mCherry-positive spot in close proximity to one of the two centrioles were selected. "Z stacks ([usually] 17 […] focus steps, 0.4µm each) of relevant positions were recorded at 22°C using an inverted light microscope" (Buerger *et al.* 2021) operating "with a HXP 120V Compact Light Source[,] […] [a] Fluar 40x/1.30 oil immersion objective[,] […] [a] cooled pco.edge 4.2 sCMOS camera[,] […] [and the] VisiView software package […]" (Buerger *et al.* 2021). The following filters were used: ET 470/40 excitation, ET 525/50 emission filter for EGFP and ET 560/40 excitation, ET 630/75 emission filter for mCherry. "Additional bright-field images were recorded for [...] [each] position[...]" (Buerger *et al.* 2021) using both, a Fluar 40x/1.30 and a Ph2 Plan-NEOFLUAr 16x/0.5 oil immersion objective. Bright-field images showing both, cells and letters/numbers of the gridded glass bottom dishes were used to facilitate the orientation on resin sections when starting electron microscopy.

2.2.5.3 Preparation for electron microscopy

After fluorescence microscopy, post-fixation of cells was performed using 2% glutardialdehyde in 0.1 M sodium cacodylate buffer (pH 7.4) at room temperature for 5 min and subsequently on ice for further 55 min or overnight. Next, cells were washed five times with 0.1 M sodium cacodylate buffer for 2 min each and were processed for electron microscopy. Cells were incubated in 1% OsO_4 in 0.1 sodium cacodylate buffer (pH 7.4) at 4°C for 30 min, washed three times with 0.1 M sodium cacodylate buffer for 2 min each followed by three rinses with dH_2O for 2 min each. Cells were further incubated in 1% uranyl acetate in dH_2O at 4°C overnight. At the next day, cells were washed five times with dH_2O for 1 min each and dehydration was performed using a series with increasing ethanol concentration: 20%, 30%, 50%, 60% and 70% ethanol each twice for 2 min at 4°C. Cells were either stored in 70% ethanol at 4°C overnight and further processed on the next day or immediately after the 70% ethanol incubation at the same day. The ethanol series was continued as follows: 80%, 90%, 95%, 96% and pure ethanol each twice for 2 min at 4°C. Two additional rinses with pure ethanol were performed at room temperature for 2 min each. Ethanol

was replaced by pure acetone, dishes were additionally immersed in a bath of pure acetone and the glass bottom was carefully detached from the plastic dish using a cannula. The cells attached to the glass bottom were incubated at room temperature two times for 5 min followed by a further incubation step with a 1:1 pure acetone-Epon mix at room temperature for 5 min. Epon was prepared as described in section 2.1.4.5. Epon was filled into a mold and the glass bottom was placed upside down onto the Epon with the cells facing the Epon. Care was taken to avoid trapping of air bubbles and Epon was polymerized in an oven at 30°C for 1 h and at 60°C for 2-3 d.

2.2.5.4 Ultramicrotomy

Prior to ultramicrotomy, Pioloform-coated slot grids were prepared by Anita Zügner, Helga Othmen or Yulia Zaytseva (all Institute for Molecular and Cellular Anatomy, University of Regensburg) as already described in Gürster 2013. Briefly summarized, glass slides were immersed perpendicular in a solution consisting of 1.5% Pioloform in chloroform, incubated for 30-40 s and were carefully removed. The film formed on the surface of the glass slides was floated off using a water bath and copper slot grids were placed on it with their shiny sides facing the film (Gürster 2013).

After polymerization of Epon, the glass bottom of the former petri dish was removed by using a razor blade or cannulas and immersing the Epon disc alternately in boiling water and liquid nitrogen. Regions previously documented by fluorescence microscopy were identified using the impressions within the Epon disc caused by the petri dish's gridded bottom pattern. Subsequently, regions were cut out using a fretsaw and attached onto plastic cylinders using super glue. Trimming was performed using a razor blade and sections with a nominal thickness of 600 nm "were cut parallel to the basal surface of the cell monolayer" (Buerger *et al.* 2021) using an ultramicrotome and a histo 45° diamond knife. Sections were collected on Pioloform-coated slot grids. Ultramicrotomy was carried out by Yulia Zaytseva (Institute for Molecular and Cellular Anatomy, University of Regensburg).

2.2.5.5 Electron microscopy

Electron microscopy as well as preparation of grids for STEM tomography were carried out by Christine Maaßen, Olga Maier and Anita Zügner (all Institute for Molecular and Cellular Anatomy, University of Regensburg) and performed as described in Buerger *et al.* 2021: "Scanning of grids was performed in the [transmission electron microscopy] TEM mode […] [of] a [JEM-2100F] field

emission electron microscope operated at 200kV to re-locate the regions previously documented by fluorescence microscopy. In TEM mode, the micrographs were recorded using a TemCamF416 camera operated with the software EM-MENU [5] […]. In parallel, the software TvipsCLEM was used to obtain an initial overlay of the fluorescence and electron micrographs for better orientation. The TvipsCLEM software was installed on the same computer controlling the beam and the goniometer to acquire the images. Once the regions of interest were identified, […] electron micrographs were recorded" (Buerger *et al.* 2021) at various magnifications and samples were prepared for scanning transmission electron microscopy (STEM) tomography.

A "2–3nm thick carbon layer was applied to all [Epon] sections to increase the electrical conductivity for STEM tomography. For this purpose, a high vacuum 208carbon Carbon Coater was operated at 3.6V for 30s in an indirect manner (i.e., a shield protected the samples from direct exposure to the evaporated carbon). Then colloidal protein A-gold particles with a diameter of 15nm were applied as fiducial markers for electron tomography to both sides of the grids" (Buerger *et al.* 2021). For this purpose, a protein A conjugated gold particle solution was diluted 1:40 dH_2O (for more details see chapter 2.1.4.5), a 10 µl drop was pipetted onto a Parafilm and one side of a grid was incubated on the drop at room temperature for 4 min. The grid was washed three times briefly by successively transferring it to three drops of water before blotting was performed with a filter paper. The other side of the grid was processed in similar manner. "In a last step, the grids were plasma cleaned for 30–40s (at RF level LOW) and immediately transferred to the electron microscope" (Buerger *et al.* 2021).

"Subsequently, tilt series were recorded (pixel size: 1.34nm) by STEM tomography (electron beam with small convergence angle) at regions of interest. The field of view was ~2.7µm in both the *x* and *y* direction. Ideally, series of 90 images (-66° to +66°) with non-linear increment […] [(Rachel *et al.* 2020; Saxton *et al.* 1984)] were recorded" (Buerger *et al.* 2021). In "STEM mode […] the electron microscope [was operated] with a Universal Scan Generator and the software EM-TOOLS" (Buerger *et al.* 2021). STEM images were recorded using a bright-field detector.

2.2.5.6 Tomogram reconstruction and overlay generation

Tomogram reconstruction of acquired STEM tilt series was carried out by Anthonie Maurer (Institute for Molecular and Cellular Anatomy, University of Regensburg) and performed as described in Buerger *et al.* 2021: "3D reconstructions were obtained using the IMOD software package [(Kremer *et al.* 1996)] using the SIRT (simultaneous iterative reconstruction technique)

algorithm (number of iterations: 15). The voxel size of reconstructed tomograms was 1.34x1.34x1.34nm. The 15-nm colloidal protein A-gold fiducials were computationally removed using IMOD" (Buerger *et al.* 2021).

The cell shape in combination with the location and shape of the nucleus and the location of the centrosome was used to rotate the fluorescence microscopic image and the transmission electron micrograph in order to orientate each cell in similar manner on both images. In this way it was possible to identify the Centrin1-EGFP spot corresponding to the mother centriole/basal body on fluorescence microscopic images. "Overlays of fluorescence microscopic images with […] 3D STEM tomograms were generated using the open access software eC-CLEM [(Paul-Gilloteaux *et al.* 2017)]" (Buerger *et al.* 2021), "a plugin of the Icy software package [(Chaumont *et al.* 2012)]" (Buerger *et al.* 2021). As STEM tomograms showed only the centrosomal region of a cell, the Centrin1-EGFP signals in combination with the centrioles were the only landmarks being used for overlay generation. Subsequent image processing of all overlays was performed using the Icy software package (Chaumont *et al.* 2012) and ImageJ (Rueden *et al.* 2017).

2.2.5.7 Tomogram segmentation

Segmentation of selected tomograms was carried out by Anita Hecht (Institute for Molecular and Cellular Anatomy, University of Regensburg) and performed using the Amira software (brush size 7). The following structures of basal bodies were highlighted: the outer doublet microtubules, the subdistal and distal appendages, intra-centriolar vesicles and membrane structures docked to the distal appendages.

2.2.5.8 Data analysis

Overlays of fluorescence microscopic images with 3D STEM tomograms were used to verify that the mCherry-RAB8A signal was located at the distal end of the basal body and all tomograms showing a specific localization pattern as well as the tomograms of mCherry overexpressing cells (control group) were analyzed as follows: The number of intra-centriolar vesicles per mother centriole/basal body and daughter centriole was counted and the size of each vesicle was determined by measuring the diameter of the vesicle in *x* and *y* dimensions using the slice of the tomogram showing the vesicle with its largest dimension. For measuring, the IMOD software was used. Care was taken to use only tomograms showing the entire centriole. Statistics was performed as described in section 2.2.7.

2.2.6 Histochemistry for electron microscopy

2.2.6.1 Cell culture

For investigating the ultrastructure of the ciliary membrane an LLC-PK_1 cell line was used stably expressing an HRP and EGFP tagged version of the constitutive active M2 mutant of the murine Smoothened (SmoM2) protein. While the COOH-terminus of SmoM2 was tagged with EGFP, the cDNA of HRP (with silent point mutation to remove internal *XhoI* site) was cloned into the cDNA of SmoM2 in between the regions encoding for the signal peptide and the first transmembrane domain which resulted in the HRP facing the extracellular milieu (see sections 2.2.1-2.2.2).

For all experiments 7.5 x 10^5 wild-type LLC-PK_1 cells or LLC-PK_1 cells producing HRP-SmoM2-EGFP were plated per well of a 6-well cell culture pate with coverslips (10 mm or 22 mm diameter) or per gridded glass bottom dish (growth area of ~9.6 cm^2). Cells were cultured without antibiotic addition. Three days after plating, cells were fixed as described below for subsequent experiments.

2.2.6.2 Amplex UltraRed labeling

To ensure enzymatic activity of the peroxidase HRP prior to experiments for electron microscopy (Martell *et al.* 2017), "Amplex UltraRed labelling" was performed in a similar manner as described by Martell *et al.* 2017. Cells were fixed with 4% formaldehyde in 1x PBS (pH 7.4) at room temperature for 5 min, followed by an incubation period of 20 min on ice. The cells were kept on ice and within a light-protected environment during all further steps. Coverslips (10 mm diameter) were transferred into wells of 24-well cell culture plates and washed with ice-chilled 1x PBS five times for 2 min each. Nuclei were stained by incubating the cells in 0.5 µg/ml bisBenzimide H 33342 in 1x PBS for 15 min followed by five rinses with ice-chilled 1x PBS for 2 min each. Amplex UltraRed stock solution (10 mM in dimethyl sulfoxide) was diluted with 1x PBS to a final concentration of 50 µM. If H_2O_2 was added it was used in a final concentration of ~6.7 mM. Two hundred µl of the Amplex UltraRed solution (with or without H_2O_2 addition) were added per well of the 24-well cell culture plate. Cells were incubated for 30 min, washed with ice-chilled 1x PBS five times for 2 min each and mounted between glass slides and cover glasses using 40% glycerin in 1x PBS. Fluorescence microscopy was carried out right afterwards as described in sections 2.2.3 and 2.2.5.2.

2.2.6.3 Histochemistry for electron microscopy

One coverslip (diameter 10 mm) per well/glass bottom dish was removed, fixed with formaldehyde, nuclei were stained with bisBenzimide H 33342 and cells were mounted on glass slides as described in section 2.2.3. Having ensured the presence of EGFP-positive cilia in LLC-PK_1 cells producing HRP-SmoM2-EGFP by fluorescence microscopy for each experiment, cells grown on coverslips with 22 mm diameter or gridded glass bottom dishes were processed for electron microscopy.

Cells were fixed using 2% glutardialdehyde and 2 mM $CaCl_2$ in 0.1 M sodium cacodylate buffer (pH 7.4) at room temperature for 5 min followed by an incubation period of 55 min on ice. The cells were kept on ice during all further steps. Cells were washed five times for 2 min each with 0.1 M sodium cacodylate buffer before adding a blocking solution consisting of 20 mM glycine in 0.1 M sodium cacodylate buffer (pH 7.4) for 5 min. Cells were washed five times for 2 min each with 0.1 M sodium cacodylate buffer and two times with 50 mM Tris-HCl buffer (pH 7.6). The 3,3´-Diaminobenzidine solution was prepared by adding a 3,3´-Diaminobenzidine stock solution (10 mg/ml) to 50 mM Tris-HCl buffer (pH 7.6) to a final concentration of 0.5 mg/ml 3,3´-Diaminobenzidine and filtering it with pore size of 0.2 µm. Cells were incubated in 3,3´-Diaminobenzidine solution for 15 min with continuous shaking in a light-protected environment. To start the peroxidase enzymatic reaction, H_2O_2 was added to the 3,3´-Diaminobenzidine solution to a final concentration of ~6.7 mM and cells were incubated for further 30 min with continuous shaking in a light-protected environment. Afterwards, cells were washed five times for 2 min each with 0.1 M sodium cacodylate buffer before further processing them for electron microscopy.

2.2.6.4 Preparation for electron microscopy

Incubation in OsO_4 solution, dehydration with a series of ethanol with increasing concentration as well as pure acetone and Epon embedding was performed as described in section 2.2.5.3. Incubation in uranyl acetate solution, however, was omitted to avoid interference of the signal of the Osmium-contrasted 3,3´-Diaminobenzidine polymer (Perkins 2014) with contrast from uranyl acetate which stains membranes as well. After polymerization of Epon, the glass bottom of the former petri dish or the coverslip was removed by Helga Othmen (Institute for Molecular and Cellular Anatomy, University of Regensburg) using a razor blade or cannulas and immerging the Epon disc alternately in boiling water and liquid nitrogen. Each Epon disc was divided into small pieces using a fretsaw.

2.2.6.5 Ultramicrotomy

Epon pieces were again embedded in Epon with the cell monolayer facing up for sectioning perpendicular "to the basal surface of the cell monolayer" (Buerger *et al.* 2021). For this purpose, Epon was polymerized at 60°C overnight. Trimming was performed using a razor blade and sections with a nominal thickness of ~70 nm were generated with an ultramicrotome and a histo 45° diamond knife. Sections were collected on 200 mesh copper grids (without a support film). Ultramicrotomy was carried out by Helga Othmen (Institute for Molecular and Cellular Anatomy, University of Regensburg).

2.2.6.6 Electron microscopy and data analysis

Transmission electron microscopy was performed as described by Asam *et al.* 2019. Electron micrographs at various magnifications were recorded with an 80 kV EM 902 transmission electron microscope operating with a CCD camera and the software Image SP. The microscope was operated by Helga Othmen (Institute for Molecular and Cellular Anatomy, University of Regensburg). The approximate distance over which the Osmium-contrasted 3,3´-Diaminobenzidine polymer extended along the periciliary membrane starting from the left side of the ciliary base as well as from the right side were measured for each cell using recorded electron micrographs in combination with the software ImageJ (Rueden *et al.* 2017; Schindelin *et al.* 2012) and a mean value was calculated using Microsoft Excel (Microsoft Office Professional Plus 2019).

2.2.7 Statistics, homology modeling and image processing

Percentages as well as mean or median values and standard deviations were calculated using Microsoft Excel (Microsoft Office Professional Plus 2019) for all experiments requiring quantification. A two-tailed, heteroscedastic Student's t-test was performed using Microsoft Excel and a p value <0.05 was considered significant. Bonferroni correction was performed if it was indicated. Graphs were plotted using the software Origin (version 2020 SR1).

Homology modeling was performed by Gregor Madej (Institute of Biophysics and Physical Biochemistry, Universtiy of Regensburg) and is described in Madej *et al.* 2014. Therefore the following paragraph is a slightly modified and adapted version of the homology modeling chapter of the method section of Madej *et al.* 2014: "Homology modeling was performed using the default-modeling schedule of MODELER [sic] […] with "Thorough Variable Target Function Schedule" and "Slow MD Annealing" [(Sali & Blundell 1993)] […]." (Madej *et al.* 2014). The HRP-SmoM2-

EGFP construct model was generated based on X-ray structures of the respective proteins (PDB ID code 7atj for HRP or 6o3c for SmoM2) (Deshpande *et al.* 2019; Henriksen *et al.* 1999). The linker sequence was introduced in Coot (Emsley & Cowtan 2004) and improved by iterative MODELLER script for loop refinement (Sali & Blundell 1993). “Using Z-DOPE, a normalized atomic distance-dependent statistical potential based on known protein structures [(Shen & Sali 2006)] […], the quality of the initial models was assessed” (Madej *et al.* 2014) and selected for further modeling and loop refinement. “The final models were inspected visually and unmodeled loop regions were removed” (Madej *et al.* 2014).

For image processing the software packages ImageJ and Adobe Photoshop CS5 were used. Contrast and brightness of fluorescence microscopic images were adjusted equally for different conditions of one experiment. The model of ciliogenesis presented in the discussion chapter of the current work was generated by Anita Hecht (Institute for Molecular and Cellular Anatomy, University of Regensburg) using Adobe Illustrator CS5.

3 Results

3.1 CLEM techniques provide insight into ultrastructure of forming and outgrown cilia

The primary cilium "is a solitary organelle" (Satir *et al.* 2010) which emanates with its membrane-surrounded microtubule core from the apical plasma membrane of almost every mammalian cell type (Mukhopadhyay *et al.* 2017; Pedersen *et al.* 2012; Satir *et al.* 2010). For gaining knowledge regarding the formation of primary cilia (ciliogenesis) the visualization of the ultrastructure of the developmental stadia is indispensable (Lu *et al.* 2015; Wu *et al.* 2018). Therefore CLEM – correlative light and electron microscopy – is a "powerful [...] tool" (Boer *et al.* 2015) to investigate ciliogenesis (Wu *et al.* 2018). CLEM is an umbrella term for a variety of techniques enabling the investigation of one and the same sample by both light and electron microscopy (Boer *et al.* 2015; Bykov *et al.* 2016). Using CLEM, biological processes can be investigated on an ultrastructural level (Boer *et al.* 2015). As there are a large number of CLEM techniques the one most suitable for the respective investigation must be chosen (Buerger *et al.* 2021). Kukulski *et al.* 2011 succeeded in preserving fluorescence signals of fluorescent proteins during sample preparation for electron microscopy (Kukulski *et al.* 2011). The main steps to achieve this were cryo-immobilization of cells via high-pressure freezing instead of a chemical fixation, freeze-substitution with only 0.1% of uranyl acetate and the use of the "low temperature embedding resin[…]" (Carlemalm *et al.* 1982) Lowicryl HM20 (Kukulski *et al.* 2011). Since the *Kukulski protocol* allows to image cells expressing fluorescent proteins within resin sections by both fluorescence and electron microscopy a high correlation accuracy between the two data sets can be achieved (Kukulski *et al.* 2011).

"We […] extended the application of the *Kukulski protocol*" (Buerger *et al.* 2021) to the use of scanning transmission electron microscopy (STEM) tomography (Buerger *et al.* 2021). A detailed description of our on-section CLEM-STEM approach has already been published as part of the present work (Buerger *et al.* 2021). Results generated with this technique are therefore mentioned only in part in this chapter. For further information regarding materials and methods as well as the presentation of all results see Buerger *et al.* 2021. Using bright-field STEM at 200 kV with a low semi-convergence angle for CLEM experiments it was possible to localize "fluorescently tagged proteins [of interest] […] in three-dimensional ultrastructural environments with a volume of at

least 2.7x2.7x0.5µm" (Buerger *et al.* 2021) (Fig. 8). Therefore a large part of the ultrastructure of a primary cilium was visualized in a single STEM tomogram (Fig. 8).

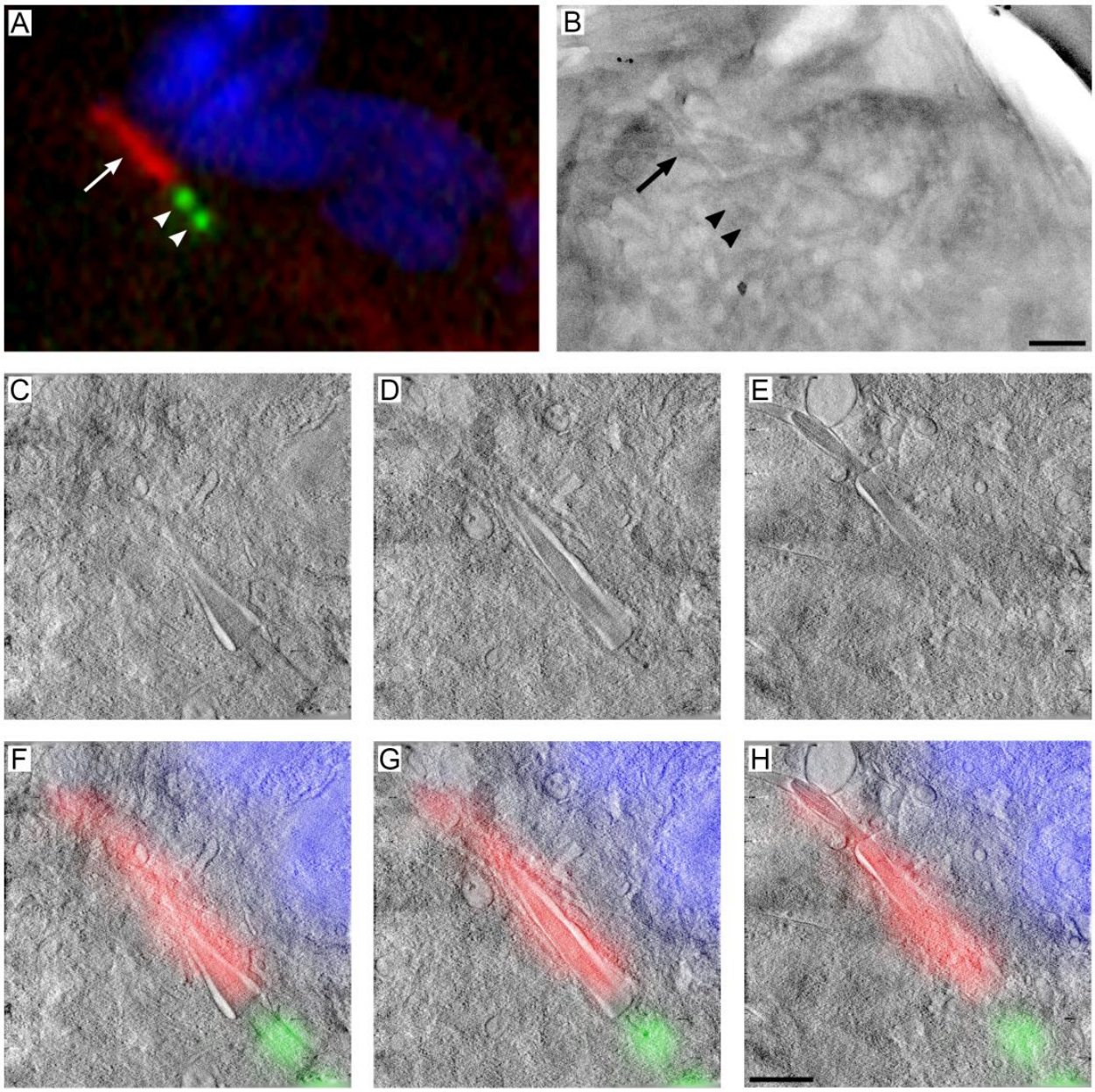

Figure 8: "**On-section CLEM of high-pressure frozen RPE1 cells constitutively producing fusion proteins of Centrin1 with GFP, and of the M2 mutant of Smoothened with miniSOG and mCherry.** Cells were serum-starved for 72h to induce ciliogenesis, stained with bisBenzimide H 33342[…] [and] high-pressure frozen […]. [Freeze-substitution was performed with 0.1% of uranyl acetate, cells were embedded in Lowicryl HM20 and resin sections with a nominal thickness of ~900 nm were generated.] (A) Fluorescence image of a Lowicryl HM20 section on a carbon-coated finder grid. The two centrioles (Centrin1-GFP, green) are marked with arrowheads, the cilium (SmoM2-miniSOG-mCherry, red) with an arrow. (B) STEM micrograph (bright-field) of the same section as in Panel (A) (centrioles marked by arrowheads, cilium marked by arrow). (C–E) At the region of interest, a tilt series of 63 images

(-58° to +46°) was recorded in STEM bright-field mode. Shown are three slices of the STEM tomogram after reconstruction using the simultaneous iterative reconstruction technique (SIRT) with 15 iterations. The three slices (each with a thickness of 1.34nm) lie ~88nm apart from each other in *z*. (F–H) An overlay of the fluorescence image shown in Panel (A) and of the respective slices shown in Panels (C–E) using the eC-CLEM software (Icy plugin). Scale bars, 1µm (A and B), 500nm (C–H)." (Buerger *et al.* 2021) The figure was copied and the figure legend was taken verbatim from Buerger *et al.* 2021. A movie of the overlay already published in Buerger *et al.* 2021 can be found in the supplement (see SFig. 8). Permission to reuse the figure as well as the movie is kindly granted by Elsevier.

In a next step we wanted to use our on-section CLEM-STEM approach to investigate the localization of the GTPase RAB8A as well as membrane remodeling during ciliogenesis on an ultrastructural level. Since signals of the fusion protein of RAB8A with the fluorescent protein mCherry were very weak during early stadia of ciliogenesis (see mCherry-RAB8A signals of Fig. 14B-D), we were not able to preserve these signals during sample preparation for electron microscopy. A high sample throughput was required as early stadia of ciliogenesis are "rare cellular […] events" (Boer *et al.* 2015). Using the high-pressure freezing machine EM PACT2 (Leica) for cryo-immobilization of cells, however, sapphire discs with a diameter of only 1.4 mm could be used for cell culture (Buerger *et al.* 2021). In addition, there was also a noticeable loss of cells during high-pressure freezing and/or sample preparation for electron microscopy. For these reasons the on-section CLEM-STEM technique was not suitable for investigating centrosomal mCherry-RAB8A recruitment during early ciliogenesis.

Instead a different, so-called pre-embedding CLEM approach (Boer *et al.* 2015; Bykov *et al.* 2016) succeeded in investigating these cellular processes. Culturing cells on gridded glass bottom dishes with a growth area of ~9.6 cm^2 resulted in a markedly higher throughput compared to the use of sapphire discs with a growth area of ~1.5 mm^2. An initial fixation step with formaldehyde did not interfere with the preservation of even weak fluorescence signals (see mCherry-RAB8A signals of Fig. 14B-D). After fluorescence microscopy a further fixation step with glutardialdehyde and sample preparation for electron microscopy were performed. Finally STEM tomography visualized a large part of the ultrastructure of centrosomes and of forming cilia in three dimensions (Fig. 11-12).

To sum it up, "depending on the scientific question asked" (Buerger *et al.* 2021) different CLEM techniques were used in the present study: an on-section CLEM-STEM approach was used for the

visualization of the ultrastructure of outgrown cilia. However, a pre-embedding CLEM-STEM approach was more suited to investigate centrosomal RAB8A recruitment during ciliogenesis.

3.2 Overexpression of dominant negative RAB8A impairs ciliogenesis

The formation of primary cilia, i.e. ciliogenesis, requires the coordinate action of a variety of proteins. The small GTPase RAB8 seems to be one of the key proteins for this process as it is indispensable for "ciliary membrane extension" (Lu *et al.* 2015) resulting in axoneme outgrowth in cell culture (Nachury *et al.* 2007). In order to verify the influence of RAB8A on ciliogenesis in our laboratory and to reproduce the results of Nachury *et al.* 2007, either the EGFP-tagged dominant negative T22N (GDP-locked) mutant of human RAB8A or EGFP as a control were transiently expressed in wild-type RPE1 cells. A localization of EGFP-RAB8A(T22N) at the primary cilium was never observed (Fig. 9A).

A

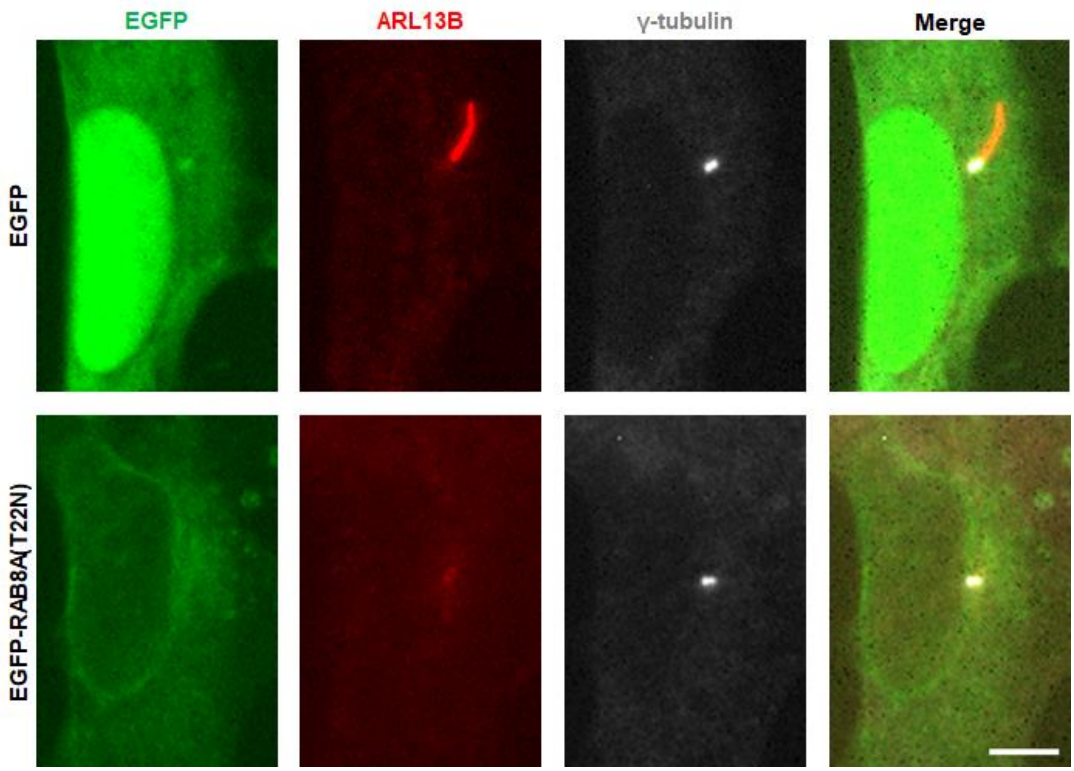

Figure 9: Inhibition of ciliogenesis by transient overexpression of the dominant-negative EGFP-RAB8A(T22N) mutant. Figure 9 to be continued on the next page.

B

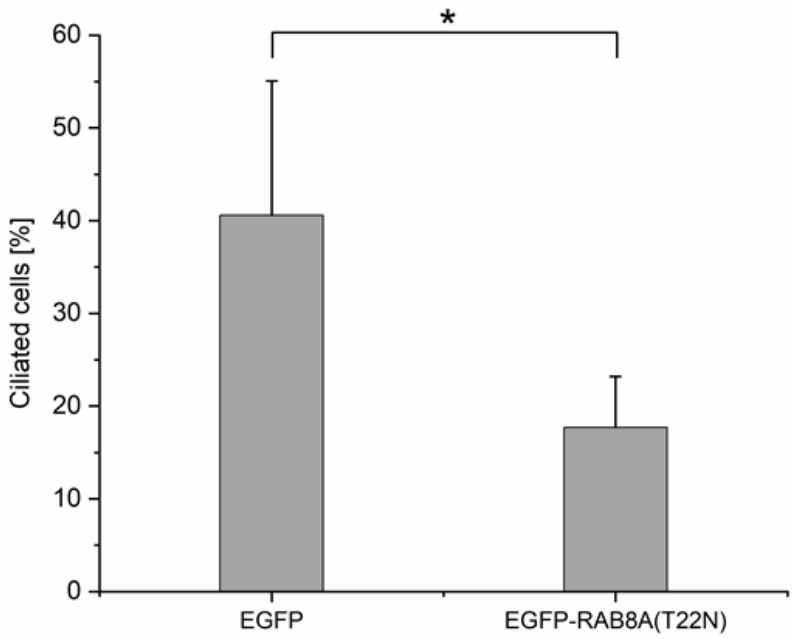

Figure 9: Inhibition of ciliogenesis by transient overexpression of the dominant-negative EGFP-RAB8A(T22N) mutant. (A) Wild-type RPE1 cells were transiently transfected with an expression plasmid containing the cDNA of EGFP (control) or EGFP-RAB8A(T22N), serum starved for 24 h one day after transfection and fixed. An antibody against ARL13B (red) was used to stain primary cilia (Caspary *et al.* 2007) and an antibody against γ-tubulin (white) to stain centrioles (Fuller *et al.* 1995). Examples of fluorescence images of a RPE1 cell either expressing the protein EGFP or EGFP-RAB8A(T22N) are shown. Bar, 5 µm. (B) Quantification of (A). Four independent experiments with at least 142 cells per experiment and condition. Statistical significance is indicated by an asterisk.

As we already detected EGFP signals at the centrosome in several RPE1 cells of the control group (Fig. 9A) we did not investigate the centrosomal EGFP-RAB8A(T22N) localization any further. Please note, that there was a noticeable difference of the percentage of ciliated EGFP-expressing or ciliated EGFP-RAB8A(T22N)-expressing RPE1 cells between different regions documented per coverslip. In comparison to the only EGFP-expressing RPE1 cells, EGFP-RAB8A(T22N)-expressing cells showed a significantly reduced percentage of ARL13B-positive cilia after 24 h of serum starvation (Fig. 9B). Therefore overexpression of dominant negative RAB8A impairs ciliogenesis in RPE1 cells.

3.3 The CLEM-STEM method enables the investigation of RAB8A recruitment during ciliogenesis

3.3.1 Generation of an RPE1 cell line constitutively producing Centrin1-EGFP and mCherry-RAB8A

Using electron microscopy of ultrathin sections Lu *et al.* 2015 demonstrated that after transfection with siRNA against RAB8A+A RPE1 cells were still able to enter the ciliary vesicle stadium of ciliogenesis but the subsequent extension of this vesicle did no longer take place (Lu *et al.* 2015). Based on this finding, Lu *et al.* 2015 concluded that RAB8 functions in extension of the ciliary vesicle. However, the authors did not investigate the localization of RAB8 in combination with the membrane remodeling processes during ciliogenesis in three dimesnions. In order to analyze RAB8A recruitment to the mother centriole/basal body by fluorescence microscopy a RPE1 cell line constitutively producing the centriolar marker protein Centrin1-EGFP, the ciliary marker protein ARL13B-EGFP and mCherry-RAB8A (Fig. 10) was generated in a two-stage process. In a first step RPE1 cells constitutively producing the protein Centrin1-EGFP (already generated by Uetake *et al.* 2007) were stably transfected with a pEGFPN1/ARL13B plasmid. After selection with the antibiotic G418 care was taken to choose a clone with bright EGFP signals at both the centrioles and the primary cilium by fluorescence microscopy for subsequent stable transfection with a pmCherryC1/RAB8A plasmid and selection with puromycin. Using fluorescence microscopy a subclone was chosen which showed a bright mCherry signal at almost all cells and upon serum starvation and a clear localization of the mCherry signal at the acetylated tubulin stained primary cilium (Fig 10A). However, after the second selection step no ARL13B-EGFP signals were detected in most of the cells and if present fluorescence intensity was weak (Fig. 10A). Therefore all further experiments were carried out without taking the ciliary marker protein ARL13B-EGFP into account. Furthermore, additional bright point-shaped cytoplasmic mCherry signals were present. However, these additional bright cytoplasmic mCherry signals did not disturb the clear localization of the mCherry signal at the centrosome and cilium.

For additional characterization we performed Western blot analysis several months after generating the cell line (Fig. 10B). Compared to wild-type RPE1 cells a band at the molecular mass of Centrin1-EGFP (~46 kDa) can be seen for all cell lines constitutively producing the fusion protein of Centrin1 with EGFP. This is in agreement with bright Centrin1-EGFP signals on fluorescence

microscopic images. No band at the molecular mass of ARL13B-EGFP (~74 kDa) was detected in any cell line investigated explaining the hardly detectable ARL13B-EGFP signals during fluorescence microscopy. For this reason the term ARL13B-EGFP is omitted in the name of the generated cell line in the rest of the present work.

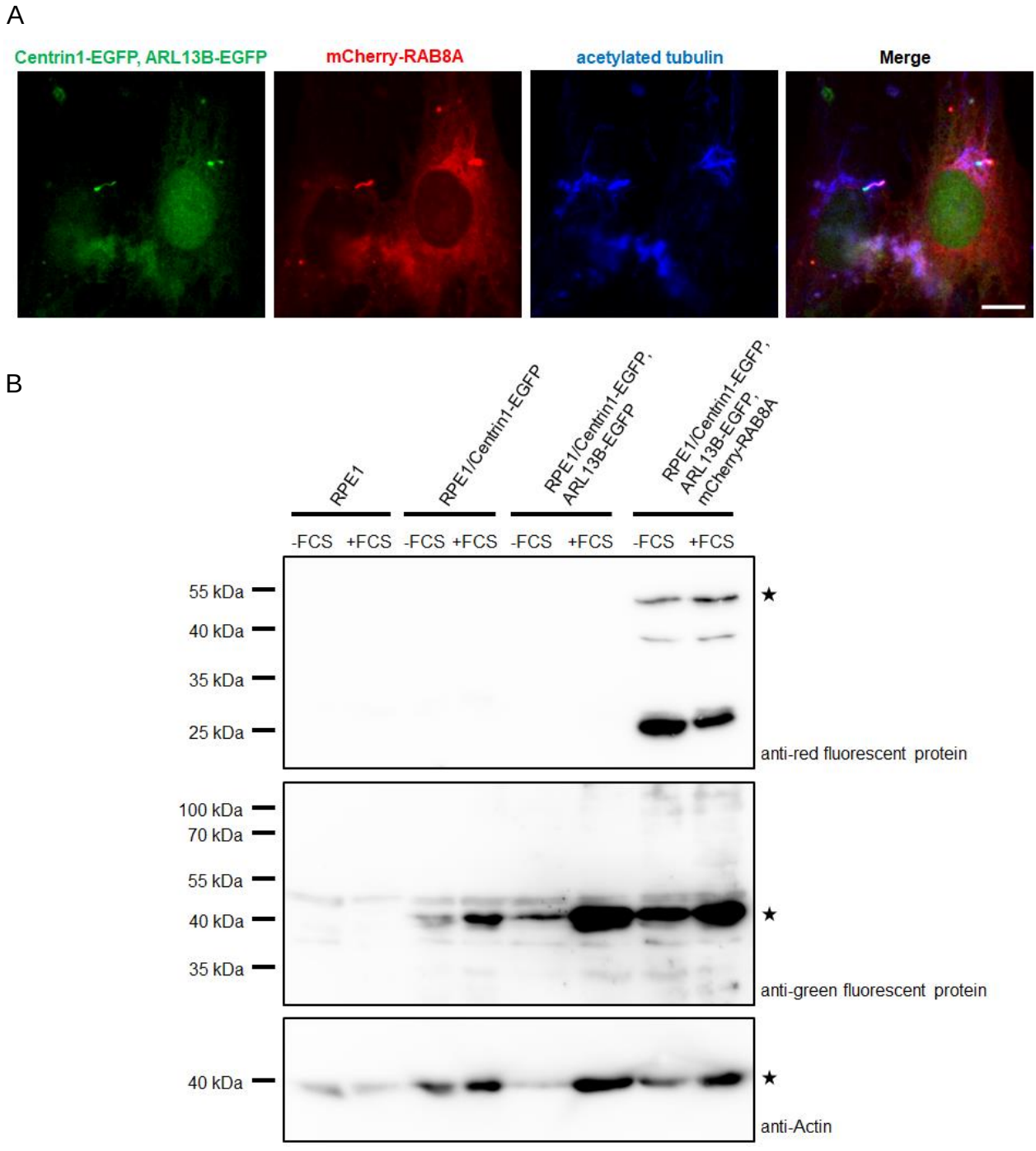

Figure 10: Characterization of the generated RPE1 cell line constitutively producing the proteins Centrin1-EGFP and mCherry-RAB8A. (A) Examples of fluorescence images of two cells after 24 h of serum starvation.

Immunolabeling of cilia was performed using an anti-acetylated tubulin antibody (Piperno & Fuller 1985). Please be aware that the anti-acetylated tubulin antibody stains cytoplasmic microtubules as well. Bar, 10 µm. (B) Western blot analysis of the RPE1 cell line constitutively producing the proteins Centrin1-EGFP and mCherry-RAB8A. Wild-type RPE1 cells, a RPE1 cell line constitutively producing the protein Centrin1-EGFP (Uetake *et al.* 2007) and a RPE1 cell line constitutively producing the proteins Centrin1-EGFP and ARL13B-EGFP were used as control. Cell lysates of all cell lines were prepared both after a period of time of 24 h of serum starvation (-FCS) and without serum withdrawal (+FCS), i.e. cycling cells. Proteins were detected with the indicated antibodies. Anti-actin staining was used as loading control. Please note that stripping of the anti-actin antibody from the PVDF membrane was not completely possible prior to staining with the anti-green fluorescent protein antibody. Bands corresponding to the molecular mass of the respective fusion proteins are marked with asterisks. Western blot images were cropped to the regions of interest. The FACS report (SFig. 10A) as well as uncropped Western blot images (SFig. 10B) can be found in the supplement.

Compared to the other three cell lines only the cell line constitutively producing the proteins Centrin1-EGFP, ARL13B-EGFP and mCherry-RAB8A showed bands after incubation with an anti-red fluorescent protein antibody. In addition to a band at a molecular mass corresponding to the one of mCherry-RAB8A (~50 kDa, asterisks) two additional smaller and specific ones were detected: one at a molecular mass of ~26 kDa corresponding to that of mCherry and a another one at a molecular mass of ~39 kDa. This is in line with bright cytoplasmic mCherry signals observed by fluorescence microscopy. Comparing cycling and noncycling cells of respective cell lines with each other in most of the cases bands of serum starved cells (-FCS) are less bright than those of cycling ones (+FCS). In summary, we generated a RPE1 cell line which is suitable for investigating centrosomal mCherry-RAB8A recruitment during ciliogenesis (see chapter 3.3.3).

3.3.2 Donut-like membrane structure formation during ciliogenesis

According to previous investigations (Lu *et al.* 2015; Sorokin 1962), the intracellular pathway of ciliogenesis can be divided into distinct ultrastructural stadia: first, small vesicles dock to the distal appendages of the mother centriole and fuse to form a larger so-called ciliary vesicle. In the last step, a RAB8-promoted membrane extension of the ciliary vesicle results in axoneme outgrowth and cilium formation (Lu *et al.* 2015; Wu *et al.* 2018). During the current work the definition is used according to which the mother centriole is called basal body from the point in time at which membrane structures are docked to its distal appendages (Kobayashi & Dynlacht 2011; Lu *et al.* 2015; Sánchez & Dynlacht 2016). Current knowledge is mainly based on results from studies using ultrathin serial sections (Lu *et al.* 2015; Schmidt *et al.* 2012; Sorokin 1962; Sorokin 1968; Wu *et al.* 2018). Three-dimensional analyzes using electron tomographic methods were only applied

rarely till today (Insinna *et al.* 2019). Therefore one major concern of the current work was to investigate the localization of RAB8A at the mother centriole/basal body during ciliogenesis in combination with the ultrastructural membrane remodeling taking place during this process by correlative fluorescence and three-dimensional electron microscopy (CLEM).

To answer this question we used the RPE1 cell line constitutively producing the proteins Centrin1-EGFP and mCherry-RAB8A (see section 3.3.1). Based on our unpublished data (generated by Kerstin N. Schmidt) indicating that a large portion of RPE1 cells forms primary cilia already within the first hours after serum starvation, we chose periods of time of ~3-3.5 h or ~10 h in order to identify cells showing the earliest point in time detectable by fluorescence microscopy at which mCherry-RAB8A localized to one centriole. In practice this was done by selecting cells showing an mCherry-positive spot in close contact to one Centrin1-EGFP signal (see Fig. 14A-C, upper image rows). After documenting their positions using fluorescence microscopy datasets, cells were resin embedded for electron microscopy, sections with a nominal thickness of ~600 nm were generated and tilt series were recorded at the centrosomal region using STEM bright-field mode. In total 45 tomograms each containing the three-dimensional volume of a mother centrioles/basal body could be generated during the present work. In many cases the three-dimensional volume of the daughter centriole was included as well. Using STEM with low semi-convergence angle at 200 kV (Rachel *et al.* 2020) it was possible to image resin sections with a nominal thickness of ~600 nm (according to Rachel *et al.* 2020 up to 900 nm thickness possible) and the majority of the centrosomal and ciliary ultrastructure could be visualized within one single tomogram. No serial sectioning was necessary. Prior to investigating the centrosomal recruitment of mCherry-RAB8A during ciliogenesis in detail, we initially focused our research only on the membrane structures docked to the basal bodies visualized by STEM tomography. Therefore we made an attempt to assign each of the 45 tomographed RPE1 cells to one of the stadium of ciliogenesis described in the literature (distal appendage vesicles, ciliary vesicle, cilium with forming axoneme) without considering/verifying whether the mCherry-RAB8A signal actually overlayed with the membrane structures docked to the basal body (see chapter 3.3.3). Due to an unfavorable position within the tomogram (e.g. basal body located at the border of the tomogram or only partially included) the ciliogenetic stadium of three of the 45 tomographed RPE1 cells was not unambiguously assessable.

A

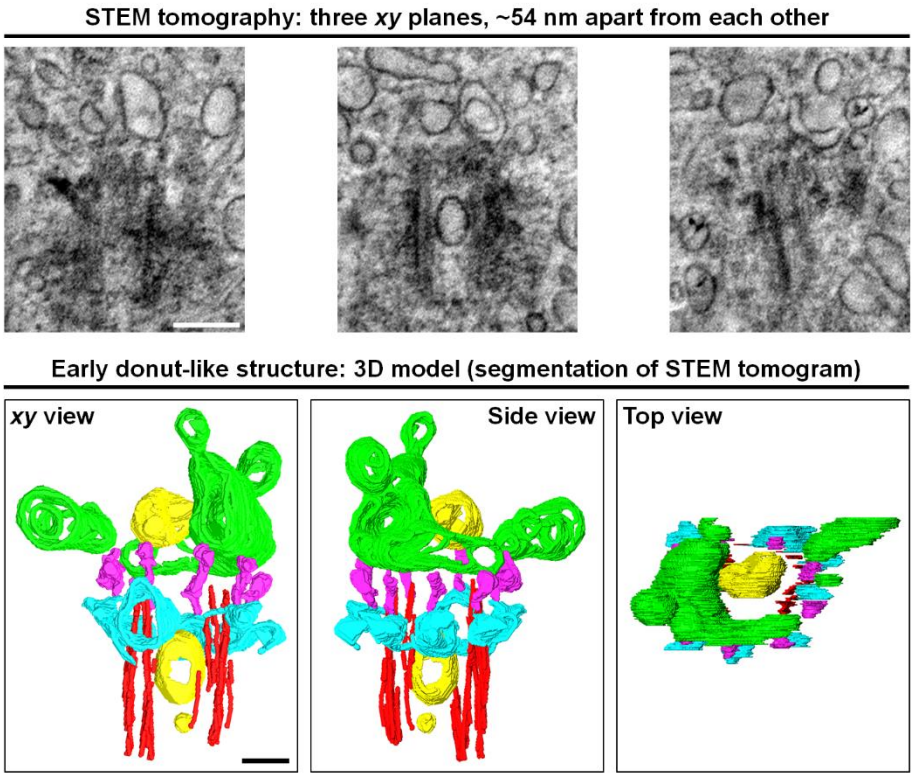

B

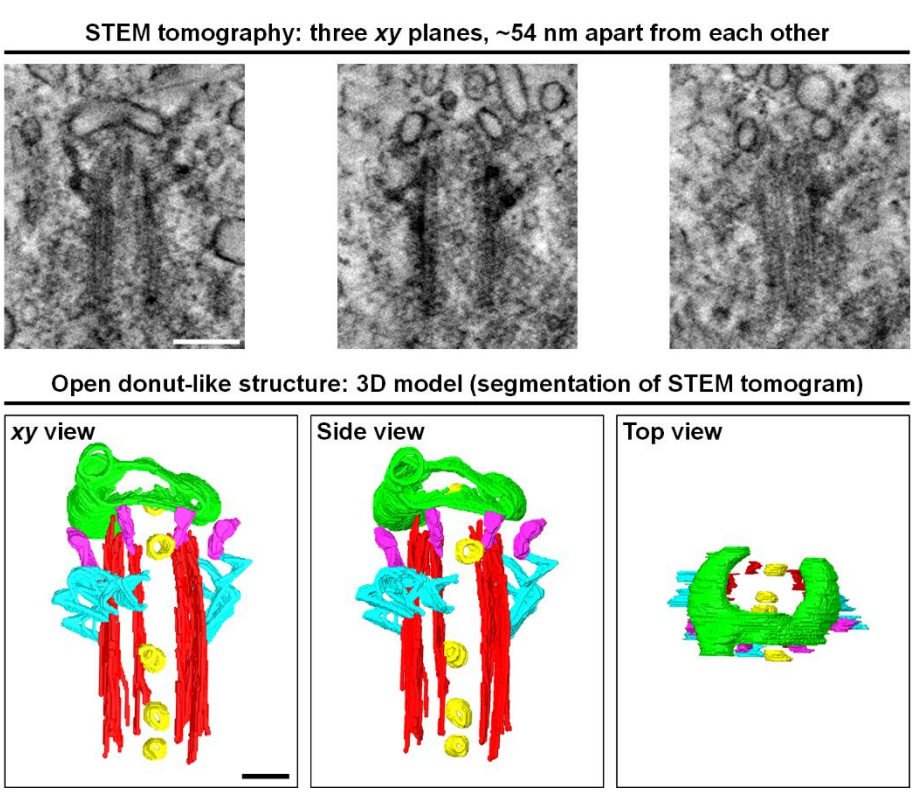

Figure 11: Identification of donut-like structure formation during ciliogenesis. Figure 11 to be continued on next pages.

C

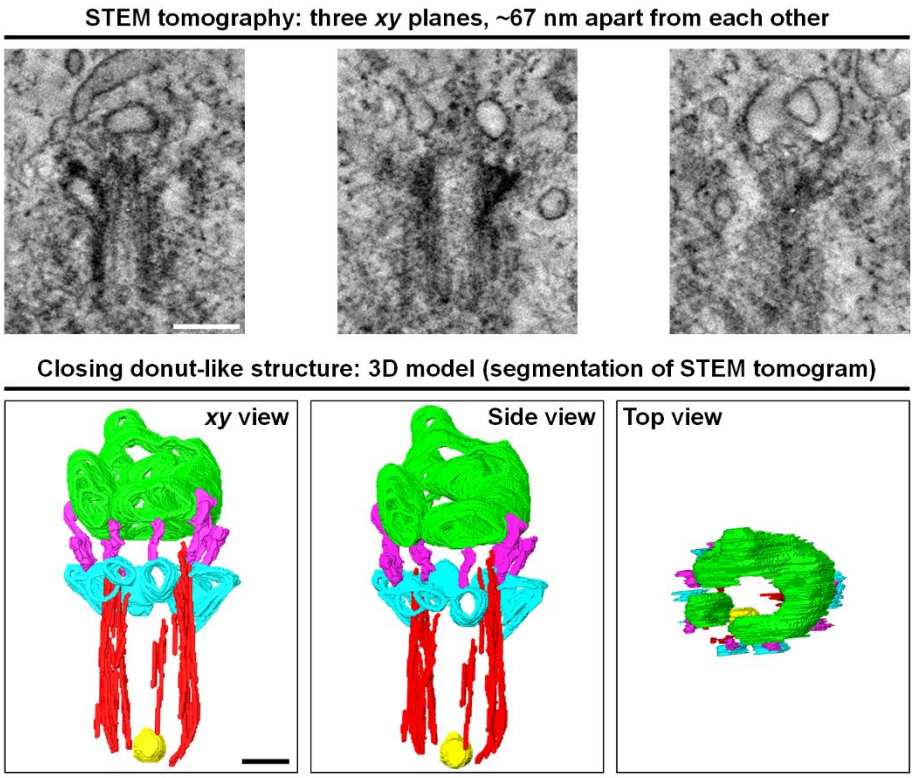

D

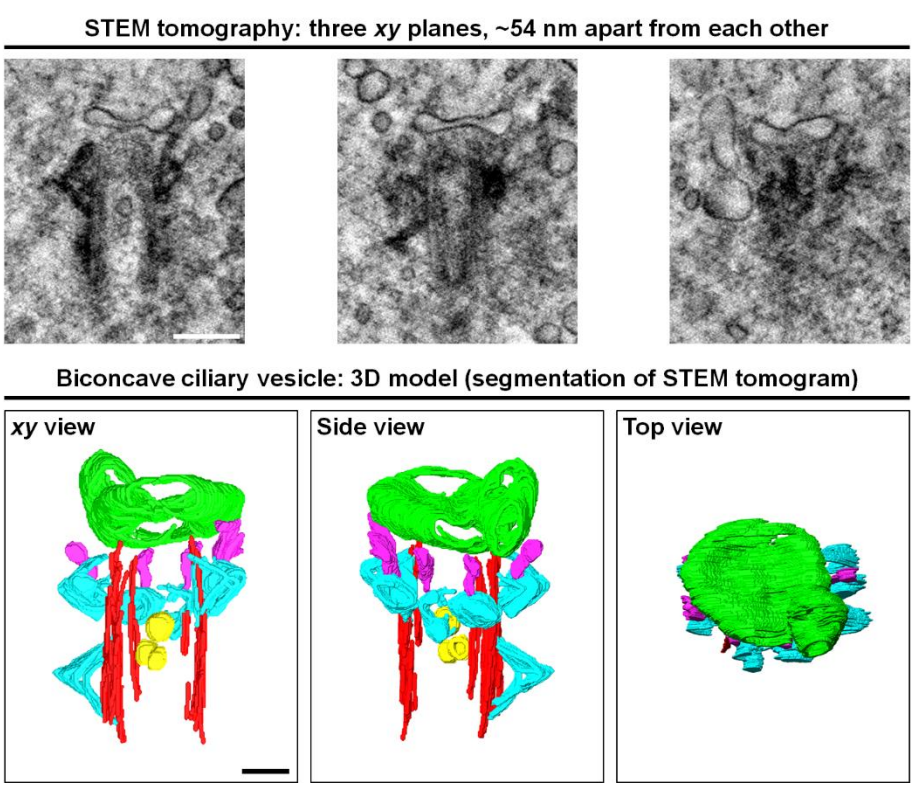

Figure 11: Identification of donut-like structure formation during ciliogenesis. Figure 11 to be continued on next page.

E

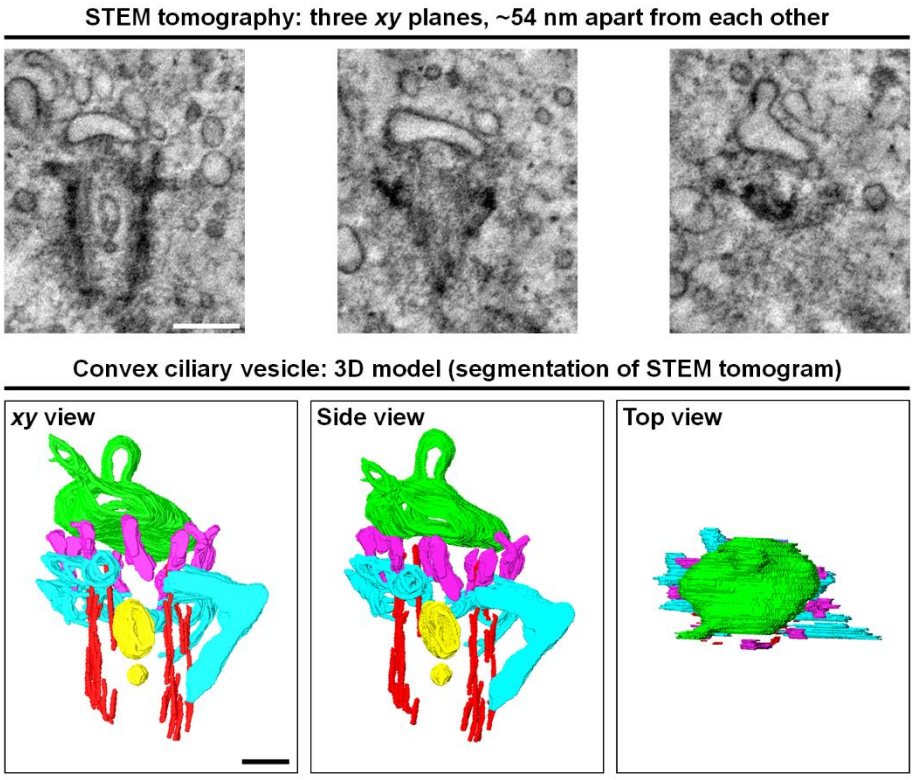

F

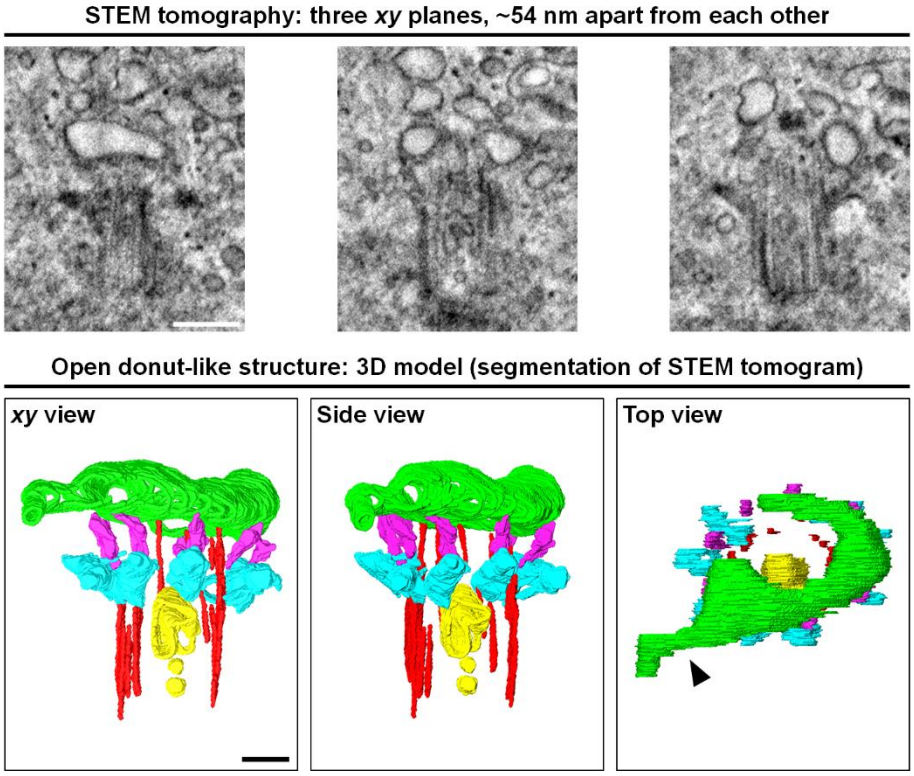

Figure 11: Identification of donut-like structure formation during ciliogenesis. (A-E) RPE1 cells constitutively producing the proteins Centrin1-EGFP and mCherry-RAB8A were serum starved for ~3, ~3.5 or ~10 h to induce

ciliogenesis and fixed. Fluorescence microscopy was used to select cells showing an mCherry-RAB8A-positive spot in close contact to one of the two Centrin1-EGFP signals, i.e. one of the earliest points in time at which mCherry-RAB8A is recruited to one centriole. Cells were further prepared for electron microscopy, Epon sections with a nominal thickness of 600 nm were generated and tilt series were recorded at the centrosomal region of each selected cell using bright-field STEM. Each upper image row of (A-F) shows three slices/*xy* planes (each with a thickness of 2.68 nm) of a STEM tomogram after reconstruction using the simultaneous iterative reconstruction technique algorithm (IMOD software package). The slices were cropped to the region of the basal body of the cell. Bars, 200 nm. Each lower image row of (A-F) shows the 3D model of the basal body after segmentation of the STEM tomogram (Amira software package). (F) RPE1 cells constitutively producing the protein Centrin1-EGFP were transiently transfected with an mCherry expression plasmid, serum starved for ~3, ~3.5 or ~10 h to induce ciliogenesis and fixed. Fluorescence microscopy was used to select mCherry-positive cells. Cells were further processed as described in (A-E). The "Membrane tubule" (Insinna *et al.* 2019) is marked with a black arrowhead in (F). Red: outermost microtubules of the basal body; turquoise: subdistal appendages; purple: distal appendages; green: membrane structures docked to the distal appendages; yellow: vesicles within the lumen of the basal body or within the membrane structures docked to the distal appendages. Shown is the *xy* view of the 3D model (lower image row, left), a side rotation of the model (lower image row, middle) and a rotation to display the top view of the model (lower image row, right). Bars, 100 nm. Movies of all reconstructed STEM tomograms as well as Amira segmentations can be found in the supplement (see SFig. 11A-F).

Furthermore, it turned out that 16 of the residual 42 visualized membrane structures docked to the distal end of the basal body could not be assigned to stadia described in literature as far as known to us. Therefore we focused on a detailed description of these membrane structures. Examples of tomograms generated during the current study as well as their respective 3D models (segmentation of STEM tomograms) are shown in Figure 11.

The earliest stadium of cilia development included in Figure 11 shows that two of the distal appendages of the basal body are associated with vesicles (Fig. 11A). Furthermore, although not all distal appendages have docked a vesicle, several distal appendage vesicles have already fused to form a larger membrane structure reminiscent of the shape of half a donut. Figure 11B and C demonstrate that completion of this membrane structure gradually progresses until it is almost completely closed. Due to its unique shape in 3D models this stadium is called the "donut-like" stadium in the following. The ciliary vesicle stadium can also be divided into two versions: the first one shows a docked vesicle with a biconcave shape, which is reminiscent of the shape of erythrocytes (Fig. 11D), in the second version the vesicle has a convex shape (Fig. 11E).

Ultimately, the ciliary vesicle forms a cap-like structure (Fig. 12A), which elongates as the axoneme will grow out (Fig. 12B). Due to fluorescence microscopic selection of cells with the earliest detectable moment of mCherry-RAB8A localizing to one centriole the ultrastructure of earlier ciliogenetic processes and the ultrastructure of "ciliary membrane extension" (Lu *et al.* 2015) and axoneme outgrowth were not analyzed in the current work. To ensure that the donut-like shape of the membrane structure docked to distal appendages of the basal body is not an artifact caused by overexpression of mCherry-RAB8A, RPE1 cells constitutively producing the protein Centrin1-EGFP were transiently transfected with an mCherry expression plasmid (i.e. no RAB8A overexpression) and processed in similar manner as mCherry-RAB8A expressing RPE1 cells. Generated STEM tomograms demonstrate that this donut-like membrane structure can also be found in cells with an endogenous RAB8A expression level (Fig. 11F): out of 47 tomographed basal bodies, the ciliogenetic stadium of 14 basal bodies could unambiguously be classified. Six of these 14 basal bodies showed a docked donut-like membrane structure.

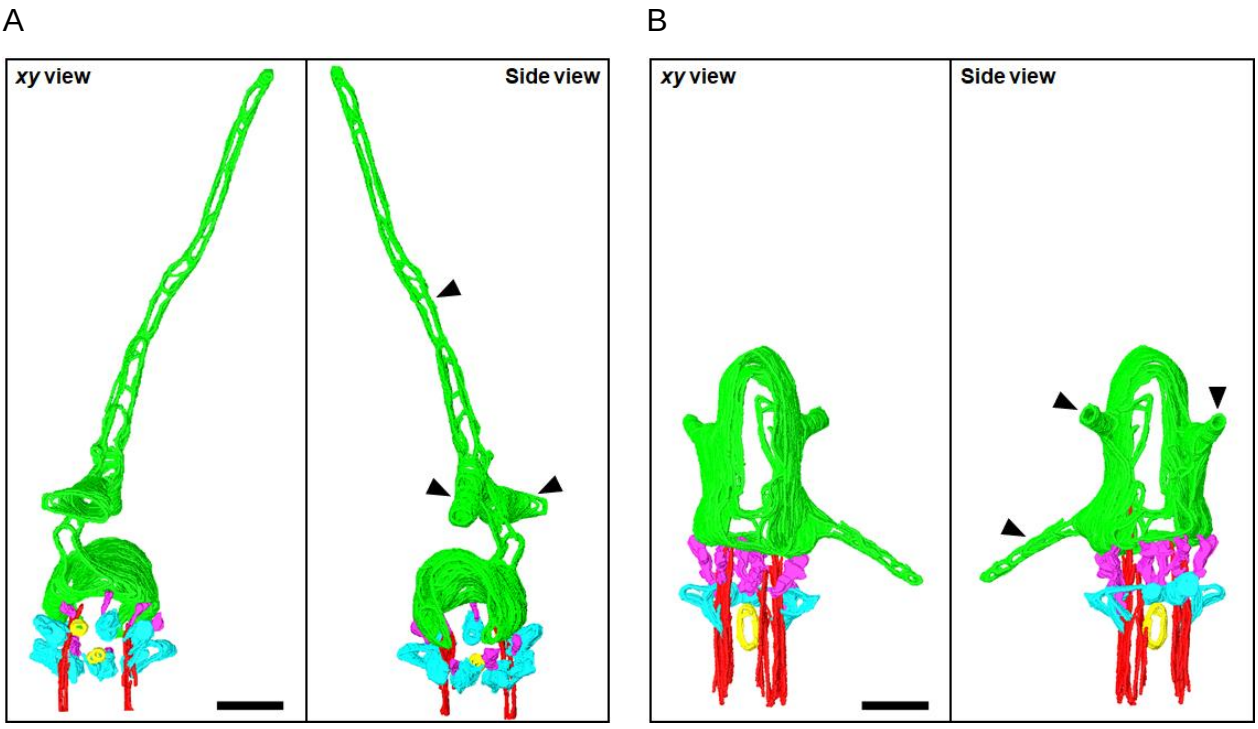

Figure 12: "Membrane tubulation" (Insinna *et al.* 2019) during ciliogenesis. RPE1 cells constitutively producing the proteins Centrin1-EGFP and mCherry-RAB8A were serum starved for ~3, ~3.5 or ~10 h to induce ciliogenesis and fixed. Fluorescence microscopy was used to select cells showing an mCherry-RAB8A-positive spot in close contact to one of the two Centrin1-EGFP signals, i.e. one of the earliest points in time at which mCherry-RAB8A is recruited to one centriole. Cells were further prepared for electron microscopy, Epon sections with a nominal thickness of 600 nm were generated and tilt series were recorded at the centrosomal region of each selected cell using bright-field

STEM. STEM tomograms were reconstructed using the simultaneous iterative reconstruction technique algorithm (IMOD software package) and 3D models of basal bodies were generated by segmentation of STEM tomograms using the Amira software package. Red: outermost microtubules of the basal body; turquoise: subdistal appendages; purple: distal appendages; green: membrane structures docked to the distal appendages; yellow: vesicles within the lumen of the basal body or within the membrane structures docked to the distal appendages. Shown is the *xy* view of each 3D model and a rotation of each model. (A) Short cilium with beginning axoneme formation. (B) Cilium with outgrowing axoneme. The axoneme present in the STEM tomogram was not segmented with the Amira software. "Membrane tubules" (Insinna *et al.* 2019) are marked with black arrowheads in (A-B). Bars, 200 nm. Movies of reconstructed STEM tomograms as well as Amira segmentations can be found in the supplement (see SFig. 12A-B).

During the investigation of the ultrastructure of forming cilia "membrane tubules" (Insinna *et al.* 2019) were observed. The tubules originated from the membrane structures docked to the distal appendages of the basal body and extended over a length of several hundred nanometers (Fig. 11F and 12). They were present in various developmental stadia of ciliogenesis with the donut-like stadium being the earliest one (Fig. 11F). Sometimes the tubules had branches with several tubules originating from one (Fig. 12A).

The appearance of several tubules per cilium was also observed (Fig. 12B). Tubules could be found in both, RPE1 cells constitutively producing the proteins Centrin1-EGFP and mCherry-RAB8A (Fig.12A-B) and in RPE1 cells constitutively producing the proteins Centrin1-EGFP and transiently transfected with an mCherry expression plasmid (Fig. 11F). Since the tubules extend over a larger volume than it could be visualized by a STEM tomogram it was not possible to identify the cellular structures that are connected with these tubules.

Furthermore, clathrin-coated pits as a sign of endocytosis were detected at early stadia of ciliogenesis during the ultrastructural investigation (Fig. 13). Clathrin-coated pits were observed at the ciliary vesicle stadium of RPE1 cells constitutively producing the proteins Centrin1-EGFP and mCherry-RAB8A (Fig. 13A) and at the donut-like stadium of RPE1 cells constitutively producing the proteins Centrin1-EGFP and transiently transfected with an mCherry expression plasmid (Fig. 13B). We did not quantify the extent of clathrin-coated pit formation but it has to be mentioned that it could only be observed in exceptional cases. Regardless of the cell line used for investigation, vesicles could be observed within the lumen of the basal body during all ciliogenetic stadia visualized in the present work (Fig. 11-12). These structures are discussed more detailed in section 3.4.

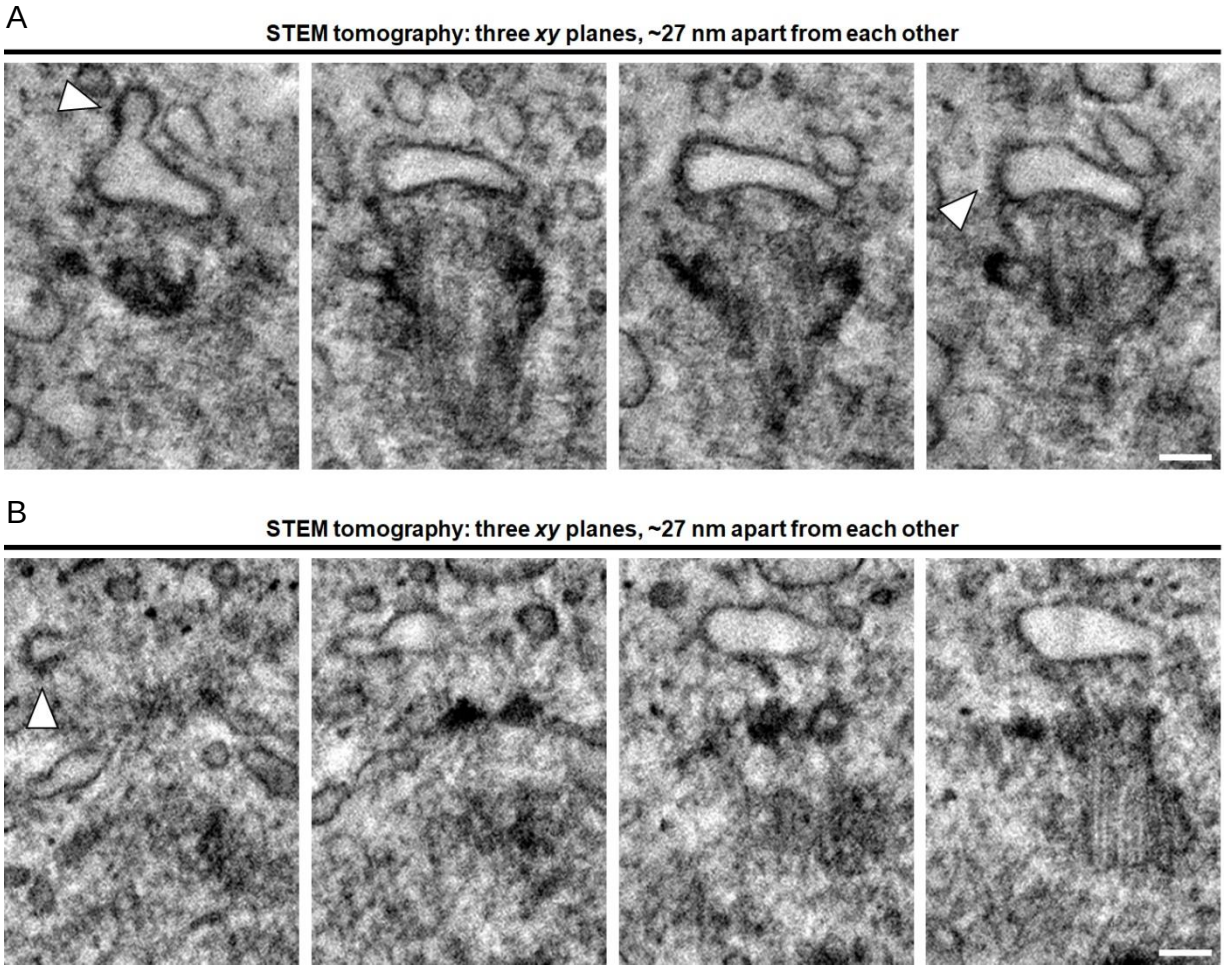

Figure 13: Clathrin-coated pit formation during ciliogenesis. Shown are four slices/*xy* planes (thickness of 1.34 nm) of the same STEM tomograms as in Fig. 11E and F. The slices were cropped to the region of the basal body of the cell. For sample preparation see Fig. 11. Clathrin-coated pits (marked by arrow heads) can be found during the early steps of ciliogenesis. (A) Ciliary vesicle stadium of a RPE1 cell constitutively producing the proteins Centrin1-EGFP and mCherry-RAB8A. (B) Donut-like stadium (same tomogram as in Fig. 11F) of a RPE1 cell constitutively producing the protein Centrin1-EGFP and transiently transfected with an mCherry expression plasmid. Bars, 100 nm. Movies of reconstructed STEM tomograms can be found in the supplement (see SFig. 11E-F).

Considering all findings of the current work, the intracellular pathway of ciliogenesis can be reconstructed as follows: simultaneously to the docking of vesicles to the distal appendages of the mother centriole, first fusion events of distal appendage vesicles occur. Thereby a donut-like structure is formed, which is gradually closed until a ciliary vesicle is established. The ciliary vesicle assumes a shape of a cap/bell. Finally, the ciliary vesicle progressively extends and the axoneme grows out.

3.3.3 RAB8A is recruited to the basal body at the donut-like stadium of ciliogenesis

Knockdown experiments of RAB8A+B in RPE1 cells from Lu *et al.* 2015 demonstrated that ciliogenesis arrests in the ciliary vesicle stadium and therefore RAB8 is required for axoneme outgrowth via an extension of the ciliary vesicle (Lu *et al.* 2015). However, characterizing RAB8 as ciliary protein also requires the identification of the ultrastructural stadia of ciliogenesis at which this GTPase localizes to the developing ciliary membrane compartment. CLEM is the method of choice to perform such an investigation (Wu *et al.* 2018).

Based on the findings of chapter 3.3.2 we divided the intracellular pathway of the ciliogenesis into the following four ultrastructural distinct stadia: the distal appendage vesicle stadium, the donut-like stadium, the ciliary vesicle stadium (including a biconcave and convex shape) and the outgrowing cilium. As already indicated, RPE1 cells showing a point-shaped mCherry-RAB8A signal in close contact to one Centrin1-EGFP signal were selected using fluorescence microscopy for the present work. As the centriolar marker protein Centrin1-EGFP is present in both the mother centriole/basal body and the daughter centriole (Uetake *et al.* 2007) it is not apparent from fluorescence microscopic images with which centriole the mCherry-RAB8A signal is in contact. In order to verify that the mCherry-RAB8A signal is associated with the membrane structures docked to the distal appendages of the basal body, overlays of fluorescence microscopic images with respective STEM tomograms of chapter 3.3.2 were generated with the eC-CLEM software package (Paul-Gilloteaux *et al.* 2017).

Using the cell shape as well as the position of the two centrioles in relation to the nucleus on both fluorescence microscopic and electron microscopic images as landmarks it was possible to assign the two Centrin1-EGFP signals to mother centriole/basal body and daughter centriole. As the two Centrin1-EGFP signals in combination with the centrioles were the only landmarks used for overlay generation of fluorescence microscopic images with STEM tomograms, correlation accuracy was limited. In total overlays of centrosomes of the same 45 RPE1 cells as in chapter 3.3.2 were generated. The mCherry-RAB8A signal overlayed completely or at least partially with the membrane structures docked to the distal appendages of the basal body in ~71.1% of all cases. Further ~24.4% of generated overlays also showed an mCherry-RAB8A signal in close contact to the basal body. However, the signal was either proximally or laterally shifted to the distal end of the basal body and therefore did not overlay with the docked membrane structures. Repeating the overlay generation process of one and the same data set resulted in different overlay versions in

several cases due to the above-mentioned limited correlation accuracy. For this reason it was not possible to clarify whether the shift of the mCherry-RAB8A signal in relation to the distal end of the basal body was due to limitations regarding overlay generation or due to a biological reason. The remaining ~4.4% of overlays were one case in which the mCherry-RAB8A signal was in close contact to the daughter centriole and one further overlay in which there was a gap (~100 nm) between the mCherry-RAB8A signal and the proximo-lateral end of the basal body. Since the mCherry-RAB8A signal was not in close contact with the mother centriole/basal body in only ~4.4% of all overlays generated during the present work it can be summarized that the current CLEM-STEM approach in combination with the RPE1 cell line constitutively producing the proteins Centrin1-EGFP and mCherry-RAB8A can be used to investigate mCherry-RAB8A recruitment to the basal body during ciliogenesis.

Figure 14 gives an overview of the ~71.1% of RPE1 cells with the mCherry-RAB8A signal overlaying completely or at least partially with the membrane structures docked to the distal appendages of the basal body. Fluorescence intensity of mCherry-RAB8A signals at the distal end of the basal body was very weak at all ciliogenetic stadia. With a portion of ~31.3% the donut-like stadium was the earliest ciliogenetic stadium with mCherry-RAB8A-positive membrane structures docked to the distal appendages of the basal body (Fig. 14A, D). While only 12.5% of RPE1 cells with mCherry-RAB8A-positive membrane structures docked to the distal appendages of the basal body showed a ciliary vesicle (Fig. 14B, D), 50% of RPE1 cells already had an outgrowing cilium (Fig. 14C, D). As the ciliogenetic stadium of two RPE1 cells (i.e. ~6.3%) was not unambiguously assessable they are represented as “Stadium unclear” in Figure 14D. Furthermore, it has to be taken into account that RAB8 also localizes to long, outgrown cilia in RPE1 cells (Lu *et al.* 2015), however this step of ciliogenesis was not investigated by the current study. Please note in addition to RPE1 cells included in Figure 14, there are eleven RPE1 cells with the mCherry-RAB8A signal being in close contact with the basal bodies but not overlaying with the membrane structures docked to their distal appendages. Six out of these eleven RPE1 cells showed a donut-like stadium, two out of eleven a ciliary vesicle stadium, two out of eleven a (short) cilium and the ciliogenetic stadium of one was not unambiguously assessable. In summary, we demonstrated that mCherry-RAB8A is recruited to the basal body at the donut-like stadium of ciliogenesis.

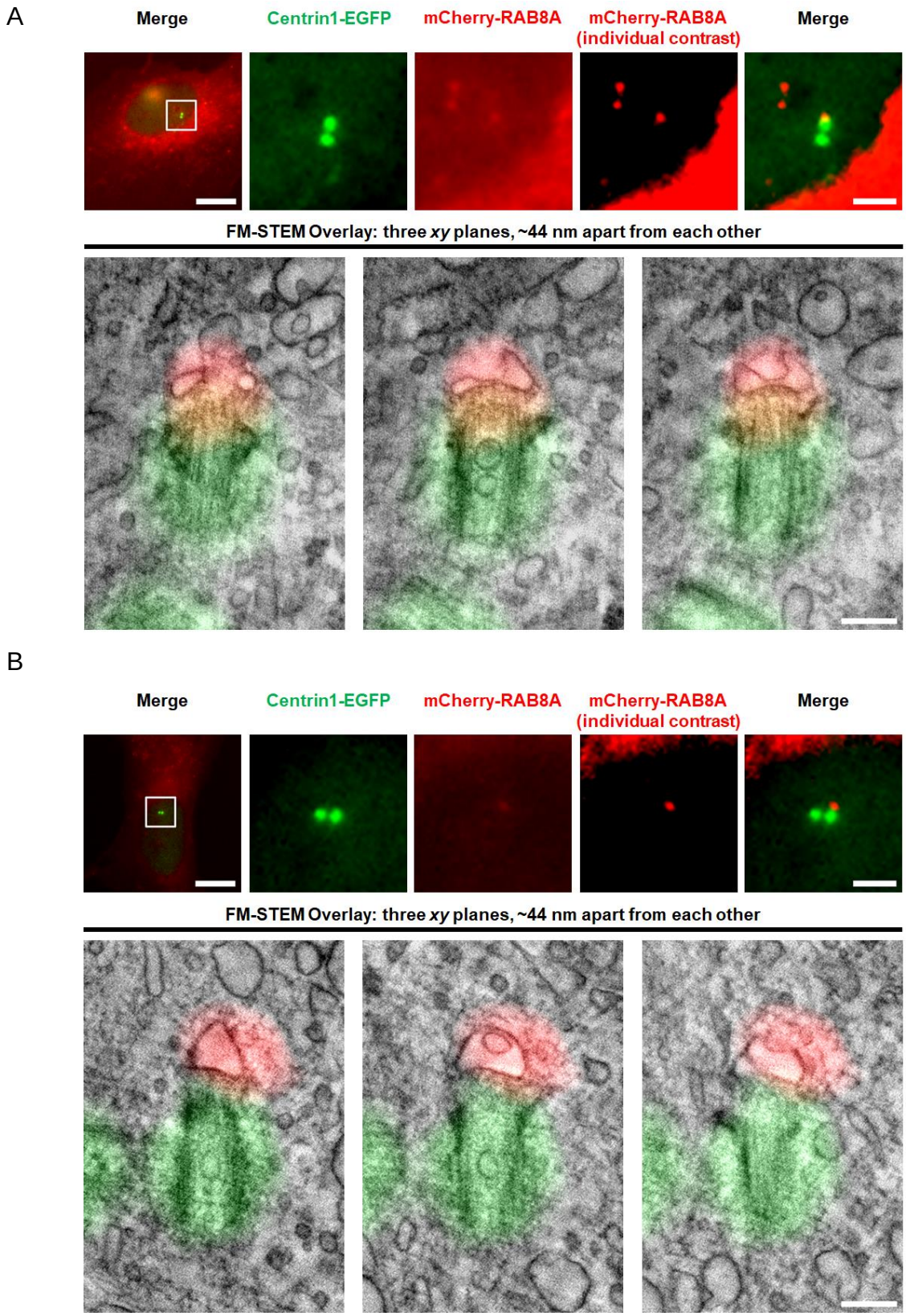

Figure 14: mCherry-RAB8A is recruited to the basal body at the donut-like stadium of ciliogenesis. Figure 14 to be continued on the next page.

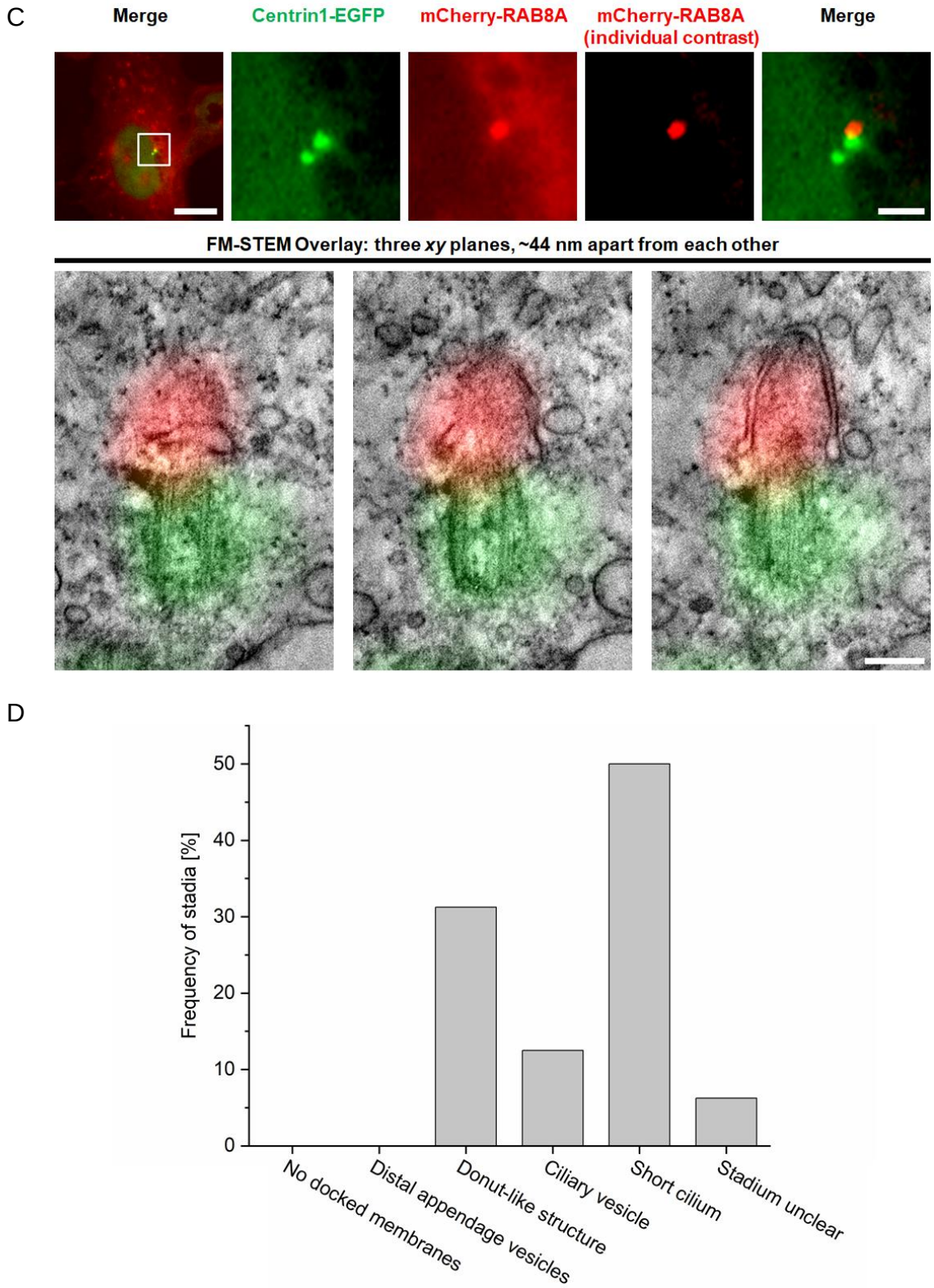

Figure 14: mCherry-RAB8A is recruited to the basal body at the donut-like stadium of ciliogenesis. RPE1 cells constitutively producing the proteins Centrin1-EGFP and mCherry-RAB8A were serum starved for ~3-3.5 or 10 h to

induce ciliogenesis and fixed. Fluorescence microscopy was used to select cells showing an mCherry-RAB8A-positive spot in close contact to one of the two Centrin1-EGFP signals, i.e. one of the earliest points in time at which mCherry-RAB8A is recruited to the basal body. Cells were further prepared for electron microscopy, Epon sections with a nominal thickness of 600 nm were generated and tilt series were recorded at the centrosomal region of each selected cell using bright-field STEM. STEM tomograms were reconstructed using the simultaneous iterative reconstruction technique algorithm (IMOD software package). Overlays of STEM tomograms and respective fluorescence images were generated with the eC-CLEM software to verify that the membrane structures docked to the distal appendages of the basal body were positive for mCherrry-RAB8A. (A-C) Examples for each developmental stadium of ciliogenesis with the mCherry-RAB8A overlaying almost complete with the membrane structures docked to the distal appendages of the basal body. Each upper image row shows fluorescence images of a cell (whole cell: upper image row, left). Bars, 10 µm. The centrosomal region is marked with a white square and shown enlarged (upper image row, four right images). Bars, 2 µm. Contrast and brightness of fluorescence images were adjusted equally for (A-C) unless indicated. Figure design is based on Fig. 2C from Schmidt *et al.* 2012. Each lower image row of (A-C) shows three *xy* planes (each with a thickness of 1.34 nm) of an overlay of a STEM tomogram with the fluorescence image using eC-CLEM software. The *xy* planes were cropped to the region of the basal body of the cell. Bars, 200 nm. (D) Quantification of (A-C). The percentage of cells with mCherry-RAB8A signal at the developing ciliary membrane at the distal end of the basal body was calculated for each developmental stadium of ciliogenesis and plotted. Figure design is based on Fig. 4B from Lu *et al.* 2015. Movies of overlays can be found in the supplement (see SFig. 14A-C).

3.4 Intra-centriolar vesicles are not enriched in RAB8A overexpressing cells during ciliogenesis

Using electron tomography Gürster 2013 was able to identify vesicular structures both within the basal part of the ciliary axoneme and within the lumen of the basal bodies of LLC-PK_1 cells (Gürster 2013). The function of these vesicles was not elucidated, but the author hypothesized that these vesicles contribute to the transport of e.g. proteins to the primary cilium of LLC-PK_1 cells (Gürster 2013). Investigating the recruitment of RAB8A to the basal body in the present work, vesicular structures within the lumen of the daughter centriole and the mother centriole/basal body could be visualized during these steps of ciliogenesis in RPE1 cells (Fig. 11, 12, 14, 15A-C). Therefore these structures are referred to as “intra-centriolar” vesicles. Since it was shown that RAB8A promotes ciliogenesis (Nachury *et al.* 2007) we investigated whether intra-centriolar vesicles are enriched and/or enlarged in the mother centriole/basal body of RAB8A overexpressing RPE1 cells as this would indicate a contribution of these vesicles to ciliogenesis. For this purpose we used both RPE1 cells constitutively producing the proteins Centrin1-EGFP and mCherry-RAB8A as RPE1 cells constitutively producing the proteins Centrin1-EGFP and transiently transfected with an mCherry expression plasmid as a control.

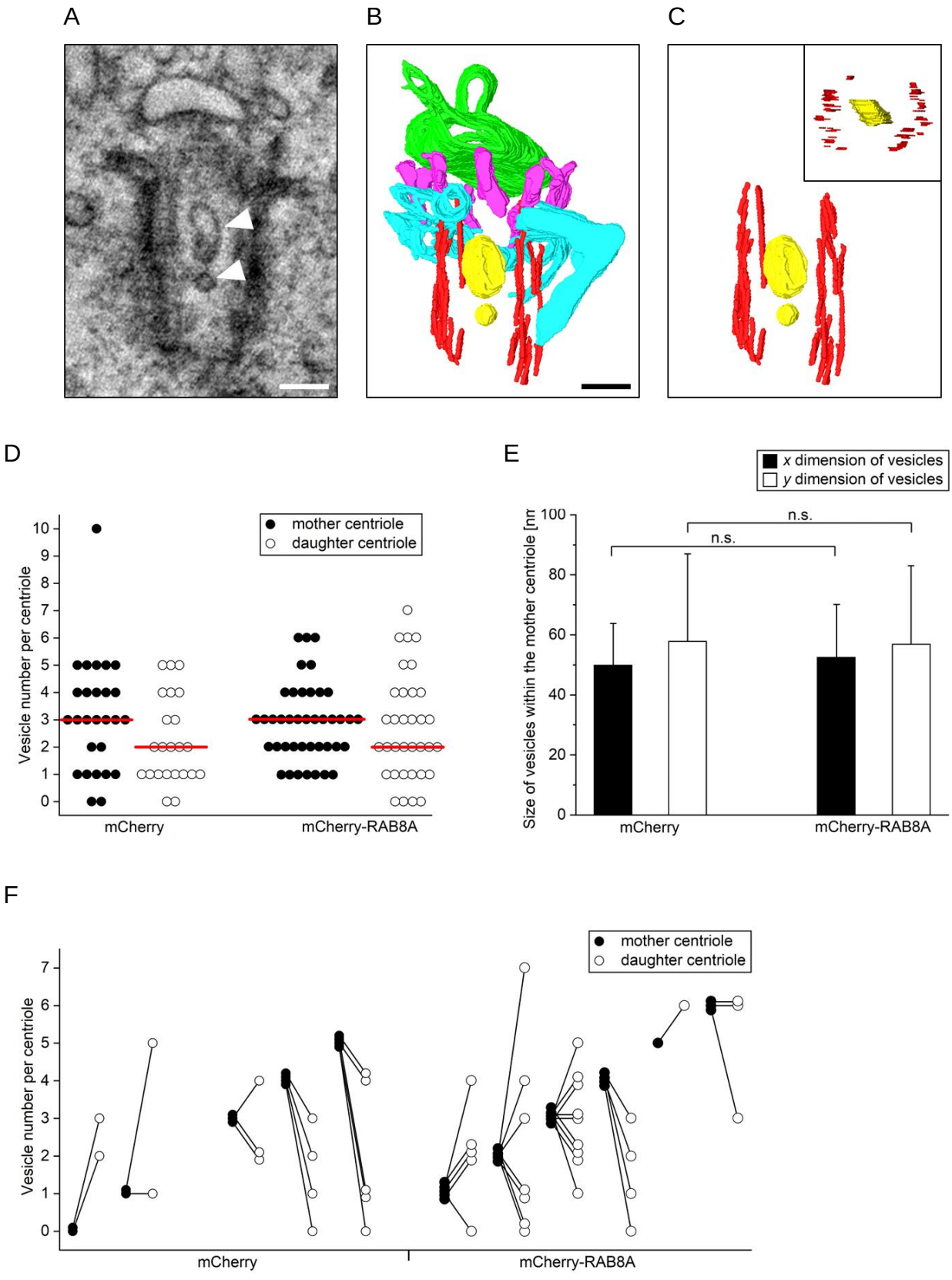

Figure 15: mCherry-RAB8A overexpression has no influence on intra-centriolar vesicle number and size. The same STEM tomograms were used as in Fig. 11E and 13A (for sample preparation see Fig. 11). (A) A *xy* plane

(thickness of 1.34 nm) of a STEM tomogram after reconstruction using the simultaneous iterative reconstruction technique algorithm (IMOD software package). The *xy* plane was cropped to the region of the basal body of the cell. Vesicles within the basal body (intra-centriolar) are marked with white arrowheads. Bar, 100 nm. A movie of the reconstructed STEM tomogram as well as the Amira segmentation can be found in the supplement (see SFig. 11E). (B) 3D model of the basal body after segmentation of the STEM tomogram from (A). Red: outermost microtubules of the basal body; turquoise: subdistal appendages; purple: distal appendages; green: membrane structures docked to the distal appendages; yellow: intra-centriolar vesicles. Shown is the *xy* view of the 3D model. Bar, 100 nm. (C) The same 3D model as in (B) but only the outermost microtubules of the basal body (red) and intra-centriolar vesicles (yellow) are shown. Image in the center of (C): *xy* view, upper right corner of (C): top view. (D) Vesicles per basal body and daughter centriole of RPE1 cells constitutively producing the proteins Centrin1-EGFP and mCherry-RAB8A or RPE1 cells constitutively producing the proteins Centrin1-EGFP and transiently transfected with an mCherry expression plasmid were counted and plotted. Median values are indicated by red lines. (E) In addition to the number of vesicles per centriole, vesicle size was also measured in *x* and *y* dimension (n.s., no statistical significance). (F) Only cells from (D) are shown of which both, mother centriole/basal body and daughter centriole could be visualized in STEM tomograms. The number of vesicles is plotted in the same way as in (D) but additionally each pair of mother centriole/basal body and daughter centriole is linked by a black line.

We determined the number of vesicles per centriole (Fig. 15D, F) and their size (Fig. 15E) using the same STEM tomograms as in chapter 3.3.2. Intra-centriolar vesicles were observed in almost every centriole of both RPE1 cell lines investigated in the present study (Fig. 15D). With a median value of three vesicles per mother centriole/basal body and two vesicles per daughter centriole for both cell lines, intra-centriolar vesicles were not enriched in mCherry-RAB8A overexpressing RPE1 cells compared to only mCherry overexpressing RPE1 cells. Furthermore, regardless of the cell line used for investigation, there were more vesicles within the mother centriole/basal body than within the daughter centriole (Fig. 15D). The ratio of the vesicle number per mother centriole/basal body to the vesicle number per daughter centriole is similar for both RPE1 cell lines as well: RPE1 cells with few vesicles within their mother centrioles/basal bodies tend to show more vesicles within their daughter centrioles and vice versa (Fig. 15F). In addition, there was no statistically significant difference between mCherry-RAB8A and only mCherry-overexpressing RPE1 cells regarding the size of the vesicles within the mother centriole/basal body (Fig. 15E). Thus intra-centriolar vesicles are neither enriched nor enlarged in the mother centriole/basal body of mCherry-RAB8A overexpressing RPE1 cells during ciliogenesis compared to RPE1 cells overexpressing mCherry only.

3.5 The recycling endosome contributes to ciliogenesis

The origin of the ciliary membrane has been debated for a long time (Pedersen *et al.* 2012; Witzgall 2018b). Since unpublished data of our group demonstrate that endocytosis provides vesicles required for cilia formation (Witzgall 2018b) we investigated the influence of endosomes on ciliogenesis. The "endosomal system" (Klumperman & Raposo 2014) which is spread out over virtually the entire cell, is a functional network consisting of various organelles and is involved in many different cellular processes (Klumperman & Raposo 2014). For example, early endosomes regulate sorting of "endocytosed cargo" (Klumperman & Raposo 2014) after its internalization (Klumperman & Raposo 2014; Mercer *et al.* 2010). In a next step, the cargo can either be recycled back to the plasma membrane via the recycling endosome or degraded via late endosomes and lysosomes (Klumperman & Raposo 2014). Members of the "Rab GTPase family" (Stenmark & Olkkonen 2001) are necessary for the functionality of the "endosomal system" (Klumperman & Raposo 2014). For each organelle one RAB protein is characteristic, e.g. RAB5 for the early endosome (Stenmark *et al.* 1994), RAB11 for the recycling endosome (Ullrich *et al.* 1996) and RAB7 for the late endosome (Feng *et al.* 1995); reviewed in (Klumperman & Raposo 2014; Mercer *et al.* 2010). The influence of the recycling endosome on ciliogenesis has been shown several times as RAB11 mediates centrosomal recruitment of RABIN8 which in turn is responsible for RAB8 activation, the prerequisite for "ciliary membrane extension" (Lu *et al.* 2015) (Knödler *et al.* 2010; Westlake *et al.* 2011).

Having focused our work on the ultrastructural localization of RAB8A during ciliogenesis (see chapter 3.3) a further experiment was performed to investigate whether components of the "endosomal system" (Klumperman & Raposo 2014) have an impact on the recruitment of RAB8A to the basal body. For this purpose an EGFP-tagged version of human wild-type RAB8A was co-expressed together with the mCherry-tagged constitutive inactive (GDP-bound) mutant of either RAB5 (Stenmark *et al.* 1994) or RAB7 (Feng *et al.* 1995) or RAB11 (Ullrich *et al.* 1996) or only mCherry as a control in wild-type RPE1 cells as each mutant inhibits a different endosomal compartment (see paragraph above). Results are shown in Figure 16. Co-transfected RPE1 cells were dysmorphic and shrunk in many cases. Accumulation of punctiform or filamentous EGFP-RAB8A signals in the pericentrosomal region of co-transfected RPE1 cells reminiscent of aggregates impeded evaluation.

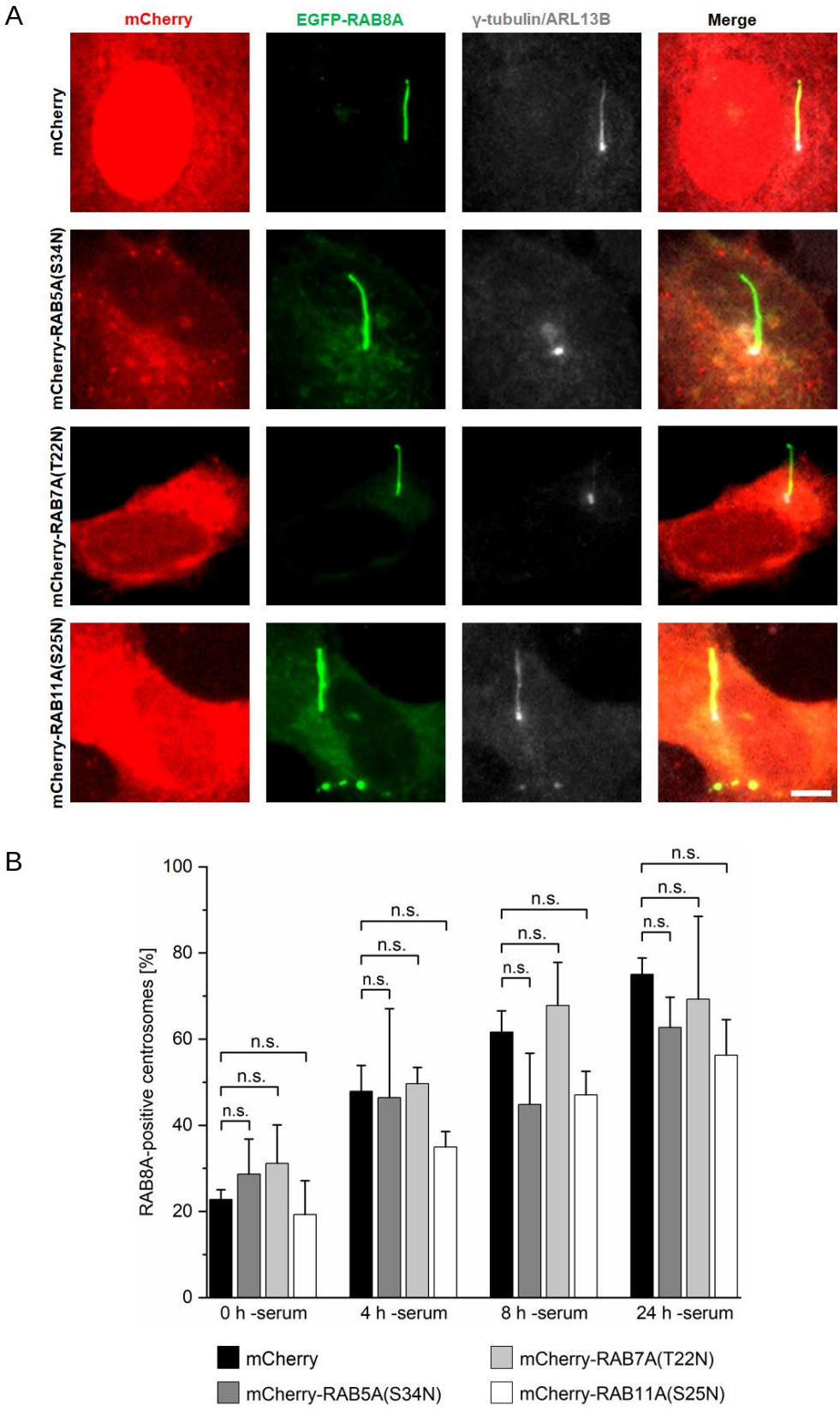

Figure 16: Inhibiting the function of early, late and recycling endosome does not impair EGFP-RAB8A recruitment to the centrosome. Wild-type RPE1 cells were transiently co-transfected with an expression plasmid

containing the cDNA of EGFP-RAB8A along with an expression plasmid containing the cDNA of only mCherry or mCherry-RAB5A(S34N) or mCherry-RAB7A(T22N) or mCherry-RAB11A(S25N), serum starved for the indicated points in time one day after transfection, fixed and stained for cilia (white) with an antibody against ARL13B (Caspary *et al.* 2007) as well as for centrioles (white) with an antibody against γ-tubulin (Fuller *et al.* 1995). (A) Examples of fluorescence images of cells expressing the indicated proteins after 24 h of serum starvation. Please note that the anti-γ-tubulin staining was not always detectable in RPE1 cells so that these cells had to be excluded. Furthermore, fluorescence intensity of anti-ARL13B staining was week in many cases or not detectable at all. Bar, 5 µm. (B) Quantification of (A). The percentage of co-transfected RPE1 cells with an EGFP-RAB8A signal at the basal body was calculated. Three independent experiments with between 33 and 127 cells per experiment and condition (n.s., no statistical significance).

If it was not possible to unambiguously identify whether the EGFP-RAB8A signal was associated with the centrosome or not, cells were excluded. EGFP-RAB8A was present at the centrosome either as a point (i.e. associated with vesicles) or as a line (i.e. associated the primary cilium) (Fig. 16A). The percentage of all co-transfected RPE1 cells showing centrosomal EGFP-RAB8A localization continuously increased during 24 h of serum starvation reaching an average value of ~75% for RPE1 cells expressing EGFP-RAB8A along with only mCherry (control) at the end of the experiment (Fig. 16B). The percentage of mCherry-RAB11A(S25N) expressing RPE1 cells with an EGFP-RAB8A signal at the centrosome was reduced compared to EGFP-RAB8A and only mCherry expressing RPE1 cells at any point in time investigated but statistical significance was never reached. In summary, inhibition of early, late or recycling endosome by overexpression of the mCherry-tagged dominant-negative mutants of RAB5, RAB7 and RAB11 did not show any statistically significant effect on centrosomal EGFP-RAB8A localization in RPE1 cells at any point in time investigated.

To analyze the influence of early, recycling and late endosomes on ciliogenesis in general without overexpression of RAB8A, wild-type RPE1 cells were transiently transfected with expression plasmids containing the cDNA of either the EGFP-tagged constitutive inactive (GDP-bound) mutant of RAB5 (Stenmark *et al.* 1994) or RAB7 (Feng *et al.* 1995) or RAB11 (Ullrich *et al.* 1996) or EGFP as a control in wild-type RPE1 cells.

No localization of EGFP-tagged RAB mutants at the primary cilium was observed (Fig. 17A). The percentage of all transfected RPE1 cells with an ARL13B-positive cilium continuously increased during 24 h of serum starvation for all proteins investigated reaching an average value of ~54% for only EGFP expressing cells (control) at the end of the experiment.

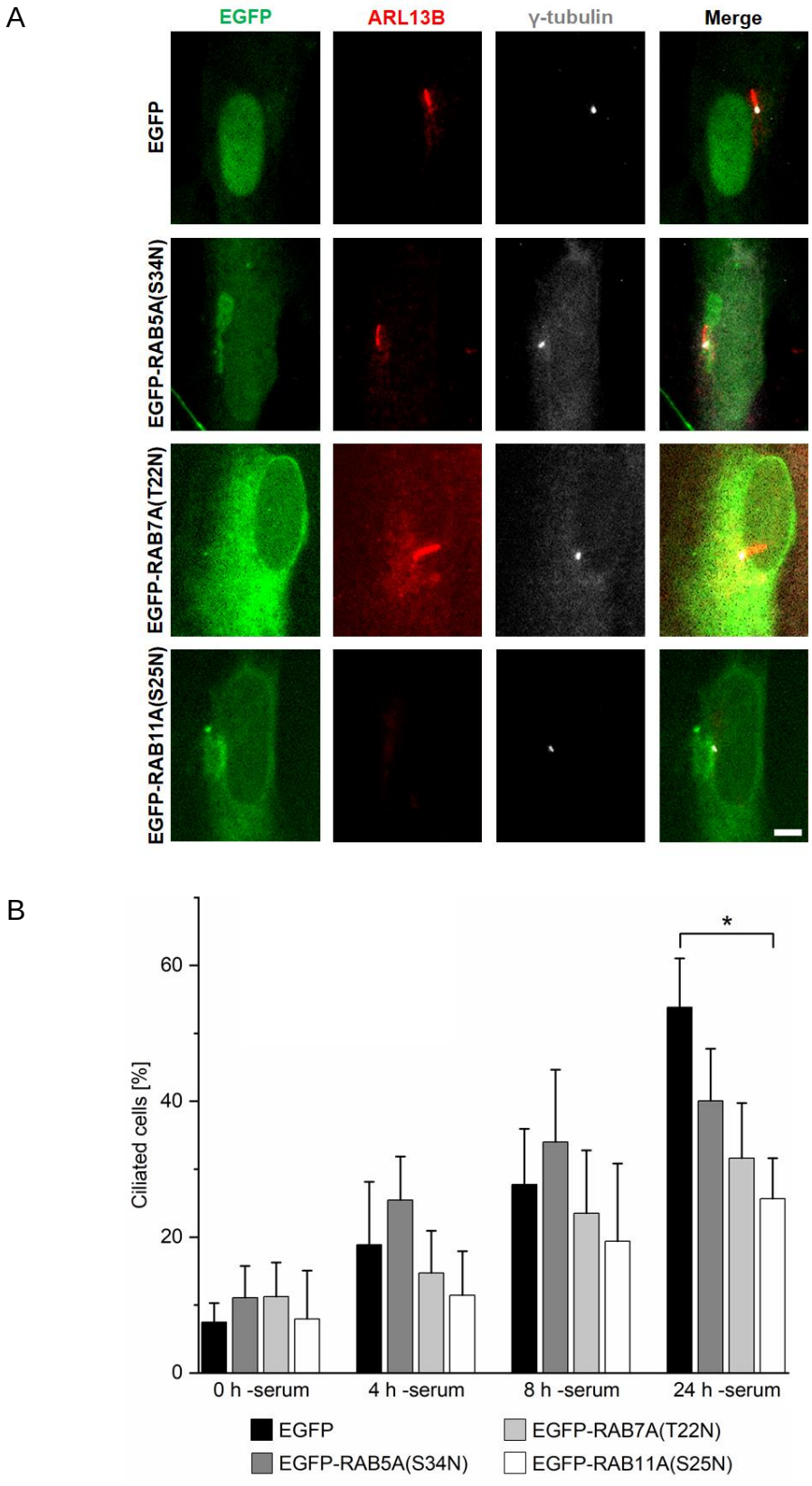

Figure 17: Inhibition of ciliogenesis by overexpression of the dominant-negative mutant EGFP-RAB11A(S25N) in RPE1 cells. Wild-type RPE1 cells were transiently transfected with an expression plasmid containing either the

cDNA of EGFP or EGFP-RAB5A(S34N) or EGFP-RAB7A(T22N) or EGFP-RAB11A(S25N), serum starved for the indicated points in time one day after transfection, fixed and stained for cilia (red) with an antibody against ARL13B (Caspary *et al.* 2007) as well as for centrioles (white) with an antibody against γ-tubulin (Fuller *et al.* 1995). (A) Examples of fluorescence images of cells expressing the indicated proteins after 24 h of serum starvation. Bar, 5 µm. (B) Quantification of (A). The percentage of transfected RPE1 cells with an ARL13B-positive cilium was calculated. Three independent experiments with between 71 and 194 cells per experiment and condition. Statistical significance is indicated by an asterisk.

The percentage of ciliated EGFP-RAB11A(S25N) expressing RPE1 cells was lower compared to only EGFP expressing RPE1 cells at any point in time investigated and the difference reached statistical significance at 24 h of serum starvation with ~26% compared to ~54% (Fig. 17B). The percentage of ciliated EGFP-RAB7A(T22N) expressing RPE1 cells was slightly reduced compared to only EGFP expressing RPE1 cells at 4 h, 8 h and 24 h of serum starvation but the difference did not reach statistical significance. Surprisingly the percentage of ciliated EGFP-RAB5A(S34N) expressing RPE1 cells was even slightly increased compared to only EGFP expressing RPE1 cells at 0 h, 4 h and 8 h of serum starvation but the difference did not reach statistical significance (Fig. 17B). In summary our data indicate a role of the recycling endosome during ciliogenesis which is in line with previous work (Knödler *et al.* 2010; Westlake *et al.* 2011).

3.6 Ultrastructural visualization of the ciliary membrane

For the outgrowth of primary cilia and maintaining its function, a large variety of molecules especially signaling receptors and lipids are required (Witzgall 2018b). Entering the primary cilium requires " gating […] a diffusion barrier mechanism" (Reiter *et al.* 2012) at the ciliary base for all molecules except small soluble proteins up to ~40 kDa (Garcia-Gonzalo & Reiter 2012; Nachury *et al.* 2010; Pedersen *et al.* 2012; Reiter *et al.* 2012; Rohatgi & Snell 2010). As the ciliary membrane is "continuous with the plasma membrane" (Porter 1957) the nature and ultrastructural location of this diffusion barrier is largely unknown; reviewed in (Nachury *et al.* 2010; Satir 2017). Therefore an experimental design was established to visualize the ciliary membrane (Garcia *et al.* 2018; Nachury *et al.* 2010) on an ultrastructural level.

3.6.1 Generation of an LLC-PK$_1$ cell line constitutively producing HRP-SmoM2-EGFP

As the "constitutively active M2 mutant of [the seven-transmembrane protein] Smoothened" (Hoffmeister *et al.* 2011) localizes to primary cilia also without activation of the Hedgehog

pathway (Corbit *et al.* 2005) we used this mutant as marker protein for the ciliary membrane during the present study. The COOH-terminus of SmoM2 was tagged with EGFP for visualizing the protein by fluorescence microscopy (Fig. 18A). In order to depict the protein by electron microscopy as well, SmoM2 was additionally tagged with *horseradish peroxidase* (HRP). HRP is able to initiate the polymerization of 3,3´-Diaminobenzidine resulting in local precipitation of an osmiophilic polymer (Connolly *et al.* 1994; Graham & Karnovsky 1966); reviewed in (Lam *et al.* 2015; Perkins 2014; Witzgall 2018b). Electron density of this polymer is generated by incubation with an aqueous OsO_4 solution (Connolly *et al.* 1994; Graham & Karnovsky 1966); reviewed in (Lam *et al.* 2015; Perkins 2014).

As it is known that HRP shows no enzymatic activity within a cytosolic environment (Lam *et al.* 2015; Martell *et al.* 2012; Martell *et al.* 2017), the cDNA of HRP was inserted into the cDNA of SmoM2 in between the base pairs encoding for the signal sequence for "protein translocation into the endoplasmic reticulum" (Zimmermann *et al.* 2011) and the first transmembrane domain of SmoM2 (Fig. 18B), i.e. HRP faced the extracellular site of the membrane. By flanking both the NH_2- and COOH-terminus of HRP with flexible linker sequences, HRP was separated from SmoM2 resulting in proper folding of the peroxidase (Fig. 18B). The idea to add such flexible linker sequences as well as their amino acid sequences (slightly modified in the present work) were taken from Martell *et al.* 2017. Having generated a DNA plasmid encoding for a fusion protein of SmoM2 with HRP and EGFP as described above an LLC-PK_1 cell line constitutively producing HRP-SmoM2-EGFP was generated within cells following the extracellular pathway of ciliogenesis (Breslow & Holland 2019; Miyamoto *et al.* 2019). The cell line was characterized by fluorescence microscopy and Western blot analysis (Fig. 18A-C). Almost all LLC-PK_1 cells showed an EGFP-positive cytoplasm and many (extent was not quantified) an EGFP signal co-localizing with the anti-ARL13B staining therefore representing EGFP-positive cilia (Fig. 18A). Ciliary EGFP signals were bright enough to be detected by eye piece of the fluorescence microscope indicating high expression levels of the fusion protein which is important for detectability of the subsequent histochemical reaction on electron micrographs (see section 3.6.2). Western blot analysis also reveals a specific band at a molecular mass corresponding to that of the HRP-SmoM2-EGFP protein (~152 kDa) (Fig. 18C).

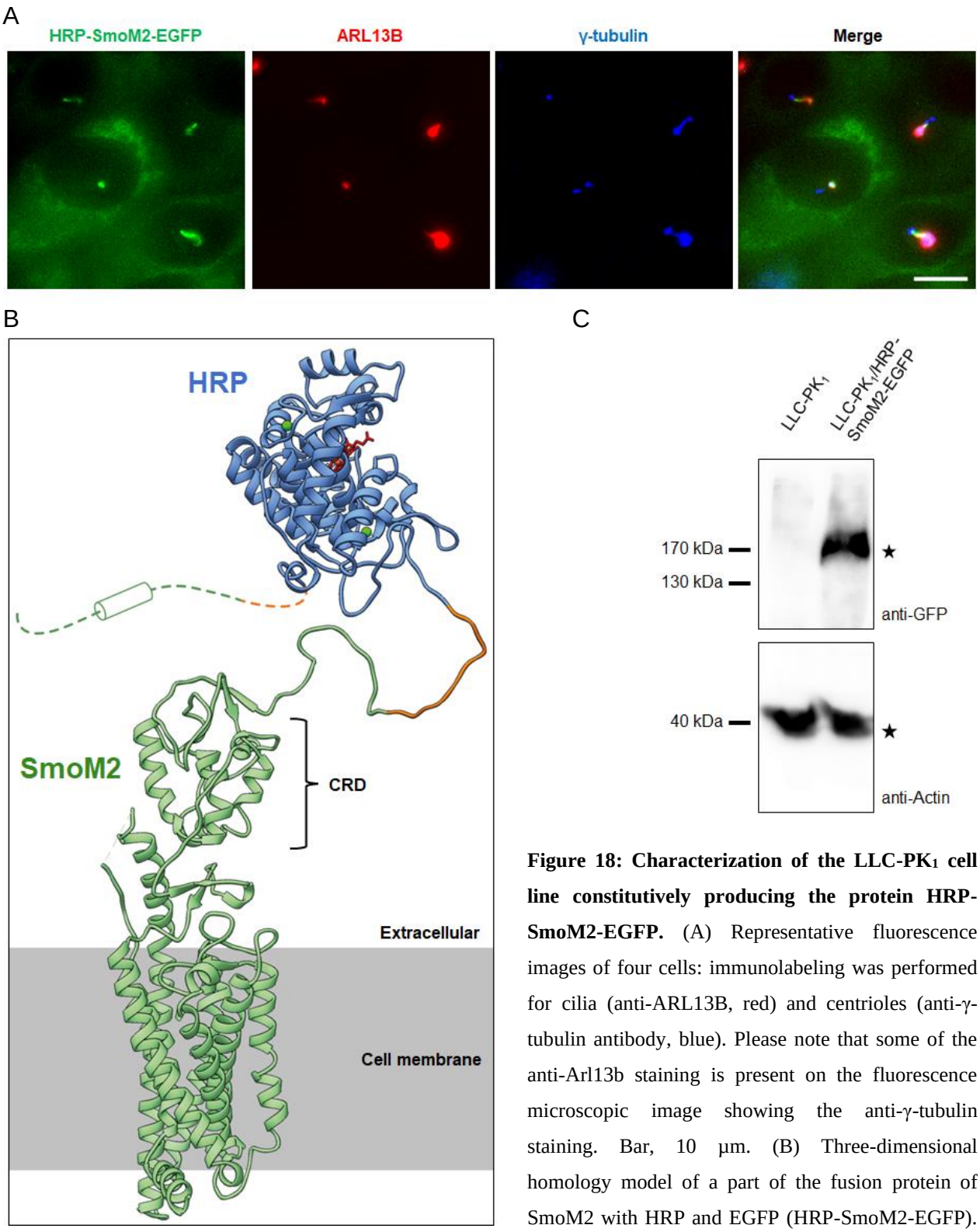

Figure 18: Characterization of the LLC-PK$_1$ cell line constitutively producing the protein HRP-SmoM2-EGFP. (A) Representative fluorescence images of four cells: immunolabeling was performed for cilia (anti-ARL13B, red) and centrioles (anti-γ-tubulin antibody, blue). Please note that some of the anti-Arl13b staining is present on the fluorescence microscopic image showing the anti-γ-tubulin staining. Bar, 10 µm. (B) Three-dimensional homology model of a part of the fusion protein of SmoM2 with HRP and EGFP (HRP-SmoM2-EGFP). The NH_2-terminal region of SmoM2 as well as the linker at the NH_2-terminus of HRP were not modeled due to the lack of suitable templates but instead indicated as dashed lines and the predicted helix as cylinder. The intracellular COOH-terminal region of SmoM2 as well as the cytosolic EGFP tag of the fusion protein are not shown. Green: SmoM2; blue: HRP; red: heme group; neon green dots: Ca^{2+}; orange: linker sequences; gray: cell membrane. The

cysteine-rich domain (CRD) of SmoM2 is marked analogous to Deshpande *et al.* 2019. A movie of the 3D homology model can be found in the supplement (see SFig. 18B). (C) The LLC-PK_1 cell line constitutively producing the protein HRP-SmoM2-EGFP was subjected to Western blot analysis along with wild-type LLC-PK_1 cells as a control. Proteins were detected with the indicated antibodies. Anti-actin staining was used as loading control. Bands representing the fusion protein HRP-SmoM2-EGFP (~152 kDa) and actin (~41 kDa) were marked with asterisks. Uncropped Western blot images can be found in the supplement (see SFig. 18C).

In addition to visualizing the expression of the HRP-SmoM2-EGFP protein by fluorescence microscopy and Western blot analysis we verified its enzymatic activity in the present setup using the Amplex UltraRed reagent (Fig. 19) as "Amplex UltraRed labeling" (Martell *et al.* 2017) has already been used successfully several times in literature (Lam *et al.* 2015; Martell *et al.* 2012; Martell *et al.* 2017). Peroxidases like HRP convert the non-fluorescent Amplex UltraRed into the red fluorescent resorufin upon H_2O_2 addition (Martell *et al.* 2017). Whereas most LLC-PK_1 cells constitutively producing HRP-SmoM2-EGFP were able to generate a bright red fluorescent resorufin signal especially within their cytoplasm upon H_2O_2 addition, wild-type LLC-PK_1 cells as negative control showed hardly detectable fluorescence signals (Fig. 19). Incubating LLC-PK_1 cells constitutively producing HRP-SmoM2-EGFP without H_2O_2 addition resulted in an almost undetectable amount of resorufin production as well (Fig.19). Since contrast and brightness of fluorescence images was adjusted equally in Figure 19 it was not possible to visualize these weak resorufin signals. Resorufin-positive cilia were not detected at any circumstances. Martell *et al.* 2017 already mentioned that resorufin is not "strictly localized to the membrane" (Martell *et al.* 2017) of its origin. Since HRP faces the extracellular side of the ciliary membrane within our setup, resorufin could have diffused away and/or be washed out before mounting the cells for fluorescence microscopy. It has to be mentioned that during the present study there were some further Amplex UltraRed experiments in which resorufin signals started arising also for negative controls (e.g. H_2O_2 omission) within the first seconds of illumination by fluorescence microscopy. Resorufin intensity increased the longer the cells were irradiated.

In summary we generated an LLC-PK_1 cell line constitutively producing a fusion protein of the "constitutively active M2 mutant of Smoothened" (Hoffmeister *et al.* 2011) with HRP and EGFP and we were able to demonstrate the ciliary localization of this fusion protein as well as enzymatic activity of HRP within the cellular context.

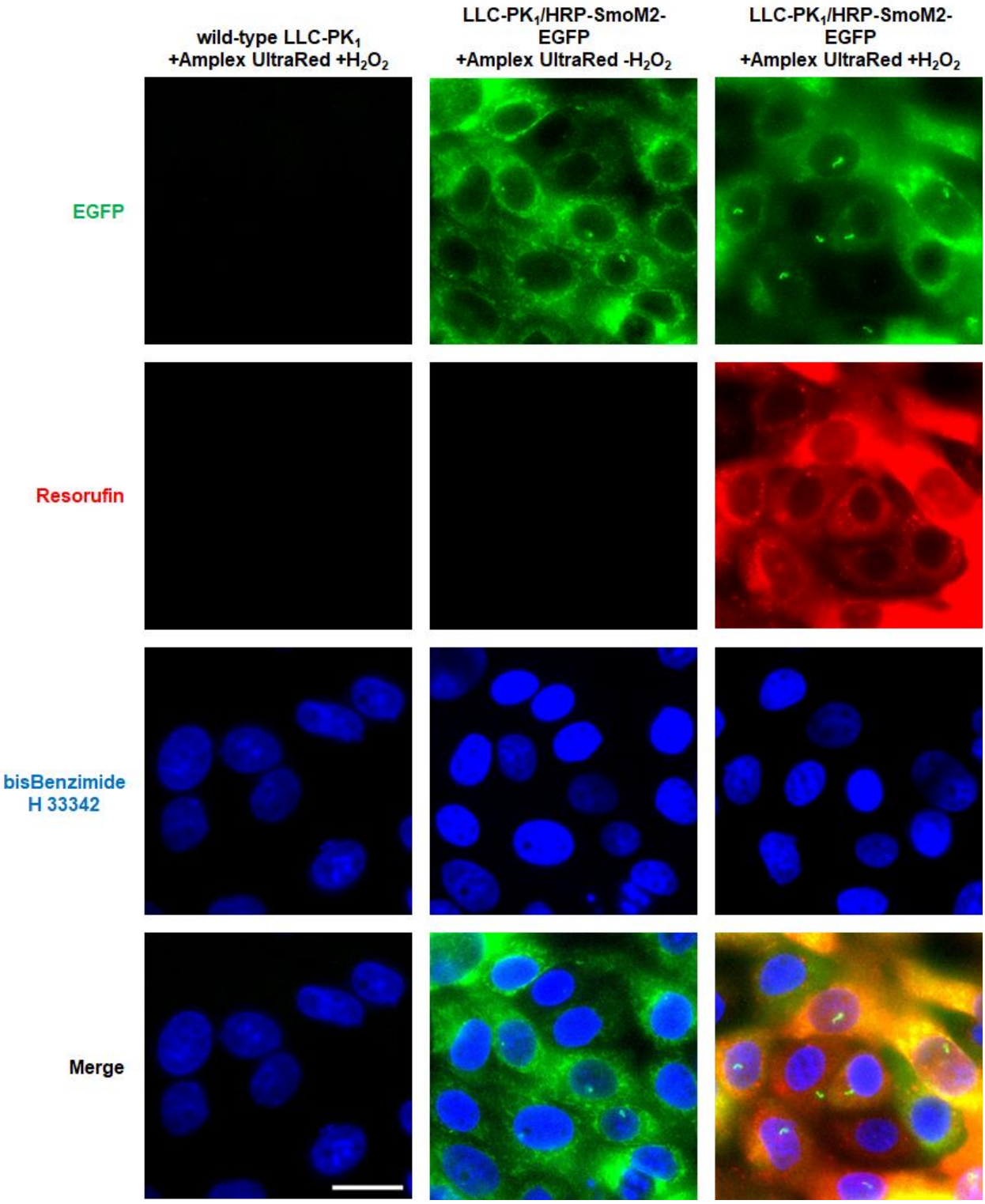

Figure 19: Peroxidase activity evaluation of HRP-SmoM2-EGFP in LLC-PK$_1$ cells using the Anplex UltraRed reagent. LLC-PK$_1$ cells constitutively producing the protein HRP-SmoM2-EGFP as well as wild-type LLC-PK$_1$ cells were fixed using formaldehyde, the nuclei were stained with bisBenzimide H 33342 and cells were incubated in a solution consisting of 50 µM Amplex UltraRed either with or without the addition of ~6.7 mM H_2O_2 for 30 min. Shown

are fluorescence images of representative cells. Figure design is based on Supplementary Fig. 4C from Lam *et al.* 2015. Bar, 20 µm.

3.6.2 The constitutive active M2 mutant of murine Smoothened is present at the ciliary and periciliary membrane

To localize the transition from the ciliary to the plasma membrane we visualized the distribution of the HRP-SmoM2-EGFP protein on an ultrastructural level within the cellular context by electron microscopy. Therefore LLC-PK_1 cells constitutively producing the protein HRP-SmoM2-EGFP (see chapter 3.6.1) as well as wild-type LLC-PK_1 cells as a control were fixed, incubated in a solution consisting of 3,3´-Diaminobenzidine in Tris-HCl buffer with or without the addition of H_2O_2 for 30 min and prepared for transmission electron microscopy. Electron micrographs of ultrathin Epon sections are shown in Figure 20.

For both control groups, i.e. incubation of wild-type LLC-PK_1 cells with H_2O_2 addition (Fig. 20A) or of LLC-PK_1 cells constitutively producing the protein HRP-SmoM2-EGFP without H_2O_2 addition (Fig. 20B), no Osmium-contrasted 3,3´-Diaminobenzidine polymer was detected at the ciliary membrane. However, LLC-PK_1 cells constitutively producing the protein HRP-SmoM2-EGFP showing an Osmium-contrasted 3,3´-Diaminobenzidine polymer at both the ciliary membrane and the membrane surrounding the basal body could be detected after incubation with H_2O_2 addition (Fig. 20C-E). This membrane region at the ciliary base is referred to as periciliary membrane in literature (Garcia-Gonzalo & Reiter 2012; Lee & Chung 2015; Long & Huang 2019). Ciliary and periciliary membrane with an Osmium-contrasted 3,3´-Diaminobenzidine polymer had a higher electron density compared to the rest of the plasma membrane or the ciliary membrane of both control groups (Fig. 20A-B). Furthermore, the Osmium-contrasted 3,3´-Diaminobenzidine polymer was inhomogeneously distributed with alternating more and less concentrated regions at the ciliary and periciliary membrane and its concentration decreased continuously along the periciliary membrane. Electron micrographs of Epon sections containing a large part of the primary cilium demonstrated that the Osmium-contrasted 3,3´-Diaminobenzidine polymer was present over a large area of the ciliary membrane (Fig. 20E). It has to be mentioned, however, that in some cases (extent was not quantified) there was no Osmium-contrasted 3,3´-Diaminobenzidine polymer within cells or at the ciliary membrane at all.

A

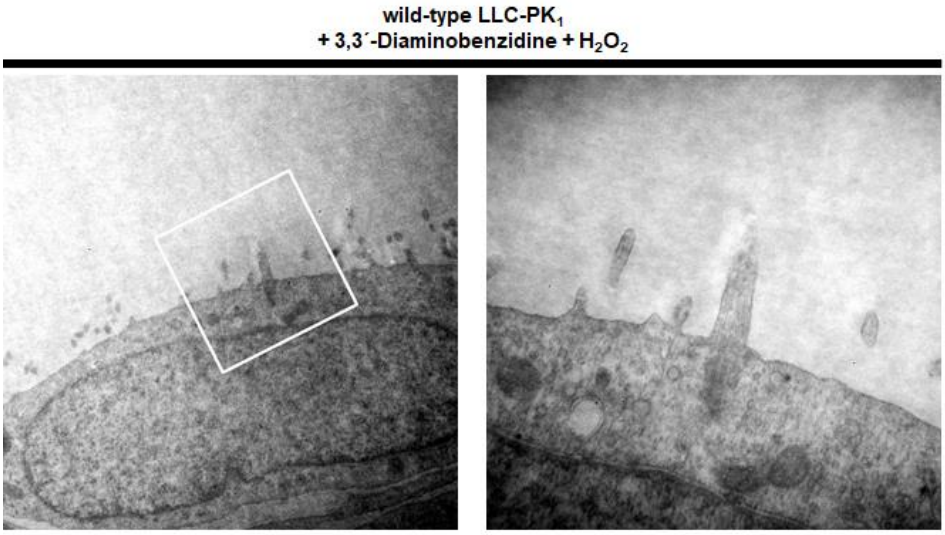

B

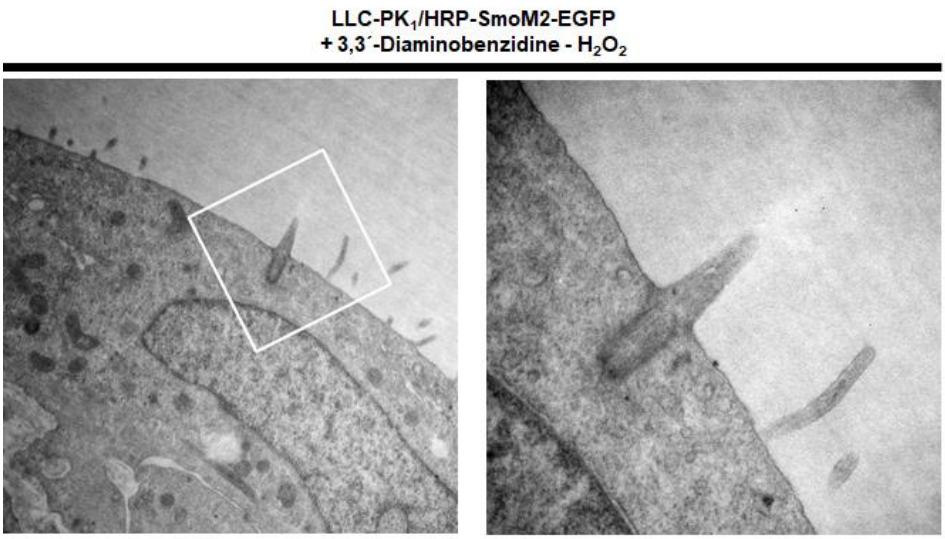

C

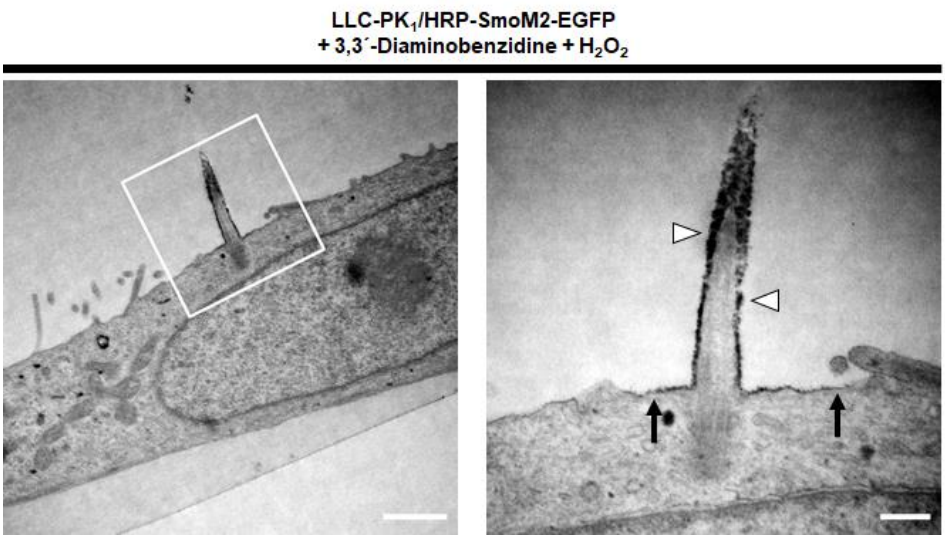

Figure 20: Ultrastructural localization of the HRP-SmoM2-EGFP fusion protein. Figure 20 to be continued on the next page.

D

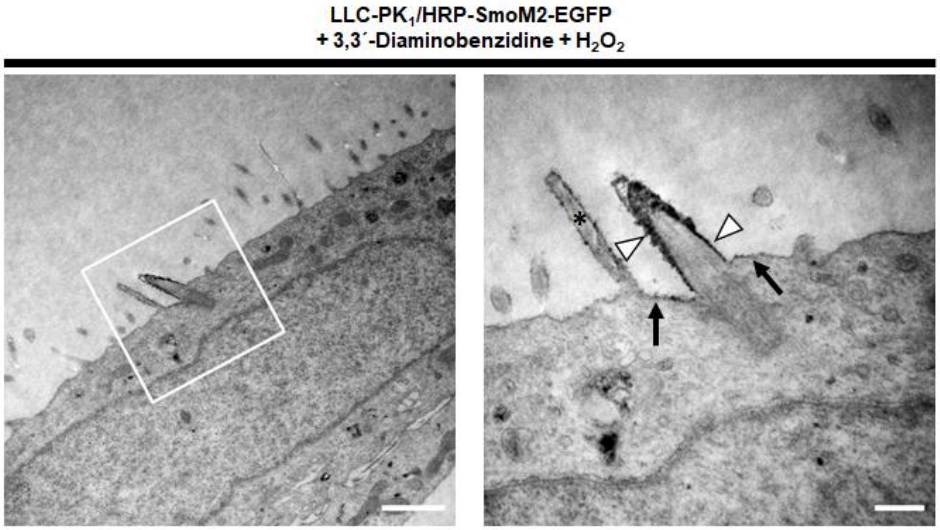

E

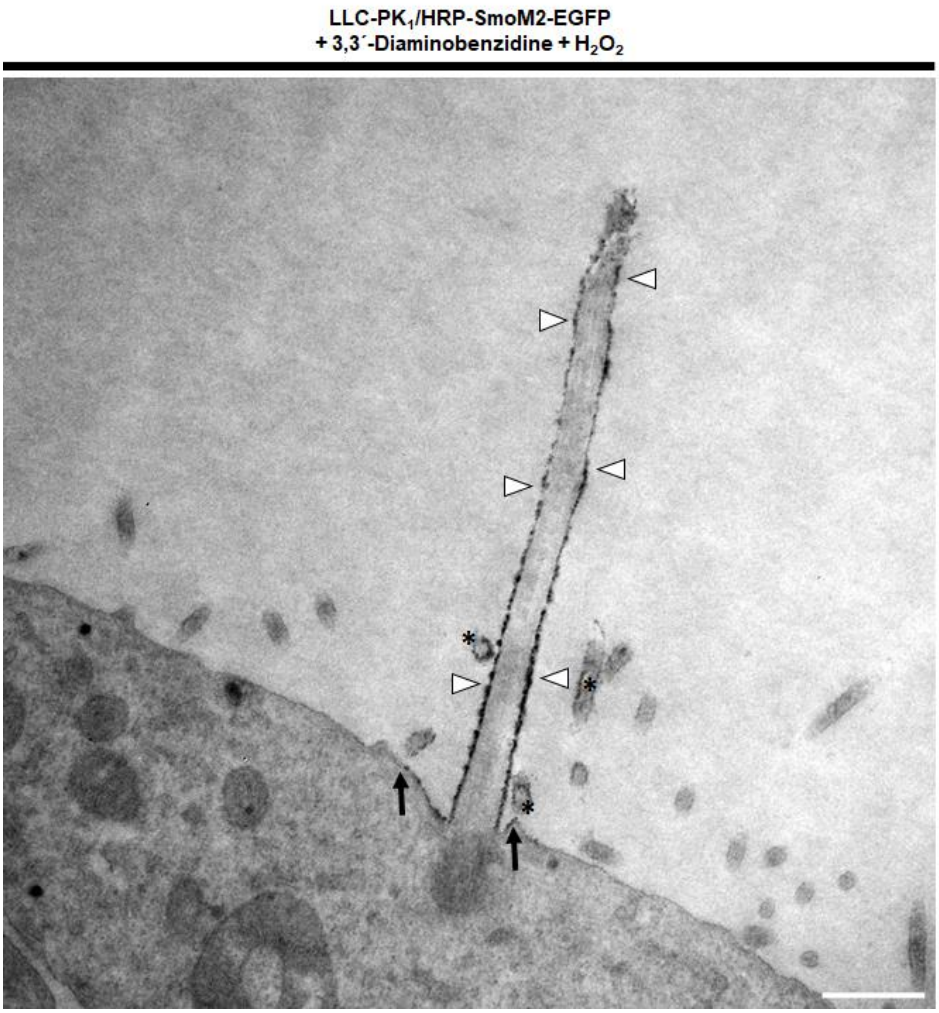

Figure 20: Ultrastructural localization of the HRP-SmoM2-EGFP fusion protein. LLC-PK_1 cells constitutively producing the protein HRP-SmoM2-EGFP as well as wild-type LLC-PK_1 cells as control were fixed using glutardialdehyde and incubated in 0.5 mg/ml 3,3´-Diaminobenzidine with or without the addition of H_2O_2 for 30 min. Cells were treated with a 1% OsO_4 solution, dehydrated and embedded in Epon. Ultrathin sections were generated and

imaged by electron microscopy. Shown are electron micrographs of representative cells (left images). At the ciliary region (marked with a white square) electron micrographs with higher magnification were recorded (right images). (A) Electron micrographs of a representative wild-type LLC-PK_1 cell incubated in a solution consisting of 3,3´-Diaminobenzidine with H_2O_2 addition. (B) Electron micrographs of a representative LLC-PK_1 cell constitutively producing the protein HRP-SmoM2-EGFP incubated in a solution consisting of 3,3´-Diaminobenzidine without H_2O_2. (C-E) Electron micrographs of three representative LLC-PK_1 cells constitutively producing the protein HRP-SmoM2-EGFP incubated in a solution consisting of 3,3´-Diaminobenzidine H_2O_2 addition. The Osmium-contrasted 3,3´-Diaminobenzidine polymer could be detected along the ciliary membrane enclosing the axoneme (arrowheads) as well as at the periciliary membrane. The region of the periciliary membrane at which the Osmium-contrasted 3,3´-Diaminobenzidine polymer terminates is marked by arrows. Non-ciliary cellular structures with an Osmium-contrasted 3,3´-Diaminobenzidine polymer at their membranes are marked with an asterisk. Bars, 1000 nm (left image column) and 250 nm (right image column) for (A-D), 500 nm for (E).

To measure the distance over which the Osmium-contrasted 3,3´-Diaminobenzidine polymer extended along the periciliary membrane we used ultrathin sections containing the ciliary base and showing a clearly contrasted ciliary membrane. One ultrathin section of each of 16 cells was analyzed. These 16 cells showed an Osmium-contrasted 3,3´-Diaminobenzidine polymer at the periciliary membrane extending over a mean distance of ~193 nm measured from the base of primary cilia. As there was no sharp border discernible but rather a continuous decline of the Osmium-contrasted 3,3´-Diaminobenzidine polymer along the periciliary membrane, measured values are based on estimates made by investigators. It has to be pointed out that diffusion of the Osmium-contrasted 3,3´-Diaminobenzidine polymer away from the site of its generation is a problem of this type of histochemical technique (Shu *et al.* 2011; Sosinsky *et al.* 2007). Indeed, we detected several cells in which the Osmium-contrasted 3,3´-Diaminobenzidine polymer looked like to have detached from the ciliary membrane and adhered to membranes of adjacent structures, e.g. microvilli (marked by asterisks in Fig. 20D-E).

Based on our ultrastructural investigation we could detect the HRP-SmoM2-EGFP protein at the ciliary and periciliary membrane demonstrating both membrane compartments are similar regarding the content of HRP-SmoM2-EGFP.

3.6.3 The constitutively active M2 mutant of Smoothened is not present at the Golgi apparatus

In a further step we searched for hints indicating which route the M2 mutant of Smoothened takes to the primary cilium. Investigating the ciliary ultrastructure Osmium-contrasted 3,3´-

Diaminobenzidine polymer was not only detected at the ciliary and periciliary membrane but also at the endoplasmic reticulum in several (extent not quantified) LLC-PK_1 cells constitutively producing the protein HRP-SmoM2-EGFP but not in wild-type LLC-PK_1 cells, i.e. the control group (Fig. 21).

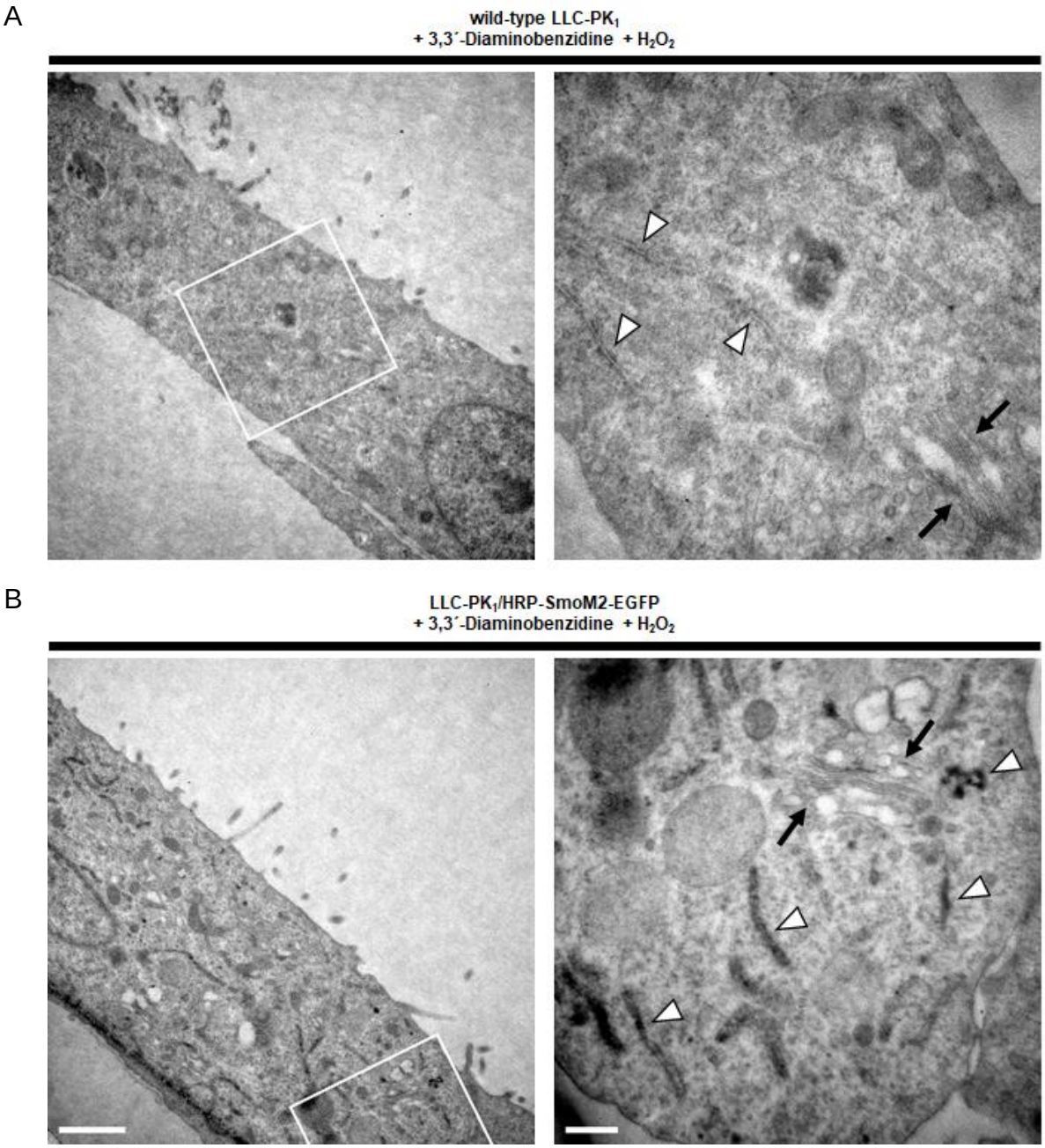

Figure 21: The constitutively active M2 mutant of Smoothened can be detected at the endoplasmic reticulum but not at the Golgi apparatus in LLC-PK_1 cells. Figure 21 to be continued on the next page.

C

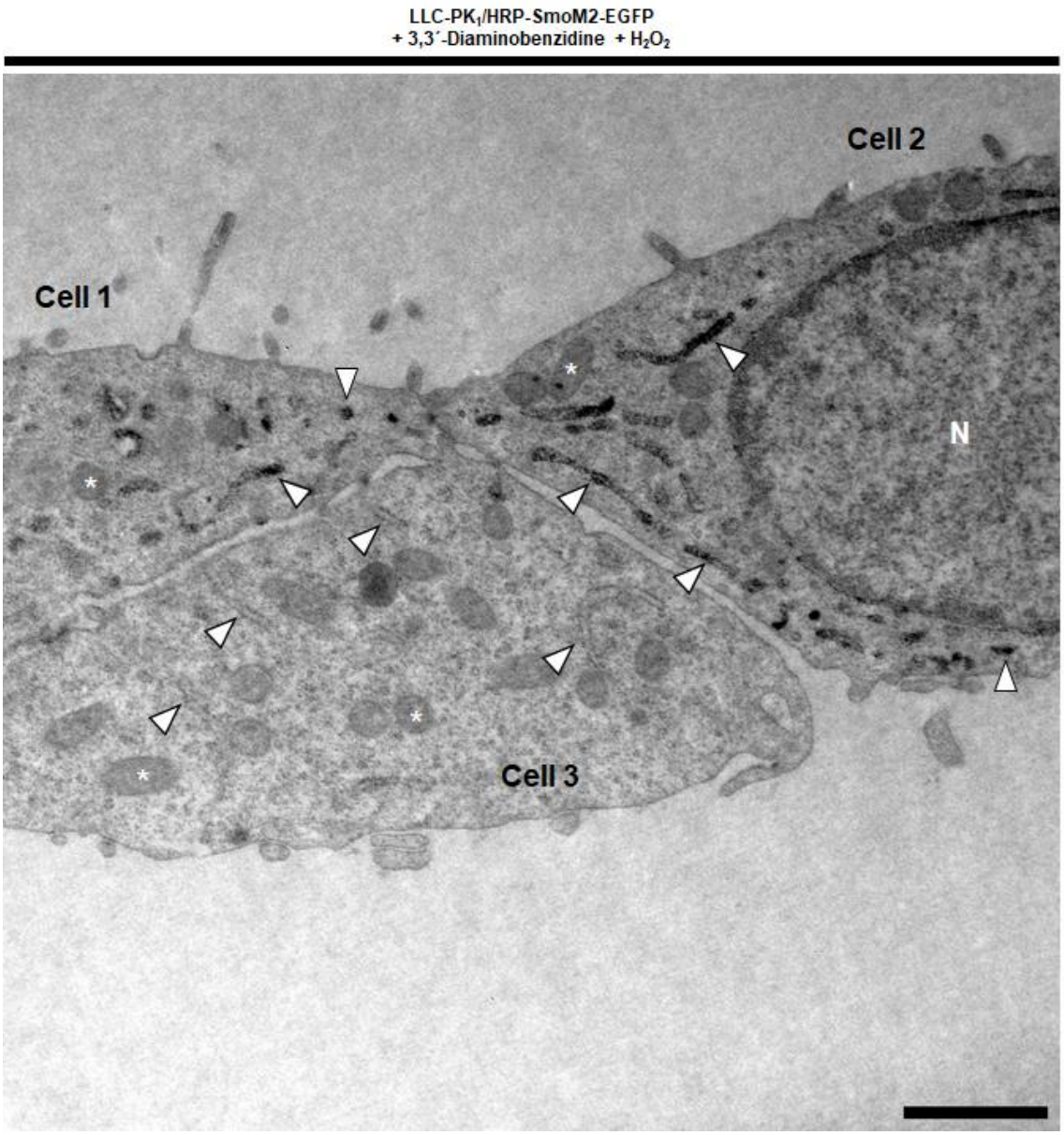

Figure 21: Enzymatic activity of the constitutively active M2 mutant of Smoothened can be detected at the endoplasmic reticulum but not at the Golgi apparatus in LLC-PK$_1$ cells. Shown are electron micrographs of cells that were processed together with those of Figure 20. At the region marked with a white square electron micrographs with higher magnification were recorded (right images). (A) Electron micrographs of a wild-type LLC-PK$_1$ cell incubated in a solution of 3,3´-Diaminobenzidine with H_2O_2 addition. (B-C) Electron micrographs of LLC-PK$_1$ cells constitutively producing the protein HRP-SmoM2-EGFP incubated in a solution with 3,3´-Diaminobenzidine with H_2O_2 addition. Golgi apparatus is marked by black arrows, the endoplasmic reticulum by arrowheads and mitochondria exemplary by asterisks. N= nucleus. Bar, 1000 nm (left image column), 250 nm (right image column) for (A-B), 1000 nm for (C).

The endoplasmic reticulum with Osmium-contrasted 3,3´-Diaminobenzidine polymer had a higher electron density compared to that one of wild-type LLC-PK1 cells. In some LLC-PK$_1$ cells

constitutively producing the protein HRP-SmoM2-EGFP large areas of high electron-dense endoplasmic reticulum were present and distributed over the entire cytoplasm of the cells (Fig. 21C: cell 1 and cell 2). It has to be mentioned that some LLC-PK_1 cells constitutively producing the protein HRP-SmoM2-EGFP had no Osmium-contrasted 3,3´-Diaminobenzidine polymer within their cytoplasm at all (Fig. 21C: cell 3).

In contrast, Osmium-contrasted 3,3´-Diaminobenzidine polymer at the Golgi apparatus was neither observed in LLC-PK_1 cells constitutively producing the protein HRP-SmoM2-EGFP nor in wild-type LLC-PK_1 cells (Fig. 21); i.e. even cells with Osmium-contrasted 3,3´-Diaminobenzidine polymer at the endoplasmic reticulum showed none at their Golgi apparatus (Fig. 21B).

The current work has two limitations: on the one hand we did not correlate these ultrastructural findings with the expression level of the HRP-SmoM2-EGFP protein visible by fluorescence intensity of the fusion protein during light microscopy. On the other hand we did not investigate whether LLC-PK_1 cells constitutively producing the protein HRP-SmoM2-EGFP and showing an Osmium-contrasted 3,3´-Diaminobenzidine polymer at the endoplasmic reticulum but not at the Golgi apparatus had one at their ciliary membrane as well. Considering all limitations our data indicate that the HRP-SmoM2-EGFP protein does not pass through the Golgi apparatus on its way to the primary cilium.

3.6.4 Ciliary pocket formation in LLC-PK_1 cells

An ultrastructural characteristic of the intracellular pathway of ciliogenesis is the formation of a ciliary pocket (Molla-Herman *et al.* 2010). However, Molla-Herman *et al.* 2010 already demonstrated that primary cilia of inner medullar collecting duct cells which follow the extracellular pathway of ciliogenesis can be partially embedded within the cell body as well.

In addition to Molla-Herman *et al.* 2010 we detected ciliary pockets in some LLC-PK_1 cells (extent was not quantified) during the present study (Fig. 22) although this polarized epithelial cell line follows the extracellular pathway (Breslow & Holland 2019; Miyamoto *et al.* 2019). Ciliary pockets were observed at both, a primary cilium of a wild-type LLC-PK_1 cell and at cilia of LLC-PK_1 cells constitutively producing the protein HRP-SmoM2-EGFP. As expected, for the wild-type LLC-PK_1 cell no Osmium-contrasted 3,3´-Diaminobenzidine polymer was visible whereas it could be detected in LLC-PK_1 cells constitutively producing the protein HRP-SmoM2-EGFP after incubation with 3,3´-Diaminobenzidine and H_2O_2 (Fig. 22B). Due to the close proximity of ciliary

and pocket membranes it was not possible to distinguish whether the Osmium-contrasted 3,3´-Diaminobenzidine polymer was present only at one or at both membrane compartments.

In combination with the findings of Molla-Herman *et al.* 2010 our data indicate that "ciliary pocket formation" (Rachel *et al.* 2015) can be found in several cell types following the extracellular pathway of ciliogenesis.

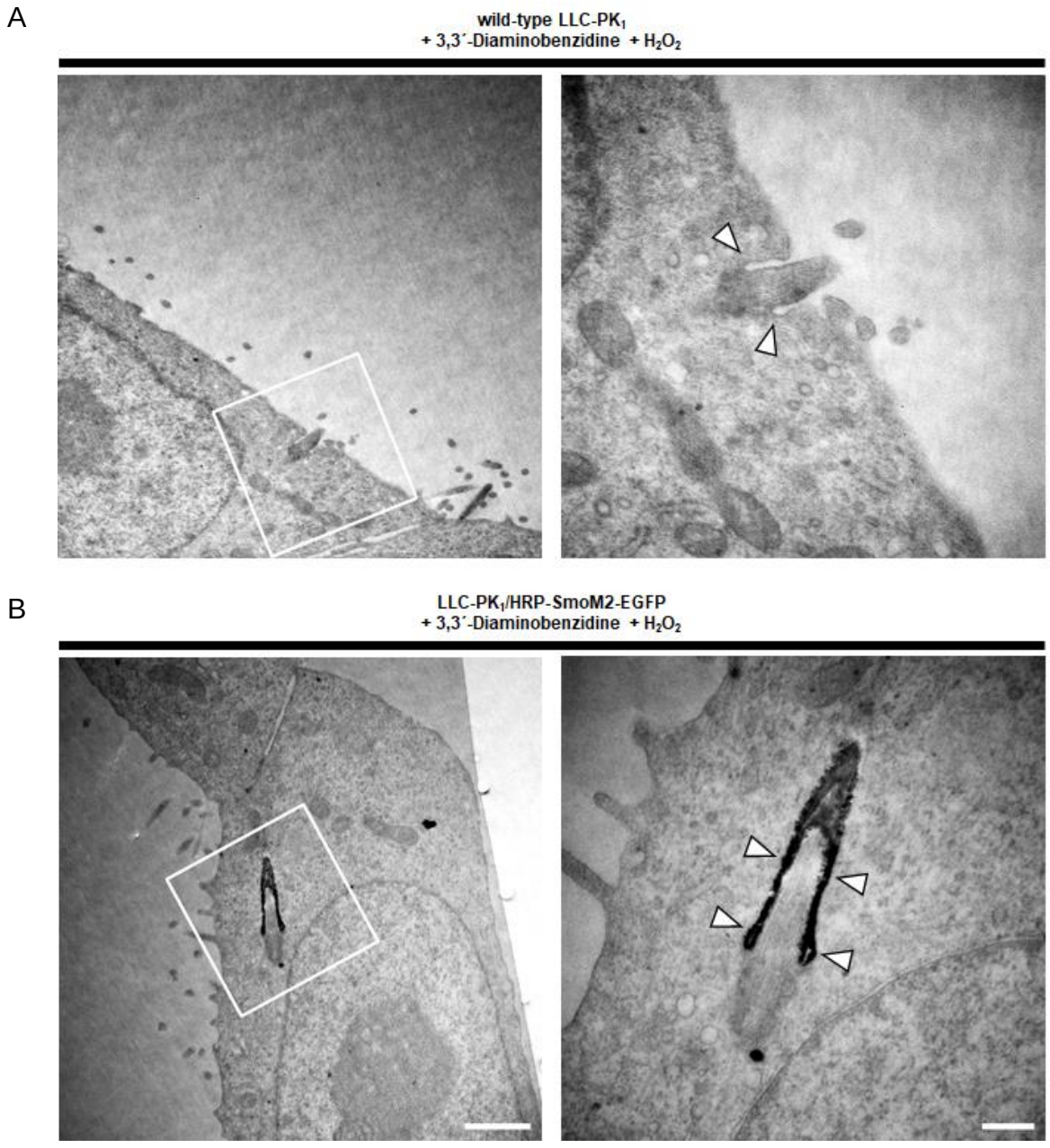

Figure 22: Ciliary pocket formation in LLC-PK$_1$ cells. Shown are electron micrographs of cells that were processed together with those of Figure 20. At the ciliary region (marked with a white square) electron micrographs with higher magnification were recorded (right images). (A) Electron micrographs of a wild-type LLC-PK$_1$ cell with ciliary pocket

incubated in a solution consisting of 3,3´-Diaminobenzidine with H_2O_2 addition. The cilium is partially embedded in the cell body (ciliary pocket marked by arrowheads). No Osmium-contrasted 3,3´-Diaminobenzidine polymer can be seen. (B) Electron micrographs of an LLC-PK_1 cell with ciliary pocket constitutively producing the protein HRP-SmoM2-EGFP incubated in a solution consisting of 3,3´-Diaminobenzidine with H_2O_2 addition. The proximal part of the cilium is embedded in the cell body and the Osmium-contrasted 3,3´-Diaminobenzidine polymer fills almost the entire ciliary pocket (arrowheads). Bar, 1000 nm (left image column), 250 nm (right image column).

4 Discussion

4.1 Correlative light and electron microscopy in cilia research

4.1.1 Combining on-section and pre-embedding techniques with STEM tomography

As summarized by Boer *et al.* 2015 CLEM techniques are very important for the biological field as they combine the advantages of both light and electron microscopy (Boer *et al.* 2015). For example the application of CLEM gained fundamental knowledge regarding the formation of primary cilia (Wu *et al.* 2018). There is a large number of different CLEM approaches and one has to find the technique most suited for his respective research (Buerger *et al.* 2021). Investigating the RAB8A recruitment to the basal body weak mCherry-RAB8A signals during the early stadia of ciliogenesis turned out to be the limiting factor in the present work. On-section CLEM enables the visualization of one and the same sample with both imaging modalities (Buerger *et al.* 2021; Kukulski *et al.* 2011, 2012; Santarella-Mellwig *et al.* 2018). However, as already shown (Buerger *et al.* 2021; Kukulski *et al.* 2012) sample preparation for electron microscopy results in a noticeable reduction of fluorescence of EGFP and in the context of the current study of mCherry as well. In addition, there was a loss of cells during sample preparation in the present work. Taken these circumstances together on-section CLEM proved impractical to investigate the centrosomal recruitment of mCherry-RAB8A during ciliogenesis. Instead we applied a so-called pre-embedding technique (Bykov *et al.* 2016). Applying an initial fixation step with formaldehyde allowed to detect even weak fluorescence signals whereas the fixation with glutardialdehyde carried out after fluorescence microscopy preserved the cellular ultrastructure.

One disadvantage of this type of pre-embedding CLEM technique, however, is that after chemical fixation cells are not imaged in their native state (McDonald 2009). In contrast cryoimmobilization results in less artifacts (McDonald 2009). Based on this finding it would be necessary to prove that the ultrastructural stadia of ciliogenesis described in the current study – and in particular the donut-like stadium – can be visualized after e.g. high-pressure freezing as well. Comparing chemical fixation with formaldehyde and high-pressure freezing we were able to show that the fixation method has an influence on the preservation of the ultrastructure of membranous compartments such as the Golgi apparatus, the mitochondria or the nuclear envelope but not on the preservation of the ultrastructure of ciliary membranes (Buerger *et al.* 2021). The ciliary membrane and the

sheath membrane which surrounds the cilium (Benmerah 2013; Sorokin 1962) but also the microtubule core (in particular the basal body) of primary cilia are comparably preserved both after chemical fixation and after high-pressure freezing (Buerger *et al.* 2021). For this reason we omitted an additional experiment to visualize the donut-like stadium of ciliogenesis after high-pressure freezing.

Another challenge in performing CLEM experiments is the generation of an accurate and unbiased overlay of fluorescence and electron microscopic data (Buerger *et al.* 2021). We demonstrated that on-section CLEM is an elegant method to achieve this even with resin sections with an estimated actual thickness of ~770 nm (Buerger *et al.* 2021). On the one hand fluorescence microscopic image and electron tomogram are acquired from one and the same object (Buerger *et al.* 2021). On the other hand fluorescent and electron-dense particles can be applied to resin sections and thus serving as fiducials for the overlay generation if internal landmarks are not sufficient (Buerger *et al.* 2021). There are different types of particles available, for sections up to a nominal thickness of ~300 nm e.g. FluoSpheres (Kukulski *et al.* 2011), for thicker sections particles with a more electron-dense core as e.g. fluorescently labeled gold nanoparticles (Buerger *et al.* 2021; Fokkema *et al.* 2018). Applying these fiducials we even assign fluorescence signals of proteins present in multi-copy organelles such as the fibroblast growth factor receptor 1 to their corresponding structures in electron tomograms (Buerger *et al.* 2021). However, overlay generation of pre-embedding CLEM experiments is less straight forward and more time consuming than those during on-section CLEM (Bykov *et al.* 2016). In a first step we verified that it is possible to generate overlays of single-copy organelles such as the primary cilium without additional fluorescent fiducial markers (Buerger *et al.* 2021). Next we adapted this workflow of overlay generation initially established during on-section CLEM experiments to our pre-embedding CLEM experiments. In a multi-step procedure the gridded pattern of the MatTek cell culture dishes and the position of the cells in relation to each other were used to find the cell of interest back during electron microscopy. Using the cell shape as well as the orientation and shape of its nucleus in combination with the position of the centrosome the cell of interest was oriented in the same way on fluorescence and electron microscopic images. Finally the Centrin1-EGFP signal in combination with the two centrioles was sufficient to assign the mCherry-RAB8A signal to its respective structure in STEM tomograms in the majority of cases. However, in ~28.9% of the overlays of STEM tomograms the mCherry-RAB8A signal did not overlay with the structure(s) docked to the distal appendages of the basal

body. There are several disadvantages of the pre-embedding technique without additional fluorescent fiducial markers which could be responsible for this discrepancy. As sample preparation for electron microscopy was carried out after fluorescence microscopy, sample deformation could have occurred prior to electron microscopy (Bykov *et al.* 2016). In addition, overlays themselves have a limited accuracy. For overlay generation the eC-CLEM software uses point pairs placed on one and the same object visible on both, the fluorescence and electron microscopic image (Paul-Gilloteaux *et al.* 2017). For a two-dimensional registration (*x* and *y* dimension) at least three point pairs are required (Paul-Gilloteaux *et al.* 2017). Since Centrin1-EGFP signals in combination with both centrioles were the only two fiducials for overlay generation, several point pairs were placed on one Centrin1-EGFP signal/centriole. This involves considerable user bias and results in impaired reproducibility in some cases. Furthermore, in contrast to additionally applied fluorescent fiducial markers which are equally distributed over the entire resin section, centrosomes are only present at one place within a tomographed region resulting in insufficient correlation accuracy in some cases. Finally the limited resolution in *z* dimension of widefield fluorescence microscopy (Inoué 2006) used in the present study is an issue. Based on the equation from Inoué 2006 there is a maximum axial resolution of ~1 µm for mCherry signals with the current setup (1.3 numerical aperture objective, immersion oil with a refractive index of 1.518, excitation wavelength of ~560 nm). Please note that resin sections with a nominal thickness of ~600 nm were generated and the dimensions of a centriole are ~250 nm in diameter and ~500 nm in length (Winey & O'Toole 2014). Therefore due to limited axial resolution of fluorescence microscopy (~1 µm for mCherry in our setup) it is not possible to clarify whether the cellular structure responsible for the mCherry signal is located within the same *xy* planes of the STEM tomogram as the basal body although *z* stacks were recorded during fluorescence microscopy and only cells were selected with an mCherry-RAB8A signal in the same focal plane as the Centrin1-EGFP signal.

In general there are two options for further optimizing our overlay generation procedure to achieve a more accurate localization of the mCherry-RAB8A signal within STEM tomograms: fluorescently labeled gold nanoparticles – fiducials for overlay generation in combination with thick resin sections – can be endocytosed by cells and also embedded in Epon (Fokkema *et al.* 2018). Therefore these nanoparticles would not only be suitable as fiducials for on-section CLEM but also during pre-embedding CLEM experiments. However, endocytosis of particles is a cell

manipulation. Additionally, a huge amount of nanoparticles would have to be endocytosed so that the volume to be tomographed – currently ~2.7 µm in *x* and *y* and limited by the nominal section thickness in *z* – contains a sufficient number of particles for overlay generation. Finally, the main problem is that currently available fluorescently labeled gold nanoparticles are unsuitable for use in combination with mCherry: the nanoparticles are coupled with rhodamine B, a dye that has an excitation and emission spectrum similar to mCherry (Cranfill *et al.* 2016; Fokkema *et al.* 2018). Therefore new particles coupled with different dyes would have to be synthesized at first which in principle is possible (Fokkema *et al.* 2018) but requires a substantial amount of work. Another technique for the investigation of rare cellular events is the triCLEM method (Ader & Kukulski 2017). After cryoimmobilization fluorescence microscopy is performed under cryogenic condition to screen for cells showing rare events (e.g. early stadia of ciliogenesis during the present study) (Ader & Kukulski 2017). This first screening step is possible due to reduced photobleaching of fluorescent proteins at cryogenic temperatures (Ader & Kukulski 2017). Next cells are embedded according to the *Kukulski method*, fluorescent fiducial markers "are applied to the resin sections" (Buerger *et al.* 2021) and then a second fluorescence microscopic evaluation takes place at room temperature (Ader & Kukulski 2017). Precise overlays with electron microscopic data can be generated using this triCLEM method (Ader & Kukulski 2017). However, this technique results in two major problems in combination with our CLEM experiments: the aforementioned loss of RPE1 cells during high-pressure freezing with the EM PACT2 (Leica Microsystems GmbH, Wetzlar, Germany) and/or sample preparation for electron microscopy and the fact that mCherry-RAB8A signals are so weak during early stadia of ciliogenesis that we cannot preserve them during resin embedding. A more modern high-pressure freezing machine (e.g. HPF Compact 03, Engineering Office M. Wohlwend GmbH, Sennwald, Switzerland) and an expensive cryo-fluorescence microscope (Schorb *et al.* 2017) would be necessary to minimize these problems. Thus the triCLEM method is no direct option to our current CLEM approach, it rather has to be modified/adapted. In summary despite its limitations, the pre-embedding CLEM approach used in the present work is currently the most suited method to investigate the centrosomal recruitment of mCherry-RAB8A during ciliogenesis.

We successfully expanded the field of CLEM techniques by combining fluorescence microscopy with bright-field STEM tomography with "a semi-convergence angle of 1.46 mrad" (Rachel *et al.* 2020) (Buerger *et al.* 2021). As mentioned in our publication (Buerger *et al.* 2021), Ader and

Kukulski were the first to apply STEM tomography during CLEM experiments; however, these authors did not exploit the full potential of STEM tomography in terms of section thickness (Ader & Kukulski 2017). Rachel *et al.* 2020 demonstrated that using STEM tomography the three-dimensional visualization of resin sections with a nominal thickness of up to 900 nm is possible while maintaining the high resolution of conventional electron tomography in the *z* dimension (~5 nm) (Rachel *et al.* 2020). This was possible as there is no chromatic aberration in STEM and because the depth of focus could be increased by reducing the semi-convergence angle to 1.46 mrad (Rachel *et al.* 2020). Implementing this type of STEM tomography in a conventional 200 kV transmission electron microscope (Rachel *et al.* 2020) enables its combination with all CLEM techniques established for transmission electron microscopy without modifying the sample preparation procedure (Buerger *et al.* 2021). Therefore STEM tomography could be used for on-section CLEM (Buerger *et al.* 2021) as well as pre-embedding CLEM experiments during the current work. This CLEM-STEM technique is particularly helpful in visualizing the ultrastructure of primary cilia (Buerger *et al.* 2021) as well as the processes contributing to their formation as cilia are large "structures with about 300nm in diameter and up to several micrometers in length" (Buerger *et al.* 2021). Generating and imaging thicker resin sections increases the possibility that centrosomal and ciliary structures are present in one section. This proved to be an advantage especially in combination with RPE1 cells since in the majority of cases the centrosomes and primary cilia were contained in the first few sections cut in parallel to the surface of resin blocks after removing the glass substratum on which the cells were cultured. This simplified and accelerated the workflow.

"The main advantage of STEM" (Rachel *et al.* 2020) tomography in investigating ciliogenesis, however, is a high resolution in the *z* dimension (~5 nm) of a volume of several hundred nanometers (Rachel *et al.* 2020). Up to now CLEM experiments to study ciliogenesis were mainly performed using serial ultrathin or thin sections (Lu *et al.* 2015; Wu *et al.* 2018) which results in a poorer depth resolution (McEwen & Marko 1999). The more limited resolution in *z* dimension of "serial section reconstruction" (McEwen & Marko 1999) compared to STEM tomography could be a reason why the donut-like stadium of ciliogenesis has not yet been identified. In addition, this stadium can easily be misinterpreted as a distal appendage vesicle structure or a ciliary vesicle structure as it looks identical to both stadia depending on the *xy* plane examined. Only if the entire

membrane structure docked to the distal appendages of the basal body is contained in one tomogram the donut-like structure can be unambiguously identified (see Fig. 14A).

A limitation of STEM tomography, however, is that the volume to be tomographed is restricted, in our case currently to ~2.7 µm each in *x* and *y* dimension as well as to a nominal section thickness of ~0.9 µm (Rachel *et al.* 2020). As larger structures extending over several micrometers can not be visualized in one tomogram so far, we are working on extending especially the *x* and *y* dimensions of one single STEM tomogram up to ~5 µm each. However, with the current configuration (status September 2020), it was not possible to visualize tubules originating from the membrane structures docked to the distal appendages of the basal body along their entire length. Insinna *et al.* 2019 who first described these "membrane tubules" (Insinna *et al.* 2019) used focused ion beam scanning electron microscopy during CLEM experiments to demonstrate that these tubules, which form very early during ciliogenesis ultimately gain contact to the plasma membrane to form "open channel[s] to the extracellular space" (Insinna *et al.* 2019). Nevertheless, applying our CLEM-STEM approach we were able to reproduce the results of Insinna *et al.* 2019, i.e. to confirm the existence of "membrane tubules" (Insinna *et al.* 2019). Moreover we showed that these tubules started already forming during the donut-like stadium of ciliogenesis (see Fig. 11F). Insinna *et al.* 2019 discovered the tubes not before the ciliary vesicle stadium (Insinna *et al.* 2019). It must be mentioned, however, that although we carried out no quantification, donut-like structures with "membrane tubules" (Insinna *et al.* 2019) were only found in exceptional cases during the current work. In contrast to Insinna *et al.* 2019 who observed a localization of the of RAB8A fused to Tag-red fluorescent protein we did not detect mCherry-RAB8A at these tubules. The function of these "membrane tubules" (Insinna *et al.* 2019) is still unknown. However, as they expose the cilium to the extracellular milieu (Insinna *et al.* 2019) they could be important for signaling pathways of primary cilia.

Compared to conventional TEM tomography, STEM tomography has a great potential for the three-dimensional visualization of the cellular ultrastructure. Cellular structures such as the donut-like structure during ciliogenesis which are difficult to identify using serial sections can be easily and unambiguously visualized by STEM tomography. If STEM is implemented in a transmission electron microscope (Rachel *et al.* 2020), as in our case, it is ideally suited for use during CLEM experiments and can be easily integrated into the workflow of both pre-embedding and on-section

CLEM techniques. Using a CLEM-STEM approach, we e.g. gained new insights into ciliogenesis and thus visualized its processes more detailed than so far.

4.1.2 Histochemical techniques

In addition to fluorescent proteins there are other "probes for CLEM" (Boer *et al.* 2015) which were summarized in a review of Boer *et al.* 2015. Especially "genetically encoded probes" (Boer *et al.* 2015) facilitating the visualization of proteins of interest in electron microscopy have been developed in recent years (Connolly *et al.* 1994; Gaietta *et al.* 2002; Kuipers *et al.* 2015; Lam *et al.* 2015; Martell *et al.* 2012; Shu *et al.* 2011); reviewed in (Boer *et al.* 2015; Sosinsky *et al.* 2007). The underlying principle is a histochemical reaction (Witzgall 2018b) by which the polymerization of the membrane-permeable molecule 3,3´-Diaminobenzidine is initialized (Graham & Karnovsky 1966); reviewed in (Boer *et al.* 2015; Connolly *et al.* 1994; Gaietta *et al.* 2002; Martell *et al.* 2012; Martell *et al.* 2017; Shu *et al.* 2011). By this reaction a "localized osmiophilic precipitate" (Adams *et al.* 2016) is generated which appears as "electron-dense label" (Boer *et al.* 2015) after incubation with aqueous OsO_4 solutions (Graham & Karnovsky 1966); reviewed in (Boer *et al.* 2015; Gaietta *et al.* 2002; Perkins 2014). 3,3´-Diaminobenzidine polymerization can be initialized either via photo-oxidation using the fluorescent flavoprotein mini Singlet Oxygen Generator (miniSOG) (Shu *et al.* 2011) or via an enzymatical reaction using peroxidases such as *horseradish peroxidase* (HRP) (Connolly *et al.* 1994; Graham & Karnovsky 1966; Kuipers *et al.* 2015) or derivatives of the *ascorbate peroxidase* (APEX/APEX2) (Lam *et al.* 2015; Martell *et al.* 2012); reviewed in (Boer *et al.* 2015; Sosinsky *et al.* 2007). As shown by Gaietta *et al.* 2002 and reviewed by Sosinsky *et al.* 2007 a major improvement of these techniques compared to immunogold labeling is that the whole amount of tagged protein can be visualized by electron microscopy and not only "a small, random fraction" (Gaietta *et al.* 2002) on the section surface (Gaietta *et al.* 2002; Sosinsky *et al.* 2007).

To localize the transition from the ciliary to the plasma membrane we visualized the ultrastructural distribution of "constitutively active M2 mutant of Smoothened [SmoM2]" (Hoffmeister *et al.* 2011) which localizes to primary cilia also without activation of the Hedgehog pathway (Corbit *et al.* 2005). Therefore we tested different 3,3´-Diaminobenzidine polymerization techniques. The fluorescent flavoprotein miniSOG can be used as a genetically encoded tag similar to EGFP (Shu *et al.* 2011) and initiates the 3,3´-Diaminobenzidine polymerization "upon blue light illumination" (Shu *et al.* 2011). We generated a fusion protein of SmoM2 with miniSOG and mCherry as additional fluorescent tag as photobleaching of miniSOG is known to occur very fast (Perkins

2014). RPE1 cells constitutively producing Centrin1-EGFP were used to express this fusion protein. Photo-oxidation experiments with miniSOG, however, are very time-consuming as each cell has to be illuminated separately. Individual illumination could also be the reason for lack of reproducibility in our experiments (data not shown). Therefore we switched to APEX2, a peroxidase that enzymatically initializes 3,3´-Diaminobenzidine polymerization upon H_2O_2 addition (Lam *et al.* 2015). We generated a fusion protein of SmoM2 with APEX2 and mCherry as fluorescent tag. One advantage of peroxidases is time saving during experiments since the cells under investigation do not need to be illuminated individually compared to miniSOG. However, additional contrasting of ciliary structures as a result of osmiophilic 3,3´-Diaminobenzidine polymer generation initialized by APEX2 was hardly detectable in the STEM tomogram (data not shown). Catalytic efficiency of APEX2, although already optimized compared to its predecessor APEX (Lam *et al.* 2015), is probably still too low (Kuipers *et al.* 2015) to generate electron density in combination with the amount of fusion protein present in primary cilia.

To overcome the above mentioned problems we finally applied a conventional and widely used technique in which the polymerization of 3,3´-Diaminobenzidine is initialized by HRP (Graham & Karnovsky 1966); reviewed in (Sosinsky *et al.* 2007). Furthermore, we worked with LLC-PK_1 cells which follow the extracellular pathway of ciliogenesis (Breslow & Holland 2019; Miyamoto *et al.* 2019) and therefore show no ciliary pocket in most of the cases (Molla-Herman *et al.* 2010). Since the ciliary and the pocket membrane lie closely adjacent to each other, the space between the two membranes is often less than the maximum resolution achievable with 3,3´-Diaminobenzidine polymerization techniques (see discussion below for details regarding the resolution). Therefore this problem does not exist in cells which do not form a ciliary pocket.

Similar to APEX/APEX2, HRP can be used as a genetically encoded tag (Connolly *et al.* 1994). As it has no fluorescent properties we used HRP in combination with EGFP. Combining fluorescent proteins with HRP was already performed in developing FLIPPER (Kuipers *et al.* 2015). In contrast to FLIPPER probes (Kuipers *et al.* 2015), however, HRP was not “fused in tandem with” (Martell *et al.* 2017) EGFP in our work. Compared to miniSOG with its molecular mass of ~14 kDa our CLEM probe consisting of HRP and EGFP is much larger (Shu *et al.* 2011) which is a disadvantage. CLEM probes with a large molecular mass can perturb “the endogenous function and/or localization of the protein of interest” (Martell *et al.* 2017). One option for reducing the molecular mass of the fusion protein would be not to use full-length SmoM2 protein or as

already done by Mick *et al.* 2015 for other proteins, only its ciliary targeting signal (Mick *et al.* 2015). However, despite its large molecular mass of ~152 kDa we observed clear ciliary localization of the fusion protein of SmoM2 with HRP and EGFP by light microscopy.

In contrast to APEX2 in RPE1 cells the catalytic efficiency of HRP in combination with the amount of fusion protein expressed in primary cilia of LLC-PK_1 cells was sufficient to generate detectable electron-density. As electron micrographs are grayscale images (Boer *et al.* 2015) electron-density of the Osmium-contrasted 3,3´-Diaminobenzidine polymer must be higher than the one of the cellular environment in order to visualize the ultrastructural localization of a protein by electron microscopy (Sastri *et al.* 2017). On the one hand, background can be reduced by an initial incubation step of cells with a 3,3´-Diaminobenzidine solution prior to H_2O_2 addition (Martell *et al.* 2017). This gives the 3,3´-Diaminobenzidine molecules enough time to diffuse into cells and the peroxidase reaction can subsequently be shortened which reduces background signal (Martell *et al.* 2017). Another possibility is to omit incubating cells in an uranyl acetate solution "as it may mask the […] signal" (Perkins 2014) generated by the Osmium-contrasted 3,3´-Diaminobenzidine polymer (Perkins 2014). By integrating these two options into our workflow we succeeded in most of the cases to get a clear difference in electron density between the membranes associated with an Osmium-contrasted 3,3´-Diaminobenzidine polymer and all other membranes. One possibility to significantly optimize the signal/background ratio would be the approach of Sastri *et al.* 2017: these authors conjugated Cerium with 3,3´-Diaminobenzidine and initialized its polymerization (Sastri *et al.* 2017). The distribution of the deposited Cerium can be visualized on elemental maps which in turn can be overlayed with electron micrographs (Sastri *et al.* 2017). This technique is not only very sensitive but, since 3,3´-Diaminobenzidine can also be conjugated with various lanthanides even multi-color imaging is possible (Adams *et al.* 2016). However, a transmission electron microscope with a fine probe – ideally with a field emission gun – and a suitable detector for elemental maps is needed (Adams *et al.* 2016; Sastri *et al.* 2017).

A frequently discussed issue is the resolution being achieved with enzymatically initiated 3,3´-Diaminobenzidine polymerization (Ariotti *et al.* 2015; Shu *et al.* 2011; Sosinsky *et al.* 2007). In this context detachment and diffusion of the polymer away from the site of its generation as well as attachment to adjacent membranes is a problem (Shu *et al.* 2011; Sosinsky *et al.* 2007). Optimizing the experimental design, however, resulted in a resolution of ~10 nm for enzymatically initiated 3,3´-Diaminobenzidine polymerization by APEX2 (Ariotti *et al.* 2015) which roughly

corresponds to that one achieved by photo-oxidation using miniSOG (Perkins 2014). We included several improvements in our workflow for our experiments with HRP which are described in detail by Martell *et al.* 2017 for the use of APEX2. First we started 3,3´-Diaminobenzidine polymerization only after strong fixation using glutardialdehyde. Glutardialdehyde fixation reduces both the lateral diffusion of transmembrane proteins (Tanaka *et al.* 2010) as well as – according to current knowledge – diffusion of the 3,3´-Diaminobenzidine polymer almost completely (Martell *et al.* 2017; Perkins 2014; Sosinsky *et al.* 2007). A further reduction of polymer diffusion can be achieved by performing the peroxidase reaction at 0°C, i.e. on ice (Martell *et al.* 2017). Finally we incubated the cells with an OsO_4 solution immediately after the peroxidase reaction which is thought to result in fixation of membrane lipids (Collin *et al.* 1973; Griffiths 1993). Nevertheless, although we exploited all options for reducing polymer diffusion currently known, we did not succeed in suppressing it completely as there was also Osmium-contrasted 3,3´-Diaminobenzidine polymer at membranes of structures such as microvilli which were located in proximity to the primary cilium. Due to this diffusion problem further experiments are required to verify our results which indicate that the constitutively active mutant M2 of Smoothened is not only located at the ciliary but also periciliary membrane. For example superresolution microscopy like stimulated emission depletion could be performed for this purpose as it was already used successfully to visualize the localization of ciliary proteins (Kohli *et al.* 2017). Furthermore, if nanobodies (Carrington *et al.* 2019) against the endogenous Smoothened protein would be used this would even enable an investigation without protein overexpression which can cause artifacts (Ratz *et al.* 2015).

In summary, we expanded the use of HRP to the visualization of the ultrastructural localization of ciliary transmembrane proteins. By optimizing the experimental design (Martell *et al.* 2017) we succeeded in reducing the deficiencies of an enzymatically initiated 3,3´-Diaminobenzidine polymerization. Especially for electron microscopic detection of small amounts of protein – e.g. within primary cilia – high catalytic efficiency of HRP (Kuipers *et al.* 2015; Lam *et al.* 2015) is beneficial.

4.2 Ultrastructural stadia of ciliogenesis and RAB8A recruitment

As reviewed by Blacque *et al.* 2018 the contribution of the GTPase RAB8A to ciliogenesis is documented several times in literature (Blacque *et al.* 2018). Although Nachury *et al.* 2007 used a

different control for their experiment – wild-type RAB8 expression in contrast to EGFP expression in the present work – we observed the same results: transient expression of the EGFP-tagged GDP-locked mutant RAB8A(T22N) "prevented ciliation" (Nachury *et al.* 2007) and EGFP-RAB8A(T22N) was not recruited to primary cilia. Please note that RAB8 is also required for the transport of membrane proteins such as rhodopsin of photoreceptor cells (Welsch 2014) to the cilium (reviewed in Blacque *et al.* 2018). As ARL13B is a membrane-associated protein (Revenkova *et al.* 2018) we cannot exclude that EGFP-RAB8A(T22N) expression could have impaired "ciliary-membrane targeting" (Emmer *et al.* 2010) of ARL13B. Therefore an additional marker for the ciliary axoneme such as anti-acetylated tubulin staining (Piperno & Fuller 1985) would be helpful to verify our data. Nevertheless, our results are a further hint for the central role of RAB8A during ciliogenesis in cell culture and in line with findings of several previous studies. For example an siRNA-mediated knockdown of RAB8A in RPE1 cells reduces the percentage of ciliated cells (Yoshimura *et al.* 2007). In addition, expression of EGFP-tagged RAB8A(T22N) in rod photoreceptors of *Xenopus laevis* resulted in accumulation of vesicles at the base of the cilium connecting the inner and outer segment of the cell and finally in retinal degradation in general (Moritz *et al.* 2001).

An important topic of our work was the investigation of the centrosomal localization of RAB8A during ciliogenesis as well as the ultrastructural membrane remodeling processes taking place at forming primary cilia. Furthermore, the role of the "endosomal system" (Klumperman & Raposo 2014) in centrosomal RAB8A recruitment was investigated. By analyzing STEM tomography datasets, we demonstrate that – to the best of our knowledge – the ultrastructural details of ciliogenesis have not been fully described yet. Fusion events between distal appendage vesicles took place although not all distal appendages had docked membrane structure at that time. Next, an open donut-like structure was formed, which subsequently was almost completely closed by further fusion events. The central hole of the donut-like structure was filled so that a ciliary vesicle structure emerged, first with a biconcave then with a convex shape (an overview is given in Fig. 23). It must be mentioned, however, that electron microscopic data are snapshots, time sequences of events are not evident in direct manner.

There are two possibilities by which distal appendage vesicles can form a ciliary vesicle: on the one hand additional incoming vesicles result in the fusion of distal appendage vesicles via a centrally directed process. On the other hand a donut-like membrane structure is formed in a first

step due to fusion events of vesicles with the distal appendage vesicles via a laterally directed process. Finally the central hole of the donut-like structure is closed by further incoming vesicles.

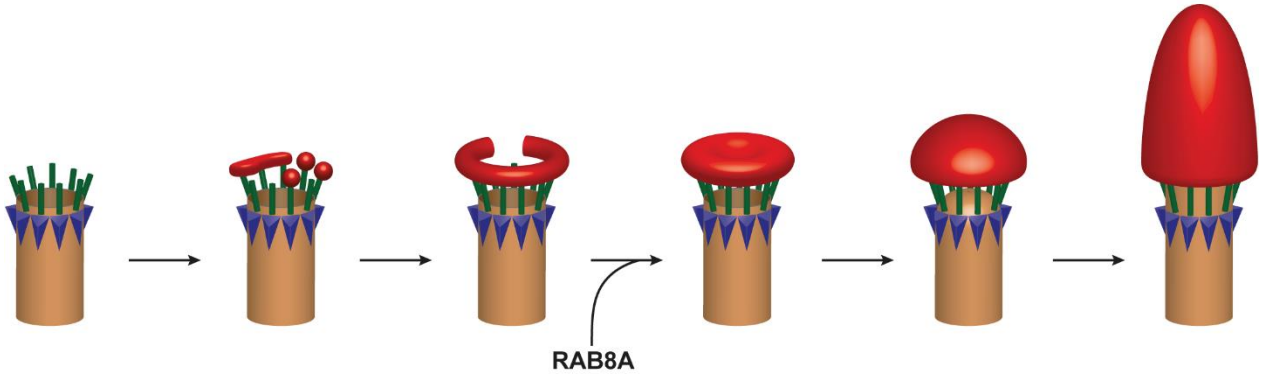

Figure 23: Schematic overview of different stadia of ciliogenesis described during the present work. Vesicles (red) dock to the distal appendages (green) of the mother centriole/basal body (brown) and fuse with additional incoming vesicles to form a donut-like structure (red). By closing the central hole of the donut-like structure a biconcave ciliary vesicle (red) is formed which subsequently assumes a convex shape (red). In a last step the vesicle extends and the axoneme grows out. The earliest ciliogenetic stadium at which RAB8A could be found at the membrane structure docked to the distal appendages of the basal body in the present work was the donut-like stadium. Brown: microtubule barrel of mother centriole/basal body; blue: subdistal appendages; green: distal appendages; red: membrane material docked to the distal appendages of the basal body. The schematic overview was generated by Anita Hecht (Institute for Molecular and Cellular Anatomy, University of Regensburg) and a drawing of the centriole by Bowler *et al.* 2019 was used as the template for Fig. 23 (Bowler *et al.* 2019).

Our ultrastructural investigations indicate that the latter mechanism predominates although centrally directed fusion events were observed prior to filling the central hole of the donut-like structure as well. The mechanisms responsible for these fusion processes are poorly understood. Proteins such as EHD1/3 or SNAP29 could be involved in regulating the fusion of distal appendage vesicles (Lu *et al.* 2015). It is very unlikely that the distal appendages bend or are bent towards each other in order to bring the distal appendage vesicles in close contact with each other for subsequent fusion events. Therefore recruitment of additional membrane material is necessary. The origin of this membrane material as well as its intracellular transportation routes to the centrosome are largely obscure (Witzgall 2018b). We observed vesicles – called intra-centriolar vesicles by us – in both the lumen of the mother centriole/basal body and the daughter centriole in forming cilia of RPE1 cells. “Vesicles [...] within the walls of centrioles” (Sorokin 1962) or basal bodies during ciliogenesis were already described decades ago for a variety of cell types such as cells of the neural epithelium (Sotelo & Trujillo-Cenóz 1958), fibroblasts, smooth muscle cells (Sorokin 1962) or pulmonary cells (Sorokin 1968); reviewed in (Gürster 2013). For LLC-PK$_1$ cells these vesicular

structures within the basal body of primary cilia were identified by Gürster 2013. In contrast to Gürster who was able to detect these vesicles also within the very proximal part of the shaft of primary cilia (Gürster 2013) we did not observe them in the shaft of primary cilia of RPE1 cells.

Without clear evidence Gürster hypothesized that these vesicles contribute to transportation processes to the primary cilium (Gürster 2013). At least in RPE1 cells, neither the size nor the number of intra-centriolar vesicles was increased in cells expressing mCherry-RAB8A compared to cells expressing only mCherry. It has to be considered, however, that electron micrographs or as in the case of the current work STEM tomograms are snapshots of cellular processes. Thus there could still be a higher flow rate of vesicles through centrioles of mCherry-RAB8A expressing cells compared to those of only mCherry expressing cells assuming that intra-centriolar vesicles do not remain trapped within centrioles but rather pass them. Furthermore, we compared RPE1 cells which stably expressed mCherry-RAB8A with RPE1 cells which were transiently transfected with an mCherry expression plasmid. As transfection is a manipulation of cells it could also alter transport routes and therefore the number of intra-centriolar vesicles which was not considered in the current work. It cannot be excluded that the hub of the cartwheel structure present at the proximal part of centrioles could have been misinterpreted as one intra-centriolar vesicle since the shape of both structures is similar (Gibbons & Grimstone 1960); reviewed in (Hirono 2014). Yoshimura *et al.* 2007 showed that overexpression of EGFP-tagged wild-type RAB8A promotes growth in length of primary cilia in RPE1 cells (Yoshimura *et al.* 2007). Furthermore, based on their findings Nachury *et al.* 2007 assumed that RAB8 "[promotes] the docking and fusion of exocytic vesicles to the base of the ciliary membrane" (Nachury *et al.* 2007) in RPE1 cells. Although we did not show this for the currently used RPE1 cell line constitutively producing the proteins Centrin1-EGFP and mCherry-RAB8A but considering previous findings (Nachury *et al.* 2007; Yoshimura *et al.* 2007), it can be assumed that overexpression of RAB8A promotes ciliogenesis. However, intra-centriolar vesicles are neither enriched nor enlarged under these conditions. Furthermore, intra-centriolar vesicles were never associated with mCerry-RAB8A and all fusion/budding events observed during the present work took place at the distal part of docked membrane structures (see Figures 11A-E) but not at their proximal end. Taken together, these findings contradict a major role of intra-centriolar vesicles in ciliogenesis. Since mother centrioles are longer than daughter centrioles (Uzbekov *et al.* 2012) they could offer more space for vesicles which could explain the somewhat more frequent appearance of vesicles within the mother

centriole/basal body than within the daughter centriole. It is known that within the lumen of the distal part of centrioles there is a so-called luminal density (Winey & O'Toole 2014) and a "periodic stack of rings […] 53° [tilted] perpendicular to the centriole axis" (Ibrahim *et al.* 2009). Since these rings have a diameter of 30 nm (Ibrahim *et al.* 2009) and the mean diameter of the intra-centriolar vesicles observed during the current work was larger in both the *x* and *y* dimension it is unlikely that centrioles represent kind of channels for vesicle transport. If it is possible at all for intra-centriolar vesicles to leave the centrioles via their distal ends, they have to be deformed as they cannot pass the stack of rings due to their size. How these vesicles reach the interior of centrioles remains completely unclear. The fact that cytoplasmic components such as ribosomes are excluded from the lumen of centrioles (Pearson *et al.* 2009; reviewed in Winey & O'Toole 2014) indicates that an unhindered exchange of material between the cytosol and centriole lumen is not possible at least for some molecules. Therefore directed transport processes are presumably necessary so that vesicles can reach the interior of centrioles. As far as we know, however, it is completely unclear whether such transport mechanisms exist and, if so, how they are organized. To sum it up, the present study could not elucidate the function of intra-centriolar vesicles. We did not find any evidence for their contribution to ciliogenesis.

Clathrin-coated pits at the donut-like and ciliary vesicle stadium were detected in exceptional cases (see Fig. 13). This is in line with results of Molla-Herman *et al.* 2010 who observed clathrin-coated pits at the ciliary pocket in RPE1 cells or Clement *et al.* 2013 who demonstrated the presence of "clathrin at the ciliary base in" (Clement *et al.* 2013) mouse embryonic fibroblasts. According to the authors of these previous studies, the presence of clathrin is a hint "for the docking of vesicles coming from the secretory pathway or from endosomes" (Molla-Herman *et al.* 2010) and for the regulation of ciliary signaling via clathrin-dependent endocytosis (Clement *et al.* 2013). The presence of clathrin-coated pits already during early stadia of ciliogenesis as shown in the current work could be a hint that clathrin-dependent endocytosis is also involved in regulating or rather antagonizing the growth of the ciliary membrane already at the beginning of its formation.

Having described the ultrastructure of forming cilia in detail we focused our research on the identification of the developmental stadium at which RAB8A could be detected for the first time at the membrane structure docked to the distal appendages of the basal body. The RPE1 cell line used for this experiment constitutively produced the proteins Centrin1-EGFP and mCherry-RAB8A. Fluorescence microscopic images of this cell line showed bright mCherry signals

distributed over the entire cytoplasm of the cells. This was surprising since RPE1 cells expressing EGFP-tagged RAB8A showed a localization of EGFP-RAB8A at forming and outgrown cilia but hardly any additional cytoplasmic signals during previous studies (Schmidt *et al.* 2012; Westlake *et al.* 2011). As Western blot analysis of the cell line used in the current work revealed the presence of cleavage products of the fusion protein of RAB8A with mCherry, cytoplasmic mCherry signals are likely mCherry aggregates. For example the band at ~26 kDa corresponds to the molecular mass of the mCherry protein. However, the localization of mCherry-RAB8A at the basal body in RPE1 cells was specific despite additional cytoplasmic mCherry signals as overlays of fluorescence microscopic images with STEM tomograms revealed that in 43 out of 45 cells the mCherry-RAB8A signal was located in close contact to the mother centriole/basal body. Although the cell line was sufficient for the investigation of the recruitment of RAB8A to the basal body during ciliogenesis other red fluorescent proteins such as mRuby3 (Bajar *et al.* 2016) or mScarlet (Bindels *et al.* 2017) should be tested in order to minimize such cytoplasmic artifacts and to achieve an expression pattern similar to those of EGFP-RAB8A expressing RPE1 cells of previous studies (Schmidt *et al.* 2012; Westlake *et al.* 2011).

Using our CLEM-STEM approach we were able to demonstrate that mCherry-RAB8A is recruited to the basal body at the donut-like stadium of ciliogenesis (see Fig. 14). An investigation of the ultrastructural localization of RAB8A during ciliogenesis has never been carried out so far to our knowledge. Lu *et al.* 2015 only showed the localization of RAB8A at mature cilia by CLEM (Lu *et al.* 2015). Since mCherry-RAB8A was recruited to the basal body after a large number of fusion events had taken place at its distal end it seems to be of minor importance for distal appendage vesicle docking and subsequent fusion. For sure it is dispensable for donut-like structure formation. Strictly speaking, the presence of mCherry-RAB8A at the membrane structures docked to the distal appendages of the basal body during particular stadia of ciliogenesis is not an evidence but only a hint that these stadia are RAB8A-dependent. Live-cell imaging experiments of ciliogenesis in RPE1 cells demonstrate that a fusion protein of RAB8A with the red fluorescent protein TagRFP first localized as point-shaped signal to the mother centriole/basal body and then grows out together with the cilium (Lu *et al.* 2015). Based on these findings we selected RPE1 cells with an mCherry-RAB8A spot in close contact to one Centrin1-EGFP signal by fluorescence microscopy in order to identify cells showing one of the earliest points in time of ciliogenesis at which RAB8A was recruited to the mother centriole/basal body. As a matter of fact, about half of the cells with an

mCherry-RAB8A signal at the membrane structures docked to the distal appendages of the basal body were in the phase of forming a short cilium, as we could visualize in our STEM tomograms. A ciliary vesicle was present in only ~12.5% of these cells. Ciliogenetic stadia downstream of RAB8A recruitment must therefore be very transient and end up rapidly in short cilia with an outgrowing axoneme. Please note, that we identified the earliest point in time of RAB8A recruitment to the basal body. However, from our data we cannot conclude if RAB8A is present at the donut-like stadium of ciliogenesis in general or only in exceptional cases. Indeed there were some cells showing a donut-like structure or a ciliary vesicle by which the mCherry-RAB8A signal did not overlay with the membrane structures docked to the distal appendages of the basal body but it was either proximally or laterally shifted to the distal end of the basal body. In summary our results demonstrate that mCherry-RAB8A is recruited to the basal body at the donut-like stadium of ciliogenesis and thus indicate a role of RAB8A primarily for the outgrowth of the primary cilium. This is in agreement with the findings of Lu *et al.* 2015 who concluded that RAB8A+B are required for the extension of the ciliary vesicle as the majority of RPE1 cells arrested in the ciliary vesicle stadium after siRNA-mediated knockdown of RAB8A+B and subsequent serum starvation (Lu *et al.* 2015).

A further issue of the current work was to investigate the intracellular route of RAB8A to the forming cilium. There are studies demonstrating a major role of the "endosomal system" (Klumperman & Raposo 2014) and especially the recycling endosome in these transport processes (Knödler *et al.* 2010; Westlake *et al.* 2011). The arising question was whether in addition to the recycling endosome early and late endosomes also play a role in ciliogenesis in general and in centrosomal RAB8A recruitment in particular. For this purpose the GDP-locked mutants of GTPases – each characteristic of one endosomal compartment – were transiently expressed in RPE1 cells. The expression of EGFP-RAB11A(S25N) in wild-type RPE1 cells resulted in a reduction of the percentage of ciliated cells compared to EGFP-expressing cells at each point in time after serum starvation investigated. However, statistical significance was reached only after 24 h of serum starvation. Our results indicate a role of the recycling endosome in ciliogenesis and are therefore in line with previous works. Using siRNA-mediated knockdown of RAB11A+B in RPE1 cells Westlake *et al.* 2011 observed an impairment of ciliogenesis (Westlake *et al.* 2011). In addition, Knödler *et al.* 2010 showed a reduced cilia length (immunostaining with an anti-

acetylated α-tubulin antibody) after transfection of RPE1 cells with EGFP-RAB11A(S25N) (Knödler *et al.* 2010).

Although there was a statistically significant impairment of ciliogenesis in RPE1 cells expressing RAB11A(S25N) only a slight but not statistically significant reduction of centrosomal EGFP-RAB8A localization after serum starvation was detected within these cells. This is in contrast to a well-established model the so-called "Rab11-Rabin8-Rab8 signaling cascade" (Wu *et al.* 2018). In this cascade RAB11 mediates the centrosomal recruitment of RABIN8 which activates RAB8 (Knödler *et al.* 2010; Westlake *et al.* 2011). Only activated RAB8 is able to localize to the developing cilium (Nachury *et al.* 2007). Several previous studies support this model: for example Westlake *et al.* 2011 observed a reduction of RAB8A ciliated RPE1 cells after an siRNA-mediated knockdown of RAB11A or RAB11B or RAB11A+B (Westlake *et al.* 2011). Knödler *et al.* 2010 were not able to demonstrate "a complete loss of Rab8 staining along the cilium" (Knödler *et al.* 2010) after an siRNA-mediated knockdown of RAB11A+B in RPE1 cells but still report of a reduction of "the average length of Rab8 fluorescence along the cilia" (Knödler *et al.* 2010). There are several possible reasons why we did not observe a statistically significant reduction of centrosomal EGFP-RAB8A localization in mCherry-RAB11A(S25N) expressing RPE1 cells. First, Westlake *et al.* 2011 performed knockdown experiments, we expressed the GDP-locked mutant of RAB11A in RPE1 cells. In order to achieve a dominant-negative effect a certain amount of protein of the mutant is required but we took all, i.e. also weakly expressing cells into account. However, this explanation is rather unlikely since there probably was remaining enzymatic activity after siRNA-mediated knockdown of RAB11A+B during the experiments of Westlake *et al.* 2011 as well. Second, not only mCherry-RAB11A(S25N) but also wild-type EGFP-RAB8A was expressed in the RPE1 cells during our experiments. Since RAB8A promotes ciliogenesis (Nachury *et al.* 2007) there are data in literature indicating transient expression of RAB8A can result in a kind of rescue effect for ciliogenesis (Schmidt *et al.* 2012). Effects of mCherry-RAB11A(S25N) expression on centrosomal EGFP-RAB8A recruitment could therefore be impaired during the current work as well. To minimize this problem expression level of EGFP-RAB8A in RPE1 cells should be reduced in future studies, e.g. by choosing a promoter that causes not as high protein expression as the human cytomegalovirus immediate early promoter used in the current work. Third, expression of dominant-negative RAB11A perhaps has less effect on centrosomal localization RAB8A in general than on "the average length of Rab8 fluorescence along the cilia"

(Knödler *et al.* 2010) as described by Knödler *et al.* 2010. As we did not carry out any length measurements and thus cannot make a statement regarding this hypothesis made by Knödler *et al.* 2010. Fourth, RAB8A is known to be displaced from mature cilia after its initial localization during ciliogenesis (Westlake *et al.* 2011). As a result it cannot be excluded that RPE1 cells with mature cilia were falsely categorized negative regarding the centrosomal EGFP-RAB8A localization within the current work. Therefore it is still possible that there is a different amount of RPE1 cells which show centrosomal RAB8A recruitment during ciliogenesis over a period of time although there is the same percentage of RAB8A-positive centrosomes at investigated points in time after serum starvation. One possibility to solve this problem would be an additional staining of cilia with antibodies e.g. against ARL13B or acetylated tubulin. An anti-ARL13B staining of the ciliary membrane was indeed carried out during the present study but resulted in only weak fluorescence signals in many cases and could therefore not be used for evaluation. Since ARL13B and RAB8A are both located at the ciliary membrane (Wu *et al.* 2018) overexpression of EGFP-RAB8A could partially displace ARL13B, which would be the reason for the weak ARL13B signals in the present study. Therefore antibodies directed against components of the ciliary axoneme such as e.g. anti-acetylated tubulin antibodies (Piperno & Fuller 1985) should be used for future experiments. Finally, as already mentioned by Knödler *et al.* 2010 there is the possibility that in addition to RAB11 other factors contribute to the recruitment of RAB8A to the basal body during ciliogenesis as well (Knödler *et al.* 2010). For example components of the Golgi apparatus could also be involved in centrosomal RAB8 recruitment as RAB8 can be found at Golgi and post-Golgi membranes rod photoreceptors of *Xenopus laevis* tadpoles (Moritz *et al.* 2001). In summary the influence of RAB11A on centrosomal RAB8A recruitment cannot be unequivocally confirmed within the current work. Therefore the experimental setup should be further optimized: the rescue effect due to RAB8A overexpression has to be reduced as well as a reliable ciliary staining should be established.

In contrast to the recycling endosome, impaired function of the early (expression of RAB5A(S34N)) and late endosome (expression of RAB7A(T22N)) had no influence on ciliogenesis in general and on the centrosomal RAB8A localization. Knödler *et al.* 2010 did not detect a reduction in cilia length after expression of RAB5A(S34N) in RPE1 cells which is a further contradicts for the involvement of the early endosome in ciliogenesis (Knödler *et al.* 2010).

A recent knockdown screen showed that out of 62 human RAB proteins only RAB34 has an influence on ciliogenesis in RPE1 cells (Oguchi *et al.* 2020). Even knockdown of RAB8 had no impact (Oguchi *et al.* 2020). This is in contrast to findings of several previous studies (Knödler *et al.* 2010; Lu *et al.* 2015; Nachury *et al.* 2007; Westlake *et al.* 2011) as well as to our results. Many RAB proteins have different isoforms (Oguchi *et al.* 2020; Witzgall 2018b). If a knockdown is performed against only one isoform of a RAB protein – e.g. the case in the work of Oguchi *et al.* 2020 for RAB8A in RPE1 cells (Oguchi *et al.* 2020) – remaining isoform(s) as well as other RAB proteins can establish compensatory effects (Sato *et al.* 2014). For example Rab8a+b double knockout mice show abnormalities of the small intestine but form normal cilia (Sato *et al.* 2014). Only the additional knockdown of Rab10 in Rab8a+b double knockout mouse embryonic fibroblasts impaired ciliogenesis (Sato *et al.* 2014). Such compensatory mechanisms are no issue for the expression of constitutively inactive mutants of one isoform. To further validate their results from knockdown experiments Oguchi *et al.* 2020 generated RAB8A+B double knockout and RAB8A+B+RAB10 triple knockout RPE1 cell lines using CRISPR/Cas but still were unable to detect impaired ciliogenesis within these cell lines. As explained by Witzgall 2018b knockout of (RAB) proteins by CRISPR/Cas (Oguchi *et al.* 2020) gives cells enough time to develop compensatory mechanisms, which is unlikely in the case of transient transfection (Witzgall 2018b) as performed in the present study. Due to the currently existing data inconsistency great care must be taken when assessing the role of RAB proteins during ciliogenesis.

4.3 Visualization of the ciliary membrane

In addition to the investigation of processes contributing to ciliogenesis (e.g. RAB8A recruitment) the visualization of the ciliary membrane on an ultrastructural level was a further issue of the current work. Since the ciliary membrane and plasma membrane are continuous (Porter 1957) but different in composition there must be a barrier separating both membrane compartments; reviewed in (Hu & Nelson 2011; Nachury *et al.* 2010; Satir 2017). As already reviewed by Nachury *et al.* 2010 the arising questions are which routes membrane proteins take to the ciliary membrane and how these proteins manage to pass this barrier at the ciliary base (Hu & Nelson 2011; Nachury *et al.* 2010; Witzgall 2018a). The ultrastructural localization of a barrier separating ciliary and plasma membrane could not be elucidated so far (Francis *et al.* 2011; Nachury *et al.* 2010). Therefore two hypotheses are discussed in the review of Nachury *et al.* 2010: on the one hand the barrier could be located at the base of the primary cilium. Within this region there are nine counterclockwise

faced trapezoidal so-called alar sheets which extend from the microtubules of the basal body at the ciliary base to the cell membrane (Anderson 1972; Anderson & Brenner 1971). Distal from the alar sheets there are champagne glass-shaped structures linking the axoneme with the ciliary membrane (Gilula & Satir 1972). On the other hand the barrier could be located a certain distance away from the ciliary base towards the circumjacent plasma membrane (Vieira *et al.* 2006).

Smoothened is an important component of Hedgehog signaling and contributes to the function of primary cilia (Reiter & Leroux 2017). Smoothened is recruited to the ciliary membrane after activation of this pathway (Reiter & Leroux 2017). The "constitutively active M2 mutant of [the seven-transmembrane protein] Smoothened" (Hoffmeister *et al.* 2011) – referred to as SmoM2 in the current work – localizes to primary cilia also without activation of the Hedgehog pathway (Corbit *et al.* 2005) and therefore was used in the current study. Interestingly we were able to detect a fusion protein of SmoM2 with HRP and EGFP not only at the ciliary membrane but also at a part of the membrane surrounding the ciliary base which is referred to as periciliary membrane in literature (Garcia-Gonzalo & Reiter 2012; Lee & Chung 2015; Long & Huang 2019). HRP-SmoM2-EGFP was present at the periciliary membrane extending over a mean distance of ~193 nm measured from the base of primary cilia. Thus, we identify a membrane area surrounding the base of primary cilia that is more similar in its composition (regarding the presence of HRP-SmoM2-EGFP) to the ciliary membrane than to the apical plasma membrane. This is in line with the findings of Vieira *et al.* 2006 which report on a so-called "exclusion area" (Vieira *et al.* 2006). These authors expressed "a glycosyl phosphatidyl inositol[...]-anchored version of" (Keller *et al.* 2001) the yellow fluorescent protein designed by Keller *et al.* 2001 which marks the apical plasma membrane in Madin-Darby canine kidney (MDCK) cells. This synthetic protein could not be detected at the primary cilium and at an area with a diameter of 1.2-1.8 µm surrounding the ciliary base (Vieira *et al.* 2006); reviewed in (Nachury *et al.* 2010). The work of Vieira *et al.* 2006 prompted Nachury *et al.* 2010 to generate a hypothetical model in which the diffusion barrier is not located right at the base of primary cilia but "positioned at least 0.5 µm away from [it]" (Nachury *et al.* 2010). Considering that primary cilia had an average diameter of ~200 nm at their bases in cells we had investigated, this membrane area with a mean diameter of ~600 nm would be significantly smaller in LLC-PK_1 cells than the 1.2-1.8 µm determined by Vieira *et al.* 2006 in MDCK cells. We used LLC-PK_1 cells constitutively producing a fusion protein of SmoM2 with HRP and EGFP for the current investigation. Therefore additional confocal light microscopy as

applied in the study of Vieira *et al.* 2006 can be performed in combination with our cell line as well to validate that the localization of the HRP-SmoM2-EGFP protein at the ciliary membrane is not an artifact due to diffusion of the Osmium-contrasted 3,3´-Diaminobenzidine polymer (see section 4.1.2 for further details). However, since the diameter of the "exclusion area" (Vieira *et al.* 2006) seems to be significantly smaller than initially assumed by Vieira *et al.* 2006, superresolution light microscopy (Boer *et al.* 2015) would be a more suited alternative than conventional confocal light microscopy. Please note that as already mentioned in section 4.1.2 all experiments were performed using LLC-PK_1 cells overexpressing the protein HRP-SmoM2-EGFP, therefore the localization pattern of endogenous Smoothened can differ (Ratz *et al.* 2015).

As reviewed by Hu & Nelson 2011, however, contradictory data exist (Hu & Nelson 2011): Hu *et al.* 2010 expressed the same synthetic protein as Vieira *et al.* 2006 but in inner medullary collecting duct (IMCD) cells and although they report on its exclusion from primary cilia, they do not make any statement if they could detect an "exclusion area" (Vieira *et al.* 2006) as well (Hu *et al.* 2010). At least there are no hints for such an area on fluorescence microscopic images included in their publication (Hu *et al.* 2010). Furthermore, Hu *et al.* 2010 demonstrate that the protein Septin2 contributes to the function of the diffusion barrier. As Septin2 was located at "the base of the cilium at the boundary between the ciliary and periciliary membrane" (Hu *et al.* 2010) this further contradicts a model in which the diffusion barrier is positioned away from the ciliary base. Francis *et al.* 2011 made the attempt to reproduce results of Vieira *et al.* 2006 and therefore expressed a comparable synthetic protein (the yellow fluorescent protein was replaced by the green fluorescent protein) in MDCK cells. Francis *et al.* 2011 noticed, however, that fixation and permeabilization of cells caused artifacts and thus altered the distribution of the synthetic protein within cells: whereas the protein could neither be detected at the primary cilium nor at the "exclusion area" (Vieira *et al.* 2006) in fixed cells, it localized at both compartments in living cells (Francis *et al.* 2011). For this reason Francis *et al.* 2011 investigated the location of another apical transmembrane protein – Podocalyxin – in living cells (Francis *et al.* 2011) and were unable to detect Podocalyxin at the primary cilium and "exclusion area" (Vieira *et al.* 2006) during their live-cell imaging experiments (Francis *et al.* 2011). Stoops *et al.* 2015 managed to reproduce the results of Francis *et al.* 2011 as they report that "at steady state [Podocalyxin] […] localizes primarily to the apical membrane but is not present in the primary cilium or in the area surrounding its base" (Stoops *et al.* 2015). Although we did not perform membrane permeabilization, chemical fixation could have

caused artifacts as argued by Francis *et al.* 2011. Fixation of cells by means of cryoimmobilization would be a possibility to minimize such fixation artifacts (McDonald 2009). Combining the enzymatically initiated 3,3´-Diaminobenzidine with cryoimmobilization, however, would require an extensive adaptation of the currently available experimental designs (Martell *et al.* 2017). In addition, Francis *et al.* 2011 demonstrated that an intact link of Podocalyxin to the subapical actin network is indispensable for excluding it from the primary cilium and the membrane region surrounding its base. In contrast, the ability of proteins to bind to microtubules causes their inclusion within these compartments (Francis *et al.* 2011). Therefore – according to the hypothesis of Francis *et al.* 2011 – the diffusion barrier is not only a physical barrier formed by ciliary components such as alar sheets (Anderson 1972; Anderson & Brenner 1971), champagne glass-shaped structures (Gilula & Satir 1972) or a Septin2 "ring-like structure" (Hu & Nelson 2011) but rather is the result of "a hierarchical interplay of several elements" (Francis *et al.* 2011). Data of the current work, however, do not allow any conclusions about whether the nature of this diffusion barrier is structural or functional or a combination of both. In summary, similar to several previous studies (Francis *et al.* 2011; Stoops *et al.* 2015; Vieira *et al.* 2006) we were able to detect a membrane region surrounding the base of primary cilia which resembles rather the ciliary membrane than the plasma membrane regarding its composition. In addition to Francis *et al.* 2011 who showed that the periciliary membrane is "free of microvilli" (Francis *et al.* 2011) using scanning electron microscopy our present investigation provides a further hint for the unique composition of this membrane region on an ultrastructural level.

Studies demonstrated that membrane proteins such as Smoothened or Polycystin-2 use different transportation routes on their way to ciliary membrane (Hoffmeister *et al.* 2011; Milenkovic *et al.* 2009; Monis *et al.* 2017). According to the current data availability Smoothened uses a so-called "lateral trafficking pathway" (Monis *et al.* 2017) in which the newly synthesized protein is first taken up into the apical plasma membrane and then transported laterally into the ciliary membrane (Milenkovic *et al.* 2009; Monis *et al.* 2017). On electron micrographs generated during the current study the concentration of HRP-SmoM2-EGFP incorporated in the membrane continuously decreased with increasing distance from the ciliary base towards the surrounding plasma membrane. We did not detect a decline. This finding supports the lateral transport hypothesis. However, due to the above mentioned (see section 4.2) diffusion of the 3,3´-Diaminobenzidine polymer care must be taken not to over-interpret our data. Nevertheless, at least we could not find

any evidence contradicting the lateral transport model of Smoothened. If Smoothened is first integrated into the apical plasma membrane prior to its uptake into the ciliary membrane, this must be taken into account by interpreting our data regarding the location of the diffusion barrier (see the two models for the localization of the diffusion barrier discussed by Nachury *et al.* 2010): on the one hand, the barrier could be located at the region of the periciliary membrane (Nachury *et al.* 2010) at which the Osmium-contrasted 3,3´-Diaminobenzidine polymer terminates. On the other hand, the barrier could also be located right at the ciliary base or transition zone (Nachury *et al.* 2010) and Smoothened is taken up into the apical plasma membrane in a first step and then is laterally transported into the ciliary membrane by passing the diffusion barrier. In summary, due to the lateral transport hypothesis of Smoothened it is not possible to deduce from our data that the diffusion barrier is located at the region of the periciliary membrane at which the fusion protein HRP-SmoM2-EGFP can no longer be detected on electron micrographs. Therefore the localization of other ciliary proteins that do not make a detour via the plasma membrane should be visualized on an ultrastructural level in future as well. For example the transmembrane protein Fibrocystin which is transported directly to the ciliary base in an "IFT20- and exocyst-dependent" (Monis *et al.* 2017) manner is a potential candidate for such an investigation. As we used LLC-PK_1 cells during the present study which follow the extracellular pathway of ciliogenesis (Breslow & Holland 2019; Miyamoto *et al.* 2019) it would be interesting whether the HRP-SmoM2-EGFP fusion protein is located in similar manner in cells following the intracellular pathway of ciliogenesis (e.g. REP1 cells) and therefore have a ciliary pocket (Molla-Herman *et al.* 2010). However, this would require the development of a new technique with a higher resolution compared to the one used during our investigations.

A secondary finding of the present work was that after its overexpression in LLC-PK_1 cells the fusion protein of SmoM2 with HRP and EGFP was present at the endoplasmic reticulum but not at the Golgi apparatus. This is a hint that overexpressed HRP-SmoM2-EGFP does not pass through the Golgi apparatus "on its way to the primary cilium" (Hoffmeister *et al.* 2011). For overexpressed Polycystin-2, another ciliary membrane protein, it was shown that at least a portion of synthesized protein does not pass through the Golgi apparatus but leaves it at its cis side on the way to the primary cilium (Hoffmeister *et al.* 2011); reviewed in (Witzgall 2018a). Please note as there are several publications demonstrating that Polycystin-2 is transported to primary cilia via the Golgi apparatus (Follit *et al.* 2006; Kim *et al.* 2014) therefore likely only a portion of Polycystin-2

bypasses the mid- and trans-compartment of the Golgi apparatus (Gainullin *et al.* 2015; Witzgall 2018a). Using fluorescence microscopy Hoffmeister *et al.* 2011 were able to detect wild-type Smoothened in the Golgi apparatus of LLC-PK_1 cells but not its M2 mutant under overexpressing conditions (Hoffmeister *et al.* 2011). Thus our electron microscopic data are in line with the results of Hoffmeister *et al.* 2011 and are a hint that SmoM2 does not pass through the Golgi "on its way to the primary cilium" (Hoffmeister *et al.* 2011). This hypothesis is further supported by the fact that SmoM2 localization is largely independent from the Golgi apparatus as Golgi apparatus disruption (Lippincott-Schwartz *et al.* 1989) has no influence on the subcellular distribution SmoM2 (Incardona *et al.* 2002). However, it cannot be deduced from our and other currently available data whether SmoM2 is never present at the Golgi apparatus "on its way to the primary cilium" (Hoffmeister *et al.* 2011). Regarding this issue Hoffmeister *et al.* 2011 made the following hypothesis for Polycystin-2: the protein could only briefly be located on the cis-Golgi apparatus, which results in undetectable low protein levels (Hoffmeister *et al.* 2011). A similar scenario would also be possible for SmoM2. It must be considered that we did not systematically examine the "Golgi bypass" (Witzgall 2018a) of SmoM2 in the current work. For example, we did not correlate if the fusion protein of SmoM2 with HRP and EGFP was present in the ciliary membrane of LLC-PK_1 cells showing endoplasmic reticulum but no Golgi apparatus localization. To sum it up our results indicate that the overexpressed fusion protein of SmoM2 with HRP and EGFP "does not traverse the Golgi apparatus on its way to the primary cilium" (Witzgall 2018a). However, since overexpression of proteins can cause artifacts such as "mislocalizations and protein aggregation" (Ratz *et al.* 2015) it has to be elucidated in further experiments if there is a similar subcellular distribution of endogenous wild-type Smoothened as well.

5 Summary

The primary cilium – a “microtubule-based organelle” (Mirvis *et al.* 2018) originating from a basal body – fulfills a variety of sensory functions in “most mammalian cell types” (Satir *et al.* 2010) (Anderson *et al.* 2008; Breslow & Holland 2019; Pedersen *et al.* 2012; Witzgall 2018a). Its formation is a complex, “multistep process” (Pitaval *et al.* 2017). The small GTPase RAB8 is an important molecular player for ciliogenesis in cell culture as it contributes to the extension of the ciliary vesicle at the distal end of the basal body, a process known as prerequisite for axoneme outgrowth (Lu *et al.* 2015; Nachury *et al.* 2007). However, studies investigating centrosomal RAB8 recruitment in combination with the three-dimensional visualization of membrane remodeling processes at this period of ciliogenesis are rare to date. Correlative light and electron microscopy (CLEM) techniques provide options to achieve this.

We adapted two CLEM techniques to assign “fluorescently tagged proteins […] to their ultrastructural compartments” (Buerger *et al.* 2021). First, we extended the *Kukulski protocol* (Kukulski *et al.* 2011, 2012) and combined it with 200 kV bright-field scanning transmission electron (STEM) tomography with an electron beam with low semi-convergence angle (Rachel *et al.* 2020). Thereby it was possible to identify cellular structures such as mature primary cilia but also multivesicular bodies and to three-dimensionally visualize almost their entire ultrastructure in single tomograms. However, resin embedding prior to fluorescence microscopy resulted in loss of fluorescence intensity which made it impossible to preserve weak fluorescence signals of fluorescent proteins at the onset of cilia formation. For investigating centrosomal RAB8 recruitment, fluorescence microscopy was performed before sample preparation for electron microscopy. Retinal pigment epithelial (RPE1) cells showing the earliest moment detectable by fluorescence microscopy with RAB8A localizing to the centriole of a developing cilium were selected. Subsequent STEM tomography revealed a donut-like membrane structure formation during ciliogenesis which, according to our knowledge, has not been described so far: vesicles docked to the distal appendages of the basal body primarily fuse with incoming vesicles via a laterally directed process to form a donut-like structure. The central hole of this structure is closed afterwards to form the large so-called ciliary vesicle. Vesicles within the lumen of the microtubule barrel of the basal body are not enriched during these ciliogenetic processes. In contrast, fusion/budding events were observed at the distal part of docked membrane structures. RAB8A-positive membrane structures docked to the distal appendages of the basal body were present

starting with the donut-like stadium of ciliogenesis. This suggests a role of RAB8A during the extension of the ciliary vesicle. By overexpressing dominant-negative mutants of RAB proteins in RPE1 cells we confirmed a role of the recycling endosome during ciliogenesis but could not unambiguously reproduce its contribution to centrosomal RAB8A recruitment. Early and late endosomes are dispensable for ciliogenesis in general.

The formation of primary cilia requires incoming membrane material and a variety of proteins (Witzgall 2018b). According to the prevailing opinion, a diffusion barrier has to be passed to enter the "ciliary compartment" (Hu & Nelson 2011) (Garcia-Gonzalo & Reiter 2012; Nachury *et al.* 2010; Pedersen *et al.* 2012; Rohatgi & Snell 2010). Nature and localization of this barrier is largely obscure to date. By visualizing the ciliary membrane on an ultrastructural level, a more detailed knowledge regarding the dimension of the "ciliary compartment" (Hu & Nelson 2011) should be generated.

A fusion protein of the M2 (Incardona *et al.* 2002; Xie *et al.* 1998) mutant of murine Smoothened (SmoM2) with *horseradish peroxidase* (HRP) and EGFP was stably expressed in Lilly Laboratories cell porcine kidney 1 (LLC-PK_1) cells (Miyamoto *et al.* 2019) as marker for the ciliary membrane (Corbit *et al.* 2005); reviewed in (Hoffmeister *et al.* 2011). Via an HRP induced histochemical reaction (Connolly *et al.* 1994; Graham & Karnovsky 1966; reviewed in Witzgall 2018b) the HRP-SmoM2-EGFP fusion protein was visualized by transmission electron microscopy. Electron micrographs revealed a localization of HRP-SmoM2-EGFP not only at the membrane enclosing the ciliary axoneme but also at the membrane surrounding the base of primary cilia which is referred to as periciliary membrane in literature (Garcia *et al.* 2018; Garcia-Gonzalo & Reiter 2012; Long & Huang 2019; Pedersen *et al.* 2016). Therefore results of our work provide a hint that the composition of the membrane compartment at the ciliary base is more related to the ciliary membrane than to the plasma membrane.

6 Supplementary data

Movies of all 3D data sets including reconstructed STEM tomograms, overlays of fluorescence microscopic images with STEM tomograms, Amira segmentations and the 3D homology model of a part of the HRP-SmoM2-EGFP protein can be found on the enclosed DVD. In addition, uncropped images of Western blots as well as the FACS report for sorting of the RPE1/Centrin1-EGFP, mCherry-RAB8A cell line are included. The numbering of supplementary data sets/images is analogous to the numbering of the figures shown in the present work.

7 List of abbreviations

Please note, references for abbreviations are only given if they are not mentioned in the text. Chemical formulas as well as element symbols are not included within this list.

ADP: adenosine diphosphate

AKT: serine-threonine protein kinase; for further information regarding the name AKT see (Xie & Weiskirchen 2020)

APEX: genetical modifications of *ascorbate peroxidase* (Lam *et al.* 2015; Martell *et al.* 2012)

APS: ammonium peroxodisulfate

ARL: ADP (adenosine diphosphate) ribosylation factor like GTP(guanosine triphosphate)ase (NCBI Gene)

ARP: actin-related protein (NCBI Gene)

ATP: adenosine triphosphate

BBSome: “a complex composed of [...] highly conserved BBS [(Bardet-Biedl syndrome)] proteins” (Nachury *et al.* 2007)

bp: base pair

BSA: bovine serum albumin

cat. no.: catalog number

CCD: charged-coupled device (Mandracchia *et al.* 2020)

CCDC: coiled-coil domain containing

cDNA: complementary deoxyribonucleic acid

CEP: centrosomal protein

CLEM: correlative light and electron microscopy

CMV: cytomegalovirus

cm^2: square centimeter

COOH: carboxy terminus of proteins

CP: centriolar coiled-coil protein (NCBI Gene)

CRD: cysteine-rich domain

CV: ciliary vesicle

d: day

DA: distal appendages

dATP: deoxyadenosine triphosphate

DAV: distal appendage vesicles

dCTP: deoxycytidine triphosphate

DDSA: dodecenylsuccinic anhydride (Sigma-Aldrich/Merck)

dGTP: deoxyguanosine triphosphate

dH_2O: distilled water

DMEM: Dulbecco's Modified Eagle's Medium

DMP-30: 2,4,6-Tri(dimethylaminomethyl)-phenol (Carl Roth)

DNA: deoxyribonucleic acid

dNTP: deoxynucleoside triphosphate

DTT: 1,4-Dithiothreit

dTTP: deoxythymidine triphosphate

DZIP: DAZ (deleted in azoospermia) interacting zinc finger protein (NCBI Gene)

E. coli DH5α: *Escherichia coli DH* (Douglas Hanahan) *5α*; reviewed in (Tesfai *et al.* 2011)

EDTA: ethylenediaminetetraacetic acid

e.g.:	exempli gratia
EGFP:	enhanced green fluorescent protein (Arpino *et al.* 2012)
EHD:	EPS15 (epidermal growth factor receptor pathway substrate 15) homology domain-containing proteins (NCBI Gene)
EM:	electron microscopy
EPS:	epidermal growth factor receptor pathway substrate (NCBI Gene)
et al.:	et alii
FACS:	fluorescence-activated cell sorting
FLIPPER:	"fluorescent indicator and peroxidase for precipitation with EM resolution" (Kuipers *et al.* 2015)
FIB:	focused ion beam
Fig.:	figure
FIP:	RAB11 family-interacting protein
FTB:	freeze-thaw buffer (Inoue *et al.* 1990)
FTP:	it was not possible to find any information regarding the full name of FTP
g:	gram or acceleration of gravity (9.81 m/s^2)
GAP:	GTP(guanosine triphosphate)ase activating protein
GDI:	guanine nucleotide dissociation inhibitor
GDP:	guanosine diphosphate
GEF:	GTP (guanosine triphosphate) exchange factor
GLI:	glioma-associated oncogene family zinc finger (NCBI Gene)
GSK:	glycogen synthase kinase (NCBI Gene)
GTP:	guanosine triphosphate
G418:	Geneticin (Sigma-Aldrich/Merck)
h:	hour
HF:	high-fidelity (New England Biolabs)

HRP: *horseradish peroxidase*

hTERT: human telomerase reverse transcriptase (CLONTECH Laboratories, Inc. 1999)

i.a.: inter alia

i.e.: id est

IFT: intraflagellar transport

Ig: immunoglobulin

IGEPAL: octylphenoxy poly(ethyleneoxy)ethanol, branched (Merck)

IMCD: inner medullar collecting duct

IU: international unit

K: thousand

kb: kilobase

kDa: kilodalton

KIF: kinesin family member (NCBI Gene)

kV: kilovolt

L: leucine

l: liter

LB medium: lysogeny broth medium (Setzer 2018)

LLC-PK_1: Lilly Laboratories cell porcine kidney 1

M: molar

m: murine

MARK: microtubule affinity regulating kinase

mCherry: monomeric Cherry (Fink *et al.* 2010)

mg: milligram

min: minute

miniSOG: mini Singlet Oxygen Generator

ml:	milliliter
mM:	millimolar
mm:	millimeter
MNA:	Methyl-5-norbornene-2,3-dicarboxylic anhydride (Sigma-Aldrich/Merck)
mol:	6.022×10^{23} particles
MOPS:	3-(N-Morpholino)-propane sulphonic acid (Carl Roth)
MPP:	M(mitosis)-phase phosphoprotein (NCBI Gene)
mrad:	milliradian
mRuby3:	monomeric Ruby3 (Bajar *et al.* 2016)
mScarlet:	monomeric Scarlet (Bindels *et al.* 2017)
mSmoM2:	M2 mutant (in murine amino acid sequence: tryptophan 539 to leucine) of murine Smoothened
MW:	molecular mass
N:	asparagine
NDR:	nuclear Dbf(dumbbell former)2-related (Johnston & Thomas 1982; NCBI Gene; *Saccharomyces* Genome Database)
NEK:	NIMA (never in mitosis gene a)-related kinase (NCBI Gene)
NEURL:	neuralized homologue
ng:	nanogram
NH_2:	amino terminus of proteins
nm:	nanometer
nm^3:	cubic nanometer
n.s.:	no statistical significance
OC:	own constructs (internal laboratory database, Institute for Molecular and Cellular Anatomy, University of Regensburg)
OD:	optical density
ODF:	outer dense fiber

OFD:	Orofaciodigital Syndrome
OP:	outside plasmids (internal laboratory database, Institute for Molecular and Cellular Anatomy, University of Regensburg)
p.a.:	pro analysis
PACSIN:	protein kinase C and casein kinase II interacting protein
PBS:	phosphate buffered saline
PBS-T:	phosphate buffered saline with Tween 20
PCR:	polymerase chain reaction
Pfu:	*Pyrococcus furiosus* (Promega Corporation 2013)
pg:	picogram
pH:	pondus hydrogenii
PIPES:	piperazine-N,N'-bis-(2-ethanesulphonic acid) (Carl Roth)
PI3K:	phosphatidylinositol 3-kinase
PKD:	polycystic kidney disease
PMSF:	Phenylmethylsulfonylfluorid
PS:	phosphatidylserine
puriss.:	purissimum
PVDF:	polyvinylidene fluoride
RAB:	ras (rat sarcoma)-related protein (NCBI Gene; Tokumaru *et al.* 2020)
RAN:	RAS (rat sarcoma)-related nuclear protein (NCBI Gene; Tokumaru *et al.* 2020)
RAS:	rat sarcoma (Tokumaru *et al.* 2020)
RIPA:	radioimmunoprecipitation assay (Sigma-Aldrich/Merck)
RNA:	ribonucleic acid
RPE1 cells:	retinal pigment epithelial 1 cells
rpm:	rotations per minute
RT-PCR:	reverse transcription polymerase chain reaction

S: serine

s: second

sCMOS: scientific complementary metal-oxide semiconductor (Mandracchia *et al.* 2020)

sDA: subdistal appendages

SDS: sodium dodecyl sulphate

SEC: Secretory (Novick & Schekman 1979; *Saccharomyces* Genome Database)

SEM: scanning electron microscopy

SFig.: supplementary figure

siRNA: small interfering ribonucleic acid

SIRT: simultaneous iterative reconstruction technique

Smo: murine Smoothened

SmoM2: M2 mutant (in murine amino acid sequence: tryptophan 539 to leucine) of murine Smoothened

SNAP: soluble *N*-ethylmaleimide-sensitive-factor attachment protein (Ungar & Hughson 2003)

SNARE: soluble *N*-ethylmaleimide-sensitive-factor attachment protein receptor (Ungar & Hughson 2003)

SOB: super optimal broth (Fisher Scientific)

SSTR: somatostatin receptor

STEM: scanning transmission electron microscopy

T: threonine

TAE: Tris (tris(hydroxymethyl)aminomethane), acetic acid, EDTA (ethylenediamine-tetraacetic acid) (Setzer 2018)

TagRFP: Tag-red fluorescent protein (Lu *et al.* 2015; Westlake *et al.* 2011)

Taq: *Thermus aquaticus* (New England Biolabs)

TEM: transmission electron microscopy

TEMED: N,N,N′,N′-Tetramethylethylenediamine

TTBK:	tau tubulin kinase
TRAPPC:	transport particle protein complex
TRAPPII:	transport protein particle II
triCLEM:	three-microscope correlation procedure
TRIS:	tris(hydroxymethyl)aminomethane
TY:	tryptone-yeast extract (Bloem *et al.* 2002)
U:	unit (enzyme activity)
USA:	United States of America
UV:	ultraviolet
V:	volt
v/v:	volume per volume
W:	tryptophan
WDR:	WD (tryptophan-aspartic acid) repeat domain (Mishra *et al.* 2012)
Wnt:	“fusion of the name of the Drosophila segment polarity gene *wingless* and the name of the vertebrate homolog, *integrated* or *int-1*" (Komiya & Habas 2008)
w/v:	weight per volume
x:	-fold or multiplied by
µg:	microgram
µl:	microliter
µM:	micromolar
µm:	micrometer
3D:	three dimensions
3’:	three-prime end of nucleic acids (Simion 2018)
5’:	five-prime end of nucleic acids (Simion 2018)
%:	percentage
/:	per

<:	smaller than
>:	greater than
≥:	greater than or equal to
~:	approximately
+:	plus
-:	minus
°:	degree
°C:	degree Celsius
#:	symbol for number
: (colon):	to (in combination with ratios and dilutions)

8 References

Adamiok-Ostrowska, A. & Piekiełko-Witkowska, A. (2020). Ciliary Genes in Renal Cystic Diseases. *Cells*, 9: 907.

Adams, S.R., Mackey, M.R., Ramachandra, R., Palida Lemieux, S.F., Steinbach, P. & Bushong, E.A. *et al.* (2016). Multicolor Electron Microscopy for Simultaneous Visualization of Multiple Molecular Species. *Cell Chemical Biology*, 23: 1417–1427.

Ader, N.R. & Kukulski, W. (2017). triCLEM: combining high-precision, room temperature CLEM with cryo-fluorescence microscopy to identify very rare events. *Methods in Cell Biology*, 140: 303–320.

Allen, C. & Borisy, G.G. (1974). Structural Polarity and Directional Growth of Microtubules of *Chlamydomonas* Flagella. *Journal of Molecular Biology*, 90: 381–402.

Anderson, C.T., Castillo, A.B., Brugmann, S.A., Helms, J.A., Jacobs, C.R. & Stearns, T. (2008). Primary Cilia: Cellular Sensors for the Skeleton. *Anatomical Record (Hoboken)*, 291: 1074–1078.

Anderson, R.G. & Brenner, R.M. (1971). The formation of basal bodies (centrioles) in the Rhesus monkey oviduct. *The Journal of Cell Biology*, 50: 10–34.

Anderson, R.G.W. (1972). The three-dimensional structure of the basal body from the rhesus monkey oviduct. *The Journal of Cell Biology*, 54: 246–265.

Apodaca, G. (2018). Role of Polarity Proteins in the Generation and Organization of Apical Surface Protrusions. *Cold Spring Harbor Perspectives in Biology*, 10: a027813.

Archer, F.L. & Wheatley, D.N. (1971). Cilia in cell-cultured fibroblasts. II. Incidence in mitotic and post-mitotic BHK 21-C13 fibroblasts. *Journal of Anatomy*, 109: 277–292.

Ariotti, N., Hall, T.E., Rae, J., Ferguson, C., McMahon, K.-A. & Martel, N. *et al.* (2015). Modular Detection of GFP-Labeled Proteins for Rapid Screening by Electron Microscopy in Cells and Organisms. *Developmental Cell*, 35: 513–525.

Arpino, J.A.J., Rizkallah, P.J. & Jones, D.D. (2012). Crystal structure of enhanced green fluorescent protein to 1.35 Å resolution reveals alternative conformations for Glu222. *PloS One*, 7: e47132.

Asam, C., Buerger, K., Felthaus, O., Brébant, V., Rachel, R. & Prantl, L. *et al.* (2019). Subcellular localization of the chemotherapeutic agent doxorubicin in renal epithelial cells and

in tumor cells using correlative light and electron microscopy. *Clinical Hemorheology and Microcirculation*, 73: 157–167.

Bajar, B.T., Wang, E.S., Lam, A.J., Kim, B.B., Jacobs, C.L. & Howe, E.S. *et al.* (2016). Improving brightness and photostability of green and red fluorescent proteins for live cell imaging and FRET reporting. *Scientific Reports*, 6: 20889.

Barnes, B.G. (1961). Ciliated secretory cells in the pars distalis of the mouse hypophysis. *Journal of Ultrastructure Research*, 5: 453–467.

Baumgarten, S. (2015). miRNAs in the kidney and their role in podocyte (dys)function. University of Regensburg, Regensburg, Germany.

Benmerah, A. (2013). The ciliary pocket. *Current Opinion in Cell Biology*, 25: 78–84.

Benzing, T., Simons, M. & Walz, G. (2007). Wnt signaling in polycystic kidney disease. *Journal of the American Society of Nephrology*, 18: 1389–1398.

Berman, H.M., Westbrook, J., Feng, Z., Gilliland, G., Bhat, T.N. & Weissig, H. *et al.* (2000). The Protein Data Bank. *Nucleic Acids Research*, 28: 235–242.

Bernabé-Rubio, M., Andrés, G., Casares-Arias, J., Fernández-Barrera, J., Rangel, L. & Reglero-Real, N. *et al.* (2016). Novel role for the midbody in primary ciliogenesis by polarized epithelial cells. *The Journal of Cell Biology*, 214: 259–273.

Bernhard, W. & Harven, E. de (1960). L'ultrastructure du centriole et d'autres éléments de l'appareil achromatique. In: *Vierter Internationaler Kongress für Elektronenmikroskopie/ Fourth International Conference on Electron Microscopy/Quatrième Congrès International de Microscopie Électronique. Berlin 10.-17. September 1958* (ed. Bargmann, W., Möllenstedt, G., Niehrs, H., Peters, D., Ruska, E. & Wolpers, C.). Springer Verlag, Berlin, Heidelberg: pp. 217–227.

Bershteyn, M., Atwood, S.X., Woo, W.-M., Li, M. & Oro, A.E. (2010). MIM and cortactin antagonism regulates ciliogenesis and hedgehog signaling. *Developmental Cell*, 19: 270–283.

Bindels, D.S., Haarbosch, L., van Weeren, L., Postma, M., Wiese, K.E. & Mastop, M. *et al.* (2017). mScarlet: a bright monomeric red fluorescent protein for cellular imaging. *Nature Methods*, 14: 53–56.

Blacque, O.E., Scheidel, N. & Kuhns, S. (2018). Rab GTPases in cilium formation and function. *Small GTPases*, 9: 76–94.

Bloem, J.F., Botha, W.J., Law, I.J. & Steyn, P.L. (2002). Colony variation in *Sinorhizobium meliloti* inoculant strain U 45. *Microbiological Research*, 157: 283–292.

Boer, P. de, Hoogenboom, J.P. & Giepmans, B.N.G. (2015). Correlated light and electron microscopy: ultrastructure lights up! *Nature Methods*, 12: 503–513.

Bowler, M., Kong, D., Sun, S., Nanjundappa, R., Evans, L. & Farmer, V. *et al.* (2019). High-resolution characterization of centriole distal appendage morphology and dynamics by correlative STORM and electron microscopy. *Nature Communications*, 10: 993.

Breslow, D.K. & Holland, A.J. (2019). Mechanism and Regulation of Centriole and Cilium Biogenesis. *Annual Review of Biochemistry*, 88: 691–724.

Buerger, K., Schmidt, K.N., Fokkema, J., Gerritsen, H.C., Maier, O. & Vries, U. de *et al.* (2021). On-section correlative light and electron microscopy of large cellular volumes using STEM tomography. *Methods in Cell Biology*, 162: 171–203.

Bykov, Y.S., Cortese, M., Briggs, J.A.G. & Bartenschlager, R. (2016). Correlative light and electron microscopy methods for the study of virus-cell interactions. *FEBS Letters*, 590: 1877–1895.

Čajánek, L. & Nigg, E.A. (2014). Cep164 triggers ciliogenesis by recruiting Tau tubulin kinase 2 to the mother centriole. *Proceedings of the National Academy of Sciences of the United States of America*, 111: E2841–E2850.

Carlemalm, E., Garavito, R.M. & Villiger, W. (1982). Resin development for electron microscopy and an analysis of embedding at low temperature. *Journal of Microscopy*, 126: 123–143.

Carrington, G., Tomlinson, D. & Peckham, M. (2019). Exploiting nanobodies and Affimers for superresolution imaging in light microscopy. *Molecular Biology of the Cell*, 30: 2737–2740.

Caspary, T., Larkins, C.E. & Anderson, K.V. (2007). The graded response to Sonic Hedgehog depends on cilia architecture. *Developmental Cell*, 12: 767–778.

Chaumont, F. de, Dallongeville, S., Chenouard, N., Hervé, N., Pop, S. & Provoost, T. *et al.* (2012). Icy: an open bioimage informatics platform for extended reproducible research. *Nature Methods*, 9: 690–696.

Cherfils, J. & Zeghouf, M. (2013). Regulation of small GTPases by GEFs, GAPs, and GDIs. *Physiological Reviews*, 93: 269–309.

Cherry, J.M., Hong, E.L., Amundsen, C., Balakrishnan, R., Binkley, G. & Chan, E.T. *et al.* (2012). Saccharomyces Genome Database: the genomics resource of budding yeast. *Nucleic Acids Research*, 40: D700–D705.

Chiba, S., Amagai, Y., Homma, Y., Fukuda, M. & Mizuno, K. (2013). NDR2-mediated Rabin8 phosphorylation is crucial for ciliogenesis by switching binding specificity from phosphatidylserine to Sec15. *EMBO Journal*, 32: 874–885.

Clement, C.A., Ajbro, K.D., Koefoed, K., Vestergaard, M.L., Veland, I.R. & Henriques de Jesus, M.P.R. *et al.* (2013). TGF-β signaling is associated with endocytosis at the pocket region of the primary cilium. *Cell Reports*, 3: 1806–1814.

CLONTECH Laboratories, Inc. (1999). Infinity™ Telomerase-Immortalized Cell Line Culturing Guide.

Cockett, M.I., Ochalski, R., Benwell, K., Franco, R. & Wardwell-Swanson, J. (1997). Simultaneous expression of multi-subunit proteins in mammalian cells using a convenient set of mammalian cell expression vectors. *BioTechniques*, 23: 402-4, 406-7.

Cole, D.G., Diener, D.R., Himelblau, A.L., Beech, P.L., Fuster, J.C. & Rosenbaum, J.L. (1998). *Chlamydomonas* Kinesin-II-dependent Intraflagellar Transport (IFT): IFT Particles Contain Proteins Required for Ciliary Assembly in *Caenorhabditis elegans* Sensory Neurons. *The Journal of Cell Biology*, 141: 993–1008.

Collin, R., Griffith, W.P., Phillips, F.L. & Skapski, A.C. (1973). Staining and fixation of unsaturated membrane lipids by osmium tetroxide: crystal structure of a model osmium (VI) intermediate. *Biochimica et Biophysica Acta*, 320: 745–747.

Conkar, D. & Firat-Karalar, E.N. (2020). Microtubule-associated proteins and emerging links to primary cilium structure, assembly, maintenance, and disassembly. *The FEBS Journal*.

Connolly, C.N., Futter, C.E., Gibson, A., Hopkins, C.R. & Cutler, D.F. (1994). Transport into and out of the Golgi complex studied by transfecting cells with cDNAs encoding horseradish peroxidase. *The Journal of Cell Biology*, 127: 641–652.

Corbit, K.C., Aanstad, P., Singla, V., Norman, A.R., Stainier, D.Y.R. & Reiter, J.F. (2005). Vertebrate Smoothened functions at the primary cilium. *Nature*, 437: 1018–1021.

Craige, B., Tsao, C.-C., Diener, D.R., Hou, Y., Lechtreck, K.-F. & Rosenbaum, J.L. *et al.* (2010). CEP290 tethers flagellar transition zone microtubules to the membrane and regulates flagellar protein content. *The Journal of Cell Biology*, 190: 927–940.

Cranfill, P.J., Sell, B.R., Baird, M.A., Allen, J.R., Lavagnino, Z. & Gruiter, H.M. de *et al.* (2016). Quantitative assessment of fluorescent proteins. *Nature Methods*, 13: 557–562.

Cuenca, A., Insinna, C., Zhao, H., John, P., Weiss, M.A. & Lu, Q. *et al.* (2019). The C7orf43/TRAPPC14 component links the TRAPPII complex to Rabin8 for preciliary vesicle

tethering at the mother centriole during ciliogenesis. *The Journal of Biological Chemistry*, 294: 15418–15434.

Davenport, J.R. & Yoder, B.K. (2005). An incredible decade for the primary cilium: a look at a once-forgotten organelle. *American Journal of Physiology – Renal physiology*, 289: F1159–F1169.

Deane, J.A., Cole, D.G., Seeley, E.S., Diener, D.R. & Rosenbaum, J.L. (2001). Localization of intraflagellar transport protein IFT52 identifies basal body transitional fibers as the docking site for IFT particles. *Current Biology*, 11: 1586–1590.

Deshpande, I., Liang, J., Hedeen, D., Roberts, K.J., Zhang, Y. & Ha, B. *et al.* (2019). Smoothened stimulation by membrane sterols drives Hedgehog pathway activity. *Nature*, 571: 284–288.

Dishinger, J.F., Kee, H.L., Jenkins, P.M., Fan, S., Hurd, T.W. & Hammond, J.W. *et al.* (2010). Ciliary entry of the kinesin-2 motor KIF17 is regulated by importin-beta2 and RanGTP. *Nature Cell Biology*, 12: 703–710.

Drozdetskiy, A., Cole, C., Procter, J. & Barton, G.J. (2015). JPred4: a protein secondary structure prediction server. *Nucleic Acids Research*, 43: W389–W394.

Emmer, B.T., Maric, D. & Engman, D.M. (2010). Molecular mechanisms of protein and lipid targeting to ciliary membranes. *Journal of Cell Science*, 123: 529–536.

Emsley, P. & Cowtan, K. (2004). Coot: model-building tools for molecular graphics. *Acta Crystallographica Section D Biological Crystallography*, 60: 2126–2132.

Feng, S., Knödler, A., Ren, J., Zhang, J., Zhang, X. & Hong, Y. *et al.* (2012). A Rab8 guanine nucleotide exchange factor-effector interaction network regulates primary ciliogenesis. *The Journal of Biological Chemistry*, 287: 15602–15609.

Feng, Y., Press, B. & Wandinger-Ness, A. (1995). Rab 7: an important regulator of late endocytic membrane traffic. *The Journal of Cell Biology*, 131: 1435–1452.

Fink, D., Wohrer, S., Pfeffer, M., Tombe, T., Ong, C.J. & Sorensen, P.H.B. (2010). Ubiquitous expression of the monomeric red fluorescent protein mCherry in transgenic mice. *Genesis*, 48: 723–729.

Fokkema, J., Fermie, J., Liv, N., van den Heuvel, D.J., Konings, T.O.M. & Blab, G.A. *et al.* (2018). Fluorescently Labelled Silica Coated Gold Nanoparticles as Fiducial Markers for Correlative Light and Electron Microscopy. *Scientific Reports*, 8: 13625.

Follit, J.A., Tuft, R.A., Fogarty, K.E. & Pazour, G.J. (2006). The intraflagellar transport protein IFT20 is associated with the Golgi complex and is required for cilia assembly. *Molecular Biology of the Cell*, 17: 3781–3792.

Francis, S.S., Sfakianos, J., Lo, B. & Mellman, I. (2011). A hierarchy of signals regulates entry of membrane proteins into the ciliary membrane domain in epithelial cells. *The Journal of Cell Biology*, 193: 219–233.

Fu, W., Wang, L., Kim, S., Li, J. & Dynlacht, B.D. (2016). Role for the IFT-A Complex in Selective Transport to the Primary Cilium. *Cell Reports*, 17: 1505–1517.

Fujiwara, T., Ritchie, K., Murakoshi, H., Jacobson, K. & Kusumi, A. (2002). Phospholipids undergo hop diffusion in compartmentalized cell membrane. *The Journal of Cell Biology*, 157: 1071–1081.

Fuller, S.D., Gowen, B.E., Reinsch, S., Sawyer, A., Buendia, B. & Wepf, R. *et al.* (1995). The core of the mammalian centriole contains γ-tubulin. *Current Biology*, 5: 1384–1393.

Gaietta, G., Deerinck, T.J., Adams, S.R., Bouwer, J., Tour, O. & Laird, D.W. *et al.* (2002). Multicolor and Electron Microscopic Imaging of Connexin Trafficking. *Science*, 296: 503–507.

Gainullin, V.G., Hopp, K., Ward, C.J., Hommerding, C.J. & Harris, P.C. (2015). Polycystin-1 maturation requires polycystin-2 in a dose-dependent manner. *The Journal of Clinical Investigation*, 125: 607–620.

Ganga, A.K., Kennedy, M.C., Oguchi, M.E., Gray, S.D., Oliver, K.E. & Knight, T.A. *et al.* (2021). Rab34 GTPase mediates ciliary membrane formation in the intracellular ciliogenesis pathway. *Current Biology*, 31: 2895–2905.

Garcia, G., Raleigh, D.R. & Reiter, J.F. (2018). How the Ciliary Membrane Is Organized Inside-Out to Communicate Outside-In. *Current Biology*, 28: R421–R434.

Garcia-Gonzalo, F.R. & Reiter, J.F. (2012). Scoring a backstage pass: mechanisms of ciliogenesis and ciliary access. *The Journal of Cell Biology*, 197: 697–709.

García-Salcedo, J.A., Pérez-Morga, D., Gijón, P., Dilbeck, V., Pays, E. & Nolan, D.P. (2004). A differential role for actin during the life cycle of Trypanosoma brucei. *EMBO Journal*, 23: 780–789.

Geng, L., Okuhara, D., Yu, Z., Tian, X., Cai, Y. & Shibazaki, S. *et al.* (2006). Polycystin-2 traffics to cilia independently of polycystin-1 by using an N-terminal RVxP motif. *Journal of Cell Science*, 119: 1383–1395.

Gerdes, J.M., Davis, E.E. & Katsanis, N. (2009). The vertebrate primary cilium in development, homeostasis, and disease. *Cell*, 137: 32–45.

Ghossoub, R., Molla-Herman, A., Bastin, P. & Benmerah, A. (2011). The ciliary pocket: a once-forgotten membrane domain at the base of cilia. *Biology of the Cell*, 103: 131–144.

Gibbons, I.R. (1961). The relationship between the fine structure and direction of beat in gill cilia of a lamellibranch mollusc. *The Journal of Biophysical and Biochemical Cytology*, 11: 179–205.

Gibbons, I.R. & Grimstone, A. (1960). On flagellar structure in certain flagellates. *The Journal of Biophysical and Biochemical Cytology*, 7: 697–716.

Gibbons, I.R. & Rowe, A.J. (1965). Dynein: A Protein with Adenosine Triphosphatase Activity from Cilia. *Science*, 149: 424–426.

Gigante, E.D. & Caspary, T. (2020). Signaling in the primary cilium through the lens of the Hedgehog pathway. *Wiley Interdisciplinary Reviews. Developmental Biology*, 9: e377.

Gilula, N.B. & Satir, P. (1972). The ciliary necklace. A ciliary membrane specialization. *The Journal of Cell Biology*, 53: 494–509.

Goetz, S.C., Liem, K.F. & Anderson, K.V. (2012). The spinocerebellar ataxia-associated gene Tau tubulin kinase 2 controls the initiation of ciliogenesis. *Cell*, 151: 847–858.

Graham, R.C. & Karnovsky, M.J. (1966). The early stages of absorption of injected horseradish peroxidase in the proximal tubules of mouse kidney: ultrastructural cytochemistry by a new technique. *Journal of Histochemistry and Cytochemistry*, 14: 291–302.

Graser, S., Stierhof, Y.-D., Lavoie, S.B., Gassner, O.S., Lamla, S. & Le Clech, M. *et al.* (2007). Cep164, a novel centriole appendage protein required for primary cilium formation. *The Journal of Cell Biology*, 179: 321–330.

Griffiths, G. (1993). Fixation for Fine Structure Preservation and Immunocytochemistry. In: *Fine structure immunocytochemistry* (ed. Griffiths, G.). Springer, Berlin: pp. 26–89.

Gürster, S. (2013). Intrazellulärer Transport von Zilium-assoziierten Proteinen. University of Regensburg, Regensburg, Germany.

Händel, M., Schulz, S., Stanarius, A., Schreff, M., Erdtmann-Vourliotis, M. & Schmidt, H. *et al.* (1999). Selective targeting of somatostatin receptor 3 to neuronal cilia. *Neuroscience*, 89: 909–926.

Hao, L. & Scholey, J.M. (2009). Intraflagellar transport at a glance. *Journal of Cell Science*, 122: 889–892.

Hao, L., Thein, M., Brust-Mascher, I., Civelekoglu-Scholey, G., Lu, Y. & Acar, S. *et al.* (2011). Intraflagellar transport delivers tubulin isotypes to sensory cilium middle and distal segments. *Nature Cell Biology*, 13: 790–798.

Harris, P.C. & Torres, V.E. (2009). Polycystic kidney disease. *Annual Review of Medicine*, 60: 321–337.

Hattula, K., Furuhjelm, J., Arffman, A. & Peränen, J. (2002). A Rab8-specific GDP/GTP exchange factor is involved in actin remodeling and polarized membrane transport. *Molecular Biology of the Cell*, 13: 3268–3280.

Hehnly, H., Chen, C.-T., Powers, C.M., Liu, H.-L. & Doxsey, S. (2012). The centrosome regulates the Rab11- dependent recycling endosome pathway at appendages of the mother centriole. *Current Biology*, 22: 1944–1950.

Heinrich-Heine-Universität Düsseldorf. IN.SILICO Online Bioinformatics Resources. [WWW document]. URL http://www.insilico.uni-duesseldorf.de/.

Henriksen, A., Smith, A.T. & Gajhede, M. (1999). The Structures of the Horseradish Peroxidase C-Ferulic Acid Complex and the Ternary Complex with Cyanide Suggest How Peroxidases Oxidize Small Phenolic Substrates. *Journal of Biological Chemistry*, 274: 35005–35011.

Hirono, M. (2014). Cartwheel assembly. *Philosophical Transactions of the Royal Society of London. Series B, Biological Sciences*, 369: 20130458.

Hoffmeister, H., Babinger, K., Gürster, S., Cedzich, A., Meese, C. & Schadendorf, K. *et al.* (2011). Polycystin-2 takes different routes to the somatic and ciliary plasma membrane. *The Journal of Cell Biology*, 192: 631–645.

Hoffmeister, H.A. (2008). Struktur- und Funktionsanalyse von Polycystin-2. University of Regensburg, Regensburg, Germany.

Hu, Q., Milenkovic, L., Jin, H., Scott, M.P., Nachury, M.V. & Spiliotis, E.T. *et al.* (2010). A septin diffusion barrier at the base of the primary cilium maintains ciliary membrane protein distribution. *Science*, 329: 436–439.

Hu, Q. & Nelson, W.J. (2011). Ciliary diffusion barrier: the gatekeeper for the primary cilium compartment. *Cytoskeleton (Hoboken)*, 68: 313–324.

Huang, N., Zhang, D., Li, F., Chai, P., Wang, S. & Teng, J. *et al.* (2018). M-Phase Phosphoprotein 9 regulates ciliogenesis by modulating CP110-CEP97 complex localization at the mother centriole. *Nature Communications*, 9: 4511.

Hull, R.N., Cherry, W.R. & Weaver, G.W. (1976). The origin and characteristics of a pig kidney cell strain, LLC-PK$_1$. *In Vitro*, 12: 670–677.

Ibrahim, R., Messaoudi, C., Chichon, F.J., Celati, C. & Marco, S. (2009). Electron tomography study of isolated human centrioles. *Microscopy Research and Technique*, 72: 42–48.

Incardona, J.P., Gruenberg, J. & Roelink, H. (2002). Sonic Hedgehog Induces the Segregation of Patched and Smoothened in Endosomes. *Current Biology*, 12: 983–995.

Inoue, H., Nojima, H. & Okayama, H. (1990). High efficiency transformation of Escherichia coli with plasmids. *Gene*, 96: 23–28.

Inoué, S. (2006). Foundations of Confocal Scanned Imaging in Light Microscopy. In: *Handbook Of Biological Confocal Microscopy* (ed. Pawley, J.B.). Springer, New York: pp. 1–19.

Insinna, C., Lu, Q., Teixeira, I., Harned, A., Semler, E.M. & Stauffer, J. *et al.* (2019). Investigation of F-BAR domain PACSIN proteins uncovers membrane tubulation function in cilia assembly and transport. *Nature Communications*, 10: 428.

Ishikawa, H., Kubo, A., Tsukita, S. & Tsukita, S. (2005). Odf2-deficient mother centrioles lack distal/subdistal appendages and the ability to generate primary cilia. *Nature Cell Biology*, 7: 517–524.

Ishikawa, H. & Marshall, W.F. (2011). Ciliogenesis: building the cell's antenna. *Nature Reviews. Molecular Cell Biology*, 12: 222–234.

Ishikawa, H. & Marshall, W.F. (2017). Intraflagellar Transport and Ciliary Dynamics. *Cold Spring Harbor Perspectives in Biology*, 9: a021998.

Jin, H., White, S.R., Shida, T., Schulz, S., Aguiar, M. & Gygi, S.P. *et al.* (2010). The conserved Bardet-Biedl syndrome proteins assemble a coat that traffics membrane proteins to cilia. *Cell*, 141: 1208–1219.

Joberty, G., Tavitian, A. & Zahraoui, A. (1993). Isoprenylation of Rab proteins possessing a C-terminal CaaX motif. *FEBS Letters*, 330: 323–328.

Johnston, L.H. & Thomas, A.P. (1982). The isolation of new DNA synthesis mutants in the yeast *Saccharomyces cerevisiae*. *Molecular and General Genetics*, 186: 439–444.

Joo, K., Kim, C.G., Lee, M.-S., Moon, H.-Y., Lee, S.-H. & Kim, M.J. *et al.* (2013). CCDC41 is required for ciliary vesicle docking to the mother centriole. *Proceedings of the National Academy of Sciences of the United States of America*, 110: 5987–5992.

Kaneshiro, E.S. (1990). Lipids of Ciliary and Flagellar Membranes. In: *Ciliary and Flagellar Membranes* (ed. Bloodgood, R.A.). Springer US, Boston: pp. 241–265.

Kasahara, K., Kawakami, Y., Kiyono, T., Yonemura, S., Kawamura, Y. & Era, S. *et al.* (2014). Ubiquitin-proteasome system controls ciliogenesis at the initial step of axoneme extension. *Nature Communications*, 5: 5081.

Katoh, Y., Michisaka, S., Nozaki, S., Funabashi, T., Hirano, T. & Takei, R. *et al.* (2017). Practical method for targeted disruption of cilia-related genes by using CRISPR/Cas9-mediated, homology-independent knock-in system. *Molecular Biology of the Cell*, 28: 898–906.

Kee, H.L., Dishinger, J.F., Blasius, T.L., Liu, C.-J., Margolis, B. & Verhey, K.J. (2012). A size-exclusion permeability barrier and nucleoporins characterize a ciliary pore complex that regulates transport into cilia. *Nature Cell Biology*, 14: 431–437.

Keller, P., Toomre, D., Díaz, E., White, J. & Simons, K. (2001). Multicolour imaging of post-Golgi sorting and trafficking in live cells. *Nature Cell Biology*, 3: 140–149.

Keshava Prasad, T.S., Goel, R., Kandasamy, K., Keerthikumar, S., Kumar, S. & Mathivanan, S. *et al.* (2009). Human Protein Reference Database–2009 update. *Nucleic Acids Research*, 37: D767–D772.

Kiesel, P., Alvarez Viar, G., Tsoy, N., Maraspini, R., Gorilak, P. & Varga, V. *et al.* (2020). The molecular structure of mammalian primary cilia revealed by cryo-electron tomography. *Nature Structural & Molecular Biology*, 27: 1115–1124.

Kim, H., Xu, H., Yao, Q., Li, W., Huang, Q. & Outeda, P. *et al.* (2014). Ciliary membrane proteins traffic through the Golgi via a Rabep1/GGA1/Arl3-dependent mechanism. *Nature Communications*, 5: 5482.

Kim, J., Kato, M. & Beachy, P.A. (2009). Gli2 trafficking links Hedgehog-dependent activation of Smoothened in the primary cilium to transcriptional activation in the nucleus. *Proceedings of the National Academy of Sciences of the United States of America*, 106: 21666–21671.

Kim, J., Krishnaswami, S.R. & Gleeson, J.G. (2008). CEP290 interacts with the centriolar satellite component PCM-1 and is required for Rab8 localization to the primary cilium. *Human Molecular Genetics*, 17: 3796–3805.

Kim, S., Lee, K., Choi, J.-H., Ringstad, N. & Dynlacht, B.D. (2015). Nek2 activation of Kif24 ensures cilium disassembly during the cell cycle. *Nature Communications*, 6: 8087.

Klumperman, J. & Raposo, G. (2014). The complex ultrastructure of the endolysosomal system. *Cold Spring Harbor Perspectives in Biology*, 6: a016857.

Knödler, A., Feng, S., Zhang, J., Zhang, X., Das, A. & Peranen, J. *et al.* (2010). Coordination of Rab8 and Rab11 in primary ciliogenesis. *Cell*, 107: 6346–6351.

Kobayashi, T. & Dynlacht, B.D. (2011). Regulating the transition from centriole to basal body. *The Journal of Cell Biology*, 193: 435–444.

Kobayashi, T., Kim, S., Lin, Y.-C., Inoue, T. & Dynlacht, B.D. (2014). The CP110-interacting proteins Talpid3 and Cep290 play overlapping and distinct roles in cilia assembly. *The Journal of Cell Biology*, 204: 215–229.

Kobayashi, T., Tsang, W.Y., Li, J., Lane, W. & Dynlacht, B.D. (2011). Centriolar kinesin Kif24 interacts with CP110 to remodel microtubules and regulate ciliogenesis. *Cell*, 145: 914–925.

Kohli, P., Höhne, M., Jüngst, C., Bertsch, S., Ebert, L.K. & Schauss, A.C. *et al.* (2017). The ciliary membrane-associated proteome reveals actin-binding proteins as key components of cilia. *EMBO Reports*, 18: 1521–1535.

Komiya, Y. & Habas, R. (2008). Wnt signal transduction pathways. *Organogenesis*, 4: 68–75.

Kozminski, K.G., Beech, P.L. & Rosenbaum, J.L. (1995). The *Chlamydomonas* kinesin-like protein FLA10 is involved in motility associated with the flagellar membrane. *The Journal of Cell Biology*, 131: 1517–1527.

Kozminski, K.G., Johnson, K.A., Forscher, P. & Rosenbaum, J.L. (1993). A motility in the eukaryotic flagellum unrelated to flagellar beating. *Proceedings of the National Academy of Sciences of the United States of America*, 90: 5519–5523.

Kremer, J.R., Mastronarde, D.N. & McIntosh, J.R. (1996). Computer visualization of three-dimensional image data using IMOD. *Journal of Structural Biology*, 116: 71–76.

Kuhns, S., Schmidt, K.N., Reymann, J., Gilbert, D.F., Neuner, A. & Hub, B. *et al.* (2013). The microtubule affinity regulating kinase MARK4 promotes axoneme extension during early ciliogenesis. *The Journal of Cell Biology*, 200: 505–522.

Kuipers, J., van Ham, T.J., Kalicharan, R.D., Veenstra-Algra, A., Sjollema, K.A. & Dijk, F. *et al.* (2015). FLIPPER, a combinatorial probe for correlated live imaging and electron microscopy, allows identification and quantitative analysis of various cells and organelles. *Cell and Tissue Research*, 360: 61–70.

Kukulski, W., Schorb, M., Welsch, S., Picco, A., Kaksonen, M. & Briggs, J.A.G. (2011). Correlated fluorescence and 3D electron microscopy with high sensitivity and spatial precision. *The Journal of Cell Biology*, 192: 111–119.

Kukulski, W., Schorb, M., Welsch, S., Picco, A., Kaksonen, M. & Briggs, J.A.G. (2012). Precise, correlated fluorescence microscopy and electron tomography of lowicryl sections using fluorescent fiducial markers. *Methods in Cell Biology*, 111: 235–257.

Kurtulmus, B., Yuan, C., Schuy, J., Neuner, A., Hata, S. & Kalamakis, G. *et al.* (2018). LRRC45 contributes to early steps of axoneme extension. *Journal of Cell Science*, 131: jcs223594.

Lam, S.S., Martell, J.D., Kamer, K.J., Deerinck, T.J., Ellisman, M.H. & Mootha, V.K. *et al.* (2015). Directed evolution of APEX2 for electron microscopy and proximity labeling. *Nature Methods*, 12: 51–54.

Lee, J. & Chung, Y.D. (2015). Ciliary subcompartments: how are they established and what are their functions? *BMB Reports*, 48: 380–387.

L'Hernault, S.W. & Rosenbaum, J.L. (1983). *Chlamydomonas* α-Tubulin Is Posttranslationally Modified in the Flagella during Flagellar Assembly. *The Journal of Cell Biology*, 97: 258–263.

Li, J., Kim, S., Kobayashi, T., Liang, F.-X., Korzeniewski, N. & Duensing, S. *et al.* (2012). Neurl4, a novel daughter centriole protein, prevents formation of ectopic microtubule organizing centres. *EMBO Reports*, 13: 547–553.

Lippincott-Schwartz, J., Yuan, L.C., Bonifacino, J.S. & Klausner, R.D. (1989). Rapid redistribution of Golgi proteins into the ER in cells treated with brefeldin A: evidence for membrane cycling from Golgi to ER. *Cell*, 56: 801–813.

Lo, C.-H., Lin, I.-H., Yang, T.T., Huang, Y.-C., Tanos, B.E. & Chou, P.-C. *et al.* (2019). Phosphorylation of CEP83 by TTBK2 is necessary for cilia initiation. *The Journal of Cell Biology*, 218: 3489–3505.

Loktev, A.V., Zhang, Q., Beck, J.S., Searby, C.C., Scheetz, T.E. & Bazan, J.F. *et al.* (2008). A BBSome subunit links ciliogenesis, microtubule stability, and acetylation. *Developmental Cell*, 15: 854–865.

Long, H. & Huang, K. (2019). Transport of Ciliary Membrane Proteins. *Frontiers in Cell and Developmental Biology*, 7: 381.

Loukil, A., Tormanen, K. & Sütterlin, C. (2017). The daughter centriole controls ciliogenesis by regulating Neurl-4 localization at the centrosome. *The Journal of Cell Biology*, 216: 1287–1300.

Lu, Q., Insinna, C., Ott, C., Stauffer, J., Pintado, P.A. & Rahajeng, J. *et al.* (2015). Early steps in primary cilium assembly require EHD1/EHD3-dependent ciliary vesicle formation. *Nature Cell Biology*, 17: 228–240.

Madej, M.G., Sun, L., Yan, N. & Kaback, H.R. (2014). Functional architecture of MFS D-glucose transporters. *Proceedings of the National Academy of Sciences of the United States of America*, 111: E719–E727.

Maharjan, Y., Lee, J.N., Kwak, S.A., Dutta, R.K., Park, C. & Choe, S.-K. *et al.* (2020). TMEM135 regulates primary ciliogenesis through modulation of intracellular cholesterol distribution. *EMBO Reports*, 21: e48901.

Malicki, J. (2012). Who drives the ciliary highway? *Bioarchitecture*, 2: 111–117.

Malicki, J.J. & Johnson, C.A. (2017). The Cilium: Cellular Antenna and Central Processing Unit. *Trends in Cell Biology*, 27: 126–140.

Mandracchia, B., Hua, X., Guo, C., Son, J., Urner, T. & Jia, S. (2020). Fast and accurate sCMOS noise correction for fluorescence microscopy. *Nature Communications*, 11: 94.

Martell, J.D., Deerinck, T.J., Lam, S.S., Ellisman, M.H. & Ting, A.Y. (2017). Electron microscopy using the genetically encoded APEX2 tag in cultured mammalian cells. *Nature Protocols*, 12: 1792–1816.

Martell, J.D., Deerinck, T.J., Sancak, Y., Poulos, T.L., Mootha, V.K. & Sosinsky, G.E. *et al.* (2012). Engineered ascorbate peroxidase as a genetically encoded reporter for electron microscopy. *Nature Biotechnology*, 30: 1143–1148.

Matlock, B. (2015). Assessment of Nucleic Acid Purity. Technical Note 52646, Thermo Fisher Scientific, Wilmington, USA.

Mazo, G., Soplop, N., Wang, W.-J., Uryu, K. & Tsou, M.F.B. (2016). Spatial Control of Primary Ciliogenesis by Subdistal Appendages Alters Sensation-Associated Properties of Cilia. *Developmental Cell*, 39: 424–437.

McDonald, K.L. (2009). A review of high-pressure freezing preparation techniques for correlative light and electron microscopy of the same cells and tissues. *Journal of Microscopy*, 235: 273–281.

McEwen, B.F. & Marko, M. (1999). Three-Dimensional Transmission Electron Microscopy and Its Application to Mitosis Research. *Methods in Cell Biology*, 61: 81–111.

Mercer, J., Schelhaas, M. & Helenius, A. (2010). Virus Entry by Endocytosis. *Annual Review of Biochemistry*, 79: 803–833.

Mick, D.U., Rodrigues, R.B., Leib, R.D., Adams, C.M., Chien, A.S. & Gygi, S.P. *et al.* (2015). Proteomics of Primary Cilia by Proximity Labeling. *Developmental Cell*, 35: 497–512.

Milenkovic, L., Scott, M.P. & Rohatgi, R. (2009). Lateral transport of Smoothened from the plasma membrane to the membrane of the cilium. *The Journal of Cell Biology*, 187: 365–374.

Mirvis, M., Stearns, T. & James Nelson, W. (2018). Cilium structure, assembly, and disassembly regulated by the cytoskeleton. *The Biochemical Journal*, 475: 2329–2353.

Mishra, A.K., Puranik, S. & Prasad, M. (2012). Structure and regulatory networks of WD40 protein in plants. *Journal of Plant Biochemistry and Biotechnology*, 21: 32–39.

Miyamoto, R., Nozawa, T., Shiozuka, K. & Tabata, K. (2019). The Impact of Endogenous Breast Cancer Resistance Protein on Human P-Glycoprotein-Mediated Transport Assays Using LLC-PK1 Cells Transfected With Human P-Glycoprotein. *Journal of Pharmaceutical Sciences*, 108: 1085–1089.

Mogensen, M.M., Malik, A., Piel, M., Bouckson-Castaing, V. & Bornens, M. (2000). Microtubule minus-end anchorage at centrosomal and non-centrosomal sites: the role of ninein. *Journal of Cell Science*, 113: 3013–3023.

Molla-Herman, A., Ghossoub, R., Blisnick, T., Meunier, A., Serres, C. & Silbermann, F. *et al.* (2010). The ciliary pocket: an endocytic membrane domain at the base of primary and motile cilia. *Journal of Cell Science*, 123: 1785–1795.

Monis, W.J., Faundez, V. & Pazour, G.J. (2017). BLOC-1 is required for selective membrane protein trafficking from endosomes to primary cilia. *The Journal of Cell Biology*, 216: 2131–2150.

Moritz, O.L., Tam, B.M., Hurd, L.L., Peränen, J., Deretic, D. & Papermaster, D.S. (2001). Mutant rab8 Impairs docking and fusion of rhodopsin-bearing post-Golgi membranes and causes cell death of transgenic Xenopus rods. *Molecular Biology of the Cell*, 12: 2341–2351.

Morone, N., Fujiwara, T., Murase, K., Kasai, R.S., Ike, H. & Yuasa, S. *et al.* (2006). Three-dimensional reconstruction of the membrane skeleton at the plasma membrane interface by electron tomography. *The Journal of Cell Biology*, 174: 851–862.

Moyer, J.H., Lee-Tischler, M.J., Kwon, H.Y., Schrick, J.J., Avner, E.D. & Sweeney, W.E. *et al.* (1994). Candidate gene associated with a mutation causing recessive polycystic kidney disease in mice. *Science*, 264: 1329–1333.

Mukhopadhyay, S., Badgandi, H.B., Hwang, S.-H., Somatilaka, B., Shimada, I.S. & Pal, K. (2017). Trafficking to the primary cilium membrane. *Molecular Biology of the Cell*, 28: 233–239.

Nachury, M.V., Loktev, A.V., Zhang, Q., Westlake, C.J., Peränen, J. & Merdes, A. *et al.* (2007). A core complex of BBS proteins cooperates with the GTPase Rab8 to promote ciliary membrane biogenesis. *Cell*, 129: 1201–1213.

Nachury, M.V., Seeley, E.S. & Jin, H. (2010). Trafficking to the ciliary membrane: how to get across the periciliary diffusion barrier? *Annual Review of Cell and Developmental Biology*, 26: 59–87.

Nakagawa, Y., Yamane, Y., Okanoue, T. & Tsukita, S. (2001). Outer dense fiber 2 is a widespread centrosome scaffold component preferentially associated with mother centrioles: its identification from isolated centrosomes. *Molecular Biology of the Cell*, 12: 1687–1697.

Novick, P. & Schekman, R. (1979). Secretion and cell-surface growth are blocked in a temperature-sensitive mutant of *Saccharomyces cerevisiae*. *Proceedings of the National Academy of Sciences of the United States of America*, 76: 1858–1862.

Oguchi, M.E., Okuyama, K., Homma, Y. & Fukuda, M. (2020). A comprehensive analysis of Rab GTPases reveals a role for Rab34 in serum starvation-induced primary ciliogenesis. *The Journal of Biological Chemistry*, 295: 12674–12685.

Omega Bio-tek (2019). E.Z.N.A. Gel Extraction Kit. Product Manual. 4th edn., Norcross.

Paintrand, M., Moudjou, M., Delacroix, H. & Bornens, M. (1992). Centrosome organization and centriole architecture: Their sensitivity to divalent cations. *Journal of Structural Biology*, 108: 107–128.

Paoletti, A., Moudjou, M., Paintrand, M., Salisbury, J.L. & Bornens, M. (1996). Most of centrin in animal cells is not centrosome-associated and centrosomal centrin is confined to the distal lumen of centrioles. *Journal of Cell Science*, 109: 3089–3102.

Paul-Gilloteaux, P., Heiligenstein, X., Belle, M., Domart, M.-C., Larijani, B. & Collinson, L. *et al.* (2017). eC-CLEM: flexible multidimensional registration software for correlative microscopies. *Nature Methods*, 14: 102–103.

Pazour, G.J., Baker, S.A., Deane, J.A., Cole, D.G., Dickert, B.L. & Rosenbaum, J.L. *et al.* (2002a). The intraflagellar transport protein, IFT88, is essential for vertebrate photoreceptor assembly and maintenance. *The Journal of Cell Biology*, 157: 103–113.

Pazour, G.J., Dickert, B.L. & Witman, G.B. (1999). The DHC1b (DHC2) isoform of cytoplasmic dynein is required for flagellar assembly. *The Journal of Cell Biology*, 144: 473–481.

Pazour, G.J., San Agustin, J.T., Follit, J.A., Rosenbaum, J.L. & Witman, G.B. (2002b). Polycystin-2 localizes to kidney cilia and the ciliary level is elevated in orpk mice with polycystic kidney disease. *Current Biology*, 12: R378–R380.

Pearson, C.G., Osborn, D.P.S., Giddings, T.H., Beales, P.L. & Winey, M. (2009). Basal body stability and ciliogenesis requires the conserved component Poc1. *The Journal of Cell Biology*, 187: 905–920.

Pedersen, L.B., Mogensen, J.B. & Christensen, S.T. (2016). Endocytic Control of Cellular Signaling at the Primary Cilium. *Trends in Biochemical Sciences*, 41: 784–797.

Pedersen, L.B., Schrøder, J.M., Satir, P. & Christensen, S.T. (2012). The ciliary cytoskeleton. *Comprehensive Physiology*, 2: 779–803.

Pedersen, L.B., Veland, I.R., Schrøder, J.M. & Christensen, S.T. (2008). Assembly of primary cilia. *Developmental Dynamics*, 237: 1993–2006.

Peri, S., Navarro, J.D., Amanchy, R., Kristiansen, T.Z., Jonnalagadda, C.K. & Surendranath, V. *et al.* (2003). Development of human protein reference database as an initial platform for approaching systems biology in humans. *Genome Research*, 13: 2363–2371.

Perkins, G.A. (2014). The use of miniSOG in the localization of mitochondrial proteins. *Methods in Enzymology*, 547: 165–179.

Pettersen, E.F., Goddard, T.D., Huang, C.C., Couch, G.S., Greenblatt, D.M. & Meng, E.C. *et al.* (2004). UCSF Chimera?A visualization system for exploratory research and analysis. *Journal of Computational Chemistry*, 25: 1605–1612.

Pietrobono, S., Gagliardi, S. & Stecca, B. (2019). Non-canonical Hedgehog Signaling Pathway in Cancer: Activation of GLI Transcription Factors Beyond Smoothened. *Frontiers in Genetics*, 10: 556.

Piperno, G. & Fuller, M.T. (1985). Monoclonal antibodies specific for an acetylated form of alpha-tubulin recognize the antigen in cilia and flagella from a variety of organisms. *The Journal of Cell Biology*, 101: 2085–2094.

Piperno, G. & Mead, K. (1997). Transport of a novel complex in the cytoplasmic matrix of *Chlamydomonas* flagella. *Proceedings of the National Academy of Sciences of the United States of America*, 94: 4457–4462.

Pitaval, A., Senger, F., Letort, G., Gidrol, X., Guyon, L. & Sillibourne, J. *et al.* (2017). Microtubule stabilization drives 3D centrosome migration to initiate primary ciliogenesis. *The Journal of Cell Biology*, 216: 3713–3728.

Pitaval, A., Tseng, Q., Bornens, M. & Théry, M. (2010). Cell shape and contractility regulate ciliogenesis in cell cycle-arrested cells. *The Journal of Cell Biology*, 191: 303–312.

Plotnikova, O.V., Pugacheva, E.N. & Golemis, E.A. (2009). Primary Cilia and the Cell Cycle. *Methods in Cell Biology*, 94: 137–160.

Porter, K.R. (1957). The submicroscopic morphology of protoplasm. *Harvey Society Lectures.* Academic Press, New York.

Prevo, B., Scholey, J.M. & Peterman, E.J.G. (2017). Intraflagellar transport: mechanisms of motor action, cooperation, and cargo delivery. *The FEBS Journal*, 284: 2905–2931.

Promega Corporation (2013). Pfu DNA Polymerase Protocol. *Usage Information*, Madison, USA.

Prosser, S.L. & Morrison, C.G. (2015). Centrin2 regulates CP110 removal in primary cilium formation. *The Journal of Cell Biology*, 208: 693–701.

QIAGEN (2012). QIAGEN Plasmid Plus Purification Handbook. *For preparation of transfection-grade plasmid DNA from E. coli*, Hilden, Germany.

Rachel, R., Walther, P., Maaßen, C., Daberkow, I., Matsuoka, M. & Witzgall, R. (2020). Dual-axis STEM tomography at 200 kV: Setup, performance, limitations. *Journal of Structural Biology*, 211: 107551.

Rachel, R.A., Yamamoto, E.A., Dewanjee, M.K., May-Simera, H.L., Sergeev, Y.V. & Hackett, A.N. *et al.* (2015). CEP290 alleles in mice disrupt tissue-specific cilia biogenesis and recapitulate features of syndromic ciliopathies. *Human Molecular Genetics*, 24: 3775–3791.

Ratz, M., Testa, I., Hell, S.W. & Jakobs, S. (2015). CRISPR/Cas9-mediated endogenous protein tagging for RESOLFT super-resolution microscopy of living human cells. *Scientific Reports*, 5: 9592.

Reinhardt, C.G. & Krugh, T.R. (1978). A comparative study of ethidium bromide complexes with dinucleotides and DNA: direct evidence for intercalation and nucleic acid sequence preferences. *Biochemistry*, 17: 4845–4854.

Reiter, J.F., Blacque, O.E. & Leroux, M.R. (2012). The base of the cilium: roles for transition fibres and the transition zone in ciliary formation, maintenance and compartmentalization. *EMBO Reports*, 13: 608–618.

Reiter, J.F. & Leroux, M.R. (2017). Genes and molecular pathways underpinning ciliopathies. *Nature Reviews. Molecular Cell Biology*, 18: 533–547.

Revenkova, E., Liu, Q., Gusella, G.L. & Iomini, C. (2018). The Joubert syndrome protein ARL13B binds tubulin to maintain uniform distribution of proteins along the ciliary membrane. *Journal of Cell Science*, 131: jcs212324.

Rhee, H.-W., Zou, P., Udeshi, N.D., Martell, J.D., Mootha, V.K. & Carr, S.A. *et al.* (2013). Proteomic mapping of mitochondria in living cells via spatially restricted enzymatic tagging. *Science*, 339: 1328–1331.

Rohatgi, R., Milenkovic, L. & Scott, M.P. (2007). Patched1 regulates hedgehog signaling at the primary cilium. *Science*, 317: 372–376.

Rohatgi, R. & Snell, W.J. (2010). The ciliary membrane. *Current Opinion in Cell Biology*, 22: 541–546.

Rosenbaum, J.L. & Witman, G.B. (2002). Intraflagellar transport. *Nature Reviews. Molecular Cell Biology*, 3: 813–825.

Rueden, C.T., Schindelin, J., Hiner, M.C., DeZonia, B.E., Walter, A.E. & Arena, E.T. *et al.* (2017). ImageJ2: ImageJ for the next generation of scientific image data. *BMC Bioinformatics*, 18: 529.

Saito, M., Sakaji, K., Otsu, W. & Sung, C.-H. (2018). Ciliary Assembly/Disassembly Assay in Non-transformed Cell Lines. *Bio-protocol*, 8: e2773.

Sali, A. & Blundell, T.L. (1993). Comparative protein modelling by satisfaction of spatial restraints. *Journal of Molecular Biology*, 234: 779–815.

Sánchez, I. & Dynlacht, B.D. (2016). Cilium assembly and disassembly. *Nature Cell Biology*, 18: 711–717.

Santarella-Mellwig, R., Haselmann, U., Schieber, N.L., Walther, P., Schwab, Y. & Antony, C. *et al.* (2018). Correlative Light Electron Microscopy (CLEM) for Tracking and Imaging Viral Protein Associated Structures in Cryo-immobilized Cells. *Journal of Visualized Experiments*, 139: 58154.

Sastri, M., Darshi, M., Mackey, M., Ramachandra, R., Ju, S. & Phan, S. *et al.* (2017). Sub-mitochondrial localization of the genetic-tagged mitochondrial intermembrane space-bridging components Mic19, Mic60 and Sam50. *Journal of Cell Science*, 130: 3248–3260.

Satir, P. (2017). CILIA: before and after. *Cilia*, 6: 1.

Satir, P., Pedersen, L.B. & Christensen, S.T. (2010). The primary cilium at a glance. *Journal of Cell Science*, 123: 499–503.

Sato, T., Iwano, T., Kunii, M., Matsuda, S., Mizuguchi, R. & Jung, Y. *et al.* (2014). Rab8a and Rab8b are essential for several apical transport pathways but insufficient for ciliogenesis. *Journal of Cell Science*, 127: 422–431.

Saxton, W.O., Baumeister, W. & Hahn, M. (1984). Three-dimensional reconstruction of imperfect two-dimensional crystals. *Ultramicroscopy*, 13: 57–70.

Schindelin, J., Arganda-Carreras, I., Frise, E., Kaynig, V., Longair, M. & Pietzsch, T. *et al.* (2012). Fiji: an open-source platform for biological-image analysis. *Nature Methods*, 9: 676–682.

Schmidt, K.N. (2013). Molecular and functional characterization of the mother centriolar protein Cep164. Heidelberg University, Heidelberg, Germany.

Schmidt, K.N., Kuhns, S., Neuner, A., Hub, B., Zentgraf, H. & Pereira, G. (2012). Cep164 mediates vesicular docking to the mother centriole during early steps of ciliogenesis. *The Journal of Cell Biology*, 199: 1083–1101.

Schorb, M., Gaechter, L., Avinoam, O., Sieckmann, F., Clarke, M. & Bebeacua, C. *et al.* (2017). New hardware and workflows for semi-automated correlative cryo-fluorescence and cryo-electron microscopy/tomography. *Journal of Structural Biology*, 197: 83–93.

Seeley, E.S. & Nachury, M.V. (2010). The perennial organelle: assembly and disassembly of the primary cilium. *Journal of Cell Science*, 123: 511–518.

Setzer, M. (2018). Regulation of the actin cytoskeleton in podocytes by the transcription factor LMX1B. University of Regensburg, Regensburg, Germany.

Shen, M.-Y. & Sali, A. (2006). Statistical potential for assessment and prediction of protein structures. *Protein Science*, 15: 2507–2524.

Shisheva, A., Chinni, S.R. & DeMarco, C. (1999). General role of GDP dissociation inhibitor 2 in membrane release of Rab proteins: modulations of its functional interactions by in vitro and in vivo structural modifications. *Biochemistry*, 38: 11711–11721.

Shu, X., Lev-Ram, V., Deerinck, T.J., Qi, Y., Ramko, E.B. & Davidson, M.W. *et al.* (2011). A Genetically Encoded Tag for Correlated Light and Electron Microscopy of Intact Cells, Tissues, and Organisms. *PLoS Biology*, 9: e1001041.

Simion, T. (2018). DNA Replication. *Current Trends in Biomedical Engineering & Biosciences*, 16: 555942.

Singla, V. & Reiter, J.F. (2006). The primary cilium as the cell's antenna: signaling at a sensory organelle. *Science*, 313: 629–633.

Singla, V., Romaguera-Ros, M., Garcia-Verdugo, J.M. & Reiter, J.F. (2010). Ofd1, a human disease gene, regulates the length and distal structure of centrioles. *Developmental Cell*, 18: 410–424.

Smith, J.D., Snyder, W.R. & Law, J.H. (1970). Phosphonolipids in Tetrahymena cilia. *Biochemical and Biophysical Research Communications*, 39: 1163–1169.

Sorokin, S. (1962). Centrioles and the formation of rudimentary cilia by fibroblasts and smooth muscle cells. *The Journal of Cell Biology*, 15: 363–377.

Sorokin, S.P. (1968). Reconstructions of centriole formation and ciliogenesis in mammalian lungs. *Journal of Cell Science*, 3: 207–230.

Sosinsky, G.E., Giepmans, B.N.G., Deerinck, T.J., Gaietta, G.M. & Ellisman, M.H. (2007). Markers for Correlated Light and Electron Microscopy. *Methods in Cell Biology*, 79: 575–591.

Sotelo, J.R. & Trujillo-Cenóz, O. (1958). Electron microscope study on the development of ciliary components of the neural epithelium of the chick embryo. *Zeitschrift fur Zellforschung und mikroskopische Anatomie*, 49: 1–12.

Spektor, A., Tsang, W.Y., Khoo, D. & Dynlacht, B.D. (2007). Cep97 and CP110 suppress a cilia assembly program. *Cell*, 130: 678–690.

Stenmark, H. & Olkkonen, V.M. (2001). The Rab GTPase family. *Genome Biology*, 2: reviews3007.1.

Stenmark, H., Parton, R.G., Steele-Mortimer, O., Lütcke, A., Gruenberg, J. & Zerial, M. (1994). Inhibition of rab5 GTPase activity stimulates membrane fusion in endocytosis. *EMBO Journal*, 13: 1287–1296.

Stepanek, L. & Pigino, G. (2016). Microtubule doublets are double-track railways for intraflagellar transport trains. *Science*, 352: 721–724.

Stephens, R.E. (1970). Isolation of nexin–the linkage protein responsible for maintenance of the nine-fold configuration of flagellar axonemes. *Biological Bulletin*, 139: 438.

Stoops, E.H., Hull, M., Olesen, C., Mistry, K., Harder, J.L. & Rivera-Molina, F. *et al.* (2015). The periciliary ring in polarized epithelial cells is a hot spot for delivery of the apical protein gp135. *The Journal of Cell Biology*, 211: 287–294.

Stothard, P. (2000). The sequence manipulation suite: JavaScript programs for analyzing and formatting protein and DNA sequences. *BioTechniques*, 28: 1102, 1104.

Tachi, S., Tachi, C. & Lindner, H.R. (1974). Influence of ovarian hormones on formation of solitary cilia and behavior of the centrioles in uterine epithelial cells of the rat. *Biology of Reproduction*, 10: 391–403.

TaKaRa Bio. TaKaRa PCR Mycoplasma Detection Set. Product Manual. 201808th edn.

Tam, B.M., Moritz, O.L., Hurd, L.B. & Papermaster, D.S. (2000). Identification of an outer segment targeting signal in the COOH terminus of rhodopsin using transgenic Xenopus laevis. *The Journal of Cell Biology*, 151: 1369–1380.

Tanaka, K.A.K., Suzuki, K.G.N., Shirai, Y.M., Shibutani, S.T., Miyahara, M.S.H. & Tsuboi, H. *et al.* (2010). Membrane molecules mobile even after chemical fixation. *Nature Methods*, 7: 865–866.

Tanos, B.E., Yang, H.-J., Soni, R., Wang, W.-J., Macaluso, F.P. & Asara, J.M. *et al.* (2013). Centriole distal appendages promote membrane docking, leading to cilia initiation. *Genes & Development*, 27: 163–168.

Taschner, M., Bhogaraju, S. & Lorentzen, E. (2012). Architecture and function of IFT complex proteins in ciliogenesis. *Differentiation*, 83: S12-22.

Tesfai, A.T., Beamer, S.K., Matak, K.E. & Jaczynski, J. (2011). Radioresistance development of DNA repair deficient Escherichia coli DH5α in ground beef subjected to electron beam at sub-lethal doses. *International Journal of Radiation Biology*, 87: 571–578.

Tilney, L.G., Bryan, J., Bush, D.J., Fujiwara, K., Mooseker, M.S. & Murphy, D.B. *et al.* (1973). Microtubules: evidence for 13 protofilaments. *The Journal of Cell Biology*, 59: 267–275.

Tokumaru, Y., Takabe, K., Yoshida, K. & Akao, Y. (2020). Effects of MIR143 on rat sarcoma signaling networks in solid tumors: A brief overview. *Cancer Science*, 111: 1076–1083.

Tsang, W.Y., Bossard, C., Khanna, H., Peränen, J., Swaroop, A. & Malhotra, V. *et al.* (2008). CP110 suppresses primary cilia formation through its interaction with CEP290, a protein deficient in human ciliary disease. *Developmental Cell*, 15: 187–197.

Tyler, K.M., Fridberg, A., Toriello, K.M., Olson, C.L., Cieslak, J.A. & Hazlett, T.L. *et al.* (2009). Flagellar membrane localization via association with lipid rafts. *Journal of Cell Science*, 122: 859–866.

Uetake, Y., Loncarek, J., Nordberg, J.J., English, C.N., La Terra, S. & Khodjakov, A. *et al.* (2007). Cell cycle progression and de novo centriole assembly after centrosomal removal in untransformed human cells. *The Journal of Cell Biology*, 176: 173–182.

Ullrich, O., Reinsch, S., Urbé, S., Zerial, M. & Parton, R.G. (1996). Rab11 regulates recycling through the pericentriolar recycling endosome. *The Journal of Cell Biology*, 135: 913–924.

Ungar, D. & Hughson, F.M. (2003). SNARE protein structure and function. *Annual Review of Cell and Developmental Biology*, 19: 493–517.

Uzbekov, R.E., Maurel, D.B., Aveline, P.C., Pallu, S., Benhamou, C.L. & Rochefort, G.Y. (2012). Centrosome fine ultrastructure of the osteocyte mechanosensitive primary cilium. *Microscopy and Microanalysis*, 18: 1430–1441.

Vetter, M., Stehle, R., Basquin, C. & Lorentzen, E. (2015a). Structure of Rab11-FIP3-Rabin8 reveals simultaneous binding of FIP3 and Rabin8 effectors to Rab11. *Nature Structural & Molecular Biology*, 22: 695–702.

Vetter, M., Wang, J., Lorentzen, E. & Deretic, D. (2015b). Novel topography of the Rab11-effector interaction network within a ciliary membrane targeting complex. *Small GTPases*, 6: 165–173.

Vieira, O.V., Gaus, K., Verkade, P., Fullekrug, J., Vaz, W.L.C. & Simons, K. (2006). FAPP2, cilium formation, and compartmentalization of the apical membrane in polarized Madin-Darby canine kidney (MDCK) cells. *Proceedings of the National Academy of Sciences of the United States of America*, 103: 18556–18561.

Viol, L., Hata, S., Pastor-Peidro, A., Neuner, A., Murke, F. & Wuchter, P. *et al.* (2020). Nek2 kinase displaces distal appendages from the mother centriole prior to mitosis. *The Journal of Cell Biology*, 219: e201907136.

Walentek, P., Quigley, I.K., Sun, D.I., Sajjan, U.K., Kintner, C. & Harland, R.M. (2016). Ciliary transcription factors and miRNAs precisely regulate Cp110 levels required for ciliary adhesions and ciliogenesis. *eLife*, 5: e17557.

Walia, V., Cuenca, A., Vetter, M., Insinna, C., Perera, S. & Lu, Q. *et al.* (2019). Akt Regulates a Rab11-Effector Switch Required for Ciliogenesis. *Developmental Cell*, 50: 229–246.e7.

Walther, Z., Vashishtha, M. & Hall, J.L. (1994). The *Chlamydomonas* FLA10 gene encodes a novel kinesin-homologous protein. *The Journal of Cell Biology*, 126: 175–188.

Wang, C., Low, W.-C., Liu, A. & Wang, B. (2013). Centrosomal protein DZIP1 regulates Hedgehog signaling by promoting cytoplasmic retention of transcription factor GLI3 and affecting ciliogenesis. *The Journal of Biological Chemistry*, 288: 29518–29529.

Wang, L. & Dynlacht, B.D. (2018). The regulation of cilium assembly and disassembly in development and disease. *Development*, 145: dev151407.

Welsch, U. (2014). Sehorgan. In: *Lehrbuch Histologie* (ed. Welsch, U., Deller, T. & Kummer, W.). Elsevier Urban & Fischer, München, Germany: pp. 571–592.

Welsch, U., Deller, T. & Kummer, W. (eds.) (2014). Lehrbuch Histologie. 4th edn. Elsevier Urban & Fischer, München, Germany.

Westlake, C.J., Baye, L.M., Nachury, M.V., Wright, K.J., Ervin, K.E. & Phu, L. *et al.* (2011). Primary cilia membrane assembly is initiated by Rab11 and transport protein particle II (TRAPPII) complex-dependent trafficking of Rabin8 to the centrosome. *Proceedings of the National Academy of Sciences of the United States of America*, 108: 2759–2764.

Winey, M. & O'Toole, E. (2014). Centriole structure. *Philosophical Transactions of the Royal Society of London. Series B, Biological Sciences*, 369: 20130457.

Witzgall, R. (2018a). Golgi bypass of ciliary proteins. *Seminars in Cell & Developmental Biology*, 83: 51–58.

Witzgall, R. (2018b). Mechanisms of early ciliogenesis. In: *Tubular system and interstitium of the kidney: (Patho-)physiology and crosstalk. Proposal for the Establishment of the Collaborative Research Center 1350* (ed. Warth, R.). University of Regensburg, Regensburg, Germany: pp. 43–58.

Wood, C.R. & Rosenbaum, J.L. (2015). Ciliary ectosomes: transmissions from the cell's antenna. *Trends in Cell Biology*, 25: 276–285.

Wu, C.-T., Chen, H.-Y. & Tang, T.K. (2018). Myosin-Va is required for preciliary vesicle transportation to the mother centriole during ciliogenesis. *Nature Cell Biology*, 20: 175–185.

Wu, S., Mehta, S.Q., Pichaud, F., Bellen, H.J. & Quiocho, F.A. (2005). Sec15 interacts with Rab11 via a novel domain and affects Rab11 localization in vivo. *Nature Structural & Molecular Biology*, 12: 879–885.

Xie, J., Murone, M., Luoh, S.M., Ryan, A., Gu, Q. & Zhang, C. *et al.* (1998). Activating Smoothened mutations in sporadic basal-cell carcinoma. *Nature*, 391: 90–92.

Xie, J. & Weiskirchen, R. (2020). What Does the "AKT" Stand for in the Name "AKT Kinase"? Some Historical Comments. *Frontiers in Oncology*, 10: 1329.

Xu, S., Liu, Y., Meng, Q. & Wang, B. (2018). Rab34 small GTPase is required for Hedgehog signaling and an early step of ciliary vesicle formation in mouse. *Journal of Cell Science*, 131: jcs213710.

Yadav, S.P., Sharma, N.K., Liu, C., Dong, L., Li, T. & Swaroop, A. (2016). Centrosomal protein CP110 controls maturation of the mother centriole during cilia biogenesis. *Development*, 143: 1491–1501.

Yang, J., Liu, X., Yue, G., Adamian, M., Bulgakov, O. & Li, T. (2002). Rootletin, a novel coiled-coil protein, is a structural component of the ciliary rootlet. *The Journal of Cell Biology*, 159: 431–440.

Yang, T.T., Chong, W.M., Wang, W.-J., Mazo, G., Tanos, B. & Chen, Z. *et al.* (2018). Super-resolution architecture of mammalian centriole distal appendages reveals distinct blade and matrix functional components. *Nature Communications*, 9: 2023.

Yee, L.E. & Reiter, J.F. (2015). Ciliary vesicle formation: a prelude to ciliogenesis. *Developmental Cell*, 32: 665–666.

Yoder, B.K., Hou, X. & Guay-Woodford, L.M. (2002). The polycystic kidney disease proteins, polycystin-1, polycystin-2, polaris, and cystin, are co-localized in renal cilia. *Journal of the American Society of Nephrology*, 13: 2508–2516.

Yoshimura, S.-I., Egerer, J., Fuchs, E., Haas, A.K. & Barr, F.A. (2007). Functional dissection of Rab GTPases involved in primary cilium formation. *The Journal of Cell Biology*, 178: 363–369.

Zeng, J., Ren, M., Gravotta, D., Lemos-Chiarandini, C. de, Lui, M. & Erdjument-Bromage, H. *et al.* (1999). Identification of a putative effector protein for rab11 that participates in transferrin recycling. *Proceedings of the National Academy of Sciences of the United States of America*, 96: 2840–2845.

Zhang, B., Zhang, T., Wang, G., Wang, G., Chi, W. & Jiang, Q. *et al.* (2015). GSK3β-Dzip1-Rab8 cascade regulates ciliogenesis after mitosis. *PLoS Biology*, 13: e1002129.

Zheng, X., Baker, H., Hancock, W.S., Fawaz, F., McCaman, M. & Pungor, E. (2006). Proteomic analysis for the assessment of different lots of fetal bovine serum as a raw material for cell culture. Part IV. Application of proteomics to the manufacture of biological drugs. *Biotechnology Progress*, 22: 1294–1300.

Zheng, Y., Wong, M.L., Alberts, B. & Mitchison, T. (1995). Nucleation of microtubule assembly by a gamma-tubulin-containing ring complex. *Nature*, 378: 578–583.

9 Acknowledgement

At first, I would like to thank Prof. Dr. Ralph Witzgall, who gave me the opportunity to perform this work at his institute. I would like to thank you very much for your confidence in my work, your indefatigable input, your patiency and support, as well as for the pleasant working environment!

Furthermore, I would like to thank Dr. Kerstin N. Schmidt and Prof. Dr. Reinhard Rachel. You were a great support to me, stood by my side with your impressive knowledge and you were also a great moral support! It was a privilege to be introduced to the fields of molecular biology and electron microscopy by such experienced scientists. I am very grateful for the time we spent with each other! There is no better team to work with!

My special thanks also go to my closest colleagues, above all the technicians of the EM facility: Christine Maaßen, Olga Maier, Helga Othmen, Yulia Zaytseva and Anita Zügner. Without your commitment, this work would certainly not have been possible in its final form! I was very lucky to have such skilled and motivated people by my side. Thank you, Olga, for your constant help! You supported me in almost every stage of my current work with great dedication. Whenever there was a need, you stood by me. I hope that we will maintain our friendship in the future!

I would also like to thank Larissa Osten for her support with cloning, cell culture and Western blot analysis! With your tranquil and helpful character, you have been of great help to me in many situations!

My thanks also go to all the technicians that supported me during my work: Lucia Denk, Kerstin Hermann, Marion Kubitza and Karin Schadendorf. Thank you very much for your help.

I would like to thank Anita Hecht and Anthonie Maurer for performing segmentation and tomogram reconstruction, as well as for all other help and advices for problems regarding image processing.

I also thank Uwe de Vries for his support with many problems regarding fluorescence microscopy and data evaluation, Dr. Gregor Madej for making the homology model, Irina Fink and Rüdiger Eder for help with the FACS analysis and Prof. Dr. Silke Härteis for the pleasant cooperation.

I want to thank my mentor Prof. Dr. Paul Walther for his constructive discussions.

Many thanks also to my former and current PhD colleagues Katrin Brunner, Jasmin Karreis, Lisa Lucke, Sandra Meisinger and Dr. Markus Setzer. There was always a friendly and uncomplicated cooperation! You were very supportive and we had several funny moments as well. It was a great time with you!

Many thanks to all other people from the Institute for Molecular and Cellular Anatomy for your support and the pleasant working atmosphere!

Finally, I would like to thank my family, friends and my partner Vanilla for your friendship and support! Dear Vanilla, thank you very much for your understanding and your unconditional support! You enrich my life in every situation!